DOE grant DE-FG03-94ER61749

THE USE OF SIMULATIONS OF MESOSCALE CONVECTIVE SYSTEMS TO BUILD A CONVECTIVE PARAMETERIZATION SCHEME

by G. David Alexander

William R. Cotton, P.I.

Colorado
State
University

DEPARTMENT OF ATMOSPHERIC SCIENCE

PAPER NO. **592**

THE USE OF SIMULATIONS OF MESOSCALE CONVECTIVE SYSTEMS TO BUILD A CONVECTIVE PARAMETERIZATION SCHEME

by

G. David Alexander

Department of Atmospheric Science

Colorado State University

Fort Collins, Colorado 80523

Research Supported by

Department of Energy

under Grant DE-FG03-94ER61749.

December 1, 1995

Atmospheric Science Paper No. 592

ABSTRACT

THE USE OF SIMULATIONS OF MESOSCALE CONVECTIVE SYSTEMS TO BUILD A CONVECTIVE PARAMETERIZATION SCHEME

A method is described for parameterizing thermodynamic forcing by the mesoscale flow branches of mesoscale convective systems (MCSs) in models with resolution too coarse to resolve these flow branches. This thermodynamic portion of the parameterization contains improvements over previous schemes, including a more sophisticated convective driver and inclusion of the vertical distribution of various physical processes obtained through conditional sampling of two cloud-resolving MCS simulations. A convective momentum parameterization has also been included as a separate component of the parameterization scheme. The momentum scheme includes a parameterization of the convective-scale pressure gradient force, and therefore can account for the effect of the mesoscale organization of the convection on the large-scale momentum tendencies. The mesoscale parameterization is tied to a version of the Arakawa-Schubert convective parameterization scheme which is modified to employ a prognostic closure. The parameterized Arakawa-Schubert cumulus convection provides condensed water, ice, and water vapor which drives the parameterization for the large-scale effects of mesoscale circulations associated with the convection. In the mesoscale thermodynamic parameterization, determining thermodynamic forcing of the large scale depends on knowing the vertically integrated values and the vertical distributions of phase transformation rates and mesoscale eddy fluxes of entropy and water vapor in mesoscale updrafts and downdrafts. The relative magnitudes of these quantities are constrained by assumptions made about the relationships between various quantities in an MCS's water budget deduced from the cloud-resolving MCS simulations. The MCS simulations include one of a tropical MCS observed during the 1987 Australian monsoon season (EMEX9), and one of a midlatitude MCS observed during a 1985 field experiment in the central Plains of the U.S. (PRE-STORM 23-24 June).

G. David Alexander
Atmospheric Science Department
Colorado State University
Fort Collins, CO 80523
Spring 1996

ACKNOWLEDGMENTS

Performing the two numerical simulations presented in this study was a challenge and a frustration. Two people in particular provided invaluable assistance. Dr. Peter Olsson's simulation of the PRE-STORM MCS served as a starting point for the simulation presented here. His previous work made life much easier for me. Dr. Takemong Wong provided guidance on the configuration of the model for the EMEX9 MCS simulation along with the dataset used to initialize the simulation. The NCAR data support staff provided assistance in obtaining other datasets used to initialize the simulations. Finally, my comrades in the CSU RAMS modelling group provided continuing advice on wading through the dreaded RAMS morrass.

Thanks go to Dr. David Randall for allowing the CSU GCM convective parameterization code to be used in this study. Don Dazlich of the Randall research group is also thanked for his help in getting me up to speed on the nuances of this code.

Hongli Jiang, Scot Rafkin, and Bjorn Stevens provided helpful comments on this manuscript. I also want to thank Bjorn for being a great officemate and friend.

Finally, thanks go to my adviser Dr. William Cotton, for his unobtrusive ways and his patience. No student could expect a better adviser.

This work was funded by the Department of Energy under grant DE-FG03-94ER61749.

TABLE OF CONTENTS

LIST OF TABLES

LIST OF FIGURES

Chapter 1

INTRODUCTION

1.1 Mesoscale convective systems

Contrary to theories that conditional instability should favor convective cells separated from one another by as much distance as possible (e.g., Holton 1979), cumulus convective cells frequently organize with one another into various configurations. Zipser (1982) proposed the term mesoscale convective system (MCS) to refer to all organized precipitation systems on scales from 20 to 500 km that include deep convection during some part of their lifetime. Zipser's broad definition encompasses a incredibly wide range of weather systems. The most commonly investigated type of MCSs are those in which the convection is oriented in a line—squall lines. Often, however, the cells are more chaotically arranged. Such MCSs are often called "non-squall" MCSs. If an MCS's upper-level cloud shield meets special size and shape criteria, the MCS is called a mesoscale convective complex, or MCC (Maddox 1980). MCSs encompass a much broader range of weather systems than just squall lines and MCCs, however. In fact, as long as you have some organized collection of convective cells, you have an MCS—there are no special requirements on the number of cells, the aggregate area covered by the cells, or the nature of the mesoscale organization of the cells. As a result, other weather systems that technically qualify as MCSs would include multicell thunderstorm complexes, easterly waves, tropical depressions, and even tropical cyclones and polar lows. MCSs can occur essentially anywhere in the world, then, and in some regions (e.g., the High Plains of the U.S.) can be the dominant producers of annual precipitation (Fritsch et al. 1986).

The organization of convective cells onto larger scales frequently enables mesoscale circulations to develop. These mesoscale circulations are distinct from both the convective circulations within the cells themselves and the larger-scale synoptic circulations—indeed, these mesoscale circulations are the fundamental distinguishing factor between MCSs and isolated convective cells (or "ordinary" convection). Because convective cells in MCSs can be arranged in such a wide range of ways, the mesoscale flow branches which define the mesoscale circulations can go every which way, snaking around, between, above, and below one another in as many ways as you could imagine. However, the *net* effect of all of these flow branches is generally consistent among MCSs. As a result, researchers have proposed various conceptual models of MCSs, all of which exhibit the same general features. The following section describes one such conceptual model.

1.2 A conceptual model of MCSs

The mesoscale organization of convection and stratiform precipitation varies widely from one MCS to the next. For instance, observed patterns of mesoscale structure in MCSs in the tropical waters north of Australia during the Equatorial Mesoscale Experiment (EMEX) were (1) a leading line of convection trailed by a region of stratiform precipitation (squall line), (2) line(s) of convection embedded within stratiform precipitation, (3) loosely organized convective cells embedded within stratiform precipitation, and (4) a line of convection isolated from any stratiform precipitation (Bograd 1989). In addition, the convection in some MCSs tends to configure itself in an organized nonlinear pattern resembling a frontal wave (e.g., Fortune et al. 1992). As a result, it is simply impossible for one conceptual model to be truly representative of all MCSs. Despite their widely varying structures, however, almost all MCSs do contain two clearly identifiable precipitation regions. The convective region includes areas of localized heavy precipitation which may rain at rates on the order of 100 mmh^{-1}; the stratiform region includes areas of more widespread, lighter precipitation where rain rates are $\sim$ 1-10 mmh^{-1}. Generally, MCSs also include cloudy areas where no precipitation is occurring. The relative coverage areas of these three regions varies markedly from one MCS to the next. Most MCSs have large stratiform regions but occasionally an MCS is observed to have virtually no stratiform region (e.g., the EMEX2 MCS documented by Peters 1989). Within a single MCS the relative coverage areas of these three regions varies as the MCS evolves through its life cycle.

The most common MCS conceptual model is that of the squall line (e.g., Houze 1989). The features of a real MCS may depart significantly from this model, but the net effect remains similar. Houze's conceptual model of a mature MCS (Fig. 1.1) depicts a leading convective line and a trailing stratiform region which extends behind the convection for several hundred kilometers. The convective towers contain positively buoyant updrafts, negatively buoyant downdrafts, and heavy rain showers. The stratiform region, which in part is formed by the hydrometeors detrained from the convective towers, contains a deep stratiform cloud which extends from the mid-troposphere to the top of the cirrus shield. The idealized MCS also contains distinct mesoscale system-relative flow branches. One of the flow branches originates with upward lifting just above the boundary layer (say, between 2 and 4 km) and slopes gently into the trailing stratiform cloud at middle to upper levels (Cotton et al. 1995). In the stratiform region, this ascending flow branch comprises the "mesoscale updraft." Another flow branch begins as gently descending rear inflow which runs just under the base of the trailing stratiform cloud and enters the stratiform region just above the melting level. It continues to subside to the level of the radar bright band, passes through the melting level and then finally enters the back of the convective region at low levels. In the stratiform region, this descending flow branch comprises the "mesoscale downdraft."

The relative proportions of convective and stratiform regions in an MCS can vary considerably through its life cycle. Houze (1982) presents a four-stage conceptual model for the life cycle of an idealized MCS (Fig. 1.2). A brief summary of the stages:

(1) Early. The MCS only contains isolated convective towers.

(2) Mature. In addition to the convective towers, the MCS also contains a large region of lighter precipitation extending over at least 100-200 km. The lighter precipitation falls from a stratiform cloud located between the mid-troposphere and the top of the cirrus shield.

(3) Weakening. The convective towers disappear, and any stratiform precipitation

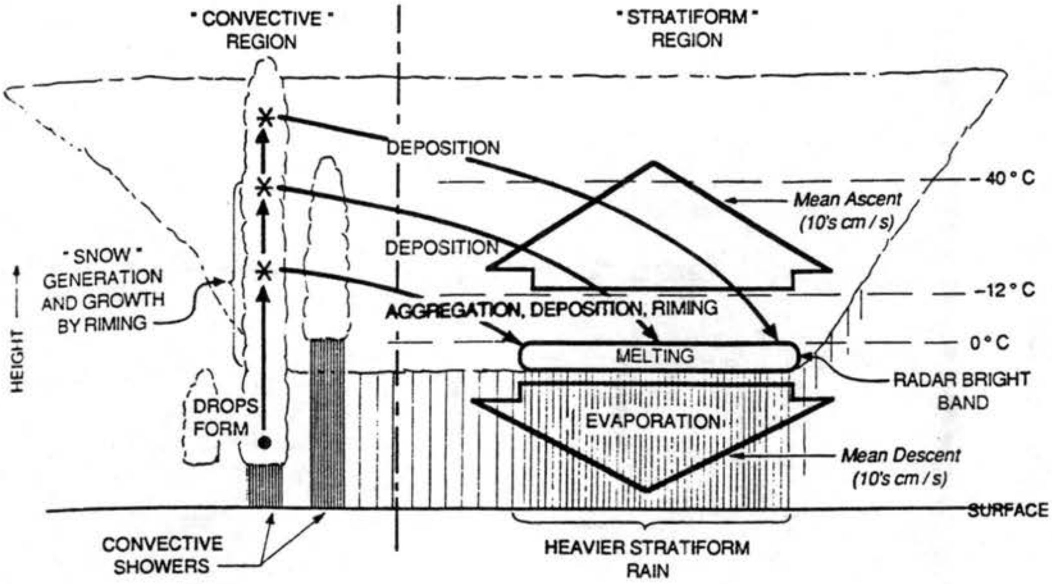

Fig. 1.1: Conceptual model of the kinematic, microphysical, and radar-echo structure of a convective line with trailing stratiform precipitation viewed in a vertical cross section oriented perpendicular to the convective line (and generally parallel to its motion). From Houze et al. (1989).

that remains is weak and often does not reach the surface.

(4) Dissipating. No precipitation remains and the upper cloud thins and breaks up.

Many MCSs tend to go through the life cycle stages described above at similar times of day. Wetzel et al. (1983) observed that midlatitude MCSs typically reached maturity during the early morning hours. McBride and Gray (1980) observed similar behavior in tropical MCSs, and attributed this behavior to nocturnal differences in the radiative heating profiles in cloudy and cloud-free regions—differences which may

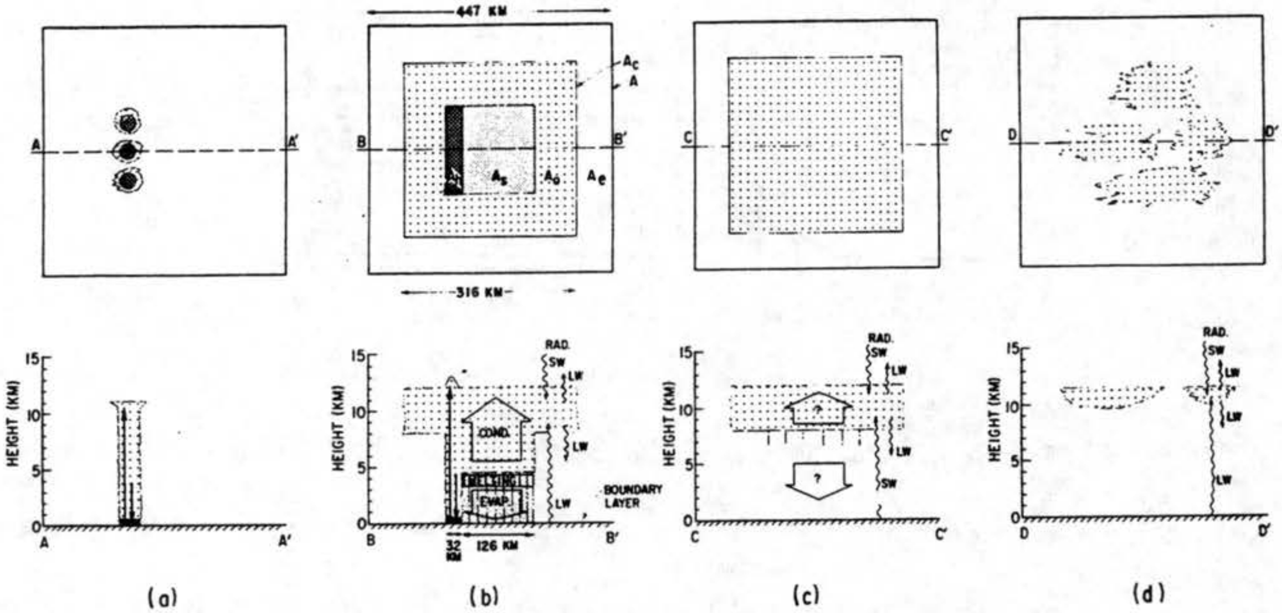

Fig. 1.2: Schematic of a tropical cloud cluster in four successive stages of development. (a) Early stage in which cluster consists of isolated precipitating towers. (b) Mature stage in which a cloud shield has developed and covers A_c, convective cells are located in area A_h, stratiform precipitation is falling from a middle-level cloud base within area A_s, and an area A_o is covered by upper-level cloud overhang. (c) Weakening stage in which convective cells have disappeared but stratiform precipitation remains. (d) Dissipating stage in which no precipitation remains and upper cloud is becoming thin and breaking up. From Houze (1982).

lead to maximum low-level convergence in the morning in the cloudy areas. Johnson and Kriete (1982) and Williams and Houze (1987) also observed tropical MCSs that attained an early morning maximum. Analysis of large samples of MCSs from both the tropics and midlatitudes provides further evidence of their preferred nocturnal nature. Miller and Fritsch (1991) studied the diurnal distributions of the times at which MCSs over a broad area of the Western Pacific were observed at various stages in their life cycles. Maddox et al. (1986) did the same for midlatitude MCSs. In both cases, the MCSs tended to develop in the evening, reach maturity during the night, and dissipate during the late morning. Because the upper-level anvil often dissipates sluggishly during the day, shortwave radiative heating of this anvil can significantly modulate the larger-scale circulation (e.g., Ackerman et al. 1988).

1.3 The effect of MCSs on the large-scale flow

Before getting into the details of how the mesoscale flow branches in MCSs may be parameterized, we consider the general question of the way in which MCSs affect the large-scale flow fields. Mapes and Houze (1992) have described how one may analyze the effects of MCSs on the large-scale flow through use of an equation for the vorticity of the resolved flow. In this equation, horizontal divergence is a thermal forcing term. This vorticity equation stems from a momentum equation governing a hydrostatic, pressure-coordinate synoptic-scale representation ($\mathbf{v}$, ω) of an actual flow field, $\mathbf{v}$ being the horizontal wind vector (u,v,0), and ω the rate of change of pressure following a parcel of air. The vorticity equation is

$$\frac{D\zeta_a}{Dt} = -\zeta_a(\nabla_p \cdot \mathbf{v}) - \hat{\mathbf{k}} \cdot \nabla_{\mathrm{p}} \times (\omega \frac{\partial \mathbf{v}}{\partial \mathrm{p}} - \mathbf{F}) \tag{1.1}$$

where t is time, p is pressure, $\hat{\mathbf{k}}$ is the vertical unit vector, $\nabla_p = (\frac{\delta}{\delta x}, \frac{\delta}{\delta y}, \frac{\delta}{\delta p})$, $\zeta = \hat{\mathbf{k}} \cdot \nabla_{\mathrm{p}} \times \mathbf{U}$ is the vertical component of relative vorticity, ζ_a is the absolute vorticity $f+\zeta$ (where f is the Coriolis parameter), and $\mathbf{F}$ is the residual or apparent acceleration on the resolved scale resulting from all sub-resolvable sources of momentum (including horizontal and vertical transports and non-hydrostatic pressure gradient forces).

The forcing of larger-scale flow by embedded MCSs is expressed by the two source terms on the right side of (1.1). The first term on the right side, called the "vortex stretching" or convergence, acts to increase the magnitude of absolute vorticity of either sign in the presence of convergence, and to decrease it in the presence of divergence. This term will be concentrated in areas of precipitation, where in general net low-level convergence and upper-level divergence prevail (this convergence and divergence are associated with the net MCS heating). The second term on the right-hand side of (2) is the curl of the apparent acceleration resulting from the total vertical advection of momentum, "mean" plus "eddy" (plus all other neglected accelerations). This term will also be concentrated in areas of precipitation, with the subgrid-scale momentum source $\mathbf{F}$ frequently dominated by vertical transports within MCSs. This second term will sometimes manifest itself as upper-tropospheric vorticity couplets straddling MCSs, positive to the left and negative to the right of $\mathbf{F}$ (e.g., Tollerud and Esbensen 1983; Sui and Yanai 1986). Equation (1.1) shows, therefore, that assessing the effect of MCSs on the large-scale flow depends critically on diagnosing (1) $\nabla_p \cdot \mathbf{v}$ the net vertical profile of divergence associated with an MCS, and (2) **F**, the acceleration resulting from sub-resolvable momentum sources.

As Mapes and Houze (1993) point out, in the tropical or warm-season midlatitude environments in which MCSs typically occur, divergence and heating are virtually inseparable quantities. To see this, consider the thermodynamic equation in isobaric coordinates

$$\frac{\partial T}{\partial t} + \mathbf{U} \cdot \nabla \mathrm{T} = \omega\sigma + \mathrm{Q}_1 \tag{1.2}$$

where T is the temperature, σ is the static-stability parameter $(\frac{T}{\theta})(\frac{\partial\theta}{\partial p})$, θ is the potential temperature, and Q_1 is the heating rate in degrees per unit time t. If temperature varies little from time to time and place to place then the left-hand side is small and the apparent heat source Q_1 is directly proportional to the mean vertical velocity. Through continuity, the vertical velocity is simply the vertical integral of the horizontal divergence.

The foregoing discussion shows that an MCS's forcing will be sensitive to the shape of its net vertical divergence (or heating) profile. Because an MCS's convective and stratiform regions have individual vertical divergence profiles of much different shapes (and magnitudes), the exact nature of the net profile will depend on how much each contributes. Fig. 1.3, for example, shows the vertical distribution of divergence associated with a tropical squall line whose precipitation is organized into a leading convective region and a trailing stratiform region (Gamache and Houze 1982). The divergence averaged over the convective region is characterized by convergence in the

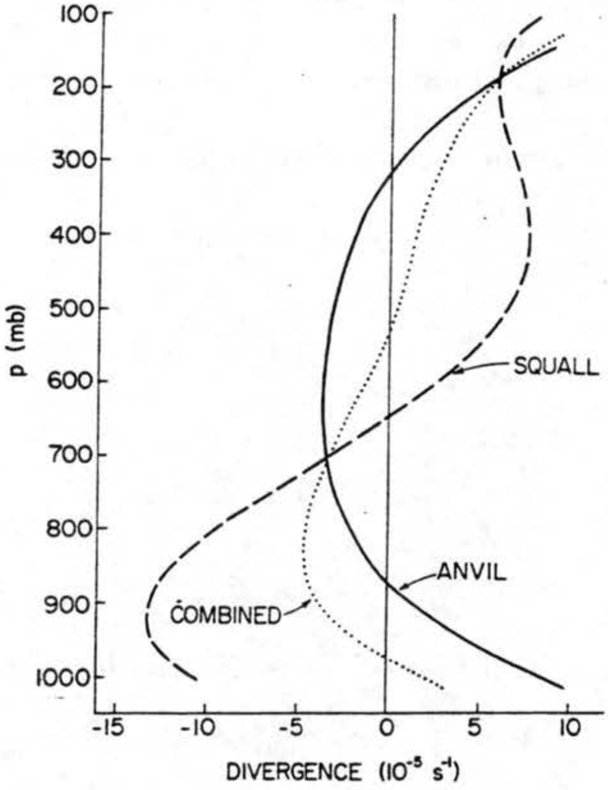

Fig. 1.3: Average divergence over the convective (dashed), stratiform (solid), and combined (dotted) regions of a tropical squall-line system. From Gamache and Houze (1982).

lower troposphere and divergence above there. The divergence averaged over the stratiform region is characterized by a layer of convergence in the middle troposphere surrounded by divergence above and below there. The net divergence profile, which is the weighted sum of the divergence profiles of the two regions shows weak divergence at low levels and a level of maximum convergence elevated well off the surface.

The Fig. 1.3 divergence profiles are typical not only of squall lines but also of MCSs that exhibit a wider variety of mesoscale organizations. Fig. 1.4, for instance,

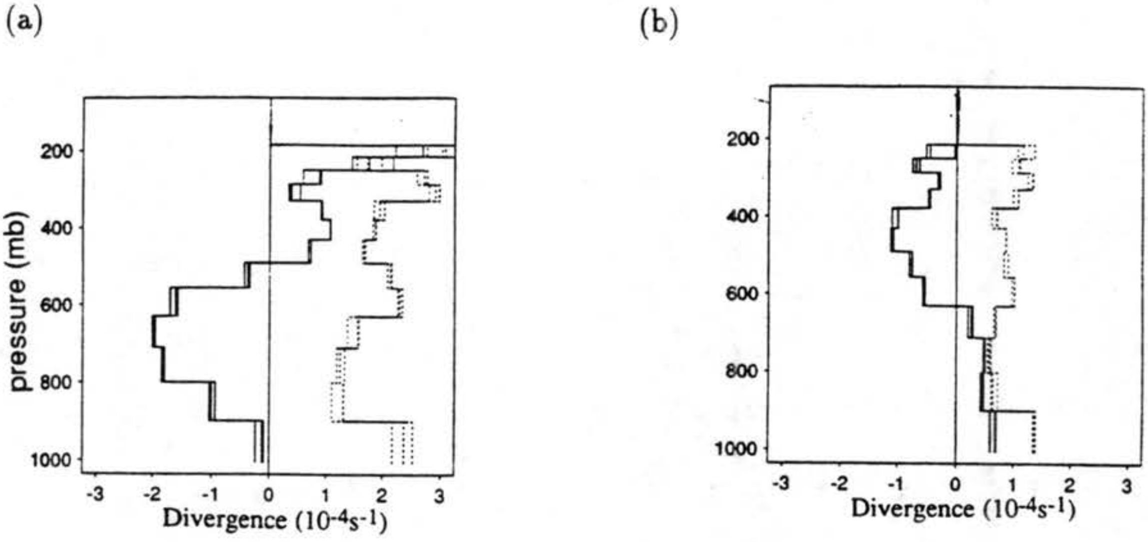

Fig. 1.4: Mean (solid) and standard deviation (dotted) of (a) convective and (b) stratiform divergence observed by airborne Doppler radar in EMEX MCSs. From Mapes and Houze (1993).

shows Doppler radar-derived divergence profiles for convective and stratiform regions of a whole range of EMEX MCSs (Mapes and Houze 1993). The shapes of these curves are generally the same as their Fig. 1.3 counterparts. In convective regions, the maximum convergence is elevated and is found at about 700 mb; above 500 mb, divergence predominates. In stratiform regions, there is convergence between 600 and 200 mb with divergence above and below there. The Doppler radar was not sensitive enough to detect any divergence that must have been present, through mass continuity, above 200 mb.

1.4 Parameterizing MCSs in large-scale models

1.4.1 Key issues

The present spatial resolution of many general circulation models (GCMs) resolves neither convection or its attendant mesoscale circulations. As a result, both should be "parameterized". This problem of insufficient model resolution is frequently given as the primary motivation for developing a convective parameterization. An even more fundamental reason to tackle the parameterization problem, however, is that convection is something that's just worth understanding. Even if we don't need to parameterize it in a model (which, eventually, we won't), we still would want to understand the nature of its fundamental components.

When parameterizing MCSs as opposed to parameterizing "ordinary" convection, two key issues covered in Section 1.2 need to be addressed. First, unlike "ordinary" convection, the convection in MCSs may be organized on the mesoscale. Second, the convection in MCSs is often accompanied by huge areas of stratiform precipitation. To understand the importance of these two issues, consider the ways in which cumulus and mesoscale processes individually contribute to the large-scale flow. First, consider cumulus contributions. These may be explained as resulting from the detrainment of heat and moisture from cumulus clouds, the subsidence of environmental air which compensates the convective mass flux, and the convective-scale horizontal pressure gradient force acting on the environment. Most operational mass-flux parameterizations (e.g., the Arakawa-Schubert scheme) consider the first two effects. The latter effect is typically neglected. This pressure gradient force effect, however, is sensitive to mesoscale organization (that is, whether and how the convection is organized). Next, consider mesoscale contributions. These primarily result from the effects of the condensation, freezing, and deposition within the stratiform cloud as well as the evaporation of rainwater and melting of frozen precipitation beneath the stratiform cloud. The eddy flux convergences of entropy and water vapor may also be important. The magnitude of mesoscale contributions depends essentially on the life-span and spatial extent of an MCS's stratiform region. We now consider, in turn, the effect of the mesoscale organization on the large-scale thermodynamic and momentum fields.

1.4.2 Thermodynamic effects

Heretofore, mesoscale effects have not been included in GCM convective parameterization schemes, leading to small (but not negligible) errors in diagnosed heating and moistening. Wu (1993), for instance, assessed the errors which arise in parameterization schemes that fail to consider mesoscale effects. Fig. 1.5, for instance, shows vertical profiles of observed Q_1 and Q_2 and diagnosed Q_{1c} and Q_{2c} for MCSs observed over the south-central U.S. on 4 June 1985 and 10 June 1985. The quantities Q_1 and Q_2 are the residuals of the heat and moisture budgets of the resolvable motion, respectively, and as such, represent the "apparent" heat source and moisture sink, respectively (Yanai et al. 1973). The quantities Q_{1c} and Q_{2c} represent the diagnosed contributions of cumulus clouds (condensation, evaporation, and convective transports) to the environment. Comparing the profiles of Q_1, Q_2, and Q_{1c}, Q_{2c}, it is clear that insufficient heating and drying appear in the upper troposphere, and excessive heating and drying in the lower troposphere. These differences in the observed and

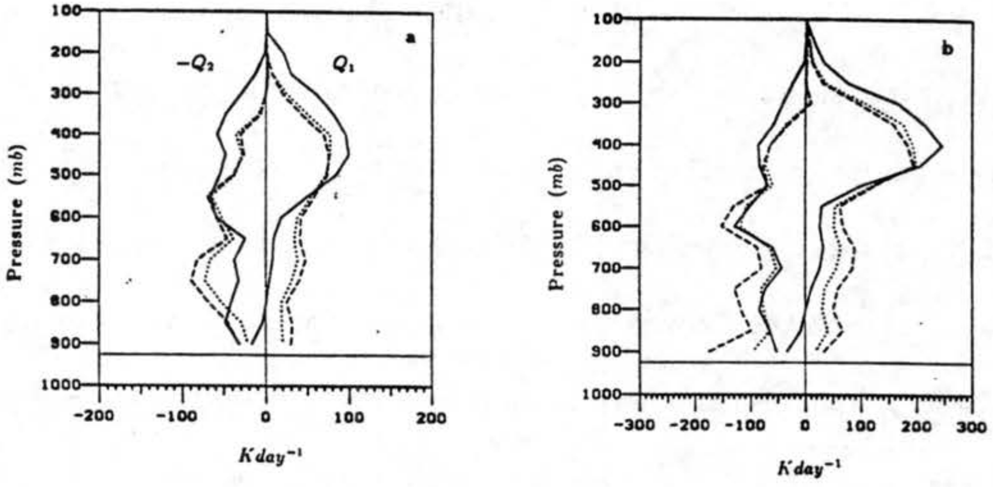

Fig. 1.5: Vertical profiles of observed Q_1 and $-Q_2$ (solid) and diagnosed Q_{1c} and $-Q_{2c}$ from Q_1-Q_2 using a cumulus ensemble model with updraft only (dashed) and with convective-scale downdrafts (dotted) for MCSs observed over the south-central U.S. at (a) 0000 UTC 4 June 1985, and (b) 0300 UTC 11 June 1985. From Wu (1993).

diagnosed profiles suggest the presence of additional heating and drying in the upper troposphere due to mesoscale updrafts and additional cooling and moistening in the lower troposphere due to mesoscale downdrafts. Estimated values of mesoscale effects Q_{1m} and Q_{2m} (Wu assumes both to be $[(Q_1\text{-}Q_{1c})+(Q_2\text{-}Q_{2c})]/2)$ show positive values in the upper troposphere and negative values in the lower troposphere whose maximum magnitudes are roughly 20-30 % as large as the maximum magnitudes of Q_{1c} and Q_{2c} (Fig. 1.6).

1.4.3 Momentum effects

Diagnosed momentum forcing, which is also expected to be sensitive to mesoscale organization, is also not typically accounted for in GCM convective parameterization

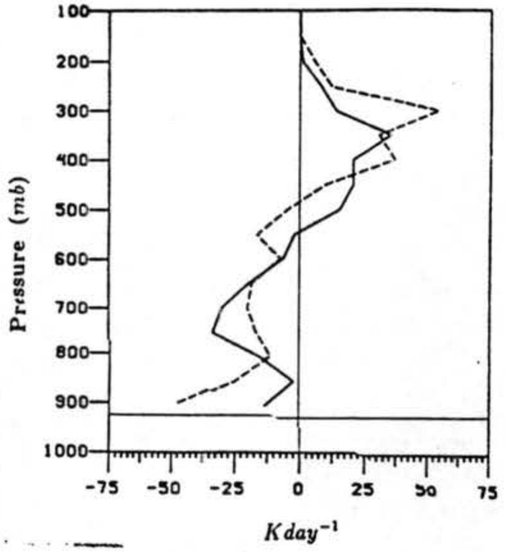

Fig. 1.6: Vertical profiles of Q_{1m} ($\approx Q_{2m}$) for MCSs observed at 0000 UTC 4 June (solid) and 0300 UTC 11 June (dashed). From Wu (1993).

schemes. As discussed by Wu and Yanai (1994), the effects of cumulus convection on the large scale flow are through the subsidence of environmental air that compensates the cloud mass flux, the detrainment of momentum from clouds, and the convective-scale horizontal pressure gradient force acting on the environment. To show how MCSs affect the horizontal wind field, consider two cases described by Wu and Yanai (1994). Fig. 1.7 shows the evolution of the horizontal wind field during the passage of a nonsquall MCS observed over the south-central U.S. between 1800 UTC 20 May and 0000 UTC 21 May 1985. As convection develops between 1800 UTC and 2100 UTC, the vertical shears of both components of the wind in the upper layer decrease, presumably as a result of vertical mixing of horizontal momentum by active cumulus convection (downgradient momentum transport). The vertical shear of the meridional component increases again between 2100 UTC and 0000 UTC as convection decays. Fig. 1.8 shows a similar analysis, except for a squall line MCS observed over the

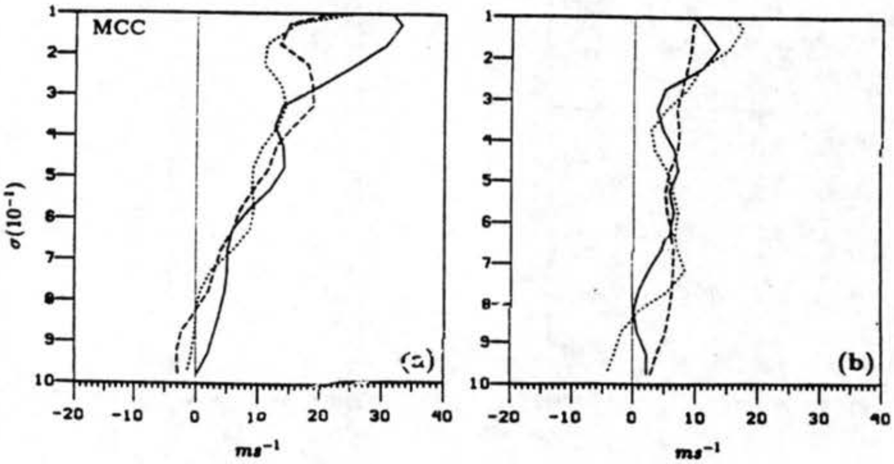

Fig. 1.7: Vertical profiles of (a) zonal and (b) meridional components of the horizontal wind averaged over a 180 km × 180 km domain at 1800 UTC 20 May (solid), 2100 UTC 20 May (dashed), and 0000 UTC 21 May 1985 (dotted).

south-central U.S. between 0300 UTC 10 May and 0900 UTC 10 May 1979. The two wind components shown are line-normal and line-parallel. Here, the vertical shear of the line-normal component increases as convection develops between 0300 UTC and 0900 UTC (upgradient momentum transport) whereas the vertical shear of the line-parallel component of the wind decreases during this six-hour period (downgradient momentum transport).

Figs. 1.7 and 1.8 above illustrate how the acceleration of the horizontal wind by the convective-scale pressure gradient force likely is sensitive to the degree and nature of mesoscale organization of convective elements. Wu and Yanai argue that for nonsquall MCSs, the vertical shear of both components of the environmental wind in the upper troposphere typically decreases as convection intensifies (as in Fig. 1.7). On the other hand, for squall line MCSs, the vertical shear of the line-normal component of the

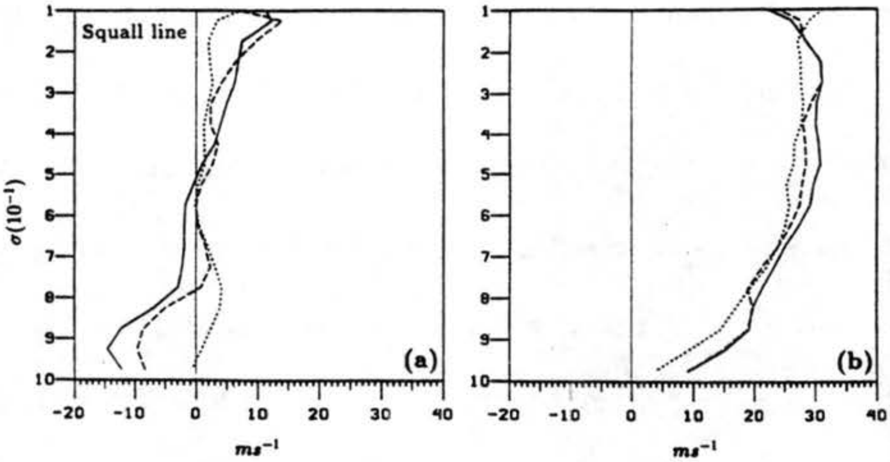

Fig. 1.8: Vertical profiles of (a) line-normal and (b) line-parallel components of the horizontal wind averaged over a 180 km × 180 km domain at 0300 UTC 10 May (solid), 0600 UTC 10 May (dashed), and 0900 UTC 10 May 1979 (dotted).

environmental wind in the upper troposphere typically *increases* whereas that of the line-parallel component typically decreases as convection intensifies (as in Fig. 1.8).

1.4.4 An alternate approach

Before moving on, in Chapter 2, to detailed discussion of the issues raised above, consider an alternate approach to parameterizing MCSs. Moncrieff (1992) proposes a dynamically-based way to parameterize the effects of organized convection on the large-scale circulation. In his parameterization, rather than considering fluxes as being defined from deviations from horizontal means, he considers organized mesoscale convection to be a complete dynamical entity. He determines momentum transport by employing a two-dimensional archetype triple-branch model (like the one in Fig. 1.1). Flow branches in his triple-branch model obey certain conservation principles and integral constraints (e.g., mass continuity and Bernoulli's equation are satisfied and the vertical divergence of the line-normal momentum flux is constrained to be zero). LeMone and Moncrieff (1994) showed that for ten real-world squall lines, Moncrieff's parameterization is able to successfully replicate the general shapes of vertical mass flux and line-normal momentum flux profiles. The parameterization was less successful in predicting the vertical flux of line-parallel momentum. As Wu and Yanai (1994) point out, a difficult problem in Moncrieff's approach is how to relate the modeled fluxes to the large-scale equations. Also, Moncrieff's approach may be oversimplified. Convective systems may frequently more closely resemble various other conceptual flow-branch models (e.g., Moncrieff 1981). So deciding which archetypal dynamic model to activate becomes a complicating factor. Also, applying the Moncrieff (1992) model in practice (as LeMone and Moncrieff did) requires a line orientation to be specified. This is not appropriate if an MCS is expected to be composed of chaotically arranged convection.

1.5 Outline

The remaining chapters describe the framework, construction, and evaluation of a scheme to parameterize the effects on the large-scale flow of mesoscale flow branches in the stratiform regions of MCSs . Chapter 2 outlines the framework of this scheme, which is suitable for use in a coarse resolution model such as a GCM but would be inappropriate for any model which might resolve an MCS's flow branches. The thermodynamic part of the scheme is analagous to that of Donner (1993), although many modifications have been made. The scheme also includes the momentum parameterization of Wu and Yanai (1994). A novel aspect of the scheme presented here is the use of two three-dimensional cloud-resolving MCS simulations in its construction—these simulations afford detailed information on (1) the vertical distributions of key physical processes occurring in the conditionally-sampled mesoscale updrafts and mesoscale downdrafts and (2) various relevant quantities in MCS water budgets. Chapter 3 describes the two cloud-resolving MCS simulations used to develop the parameterization scheme. In both simulations, interactive grid nesting is employed in order to attain cloud-resolving grid-spacing over areas of two MCSs observed in recent field experiments (one over a tropical ocean and one over a midlatitude continent). Chapter 4 discusses how output from these two simulations is conditionally-sampled in order to construct the scheme. Chapter 5 describes the performance of the scheme. Here, parameterized vertical profiles of the heating, drying, and momentum tendencies are compared to diagnosed vertical profiles of these quantities in the two cloud-resolving MCS simulations. Chapter 6 contains the conclusions of this study.

Chapter 2

PARAMETERIZATION FRAMEWORK

2.1 Overview

The present chapter describes the framework of the parameterization scheme for the mesoscale flow branches of MCSs. The scheme can theoretically be attached to any cumulus parameterization scheme which is designed for large-scale models and which provides vertical profiles of heating, drying, and hydrometeor tendencies to the host model. Here, cumulus convection will be driven by the Arakawa-Schubert parameterization (e.g., Arakawa and Cheng 1993) modified to account for the effects of convective downdrafts following Johnson (1976). In order to account for a more physically realistic coupling between cumulus convection and associated stratiform cloudiness, the scheme employs a prognostic closure (as opposed to a quasi-equilibrium closure), as described by Randall and Pan (1993). Randall and Pan point out that for the purpose of parameterizing mesoscale effects, an objection to the quasi-equilibrium closure is that it is necessary to group the contributions to the time change of the cloud-work function, A (an integral of the temperature and moisture over the convectively active layer), into "convective" and "nonconvective" components. By treating the effects of convectively-produced stratiform clouds as "nonconvective" processes, quasi-equilibrium closure incorporates some aspects of the convective feedback into the large-scale forcing. With the Randall and Pan prognostic closure, this problem is sidestepped, as it is no longer necessary to distinguish between large-scale forcing and the convective response. The Randall and Pan modification of the Arakawa-Schubert scheme employs a prognostic equation for the cumulus kinetic energy, K,

$$\frac{\partial K}{\partial t} = M_B A - \frac{K}{\tau_D}, \tag{2.1}$$

where M_B is the convective cloud-base mass flux, A is the cloud work function, and τ_D is a dissipation time scale. Cloud-base mass flux is related to K through

$$K = \alpha M_B^2 \tag{2.2}$$

where α is an empirical parameter that Randall and Pan describe as being generally proportional to the magnitude of the vertical shear of the horizontal wind.

The parameterized cumulus convection provides condensed water, ice, and water vapor which drives a parameterization for the large-scale effects of mesoscale circulations associated with the convection. The main goal of my dissertation is to diagnose MCS thermodynamic forcing, although a simple way to account for momentum forcing is also included. Both aspects of the scheme are described below.

2.2 Parameterizing MCS thermodynamic forcing

2.2.1 Tendency equations

Donner (1993) discusses the effects of cumulus convection on the large-scale fields of potential temperature $\overline{\theta}$ and water vapor mixing ratio $\overline{q}$. These effects may be obtained by decomposing these fields into large-scale and small-scale components and then averaging the thermodynamic and moisture equations over the large scale. In isobaric coordinates, tendency equations for these variables are

$$\frac{d\overline{\theta}}{dt} = \frac{\pi \overline{Q_r}^e}{c_p} + \frac{\pi \sum_{i=1}^{6} L_i \overline{\gamma_i^e}}{c_p} + \frac{\pi \overline{Q_r}^*}{c_p} + \frac{\pi \sum_{i=1}^{6} L_i \overline{\gamma_i^*}}{c_p} - \frac{\partial \overline{\omega' \theta'}}{\partial p} - \nabla \cdot \overline{\mathbf{v}' \theta'} \tag{2.3}$$

and

$$\frac{d\overline{q}}{dt} = -\sum_{i=1}^{4} \frac{\mid L_i \mid}{L_i} \overline{\gamma_i^e} - \sum_{i=1}^{4} \frac{\mid L_i \mid}{L_i} \overline{\gamma_i^*} - \frac{\partial \overline{\omega' q'}}{\partial p} - \nabla \cdot \overline{\mathbf{v}'\mathrm{q}'}, \tag{2.4}$$

where Q_r is the radiative heating, c_p is the specific heat at constant pressure, and $\pi = (\frac{p_0}{p})^{\frac{R_d}{c_p}}$, where p_0=100 kPa, and R_d is the gas constant for dry air. The summations represent phase transformations. The latent heat of vaporization is L_1, the latent heat of sublimation is L_3, and the latent heat of fusion is L_5. The latent heats for the reverse processes are given by L_2, L_4, and L_6, respectively. The phase transformations include γ_1 (condensation), γ_2 (evaporation), γ_3 (deposition), γ_4 (sublimation), γ_5 (freezing), and γ_6 (melting). Cloud properties and those of their environment are denoted by asterisks and superscripts e, respectively, while primes denote departures from the large-scale average. Equations (2.3) and (2.4) show that the effect of cumulus convection and mesoscale flow branches on the thermodynamic structure of the large-scale environment depends on fluxes and phase transformations. Thus, the thermodynamic part of the cumulus and mesoscale parameterization problem comes down to formulating the terms on the right-hand sides of (2.3) and (2.4).

To compute fluxes, one needs to recognize that the vertical eddy transport of a property χ is given by

$$\overline{\omega'\chi'} = \sum_{i=1}^{N} (\overline{\omega'\chi'})_i, \tag{2.5}$$

where

$$(\overline{\omega'\chi'})_i = \frac{a_i \omega_i^{*'} \chi_i^{*'}}{1 - a_i} \tag{2.6}$$

and a_i is the fractional area occupied by clouds of the ith of N subensembles.

Large-scale phase transformations due to cumulus convection or mesoscale flow branches are given by

$$\overline{\gamma_i}^* = \sum_{j=1}^{N} a_j \gamma_{i,j}^*, \tag{2.7}$$

where $\gamma_{i,j}^*$ is the rate of the ith phase transformation per unit mass in an updraft or downdraft belonging to subensemble j.

Thus, for any given subensemble, evaluating the forcing of the large-scale flow requires its cloud temperature, water vapor mixing ratio, and vertical velocity (T^*, q^*, and ω^*, respectively), its fractional area a, and the rates of phase transformations. Therefore, parameterizing the thermodynamic forcing of large-scale flow resulting from mesoscale effects requires making approximations of the vertical distributions of the following mesoscale processes in parameterized mesoscale updrafts and downdrafts: (1) deposition and condensation in mesoscale updrafts, (2) freezing in mesoscale updrafts, (3) sublimation in mesoscale updrafts, (4) sublimation and evaporation in mesoscale downdrafts, (5) melting in mesoscale downdrafts, and (6) mesoscale eddy fluxes of entropy and water vapor. The approach presented in this study, therefore, is analogous to that of Donner (1993), except that the explicit MCS simulations will allow us to gain much more insight into the vertical distributions of these processes. Obtaining insight on the shapes of the vertical profiles of processes (1)-(6) above requires conditional sampling of mesoscale updrafts and mesoscale downdrafts within our explicit MCS simulations. Criteria for separating these two regions (discussed in more detail in Chapter 4) are based on surface precipitation rate, following Churchill and Houze (1984) and Tao et al. (1993). The MCS simulations will also provide guidance for values of several other parameters needed to close the parameterization—most of these parameters involve relationships between various quantities in an MCS's water budget and are described in more detail in the following subsections.

In employing explicit simulations, the approach in this study resembles that of Weissbluth and Cotton (1993), who used three-dimensional simulations of isoluated cumulonimbi and two-dimensional cloud-resolving simulations of generic Florida convection to calibrate various parameters in their cloud model. This approach mirrors that of the Global Energy and Water Cycle Experiment Cloud Systems Study (GCSS), in which cloud-resolving models are used to assist in the formulation and testing of cloud parameterization schemes for larger-scale models (Browning et al. 1993). The following subsections discuss the details of the parameterization of the mesoscale processes needed to assess mesoscale heating and drying.

2.2.2 Water vapor redistribution by mesoscale updrafts

Mesoscale updrafts that occur in the stratiform region can advect water vapor. As this water vapor is advected upward, it can change phase and contribute to latent heat release in the mesoscale updraft. Following Donner (1993), this process is considered to be the sum of (1) the redistribution of water vapor provided by cumulus updrafts only, and (2) advection of water vapor present in the environment of the cumulus updrafts but not supplied by the updrafts. Process (2) is discussed in Section 2.2.3. For process (1), the water vapor provided by the convective updrafts is denoted by Q'_{mf}. A vertical profile of Q'_{mf} is provided by the Arakawa-Schubert convective scheme (no water vapor is provided to the mesoscale scheme at levels where Q'_{mf} is negative). The base of the parameterized mesoscale updraft (p_{zm}) occurs at the freezing level. The top of the mesoscale updraft (p_{ztm}) coincides with the level of deepest cumulus penetration. The mesoscale updraft vertically distributes the water vapor source Q'_{mf} at all levels in the mesoscale updraft over a period of time. That is, Q'_{mf} at pressure p contributes $\int_0^{\tau_m} Q'_{mf}(t)dt$ to the vertically averaged water vapor mixing ratio in the stratiform region over its lifetime τ_m. Thus, the water vapor is distributed uniformly between p and $p + \int_0^{\tau_m} \omega_m dt$. This integral is set to be 30 kPa (unless this would distribute water vapor above the top of the mesoscale updraft). The large-scale water vapor mixing ratio is augmented by $\overline{q}_l(p)$ when the contributions from $Q'_{mf}(p)$ are summed. The *large-scale* water vapor tendency associated with the redistribution of water vapor having cumulus cells as its source is given by $\frac{\overline{q_l}(p)}{\tau_m} - Q'_{mf}$.

The redistributed water vapor mixing ratio $\overline{q_l}$ accumulates in the mesoscale region whose fractional coverage is a_m (see Section 4.4 for a discussion of the parameteriztion of a_m). The redistributed water vapor mixing ratio in the mesoscale region is then $\frac{\overline{q_l}}{a_m}$. This quantity may exceed saturation and then change phase.

2.2.3 Deposition and condensation within mesoscale updrafts

The parameterization of the summed deposition and condensation is again patterned after Donner (1993). The region within the mesoscale updraft is assumed to consist of ice and liquid water which is furnished by deposition/condensation from water vapor and by transfer (C_A) from the convective region.

The first source of condensate is provided by the redistribution by the mesoscale updraft of water vapor that is provided by cumulus updrafts. The rate of deposition/condensation by this process is

$$\frac{\overline{q_l}(p)}{a_m \tau_m} - \frac{q_s[T_m(p)]}{\tau_m}, \tag{2.8}$$

where q_s denotes saturation mixing ratio and T_m refers to the temperature in the mesoscale updraft.

The preceding process deals only with water vapor supplied by the cumulus updrafts; additional deposition/condensation occurs as large scale water vapor in the mesoscale region surrounding the updrafts is lifted by mesoscale ascent. This process is parameterized in terms of the water vapor mixing ratio at the base of the mesoscale region, which is conserved as it undergoes mesoscale ascent until deposition/condensation begins, when

$$\overline{q}(p_{zm}) + \frac{\overline{q}_l(p_{zm})}{2a_m} = q_s[T_m(p)]. \tag{2.9}$$

Deposition/condensation then proceeds at a rate $\omega_m \frac{\partial q_s}{\partial p}$ (the factor of 2 averages the water vapor from the cumulus updrafts over τ_m).

These two processes yield a value for the vertically-integrated deposition plus condensation, $(\int_{p_{ztm}}^{p_{zm}} C_{mu})$. The shapes of the vertical profiles of deposition and condensation, and the ratio of vertically-integrated deposition to vertically-integrated condensation within the mesoscale updraft are then determined by examing the vertical structure of these processes within the conditionally-sampled mesoscale updrafts of the explicit MCS simulations.

2.2.4 Freezing in mesoscale updrafts

Vertically-integrated freezing in mesoscale updrafts is taken to be the sum of two processes. First, all liquid water which is transferred from the cumulus convection to the mesoscale updraft is assumed to freeze. This liquid water is provided by the Arakawa-Schubert cumulus parameterization. Second, all of the water which formed through the condensation process described in the preceding subsection is assumed to freeze within the mesoscale updraft. The shape of the vertical profile of the net freezing within the mesoscale updraft is then determined by examining the vertical profile of net freezing in the conditionally-sampled mesoscale updrafts of the explicit MCS simulations.

2.2.5 Sublimation in mesoscale updrafts

The vertically-integrated value of sublimation within the parameterized mesoscale updraft is determined through consideration of an MCS's water budget, following Leary and Houze (1980). That is, the sum of the mesoscale rainfall R_m, the vertically-integrated sublimation in mesoscale updrafts ($\frac{1}{g}\int_0^{p_g} E_{me}dp$), and the vertically-integrated sublimation/evaporation in mesoscale downdrafts ($\frac{1}{g}\int_0^{p_g} E_{md}dp$) must be equal to $\frac{1}{g}\int_0^{p_g} C_{mu}dp + C_A$ (the subscript g refers to the ground). The latter quantity is computed directly, as described in the preceding subsections. The ratios among R_m, $\frac{1}{g}\int_0^{p_g} E_{me}dp$, and $\frac{1}{g}\int_0^{p_g} E_{md}dp$ are determined from examing the values of these quantities in the explicit simulations. Thus, the vertically-integrated value of sublimation in mesoscale updrafts is some fraction of $\frac{1}{g}\int_0^{p_g} C_{mu}dp + C_A$; the shape of its vertical profile is determined by examining the vertical profile of sublimation in the conditionally-sampled mesoscale updrafts of the explicit MCS simulations.

2.2.6 Sublimation and evaporation in mesoscale downdrafts

As in the preceding subsection, the vertically-integrated value of sublimation plus evaporation within the parameterized mesoscale downdraft is determined through consideration of an MCS's water budget, with the ratio of $\frac{1}{g}\int_0^{p_g} E_{md}dp$ to $[\frac{1}{g}\int_0^{p_g} C_{mu}dp + C_A]$ determined from a water budget of the explicit simulations. The partioning of E_{md} between sublimation and evaporation, as well as the shapes of the vertical profiles of these two processes are also determined by examing the vertical profiles of sublimation and evaporation in the conditionally-sampled mesoscale downdrafts of the explicit MCS simulations.

2.2.7 Melting in mesoscale downdrafts

All mesoscale precipitation is assumed to fall out of the mesoscale updraft as ice. Melting may then come from one of two sources. First, vertically-integrated melting of magnitude R_m occurs. The vertically-integrated value of melting within the parameterized mesoscale downdraft is determined by examining the ratio of R_m to $\frac{1}{g}\int_0^{p_g} C_{mu}dp + C_A$ in the explicit simulations. Second, vertically-integrated melting equivalent to the vertically-integrated evaporation in the parameterized mesoscale downdraft must occur (i.e., any water that evaporates has to melt first, as water is assumed to fall out of the mesoscale updraft as ice). These two sources are added to yield the magnitude of the vertically-integrated melting in parameterized mesoscale downdrafts. The shape of the vertical profile of melting is then determined by examining the vertical profiles of melting within the conditionally-sampled mesoscale downdrafts of the explicit MCS simulations.

2.2.8 Mesoscale eddy fluxes of entropy and moisture

Eddy fluxes of entropy and water vapor are computed using Equation (2.6), where the shapes of the vertical profiles of the perturbation potential temperature, perturbation water vapor mixing ratio, and perturbation vertical velocity in parameterized mesoscale updrafts and downdrafts are determined through conditional sampling of the explicit simulations.

2.3 Parameterizing horizontal momentum forcing

One can develop equations similar to Equations (2.3) and (2.4) for horizontal momentum. Wu and Yanai (1994) have done this. Consider, for instance, the momentum budget equation used to derive (1.1), except now for the mean flow:

$$\mathbf{F} \equiv \frac{\partial \overline{\mathbf{v}}}{\partial \mathrm{t}} + \overline{\mathbf{v}} \cdot \nabla \overline{\mathbf{v}} + \overline{\omega} \frac{\partial \overline{\mathbf{v}}}{\partial \mathrm{p}} + \nabla \overline{\phi} + \mathrm{f} \hat{\mathbf{k}} \times \overline{\mathbf{v}} = -\nabla \cdot \overline{\mathbf{v}'\mathbf{v}'} - \frac{\partial}{\partial \mathrm{p}} \overline{\mathbf{v}'\omega'}. \tag{2.10}$$

Here, ϕ is the geopotential and all other symbols are the same as before.

Wu and Yanai present a parameterization for the right side of (2.10) for organized cumulus convection. Spectrally dividing a cumulus ensemble into subensembles, where at a given level all clouds of a subensemble are assumed to share similar properties, the right hand side of (2.10) may be approximated by

$$\mathbf{F}_{\mathrm{c}} = -\frac{\partial}{\partial \mathrm{p}} \overline{\mathbf{v}'\omega'} = \frac{\partial}{\partial \mathrm{p}} \sum_{\mathrm{i}} \mathrm{M}_{\mathrm{i}} (\mathbf{v}_{\mathrm{i}} - \overline{\mathbf{v}}), \tag{2.11}$$

where $M_i = \sigma_i \omega_i$ is the vertical mass flux through the fractional area coverage σ_i of the ith subensemble and $\mathbf{v}_{\mathrm{i}}$ is the characteristic value of horizontal velocity in the subensemble. The quantity $\mathbf{F}_{\mathrm{c}}$ is the cumulus-induced acceleration of the environmental flow.

Considering the budgets of mass and horizontal momentum in a subensemble yields

$$\mathbf{F}_{\mathrm{c}} = \sum_{\mathrm{i}} \delta_{\mathrm{i}} (\mathbf{v}_{\mathrm{Di}} - \overline{\mathrm{v}}) - \mathrm{M}_{\mathrm{c}} \frac{\partial \overline{\mathrm{v}}}{\partial \mathrm{p}} + \sum_{\mathrm{i}} \sigma_{\mathrm{i}} (\frac{1}{\rho} \nabla \mathrm{p}')_{\mathrm{i}}, \tag{2.12}$$

where δ is the mass detrainment per unit pressure interval, p' is the convective-scale pressure perturbation, ρ is the density of cloud air, $M_c = \sum_i M_i$ is the total cloud mass flux, and the subscript D expresses the representative value in the detraining air.

The first term on the right side of (2.12) expresses the effect of horizontal momentum detrained from cumulus clouds (cumulus friction). The second term represents the vertical advection of mean horizontal momentum by the part of the environmental vertical motion that compensates the convective mass flux. The third term represents the effect of the convective-scale horizontal pressure gradient force on the environment. The cloud mass flux and mass detrainment are determined by the Arakawa-Schubert parameterization. It is necessary to develop an additional parameterization, however, for the horizontal momentum of the detraining air and the acceleration by the convective-scale pressure gradient force.

The first quantity, the horizontal momentum of detraining air, may be determined by setting cloud-base boundary conditions of cloud momentum (e.g., the cloud-base environment momentum) and integrating the cumulus ensemble model upward (see below). The second quantity may be determined by considering a linearized approximation to the diagnostic pressure equation:

$$-\nabla^2(\frac{p'}{\rho}) = 2(\frac{\partial\overline{u}}{\partial z}\frac{\partial w}{\partial x} + \frac{\partial\overline{v}}{\partial z}\frac{\partial w}{\partial y}). \tag{2.13}$$

In (2.13), $\nabla^2 \equiv \frac{\partial^2}{\partial x^2} + \frac{\partial^2}{\partial y^2} + \frac{\partial^2}{\partial z^2}$, the quantities $\overline{u}$ and $\overline{v}$ are two components of the environmental wind, and w is the updraft. This diagnostic pressure equation demonstrates how the horizontal pressure gradient across an updraft is sensitive to the vertical shear of the horizontal wind in the environment and the structure of the updraft (several terms have been neglected here). Seeking a solution for $\frac{p'}{\rho}$ corresponding to an updraft given by

$$w = w_0 \cos kx \cos ly \sin mz, -\frac{\pi}{2} < kx, ly < \frac{\pi}{2}, \tag{2.14}$$

where w_0 is the maximum updraft velocity and k,l, and m spectrally characterize the updraft in the x, y, and z direction, respectively, Wu and Yanai go on to derive the following two equations for the two components of $\mathbf{F}_c$,

$$F_{cx} = \sum_i \delta_i (u_{Di} - \overline{u}) - M_c \frac{\partial \overline{u}}{\partial p} + \sum_i \gamma_{ki} M_i \frac{\partial \overline{u}}{\partial p} \tag{2.15}$$

and

$$F_{cy} = \sum_i \delta_i (v_{Di} - \overline{v}) - M_c \frac{\partial \overline{v}}{\partial p} + \sum_i \gamma_{ki} M_i \frac{\partial \overline{v}}{\partial p} \tag{2.16}$$

where $\gamma_k = \frac{2k^2}{k^2+l^2+m^2}$ and $\gamma_l = \frac{2l^2}{k^2+l^2+m^2}$.

The quantities u_{Di} and v_{Di} represent the values of each component of the cloud momentum at the detrainment level for each subensemble. For each subensemble, these two quantities are calculated by integrating upward from cloud base the following two momentum budget equations derived by Wu and Yanai:

$$\frac{\partial}{\partial p}[\eta(p,\lambda) u_c(p,\lambda)] = \frac{\partial}{\partial p}[\eta(p,\lambda)\overline{u}(p)] + (\gamma_k - 1)\eta(p,\lambda)\frac{\partial \overline{u}}{\partial p}, \tag{2.17}$$

and

$$\frac{\partial}{\partial p}[\eta(p,\lambda)v_c(p,\lambda)] = \frac{\partial}{\partial p}[\eta(p,\lambda)\overline{v}(p)] + (\gamma_l - 1)\eta(p,\lambda)\frac{\partial \overline{v}}{\partial p}. \tag{2.18}$$

Here, u_c and v_c are the two components of the horizontal momentum of a subensemble, η is the normalized mass flux, and λ is the fractional entrainment rate.

Thus, the acceleration of the environmental flow by the convective-scale horizontal pressure gradient force can be quite sensitive to the kinematic structure of the updraft. As a result, it may be important to know whether the convection is organized (as it often is in an MCS), and if it is, the *way* in which the convection is organized (e.g., linear or scattered). Linear convection (e.g, $l^2 \ll k^2$) can have a line-normal momentum flux which is upgradient rather than downgradient, resulting in an acceleration of upper level flow rather than a deceleration (e.g., Gallus and Johnson 1992). That is, the magnitude of the vertical shear *increases* . This behavior differs from that of "randomly" scattered convective clouds, which typically act to mix momentum and therefore decrease the magnitude of the vertical shear. The convective-scale pressure gradient force tends to compensate the vertical advection effect due to the cumulus-induced subsidence. Finally, if the convection *is* linear, ideally one would also want to know which way the convection is oriented.

Note that the acceleration of environmental flow directly by vertical momentum transport within *mesoscale* drafts is not included here. Previous work suggests that it is a relatively small component of the momentum budget of MCSs. For example, Tripoli and Cotton (1989b), who examined the processes responsible for the acceleration of air motion in a numerically simulated MCS, showed that the acceleration of horizontal momentum on the meso-β scale was dominated locally by pressure acceleration that reached peak magnitudes larger than either vertical momentum transport or Coriolis processes by nearly a factor of 4 (see their Fig. 13). Acceleration of horizontal momentum by vertical transport was significant only in their convective core region. Analysis of the MCS simulations presented here also indicates that compared to convective updrafts, mesoscale updrafts and downdrafts have a very small contribution to the large-scale acceleration of horizontal momentum (see Section 5.1.2).

2.4 Activating the parameterization

Fig. 2.1 summarizes the physical processes consisered in the MCS parameterization discussed in this chapter. While a framework for parameterizing the effect of MCSs has been outlined, another critical issue still needs to be addressed—when to activate the MCS parameterization. For MCSs, however, a simple parcel-lifting method is necessary, but not sufficient. In many cases, for instance, while the environment may easily be unstable enough to support ordinary convection and a strong trigger (e.g., low-level convergence, topographic lifting) may be present, an MCS still doesn't form. In addition, an MCS's mesoscale flow branches may persist for hours after cumulus clouds have dissipated. Are the environments of MCSs and ordinary convection fundamentally different? If so, how can the large-scale fields be used to determine whether to activate the "mesoscale" part of the parameterization? The issue of triggering this parameterization is left as an open question here, as another member of our research group, Hongli Jiang, is directing her efforts in this direction. This issue is discussed in more detail in the future work section of Chapter 6.

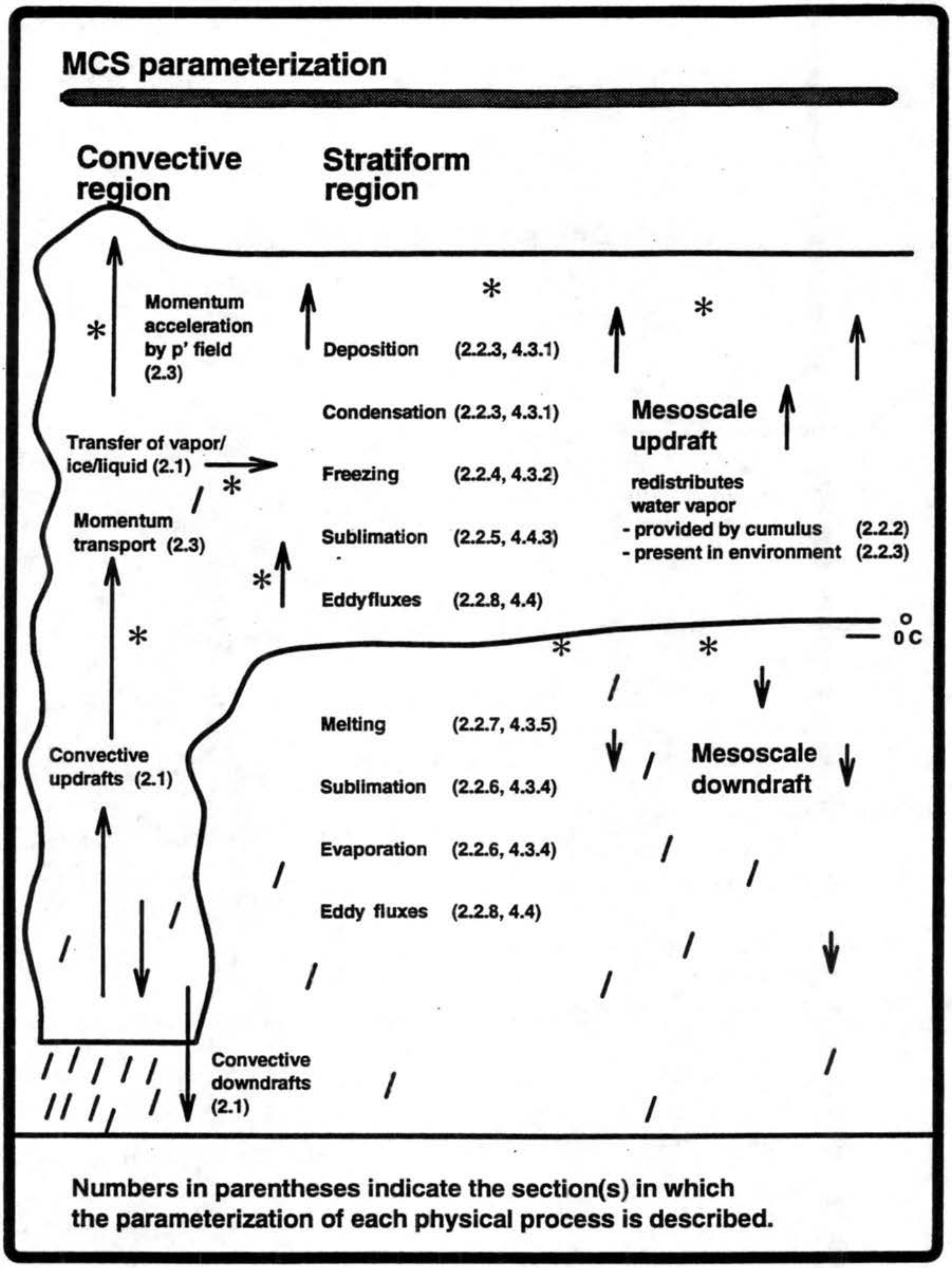

Fig. 2.1: Summary of the physical processes considered in the MCS parameterization.

Chapter 3

CLOUD-RESOLVING MCS SIMULATIONS

3.1 Overview

In the past, because of limited computer resources, researchers have had to make sacrifices in numerically simulating MCSs. One such sacrifice has been to make simulations two-dimensional, thereby enabling grid spacing fine enough to resolve convective circulations. Lafore and Moncrieff (1989), Tripoli and Cotton (1989a), Tao et al. (1993), and Szeto and Cho (1994) are among the researchers, for instance, who have performed two-dimensional simulations of MCSs—minimum grid spacing in these simulations ranges from 750-2000 m. Although two-dimensional simulations are useful (e.g., multiple sensitivity experiments are possible), they have obvious limitations (e.g., simulating the three-dimensional flow branches of MCSs in two-dimensions is impossible). Other researchers, therefore, have opted for three-dimensional simulations. These simulations, however, are often hampered by inadequate grid spacing to explicitly simulate convection; consequently, a convective parameterization scheme is necessary in order to realistically account for convective effects. For instance, Zhang et al. (1989) three-dimensionally simulated an MCS observed over Oklahoma and Kansas on 10-11 June 1985 using a grid spacing of 25 km and the Fritsch-Chappell convective parameterization scheme (Fritsch and Chappell 1980) on their fine grid.

More recently, Bélair et al. (1994) three-dimensionally simulated the 10-11 June MCS using a different model, but the same 25 km grid spacing on the fine grid and a modified version of the Fritsch-Chappell scheme. Unfortunately, as Tripoli and Cotton (1989a) demonstrated, convective parameterization schemes have difficulty in simulating the scale-interaction processes of MCSs. Still, with such coarse grid spacing, using *some* convective parameterization scheme tends to give better results than using none at all. For example, Cram et al. (1992) performed three-dimensional simulations of a squall line that occurred on 17-18 June 1978 using a grid spacing of 20 km on the fine grid, and found that experiments with no convective parameterization yielded no convection. Shaw (1995) performed three-dimensional simulations of a dryline in the U.S. Great Plains using grid spacing of 5 km on the fine grid and was unable to achieve realistic convective vertical velocities along the dryline.

Modelers are still at the mercy of available computer power, of course, and still must make sacrifices. As we become able to squeeze larger and larger simulations onto affordable computer hardware, however, the number of sacrifices diminishes. The present chapter discusses the two three-dimensional MCS simulations used to build the MCS parameterization scheme. One is a tropical MCS and one is a midlatitude MCS. The simulations are three-dimensional and employ horizontal grid spacing fine enough that no convective parameterization scheme needs to be (or should be) used. Both simulations use multiple two-way interactive nested grids in order to achieve the minimum possible horizontal grid spacing. Both simulations explicitly simulate convection on their finest grid at a horizontal grid spacing of $\sim$ 1500-2000 m over an area of $\sim$ 17,000 km^2 for a time of 3-4 hours. These two simulations required formidable computer power—both were run on an IBM RS-6000/370 workstation, and have pushed this machine literally to its limits in terms of both available memory (128 Mbytes) and disk space (2 Gbytes). When all grids are turned on in each simulation, the ratio of wall clock time to model time is $\sim$ 40:1—i.e., explicitly simulating an MCS for 4 hours requires about 1 week of dedicated computer time.

The tropical MCS that has been simulated is the ninth MCS probed by research aircraft during the Equatorial Mesoscale Experiment (EMEX)—this MCS is called EMEX9, and it occurred on 2-3 February 1987. Gunn et al. (1989), Hendon et al. (1989), and Keenan et al. (1989) overview various facets of the 1987 Australian monsoon season. Mapes and Houze (1992) provide a detailed view of the horizontal structure of the ten EMEX precipitation systems. Gamache et al. (1987), Bograd (1989), Webster and Houze (1991), and Mapes (1992) describe synoptic conditions for EMEX9. Wong et al. (1993) and Tao et al. (1993) have two-dimensionally modeled EMEX9.

The midlatitude MCS that has been simulated is the MCS observed on 23-24 June 1985 during the Oklahoma-Kansas Preliminary Regional Experiment for STORM (Stormscale Operational and Research Meteorology Program), or PRE-STORM (Cunning 1986). Stensrud and Maddox (1988), Johnson et al. (1989), Johnson and Bartels (1992), and Bernstein and Johnson (1994) are among the researchers who have investigated various aspects of the 23-24 June MCS event. This MCS has been simulated by Olsson (1995), who used a minimum grid spacing of $\sim$ 8 km.

3.2 The model

The nonhydrostatic version of the Regional Atmospheric Modeling System (Pielke et al. 1992) is used. The model uses an isentropic analysis package to derive initial conditions and time-dependent lateral boundary conditions; this package interpolates pressure-level data onto 33 isentropic levels and applies the Barnes (1973) objective analysis scheme. Time-dependent model variables are the three velocity components, the perturbation Exner function, the ice-liquid potential temperature, the total water mixing ratio, and the mixing ratio of rain droplets, snowflakes, pristine ice crystals, graupel particles, and aggregates. The bulk hydrometeors have prescribed exponential size distributions (see Cotton et al. 1986). The model diagnoses vapor mixing ratio, cloud water mixing ratio, and potential temperature. The prognostic equations use a time-splitting technique—this allows the model to explicitly compute on a small timestep those terms governing sound waves, and to compute on a long timestep those terms governing other processes. Horizontal time differencing for long time steps is a flux conservative form of second order leapfrog (Tripoli and Cotton 1982). Figure 3.1 summarizes the features of the model.

The simulations employ the following boundary conditions. The lateral boundary conditions are the Klemp and Wilhelmson (1978a,b) radiative type, in which the normal velocity component specified at a lateral boundary is effectively advected from the interior assuming a specified propagation speed. A Davies nudging condition causes model data at and near the lateral boundaries to be forced toward available

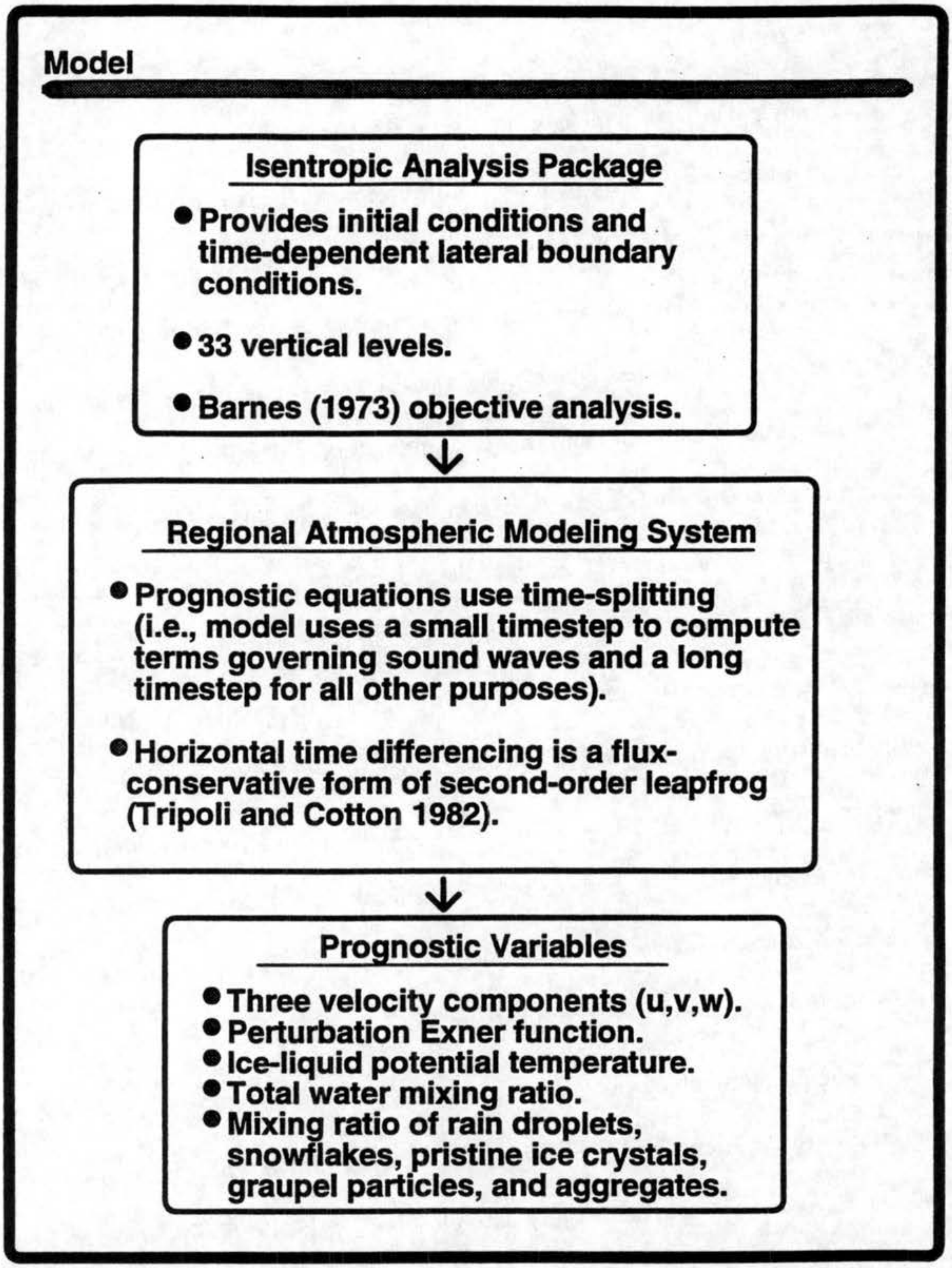

Model

Isentropic Analysis Package

- Provides initial conditions and time-dependent lateral boundary conditions.
- 33 vertical levels.
- Barnes (1973) objective analysis.

Regional Atmospheric Modeling System

- Prognostic equations use time-splitting (i.e., model uses a small timestep to compute terms governing sound waves and a long timestep for all other purposes).
- Horizontal time differencing is a flux-conservative form of second-order leapfrog (Tripoli and Cotton 1982).

Prognostic Variables

- Three velocity components (u,v,w).
- Perturbation Exner function.
- Ice-liquid potential temperature.
- Total water mixing ratio.
- Mixing ratio of rain droplets, snowflakes, pristine ice crystals, graupel particles, and aggregates.

Fig. 3.1: Summary of the key features of the model used in the MCS simulations.

observations. A rigid lid is used at the model top, in concert with a Rayleigh friction absorbing layer. The latter damps gravity wave and other disturbances which approach the top boundary. At the lower boundary there is horizontally variable topography. A vegetation parameterization (McCumber and Pielke 1981; Lee 1992) and an 11-layer prognostic soil model (Tremback and Kessler 1985) dictate fluxes of temperature and moisture over land surfaces. The soil model has 11 vertical levels located from -1 cm to -1 m.

A few of the physical parameterizations are worth mentioning. The parameterization of surface fluxes of momentum, heat, and moisture are designed according to surface similarity theory (Louis 1979). The Chen and Cotton (1983) radiation scheme accounts for longwave and shortwave radiative transfer, including the effects of liquid water and ice—the model updates radiative contributions to atmospheric and surface soil temperatures every 15 minutes. Note, however, that both MCSs are nocturnal, and therefore should not be sensitive to the shortwave radiation scheme. The Level 2.5w convective parameterization scheme (Weissbluth and Cotton 1993) is used, but only in the initial stages of each simulation. All of the results used to construct the MCS parameterization scheme are from times when the model uses no convective parameterization scheme on *any* grid (i.e., the convection is explicitly simulated).

3.3 EMEX9 simulation

3.3.1 Observations

EMEX9 occurred during an active period of the 1987 Australian monsoon, where "active" means that the mean 850 mb westerly wind in the region 110° - 140 ° E, 5°-

15° S exceeded 8 $\mathrm{ms^{-1}}$ (Webster and Houze 1991). In fact, EMEX9 occurred during the most active phase of the 1987 monsoon—850 mb westerly winds over the EMEX9 region were on the order of 25 $\mathrm{ms^{-1}}$ (Fig. 3.2). The prevailing synoptic feature at the time of EMEX9 was a deep westerly monsoon trough extending from 500 mb to the surface which oriented itself across northern Australia and into New Guinea. The interaction of this synoptic-scale monsoon trough circulation with a mesoscale land breeze circulation provided a primary lifting mechanism for EMEX9. Fig. 3.3 shows the streamlines at 850, 500, and 200 mb at the model startup time—1200 UTC 2 February. A composite sounding of the EMEX9 environment, assembled using all available aircraft and synoptic data, has a CAPE of 1484 $\mathrm{Jkg^{-1}}$ and a bulk Richardson number of 51, typical of multicellular convection (Alexander and Young 1992).

Infrared satellite images from 1530 UTC (0200 LST) 2 February 1987 through 0230 UTC (1300 LST) show the evolution of EMEX9 (Fig. 3.4). In its early stages, at 1530 UTC, EMEX9 was located just north of the Top End Peninsula, or near the center of the image in Fig. 3.4a. By 1730 UTC (0400 LST), as EMEX9 propagated into the open ocean, the MCS was fully developed, as suggested by the broad area of cold cloud top temperatures in Fig. 3.4b. The 2030 UTC (0700 LST) image (Fig. 3.4c) shows that EMEX9 merged with another cluster that had formed in the Gulf of Carpentaria. This cluster-cluster interaction occurs several hours after the simulation has ended and is not investigated here. By 0230 UTC (1300 LST), EMEX9 slowly decayed as it approached the southern coast of New Guinea (Fig 3.4e). Over EMEX9's $\sim$ 12 hour lifetime, the MCS propagated northeastward along the monsoon trough at

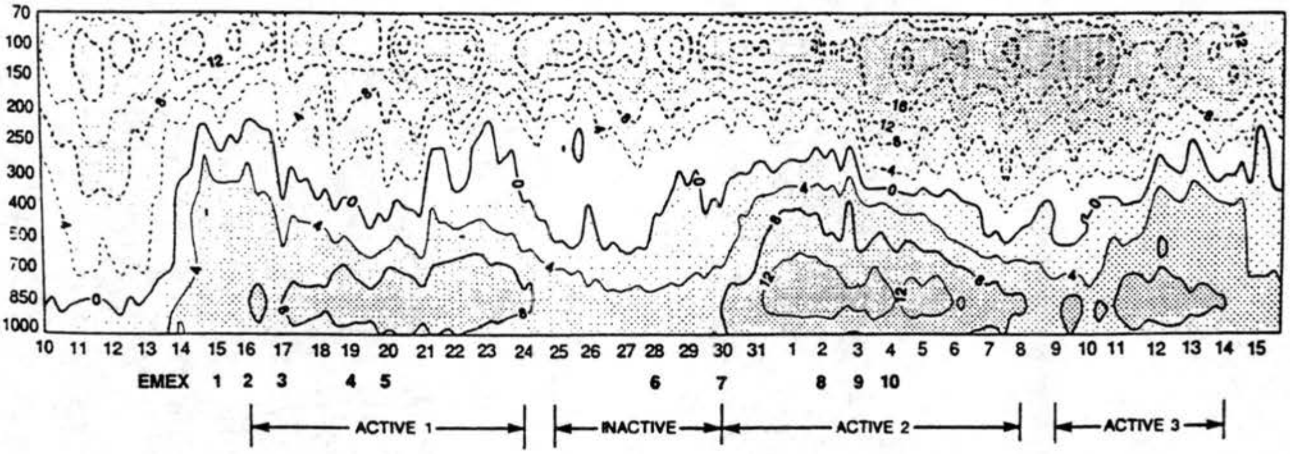

Fig. 3.2: Area mean values of the zonal wind component over the region 110°E to 140°E, 5°S to 15°S. The notation EMEX 1, 2, ... 10 refers to the ten EMEX aircraft missions. Starting date is 10 January 1987. Note that the low-level westerlies on 2-3 February during EMEX9 were among the strongest observed during the EMEX time period. From Webster and Houze (1991).

(a)

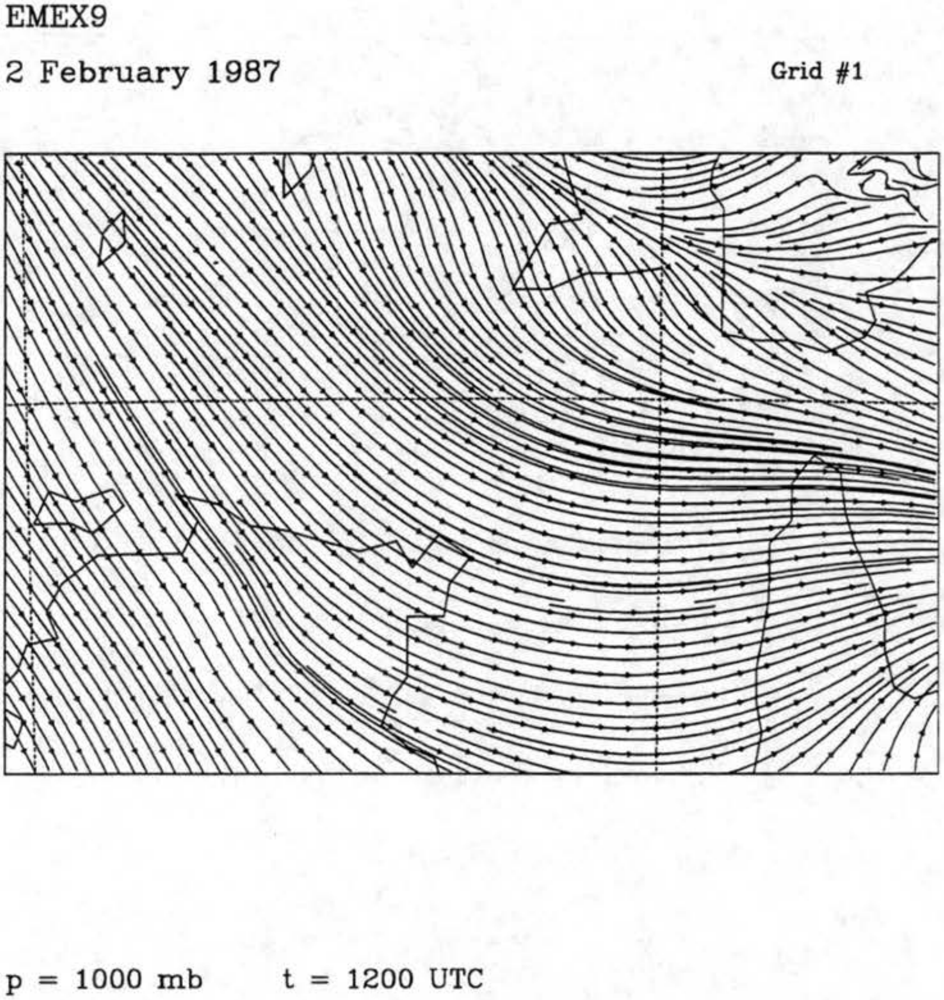

(b)

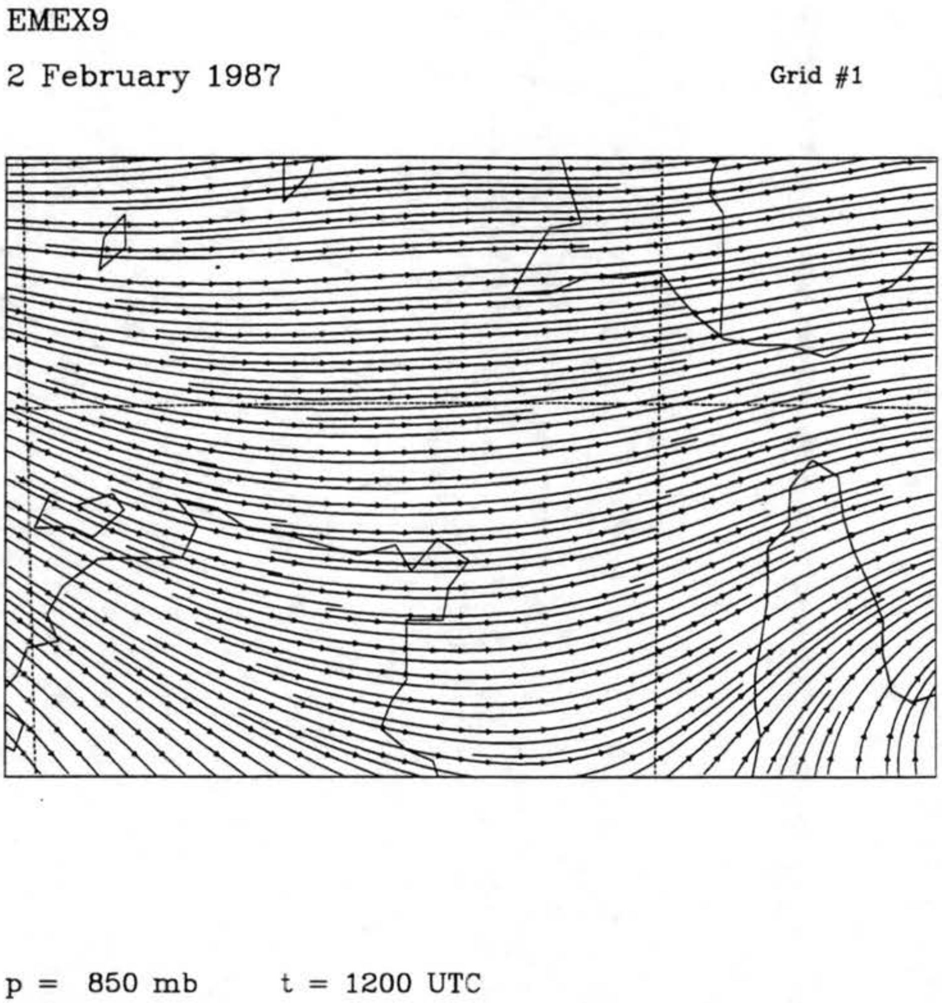

(c)

EMEX9

2 February 1987

Grid #1

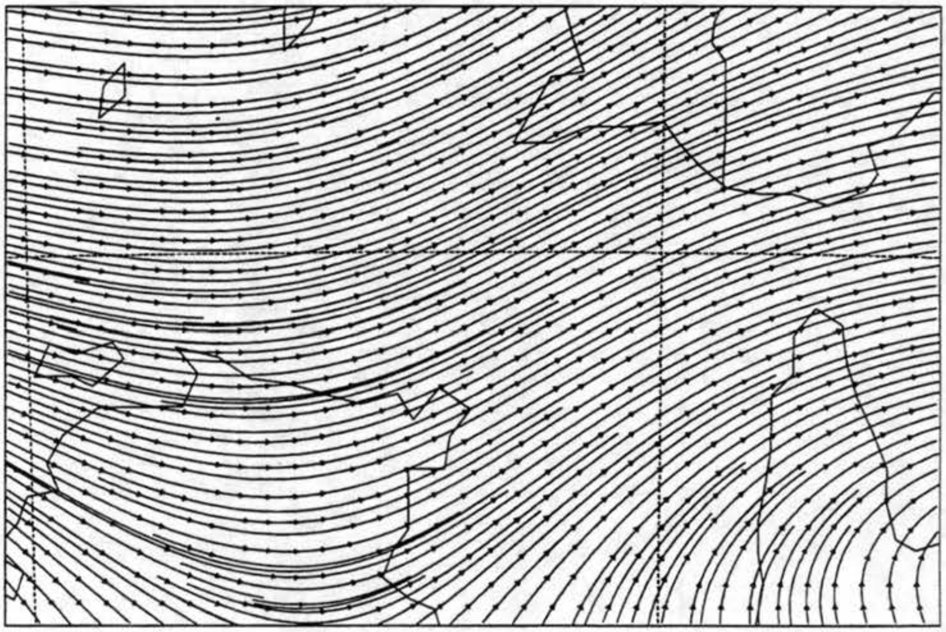

p = 500 mb   t = 1200 UTC

(d)

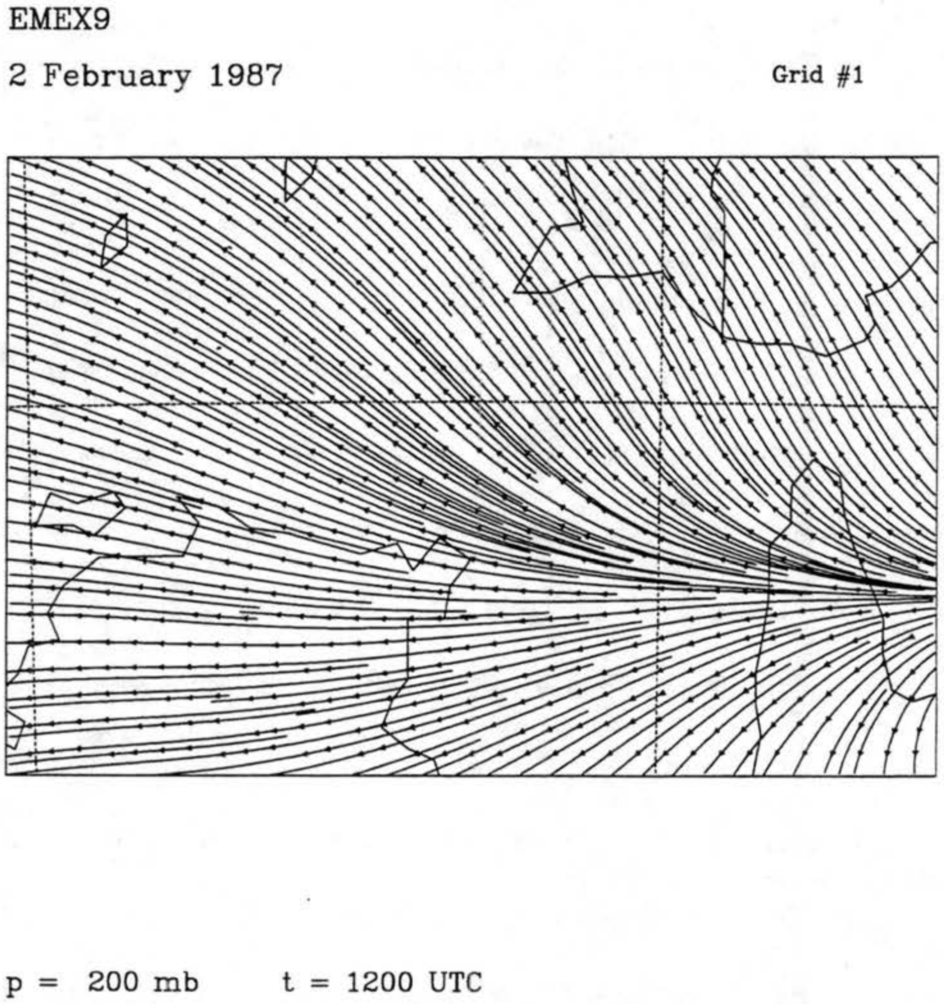

Fig. 3.3: Streamlines at (a) 1000 mb, (b) 850 mb, (c) 500 mb, and (d) 200 mb at 1200 UTC 2 February 1987.

roughly 12 ms^{-1}.

The NOAA P-3, NCAR Electra, and CSIRO F-27 aircraft penetrated EMEX9 between 2100 UTC 2 February and 0100 UTC 3 February. The P-3's lower-fuselage Doppler radar observed two separate convective lines—an initial line oriented in a west-northwest to east-southeast direction which was more than 300 km long, and a northwest to southeast oriented convective line which was about 250 km long. Fig. 3.5 shows a plan view radar image of the initial line. The P-3 radar observed two types of embedded convection associated with EMEX9—upright and rearward sloping (Webster and Houze 1991). Both types extended to about 14.5 km and had a horizontal scale of about 40 km. The vertical air motions within convective elements may be estimated using Doppler-detected vertical velocities—above the 0°C level, one should add about 1-2 ms^{-1} to the radar-detected velocities to account for snow particle fallspeeds; below 5 km, one should add 5-8 ms^{-1} to account for the raindrop fallspeeds. Vertical motions in the upright convection were weak (on the order of 1-2 ms^{-1}) and were confined to upper levels (Fig. 3.6). Vertical motions in the slanted convection were much stronger with maximum updraft strengths on the order of 7-9 ms^{-1} at about 10 km (Fig. 3.7). Radar observations of EMEX9's stratiform region indicated a more uniform precipitation field and a bright band near the freezing level. Stratiform cloud base was observed to be at 4.8 km with a top at about 15 km. Mean vertical motion in the stratiform region was upward above the freezing level and downward below the freezing level. All of these features have previously been observed extensively in the stratiform regions of tropical MCSs (e.g., Houze 1977,

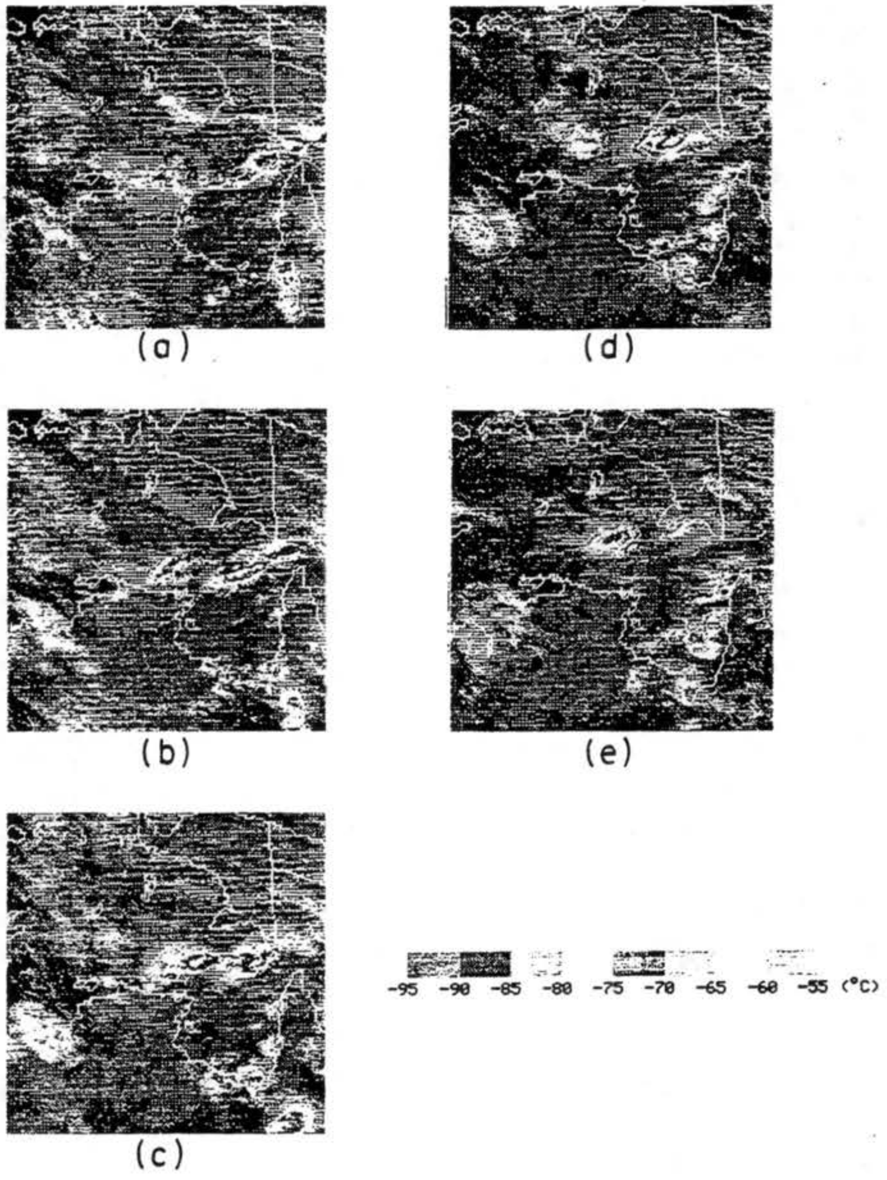

Fig. 3.4: GMS infrared satellite images at (a) 1530 UTC 2 February 1987, (b) 1730 UTC 2 February 1987, (c) 2030 UTC 2 February 1987, (d) 2330 UTC 2 February 1987, and (e) 0230 UTC 3 February 1987 over the EMEX region.

Houze 1982).

3.3.2 Initialization

The model is initialized with a special dataset prepared by Australia's Bureau of Meteorology (BOM) for the EMEX time period. The BOM analysis includes observations from (1) the normal network of sounding and surface stations, (2) a special network of sounding and surface stations which was established during EMEX, and (3) temperature and wind data retrieved from satellite and aircraft data. This dataset provides the horizontal wind components, temperature, and relative humidity at 1.25° latitude/longitude intervals and at 11 pressure levels. The model uses topographic data which has a horizontal spacing of 10 minutes latitude/longitude on all grids. Over the ocean, horizontally variable sea-surface temperatures for February 1987 from a 2° × 2° latitude/longitude NMC Climate Analysis Center dataset are used. A constant soil moisture is specified over land areas. A constant vegetation type of mixed woodland is specified over land areas, in accordance with the land cover map of Wilson and Henderson-Sellers (1985).

3.3.3 Setup

The model's horizontal grid spacing is 24 km on Grid #1, 6 km on Grid #2, and 1.5 km on Grid #3 (Fig. 3.8). All grids have 35 vertical levels, stretched from a spacing of 100 m near the surface to 1000 m at the model top ($\sim$ 22 km). The Rayleigh friction absorbing layer is in the top 5 model levels. The long timesteps are 24, 8, and 4 seconds for Grids #1, #2, and #3, respectively, with short timesteps half this long. The simulation is started at 1200 UTC (2230 LST over Grid #3) 2 February 1987. During

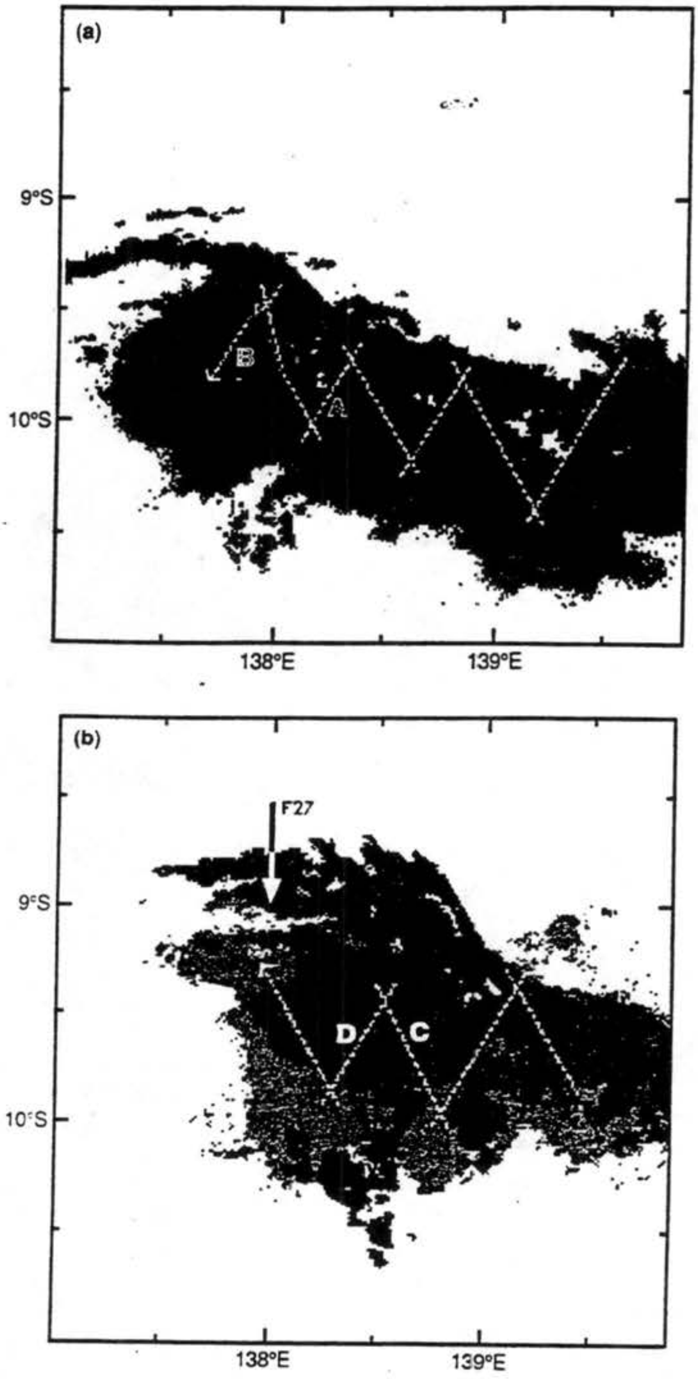

Fig. 3.5: Time composite of radar reflectivity (dBZ) from the lower-fuselage radar aboard the P3 over the time intervals (a) 2040-2201 UTC, and (b) 2302-2350 UTC 2 February 1987. Flight track of the P3 is shown in white. From Webster and Houze (1991).

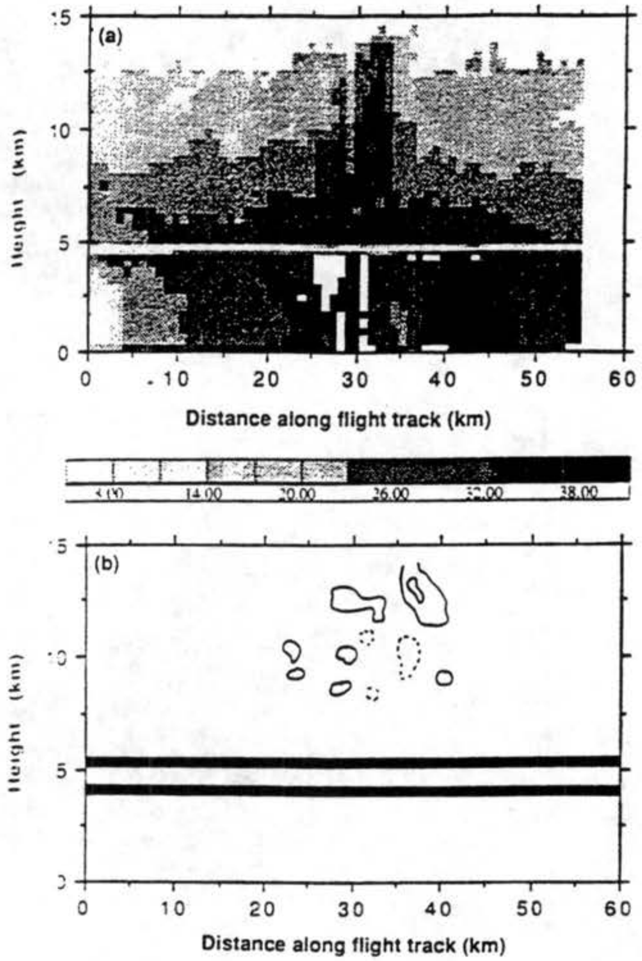

Fig. 3.6: Distance-height section of vertically pointing data from the P3 tail radar for leg A in Fig. 3.5. (a) Radar reflectivity (dBZ) and (b) Doppler vertical velocity of the precipitation particles (ms^{-1}: solid contours +1, +3; dashed contour -4). Contours are shown only above the altitude of 0°C. The Doppler range delay zones above and below the aircraft are contained within the heavy horizontal lines in (b). From Webster and Houze (1991).

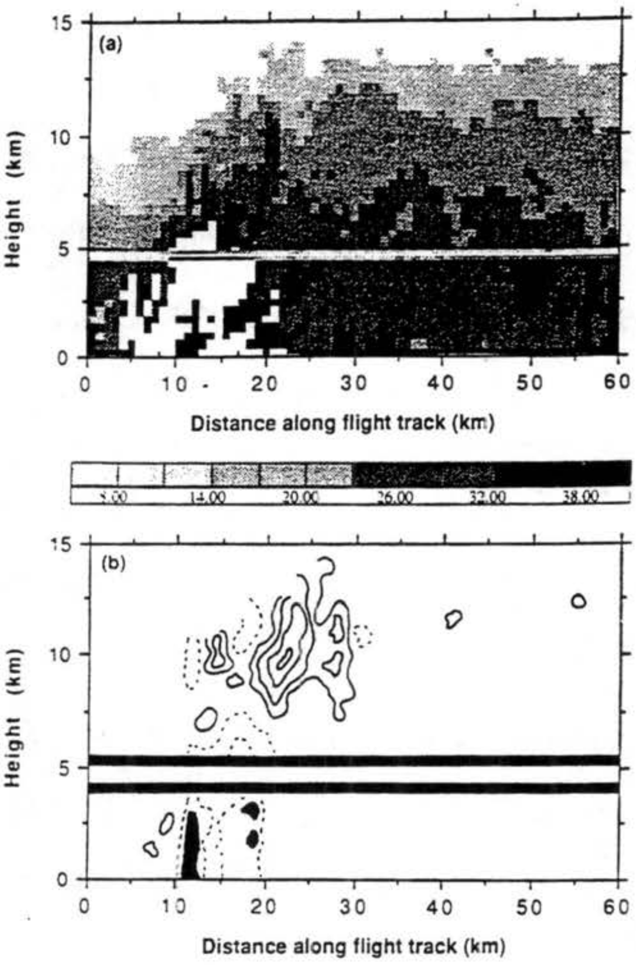

Fig. 3.7: Distance-height section of vertically pointing data from the P3 tail radar for leg B in Fig. 3.5. (a) Radar reflectivity (dBZ) and (b) Doppler vertical velocity of the precipitation particles [ms^{-1}: solid contours +1, +3, +5, and +7; dashed contour -4 (above melting level only), -10; filled areas < -12 ms^{-1}]. The Doppler range delay zones above and below the aircraft are contained within the heavy horizontal lines in (b). From Webster and Houze (1991).

the first hour of the simulation, only the coarsest grid is used. At that point, the two finer grids are activated. The Level 2.5w convective parameterization scheme is used on all grids until 1330 UTC (90 minutes into the simulation); thereafter, it is not used at all. Using a convective parameterization scheme on *all* grids (including the finest, cloud-resolving grid) is unusual—it can be thought of as an objective hot bubble.. The model results during these 30 minutes that the convective parameterization is used on all grids are not meaningful for the purposes of this study. The EMEX9 MCS is explicitly simulated for 4.5 hours, between 1330 and 1800 UTC—analysis files are written to disk every 15 minutes (1330 UTC, 1345 UTC, ...). Fig. 3.9 summarizes the key features of the EMEX9 simulation.

3.3.4 Results

The simulated EMEX9 is triggered by strong low-level convergence of two flows—the mesoscale land breeze circulation and the strong synoptic-scale circulation. The simulated land breeze circulation extends from the surface to about 2 km. This convergence is illustrated in Fig. 3.10, which shows wind vectors and values of horizontal divergence at 1000 mb at 1400 UTC on Grid #2. The robust northerly onshore flow (which has veered from the northwesterlies observed 2 hours earlier) collides with a very weak near-shoreline flow along a line which nearly parallels the coast. Clearly, the land-sea contrast plays a major role in triggering the initial convection.

Vertical velocity fields on the fine grid show the horizontal structure of the convective elements within EMEX9. Fig. 3.11 shows the 500 mb vertical velocity on Grid #3 at 1500, 1600, 1700, and 1800 UTC. At 1500 UTC, convective cells are arranged

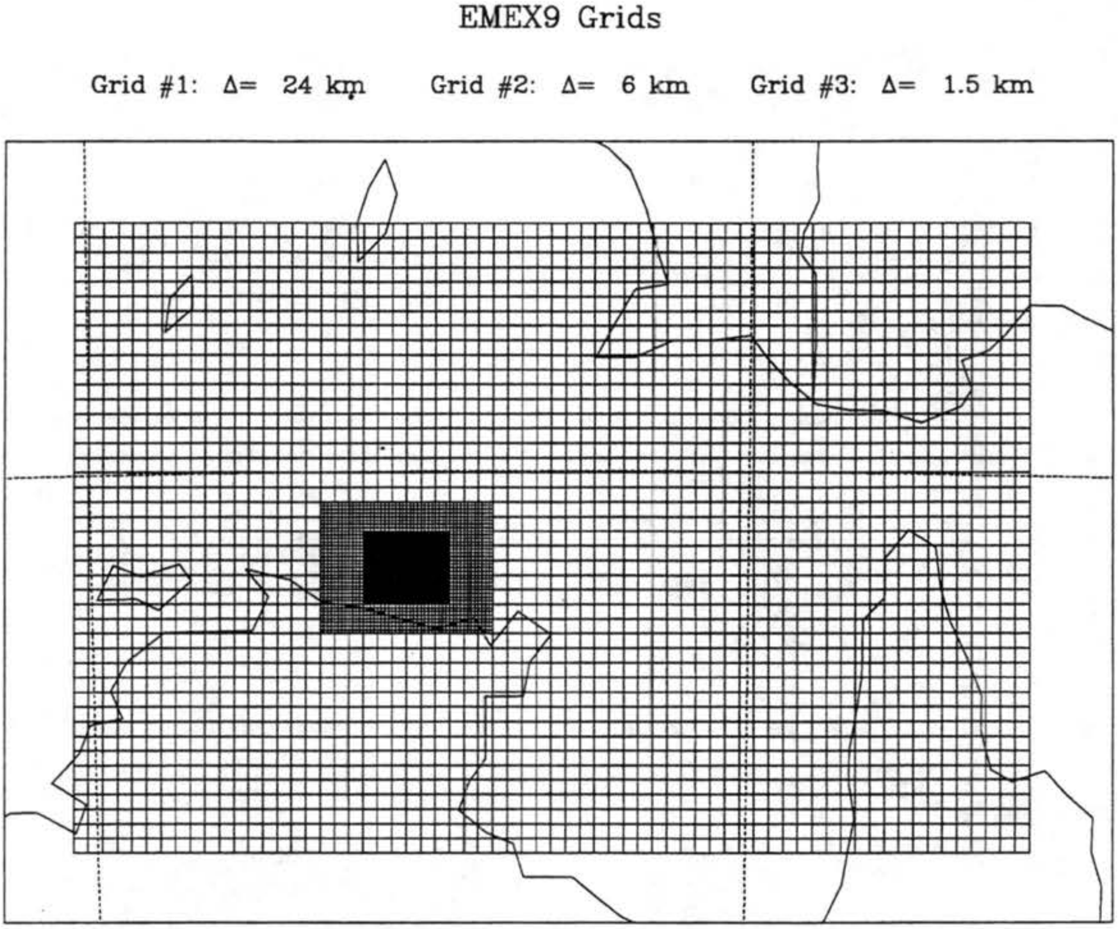

Fig. 3.8: Grid setup for the EMEX9 simulation. The horizontal grid spacing is 24 km, 6 km, and 1.5 km on Grids #1, #2, and #3, respectively.

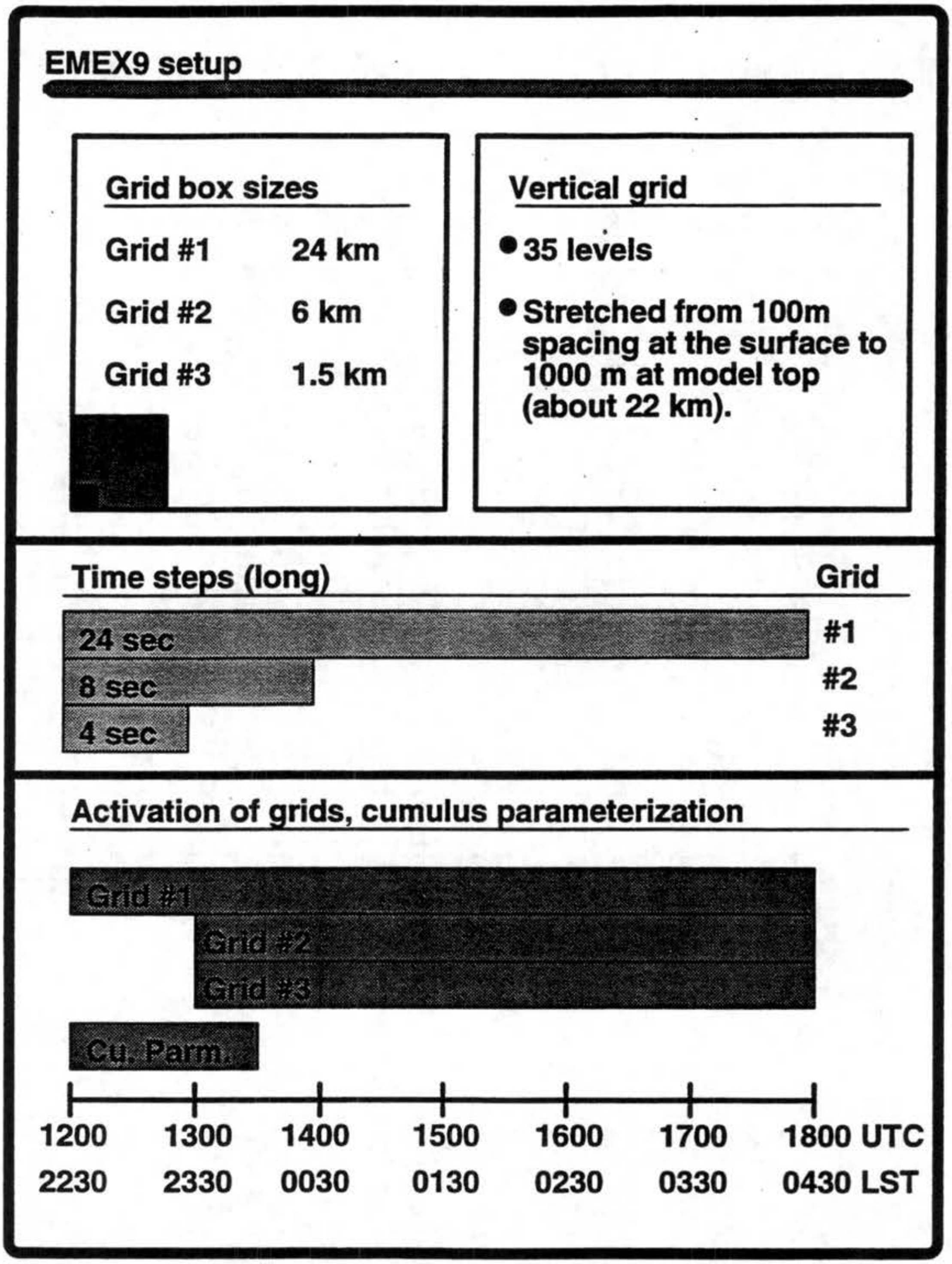

EMEX9 setup

Grid box sizes

Grid #1	24 km
Grid #2	6 km
Grid #3	1.5 km

Vertical grid

- 35 levels
- Stretched from 100m spacing at the surface to 1000 m at model top (about 22 km).

Fig. 3.9: Summary of the model setup for the EMEX9 simulation.

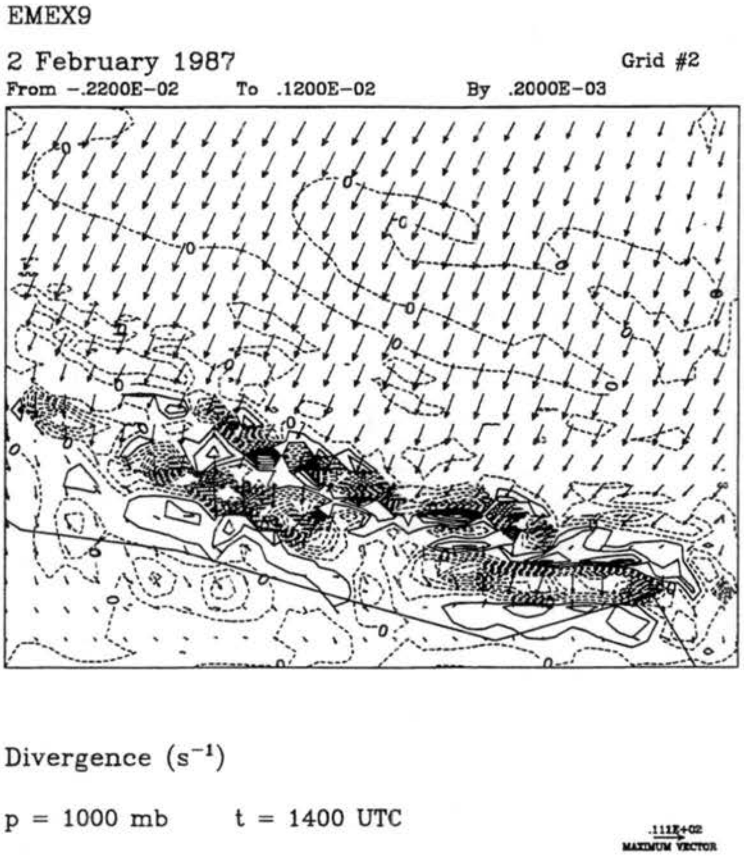

Fig. 3.10: Wind vectors and horizontal divergence at 1000 mb on Grid #2 at 1400 UTC 2 February.

in a WNW-ESE oriented line, with 500 mb vertical velocities ranging from -9 to +21 ms^{-1}. Over the next 3 hours, the whole mass of convection propagates toward the northeast at 10-15 ms^{-1} along the monsoon trough toward the south coast of New Guinea. The generally linear WNW to ESE orientation of the convective elements becomes less well-defined as time goes on. The range of vertical velocities remains about the same through the entire 3-hour period, although increasingly broader areas of weakly positive vertical velocities become apparent as the stratiform region evolves.

(a)

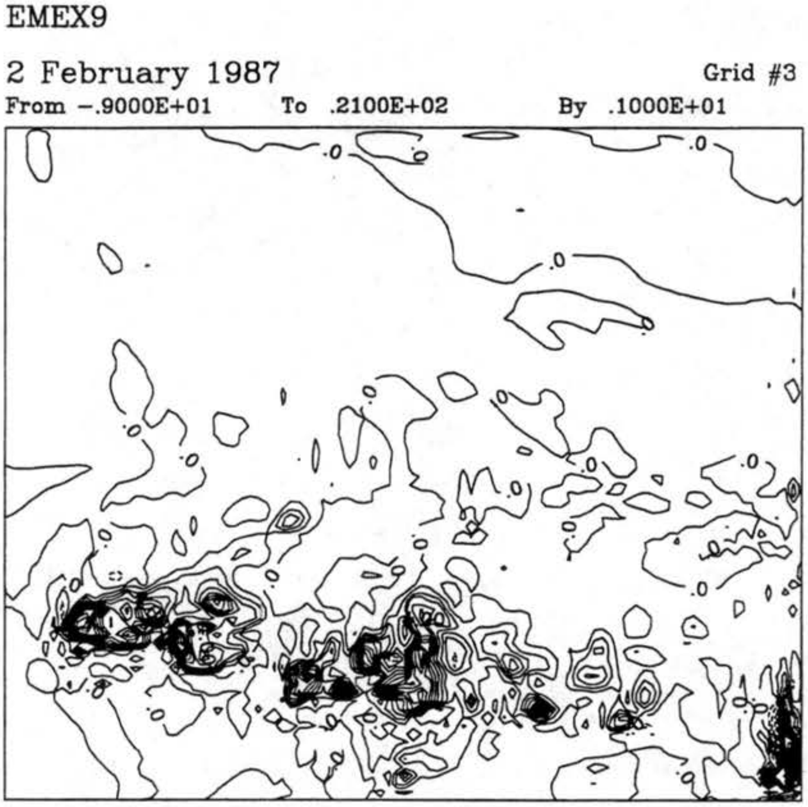

w (ms^{-1})

p = 500 mb t = 1500 UTC

(b)

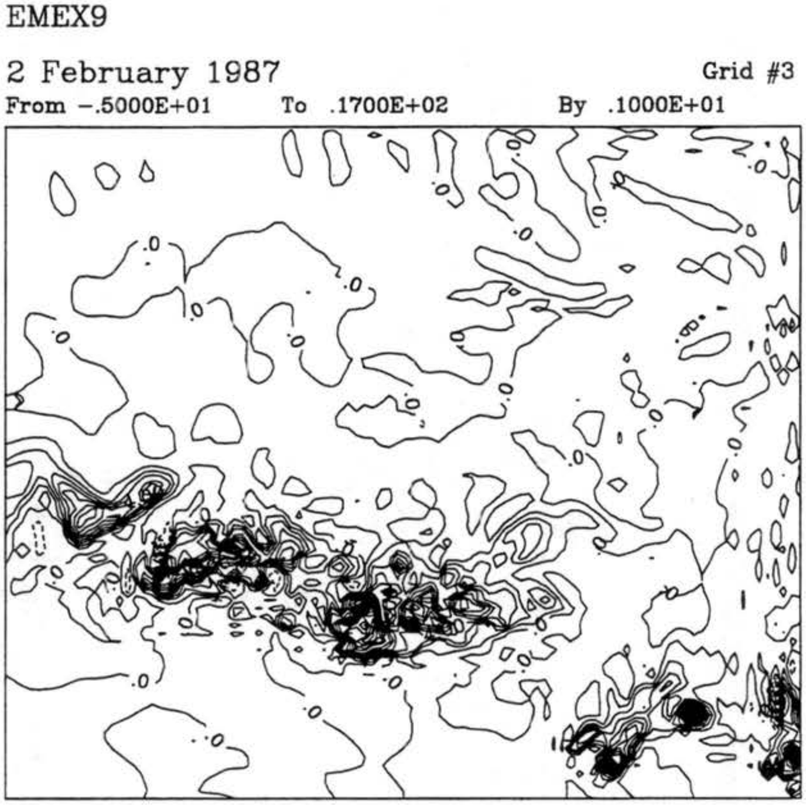

EMEX9

2 February 1987 Grid #3

From −.5000E+01 To .1700E+02 By .1000E+01

w (ms^{-1})

p = 500 mb t = 1600 UTC

(c)

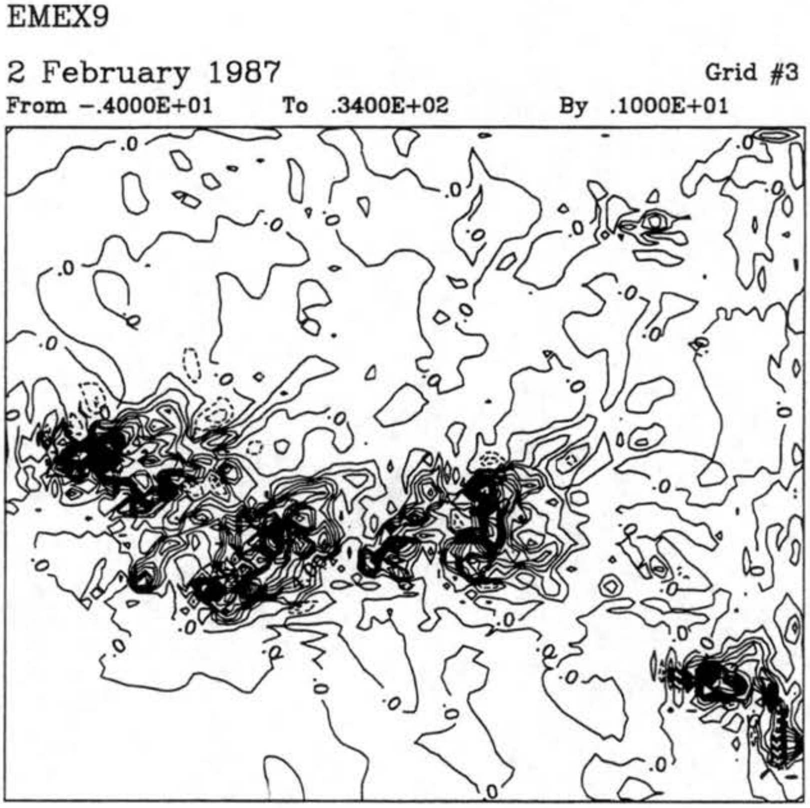

w (ms^{-1})

p = 500 mb t = 1700 UTC

(d)

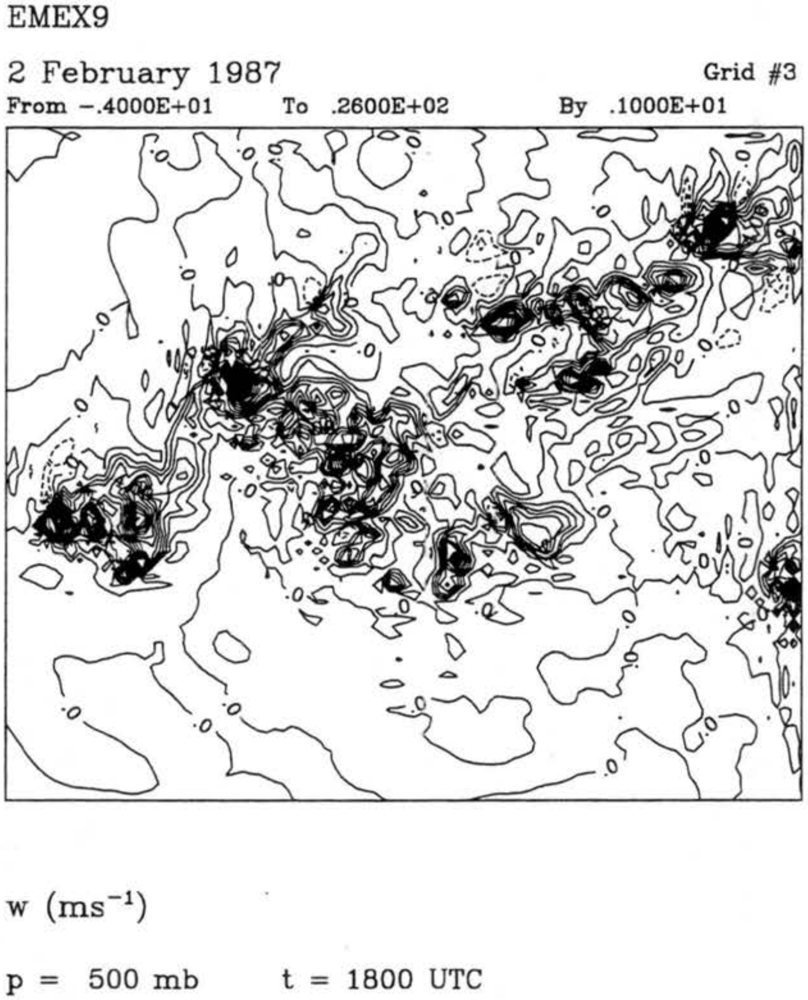

Fig. 3.11: Vertical velocity at 500 mb on Grid #3 at (a) 1500 UTC, (b) 1600 UTC, (c) 1700 UTC, and (d) 1800 UTC 2 February.

Three-dimensional plots provide another perspective of the simulated EMEX9 convection. Fig. 3.12 shows the 0.5 gkg^{-1} surface of condensate mixing ratio on Grid #3 at 1500, 1600, and 1700 UTC. At 1500 UTC a leading anvil stretches from east to west across the grid, with convective towers trailing behind. By 1600 UTC the stratiform anvil extends both ahead of and behind the convection, and blankets all of Grid #3.

Fig. 3.13 shows vertical cross-sections of the convection along a north-south line bisecting Grid #3 at 1800 UTC. The condensate cross-section shows that the deep convection penetrates to the top of the troposphere with a stratiform cloud extending both ahead of and behind the convection with a distinct base at $\sim$ 5 km. A "bright-band" is evident as well, especially behind the convective line. The vertical velocity cross section shows convective drafts which have maximum magnitudes at varying altitudes, with an especially large concentration of drafts at altitudes between 10 and 13 km. These upper-level updrafts and downdrafts appear similar in structure to those shown in the Doppler observations in Fig. 3.7. Here, draft magnitudes vary between -5 and +9 ms^{-1} although more extreme values can be found elsewhere (e.g., Fig. 3.11). The meridional wind cross section shows inflow to the storm from the north between the surface and $\sim$ 2 km. This northerly momentum is apparently carried up in convective updrafts and deposited at the top of the troposphere, where strong northerlies also appear. The cross-section of perturbation Exner function (where the perturbations are from a Grid #3 mean at each altitude) shows that the upper-tropospheric northerlies also are consistent with a north-to-south directed meridional

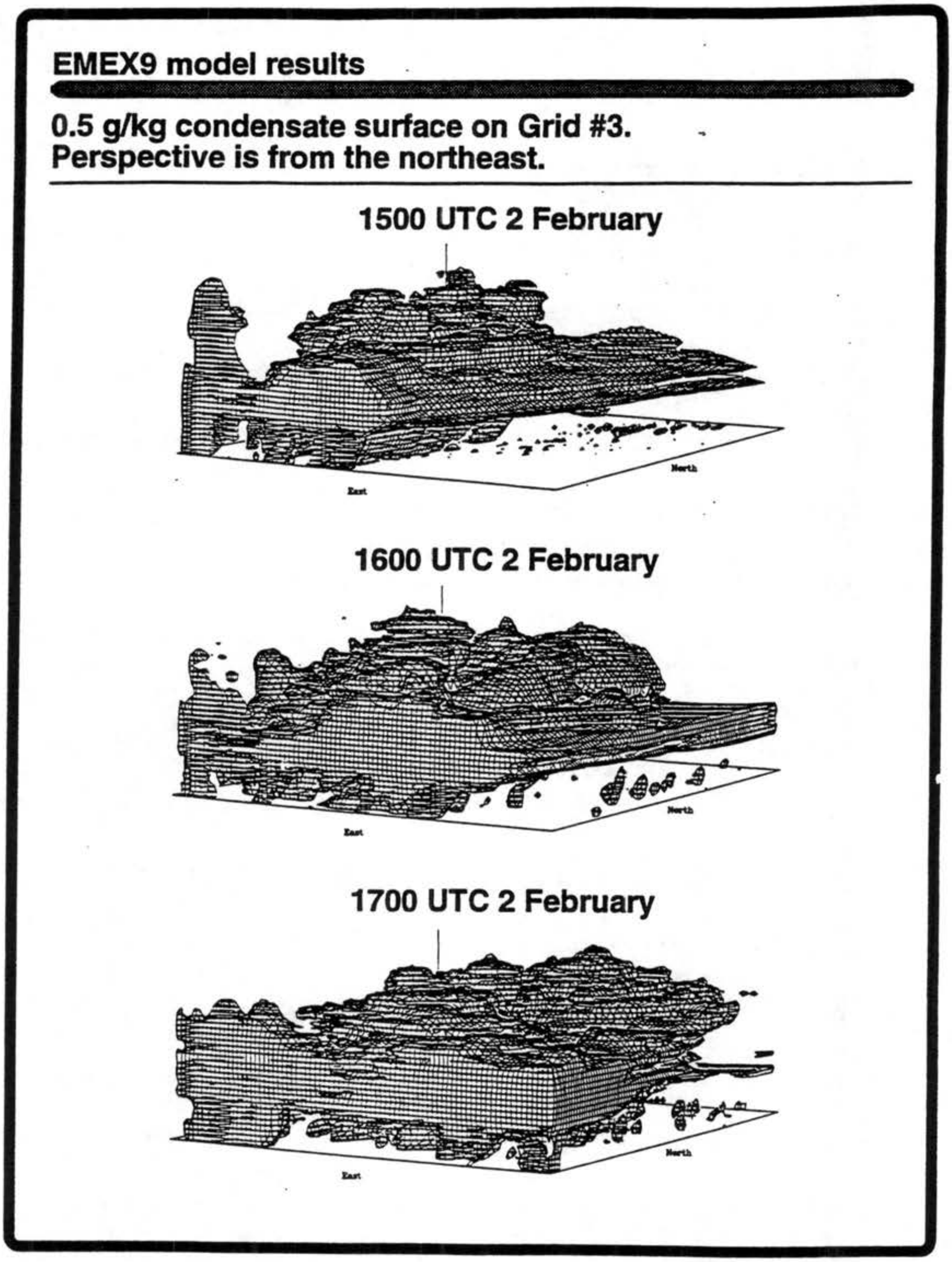

Fig. 3.12: The 0.5 gkg^{-1} condensate surface on Grid #3 at 1500 UTC, 1600 UTC, and 1700 UTC. The vertical line on the southwest corner of the grid extends from the surface to 20 km. Perspective is from the northeast.

component of the perturbation pressure gradient force above 10 km in the vicinity of the convection. Below 10 km, the meridional component of the perturbation pressure gradient force is directed from south to north in the vicinity of the convection.

Examination of precipitation rates on Grid #3 indicates that we have captured EMEX9 from its incipient stage until maturity. The total precipitation rate on Grid #3 steadily increases from 6×10^6 kgs^{-1} to 3.9×10^7 kgs^{-1} between 1400 and 1800 UTC (Fig. 3.14). In Chapter 4, the partitioning of this precipitation between the convective and stratiform regions is discussed.

3.4 PRE-STORM 23-24 June 1985 simulation

3.4.1 Observations

The PRE-STORM 23-24 June MCS formed under classic synoptic conditions. At 1200 UTC 23 June a cold front trailed from a deep surface low near Hudson Bay, with the front becoming stationary across the central U.S. By 0000 UTC 24 June the Nebraska surface low had deepened a bit with a dryline extending south from it into western Kansas. A stationary front snaked its way southeastward into the low and east-northeastward out of the low (Fig. 3.15). At this time, low-level air south of the front was hot and moist, with surface temperatures as high as 39° C and surface dewpoints as high as 24° C. Meanwhile, at 850 mb a strong southerly jet (maximum wind speeds > 15 ms^{-1}) over the southern Plains states provided a continuing supply of warm, moist air (Fig. 3.16). The 500 mb height field contained a broad, rather weak ridge over the continental U.S., with a shortwave trough passing through the ridge over the central plains (Fig. 3.17). The 850 mb warm temperature

(a)

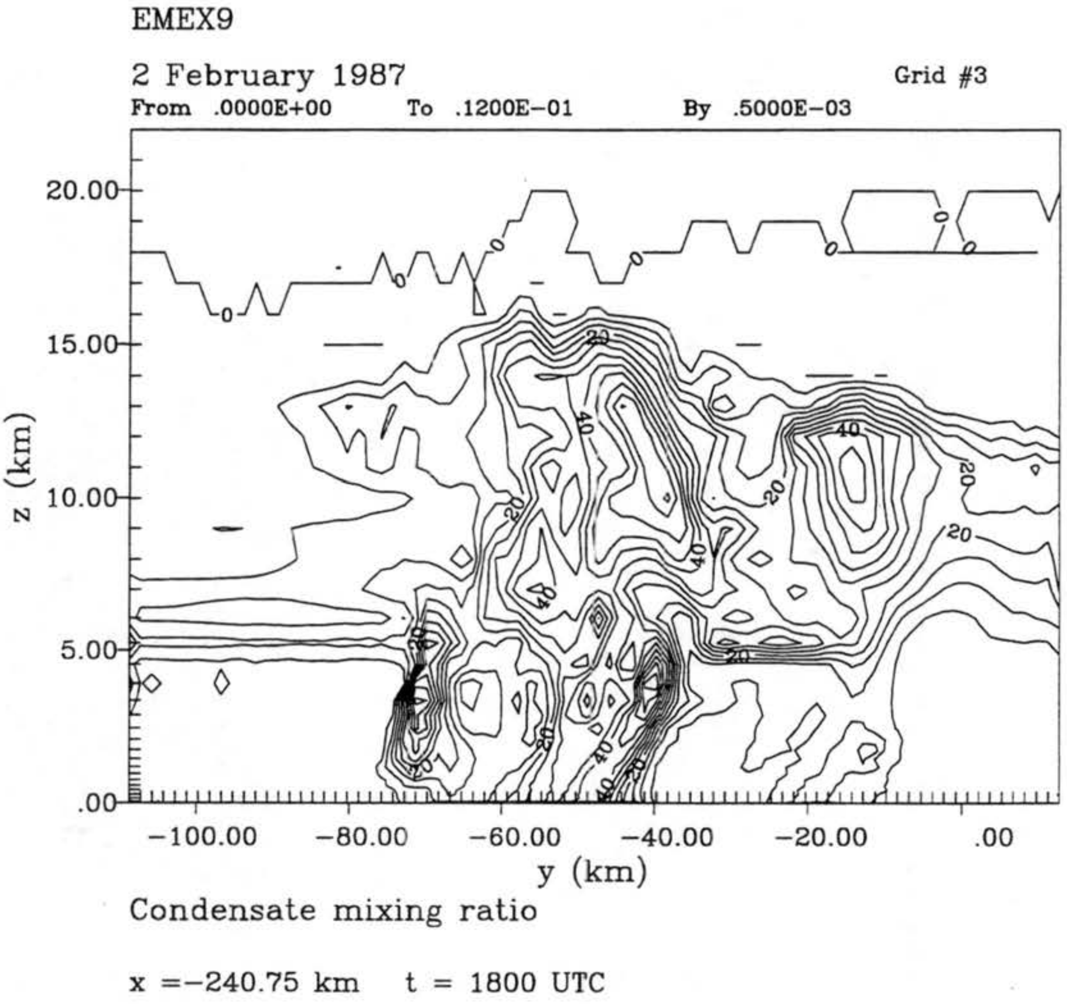
EMEX9
2 February 1987
Grid #3
From .0000E+00 To .1200E-01 By .5000E-03
20.00
15.00
10.00
5.00
.00
z (km)
−100.00
−80.00
−60.00
−40.00
−20.00
.00
y (km)
0
20
40
Condensate mixing ratio
x =−240.75 km t = 1800 UTC

(b)

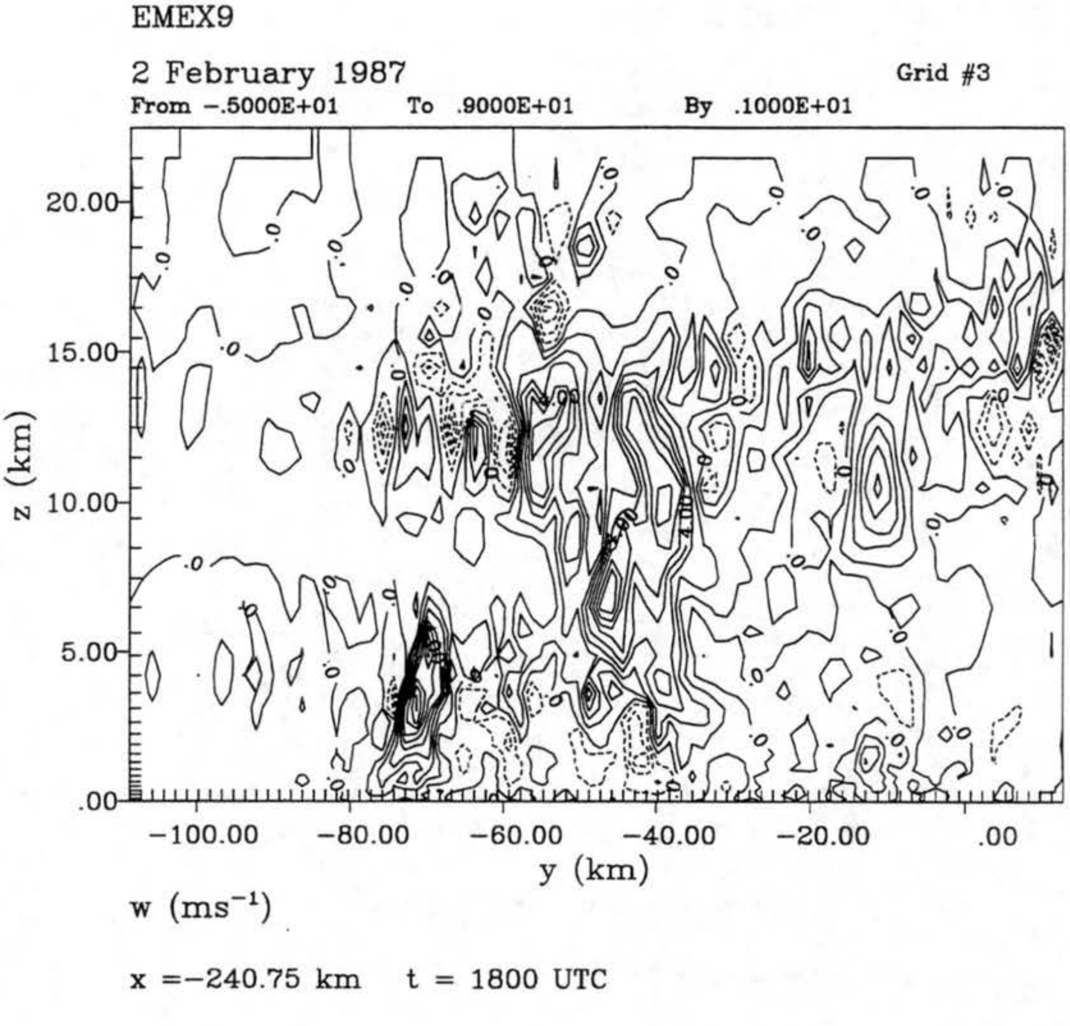
EMEX9
2 February 1987
Grid #3
From -.5000E+01
To .9000E+01
By .1000E+01
20.00
15.00
10.00
5.00
.00
z (km)
-100.00
-80.00
-60.00
-40.00
-20.00
.00
y (km)
4.00
w (ms^{-1})
x =-240.75 km
t = 1800 UTC

(c)

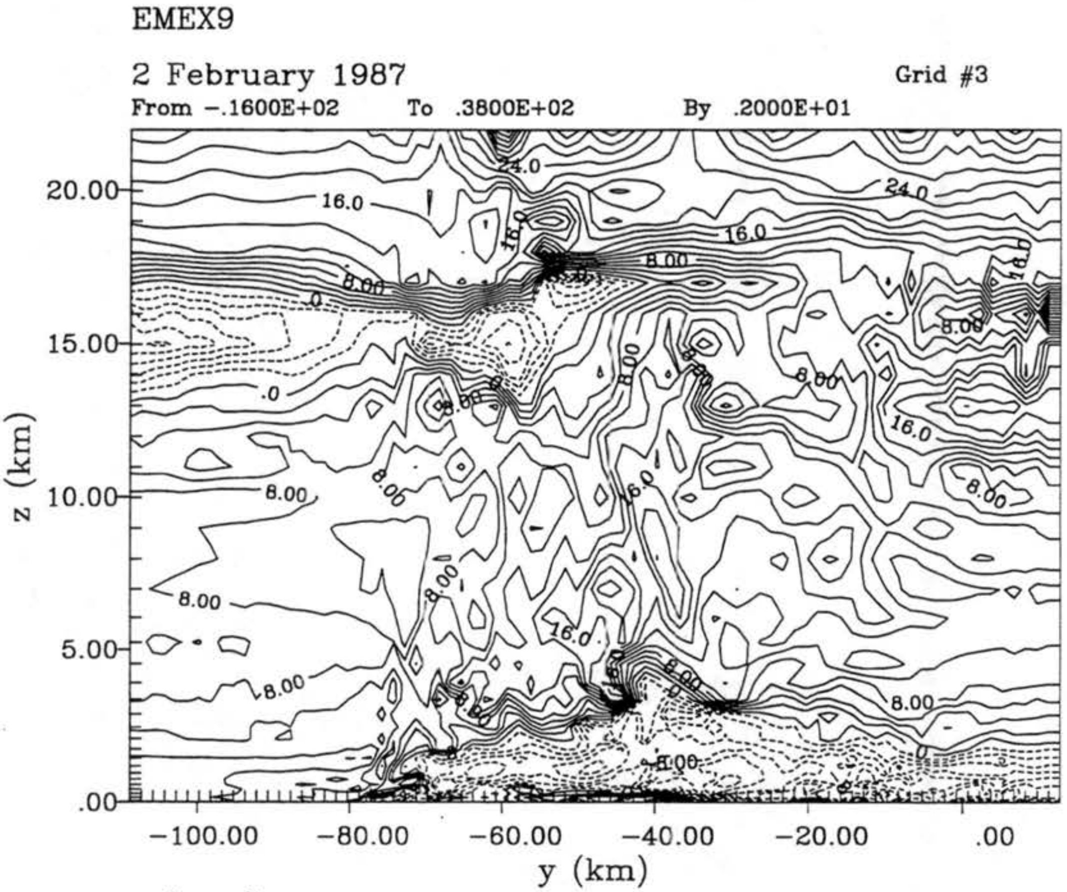

v (ms^{-1})

x =−240.75 km   t = 1800 UTC

(d)

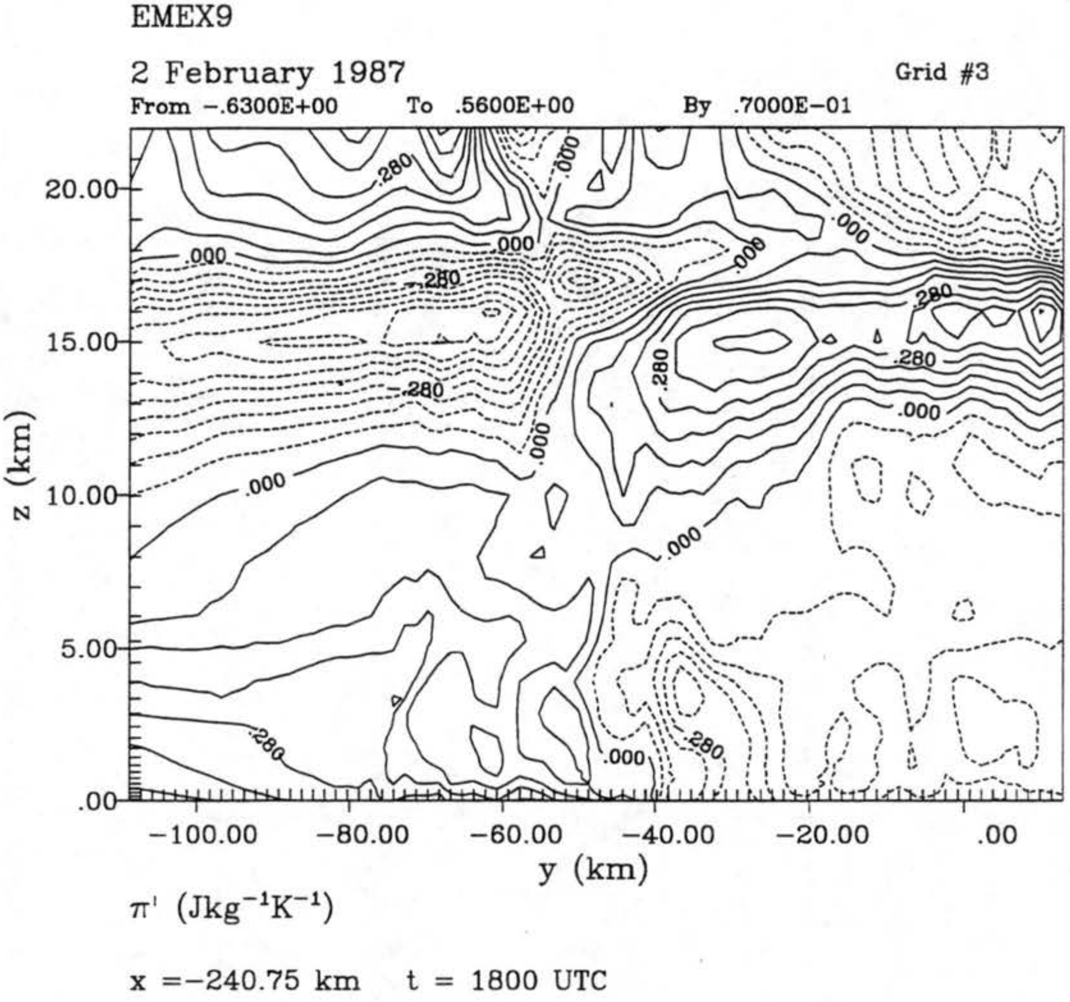

Fig. 3.13: Vertical cross-section along a north-south line bisecting Grid #3 at 1800 UTC 2 February 1987 for (a) condensate mixing ratio, (b) vertical velocity, (c) meridional velocity, (d) perturbation Exner function.

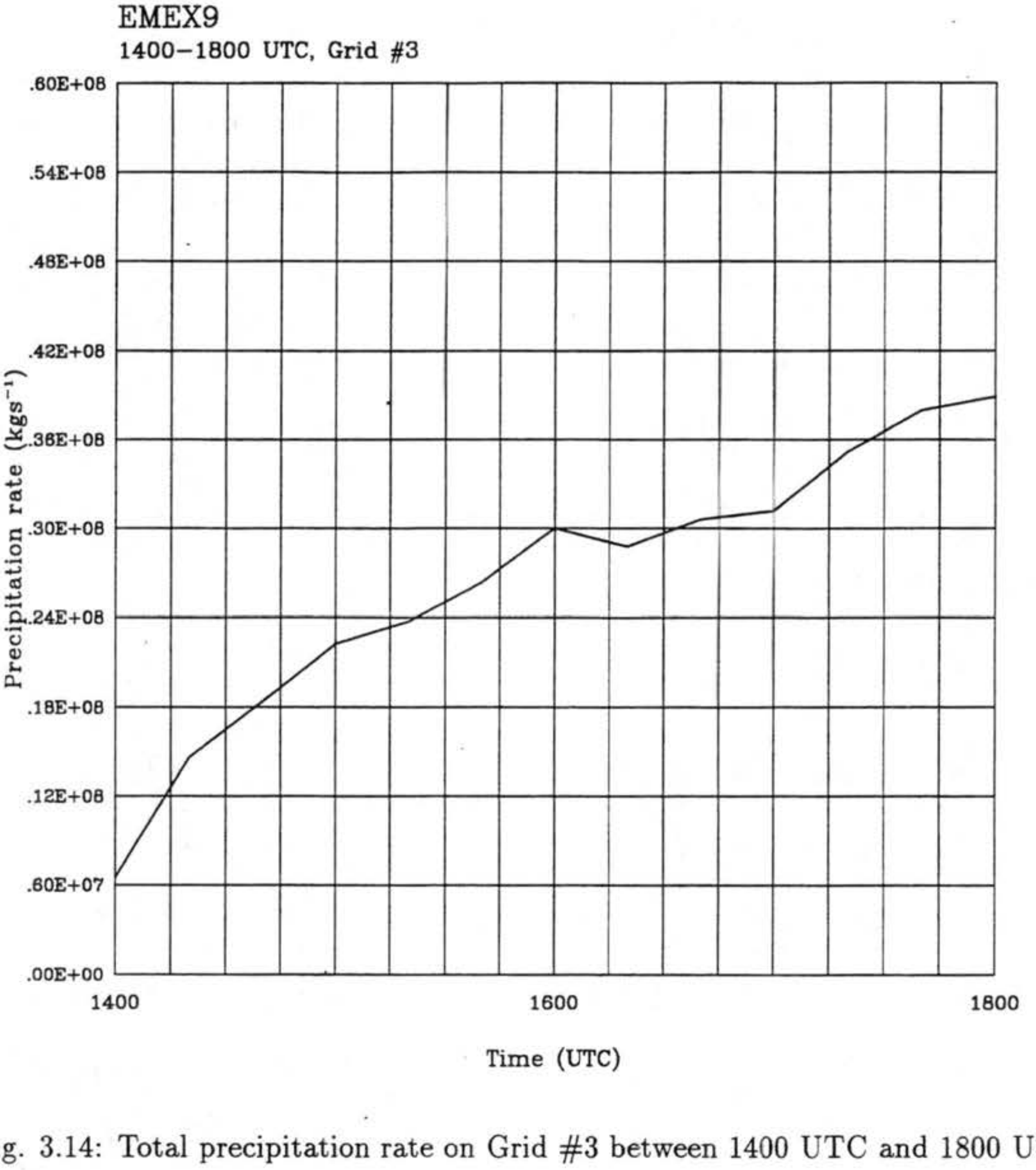

Fig. 3.14: Total precipitation rate on Grid #3 between 1400 UTC and 1800 UTC.

advection and the 500 mb shortwave teamed up to provide the primary forcing for the PRE-STORM 23-24 June MCS.

Convective cells first formed around 1900 UTC 23 June along the dryline and front. Convective cells in northern Kansas and southern Nebraska moved toward the east-southeast; those in central and southern Kansas moved toward the south. By 0000 UTC 24 June, convection in the northeastern part of the area had consolidated into a large MCS in eastern Nebraska and Iowa along and to the south of the front (courtesy of an old outflow boundary). Another area of thunderstorms was located over west-central Kansas along the dryline, and eventually blossomed into a smaller MCS. The infrared satellite images in Fig. 3.18 show the smaller MCS over western Kansas, and the larger one over northern Missouri and southern Iowa. The fine grid zeroes in on the latter MCS.

3.4.2 Initialization

The model initial fields were obtained by compositing several different data sources. The large-scale background features were obtained from European Center for Medium-Range Weather Forecasting (ECMWF) analyses, which provide the horizontal wind components, temperature, and relative humidity at 2.5° latitude/longitude intervals and at 1000, 850, 700, 500, 300, 200, and 100 mb. To resolve finer scale features, additional rawinsonde and surface observations from the National Weather Service/Federal Aviation Administration operational station network and the PRE-STORM station network supplemented the ECMWF data. At the lower boundary the model uses topographic data which has a horizontal spacing of 10 minutes lati-

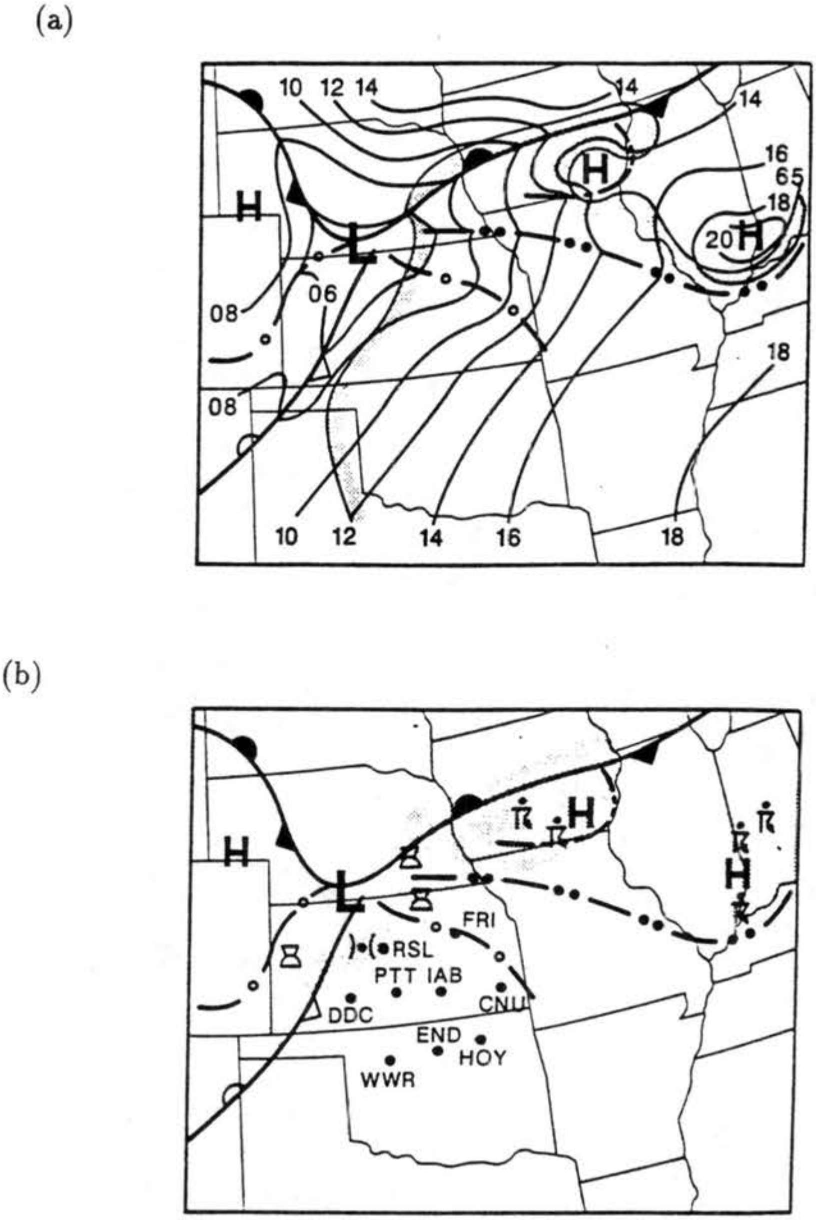

Fig. 3.15: (a) Sea level pressure (millibars minus 1000) and surface frontal analysis at 0000 UTC 24 June 1985. Outflow boundaries are indicated by a dash-dot-dot pattern, while wind shift lines are indicated by a dash-dot pattern. The shaded line highlights the region with dewpoint temperatures greater than 18°C. (b) Surface frontal analysis with shaded regions indicating infrared cloud top temperatures less than -32°C. Surface weather observations are also shown. From Stensrud and Maddox (1988).

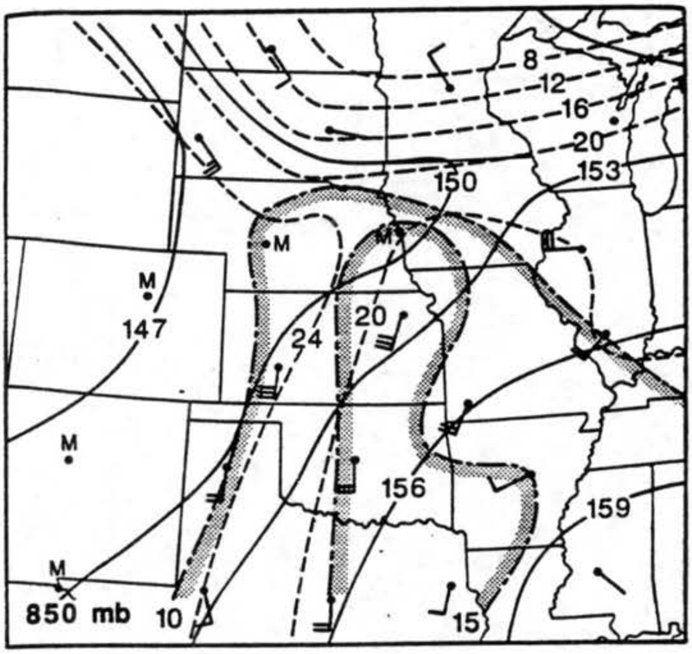

Fig. 3.16: Analysis of 850 mb height, temperature, and dewpoint temperature at 0000 UTC 24 June 1985. Winds are in knots (full barb equals 10 knots). Height contours (solid) are in decameters, while temperatures are contoured (dashed) at 4°C intervals. Regions in which dewpoint temperatures exceed 10°C and 15°C are shown. From Stensrud and Maddox (1988).

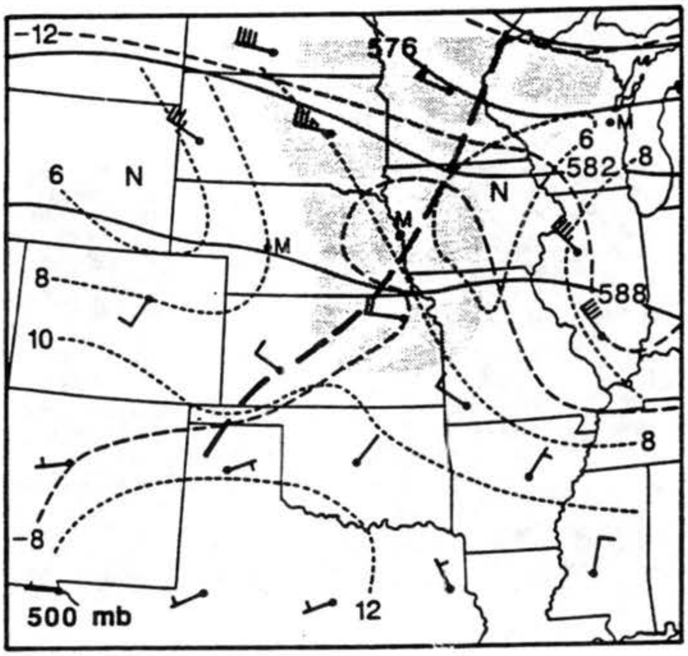

Fig. 3.17: Analysis of 500 mb height, temperature, and absolute vorticity fields at 0000 UTC 24 June 1985. Winds, height contours, and temperature contours are as in Fig. 3.16. Absolute vorticity ($\times 10^5$ s^{-1}) contours (short-dashed) are generated by objective analysis, with areas of positive vorticity advection shaded. The N denotes a minimum in absolute vorticity. The thick dashed line indicates the position of a short-wave trough. From Stensrud and Maddox (1988).

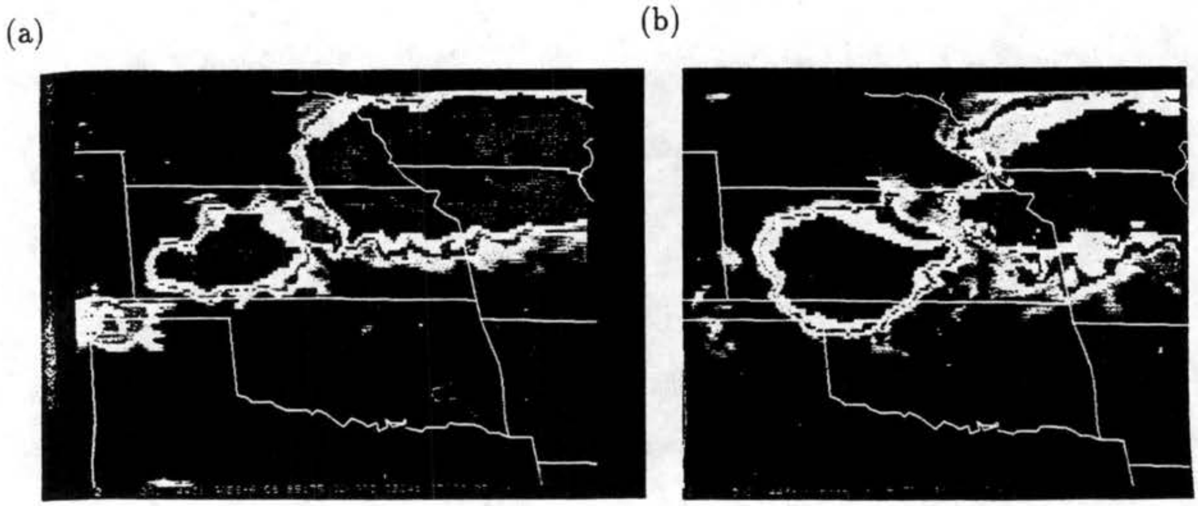

Fig. 3.18: Infrared satellite images of the 23-24 June PRE-STORM MCS at (a) 0200 UTC and (b) 0430 UTC 24 June 1985..

tude/longitude on Grid #1 and 30 seconds latitude/longitude on the other grids. A vegetation-type data set from NCAR with 11 primary vegetation types at a 5 minute latitude/longitude resolution is interpolated onto the model grids and then converted to the vegetation classification used in the model (the model recognizes 18 vegetation types). In addition, horizontally variable soil moisture is based on the soil moisture analysis in the USDA publication, Weekly Weather and Crop Bulletin (WWCB). The WWCB soil moisture index data were manually transferred to a latitude/longitude gridded data set at 1° horizontal spacing. This data set was then filtered and interpolated onto the model grid where it was converted into a soil moisture percentage.

3.4.3 Setup

The startup time is 1200 UTC (0600 LST over the fine grid) 23 June 1985. The simulation actually uses two grid setups. Prior to 0000 UTC, the model uses three grids, with horizontal grid spacings of 75 km, 25 km, and 8.333 km (Fig. 3.19). After 0000 UTC, a cloud-resolving grid is added (2.083 km) while the coarse 75 km grid is eliminated (lack of computer memory made it impossible to use all four grids). Thus, after 0000 UTC, the model's horizontal grid spacing on the three grids is 25 km, 8.333 km, and 2.083 km. Hereafter, these grids are called Grids #1, #2, and #3, respectively (Fig. 3.20). There are 32 vertical levels, stretched from a spacing of 175 m near the surface to 1000 m at the model top ($\sim$ 21 km). During the first 9 hours of the simulation, only the 75 km and 25 km grids are used. The 8.333 km grid is activated at 2100 UTC and the 2.083 km grid is activated at 0000 UTC. Between 1900 and 0000 UTC, the Level 2.5w convective parameterization scheme is used on the 25 km and 8.333 km grids; thereafter, it is not used at all. Thus, the PRE-STORM 23-24 June 1985 MCS is explicitly simulated (no convective parameterization) between 0000 and 0400 UTC, with analysis files saved every 15 minutes (0000 UTC, 0015 UTC, ...). The setup of the PRE-STORM simulation is summarized in Figs. 3.21 and 3.22.

3.4.4 Results

Before looking at the structure of the MCS on the cloud-resolving grid, we will examine the evolution of the synoptic fields and parameterized convection during the first 12 hours of the simulation, between 1200 UTC 23 June and 0000 UTC 24 June. Fig. 3.23 shows the surface field of equivalent potential temperature and horizontal winds at 1900 UTC, when the deep convective parameterization was first turned on. There is a tongue of high θ_e extending from southwest to northeast, with a θ_e maximum of 356 K near Omaha, Nebraska. The simulated surface stationary front straddles the warm side of an intense θ_e gradient and is situated within a zone of strong convergence. The simulated surface low is located along the Nebraska-Kansas border in good agreement with the 2100 UTC analysis of Johnson et al. (1989) (Fig. 3.24). However, the 1800 UTC National Meteorological Center analysis (not shown) places the low near North Platte, Nebraska—slightly to the north and west of the simulated location.

Simulated convection first occurred at 2000 UTC 23 June in east-central Iowa along the simulated cold front. Late morning surface reports from this region noted that heavy rain, damaging winds, and ping-pong ball-sized hail occurred over this area. As the simulated convective system drifted eastward, more moist soil in eastern

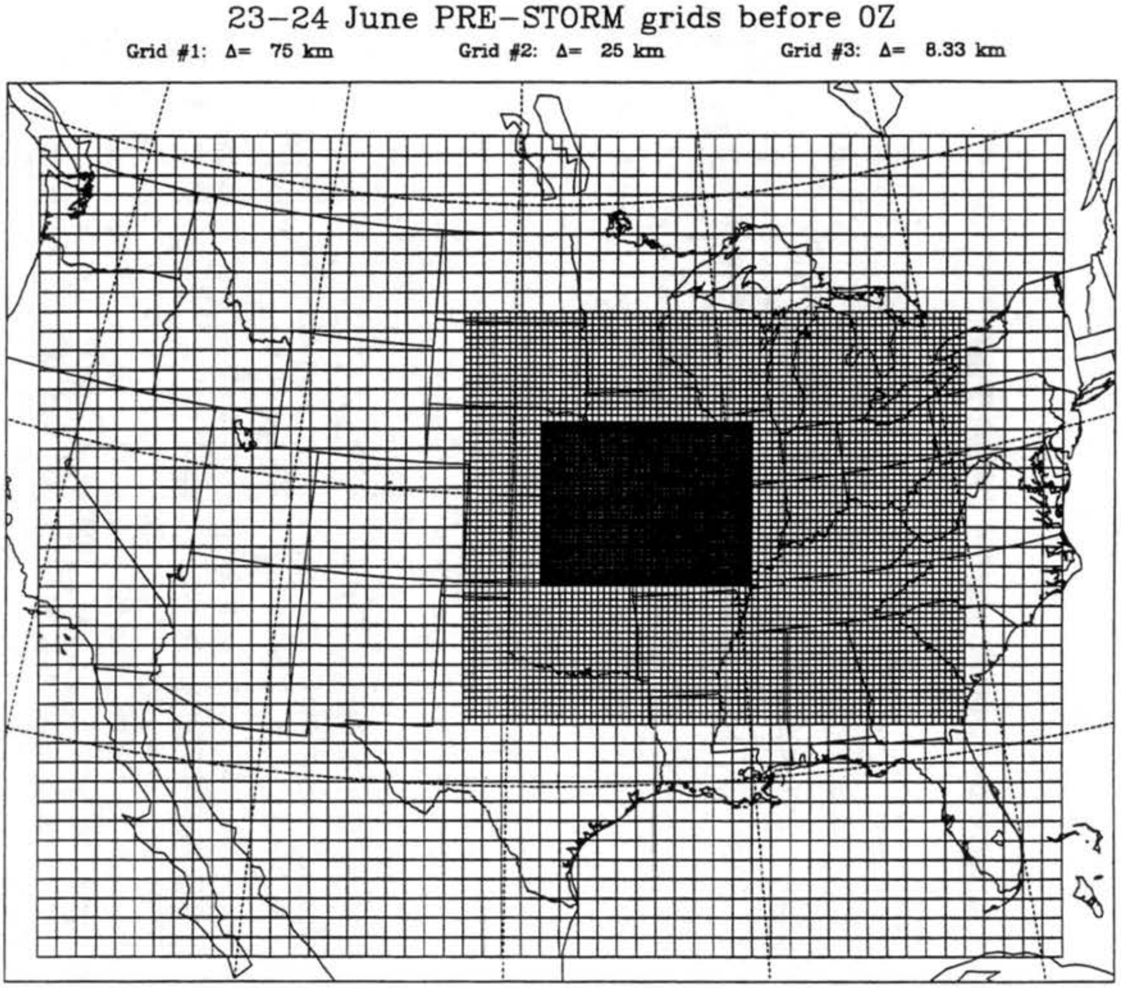

Fig. 3.19: Grid setup for the PRE-STORM simulation before 0000 UTC 24 June 1985. The horizontal grid spacing is 75 km, 25 km, and 8.333 km on Grids #1, #2, and #3, respectively.

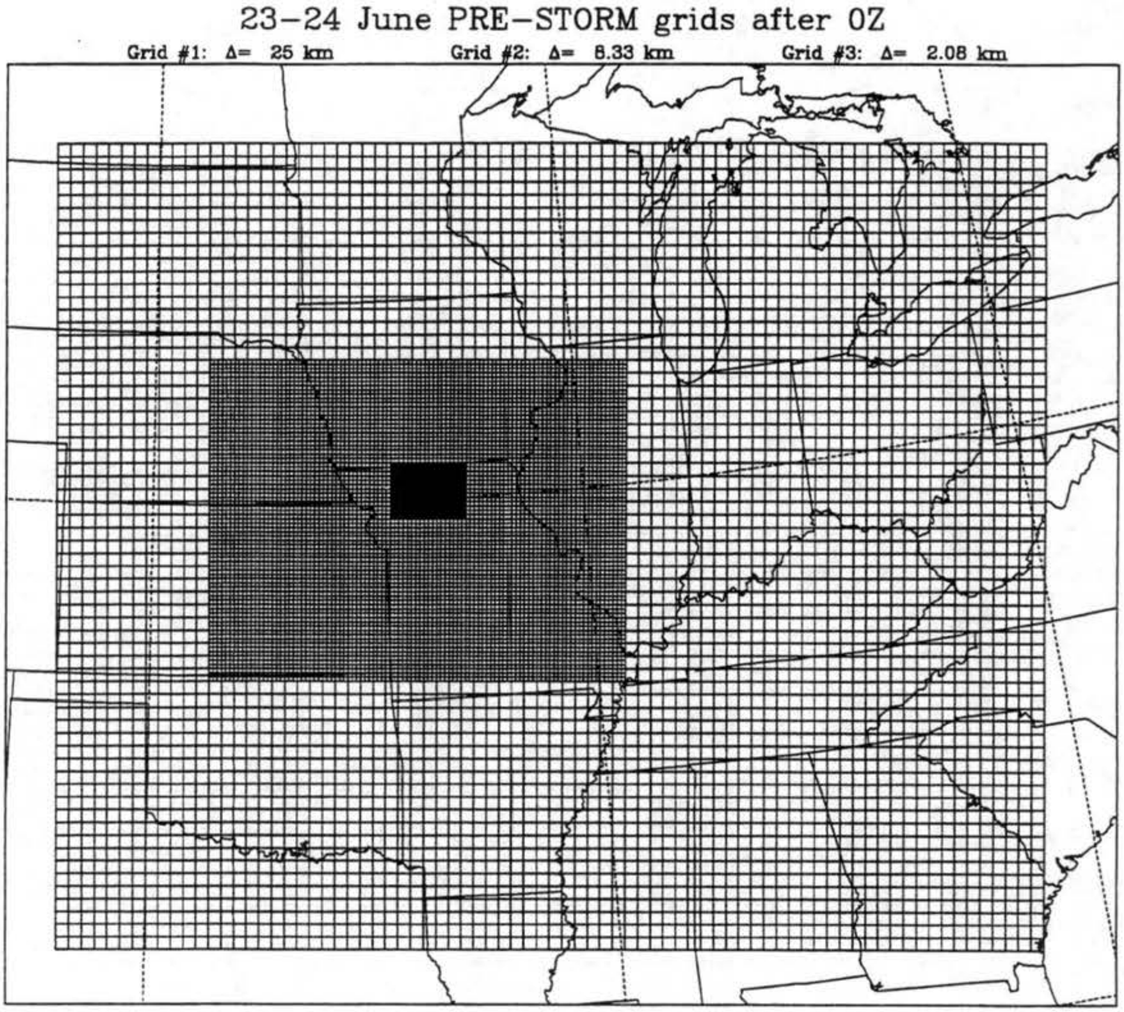

Fig. 3.20: Grid setup for the PRE-STORM simulation after 0000 UTC 24 June 1985. The horizontal grid spacing is 25 km, 8.333 km, and 2.083 km on Grids #1, #2, and #3, respectively.

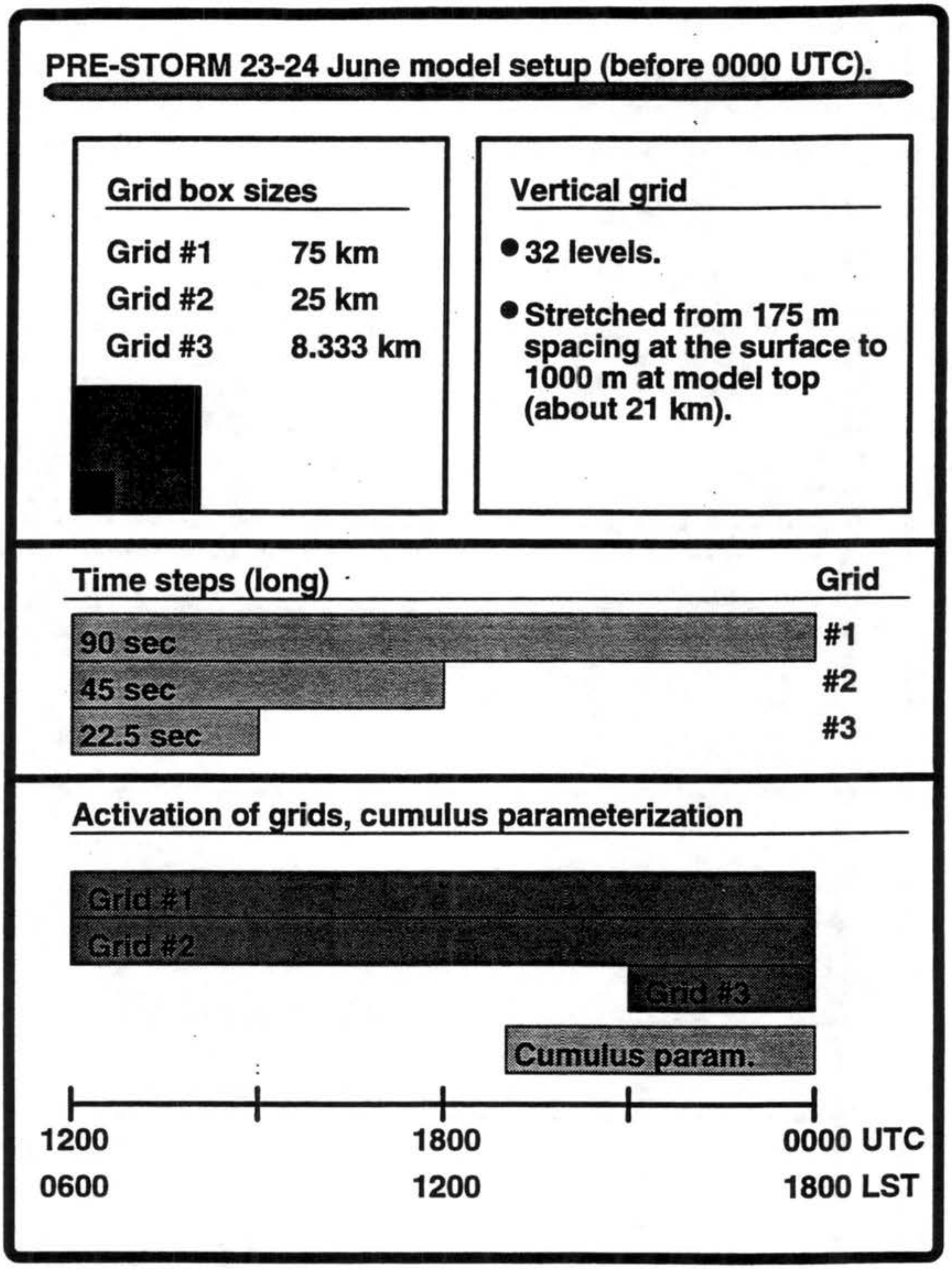

Fig. 3.21: Summary of the model setup for the PRE-STORM 23-24 June simulation before 0000 UTC 24 June.

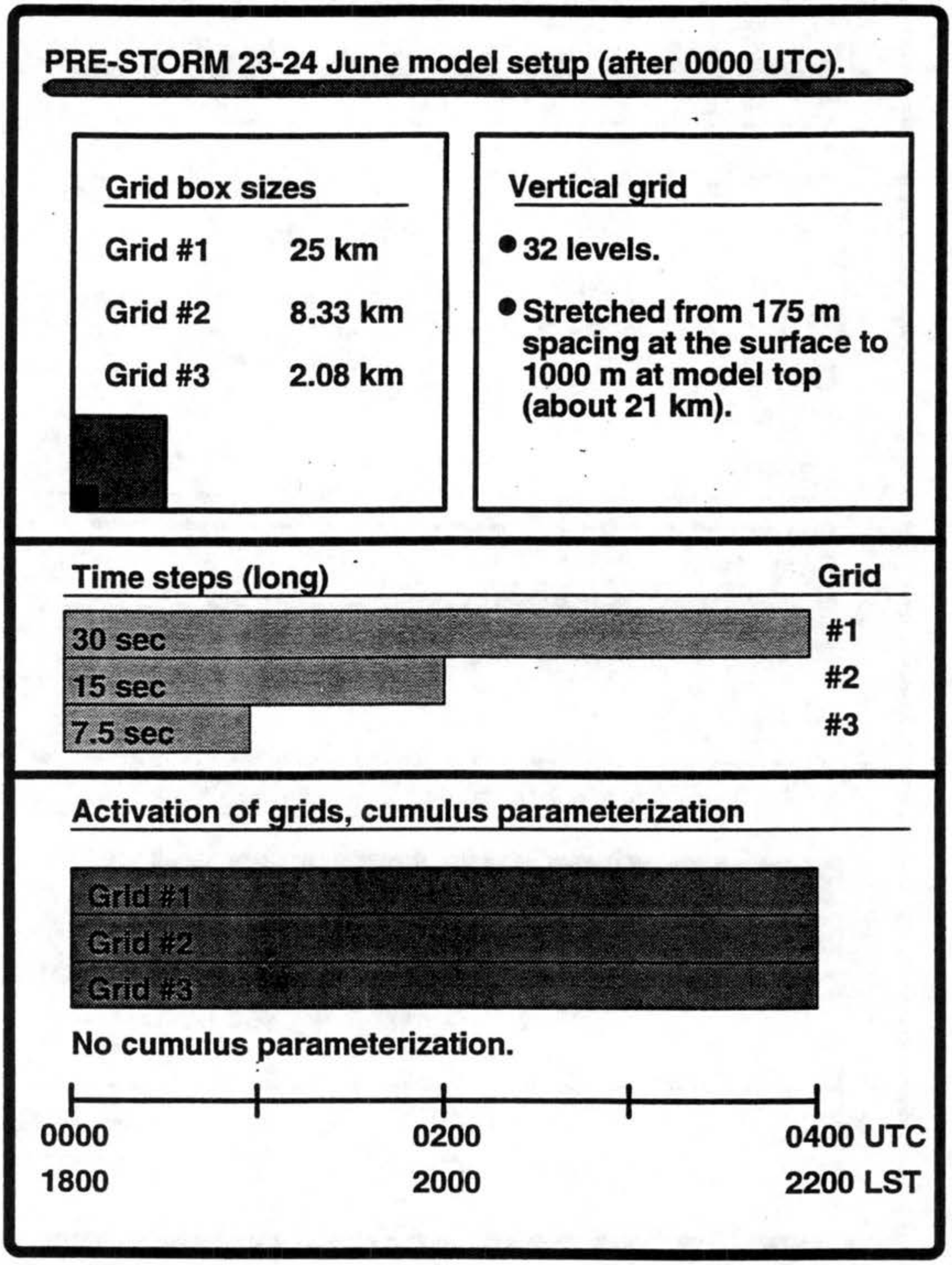

Fig. 3.22: Summary of the model setup for the PRE-STORM 23-24 June simulation after 0000 UTC 24 June.

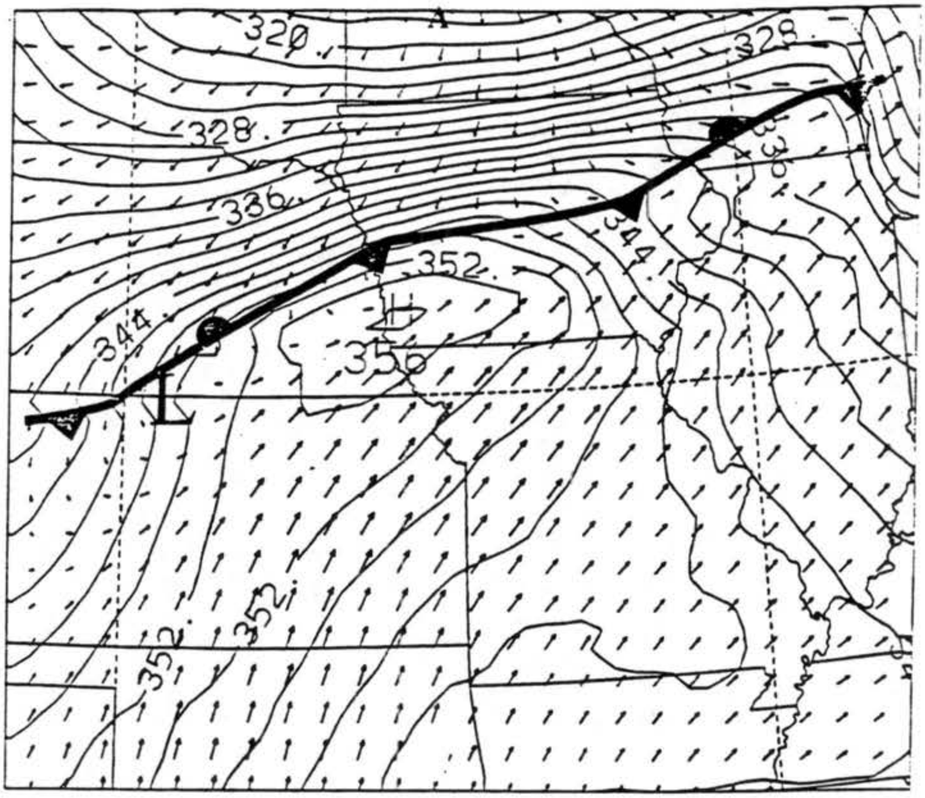

Fig. 3.23: Wind vectors and contours of equivalent potential temperature at the surface at 1900 UTC 23 June 1985. The contour level for θ_e is 2 K and the longest wind vector represents a speed of 8 ms^{-1}. The position of the surface low is indicated by a bold "L". From Olsson (1995).

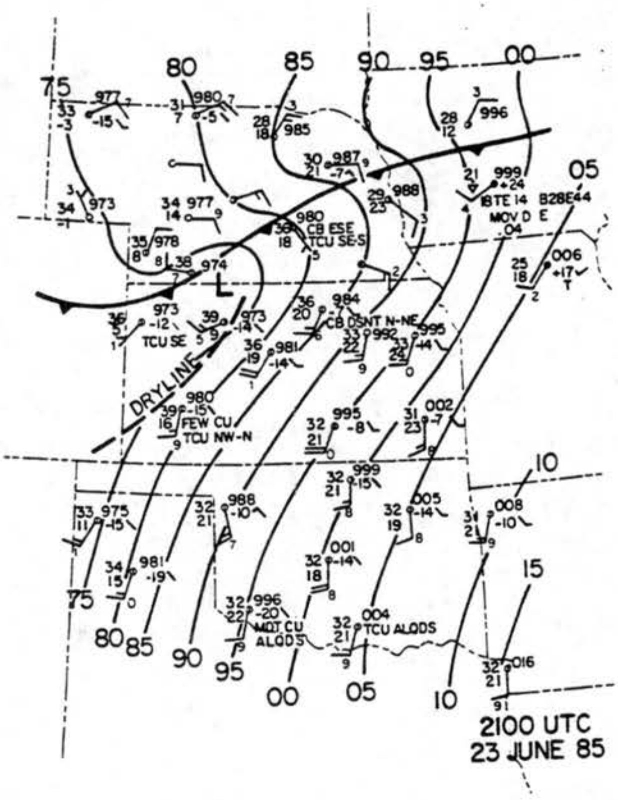

Fig. 3.24: Surface analysis for 2100 UTC 23 June 1985. Isobars are in units of Hg (e.g., 90=29.90 in Hg). For wind speed, one full barb = 5 ms^{-1}, one half barb = 2.5 ms^{-1}. From Johnson et al. (1989).

Iowa resulted in depressed surface sensible heat fluxes and ambient CAPE, causing the parameterized convection to subside. By 2030 UTC, the parameterized convection over this region had largely finished, although resolved precipitation continued to fall for the next several hours as the simulated clouds drifted eastward along the surface front.

Shortly after 2000 UTC 23 June, new convection associated with subsequent MCS development developed just to the south of the surface front along a line extending from the eastern-half of the Iowa-Missouri border westward into southeast Nebraska. Extremely hot, muggy surface air, high CAPEs, and sufficiently strong resolved vertical velocities at cloud base ($\sim$ 4 $\mathrm{cms^{-1}}$) ripened conditions for convection across this region. In southeast Nebraska, at 2000 UTC, for example, the simulated surface temperature and dewpoint temperatures were an oppressive 35°C and 22°C, respectively (compared to observed values of 36°C and 22°C). A stable layer between 810 and 760 mb here created a "lid" which permitted CAPE to build up to 3700 $\mathrm{Jkg^{-1}}$. Several tornadoes, damaging winds, and racquetball-sized hail were reported over this area between 2100 UTC and 0200 UTC 24 June. The simulated east-west convective line continued to intensify between 2030 UTC and 2200 UTC and propagated southward as new convective bands formed along the low-level convergence zone where the outflow from the old convection met the low-level jet in northeast Kansas and southeast Nebraska. During this time, simulated rainfall rates in south-central Iowa exceeded 5 $\mathrm{cmh^{-1}}$, in good agreement with observations. Storm reports in this region indicate over 12 cm of rainfall in Madison, Clark, and Warren counties of Iowa in the late afternoon. By 0000 UTC 24 June, the parameterized convection on the 8.333 km grid was concentrated in two general areas—southeast Nebraska/northeast Kansas and south-central Iowa/north-central Missouri (Fig. 3.25).

Figs. 3.26a and 3.26b shows the 850 mb wind vectors, height, and dewpoint temperature at 0000 UTC, and may be compared to Fig. 3.16. Although there are slight differences in the features shown in Figs. 3.26 and 3.16 (e.g., the orientation of the 850 mb moist tongue), generally the agreement is good. Comparison of the simulated 500 mb height and wind field at 0000 UTC 24 June (Fig. 3.27) with the observed field (Fig. 3.17) also shows good agreement, although the simulated shortwave trough axis is slightly to the east of the observed one.

Because the convection shown in Fig. 3.25 was propagating southward, it was decided to place the cloud-resolving grid in north-central Missouri and let the convection move into the grid. Now we will focus on the details of the convection on this cloud-resolving grid between 0100 and 0400 UTC. During this time, in agreement with observations, the simulated convection propagated southward at about 15 ms^{-1}. Comparison of simulated convection with contemporaneous radar observations shows generally good agreement between the simulation and observations, although the simulated convection does not extend quite as far west as the actual convection (Fig. 3.28). The vertical velocity pattern at 500 mb over Grid #3 between 0100 and 0400 UTC shows the convection entering the grid at 0100 UTC and steadily propagating southward (Fig. 3.29). The convective elements maintain their generally east-west orientation over the entire period. As for EMEX9, broad areas of weak

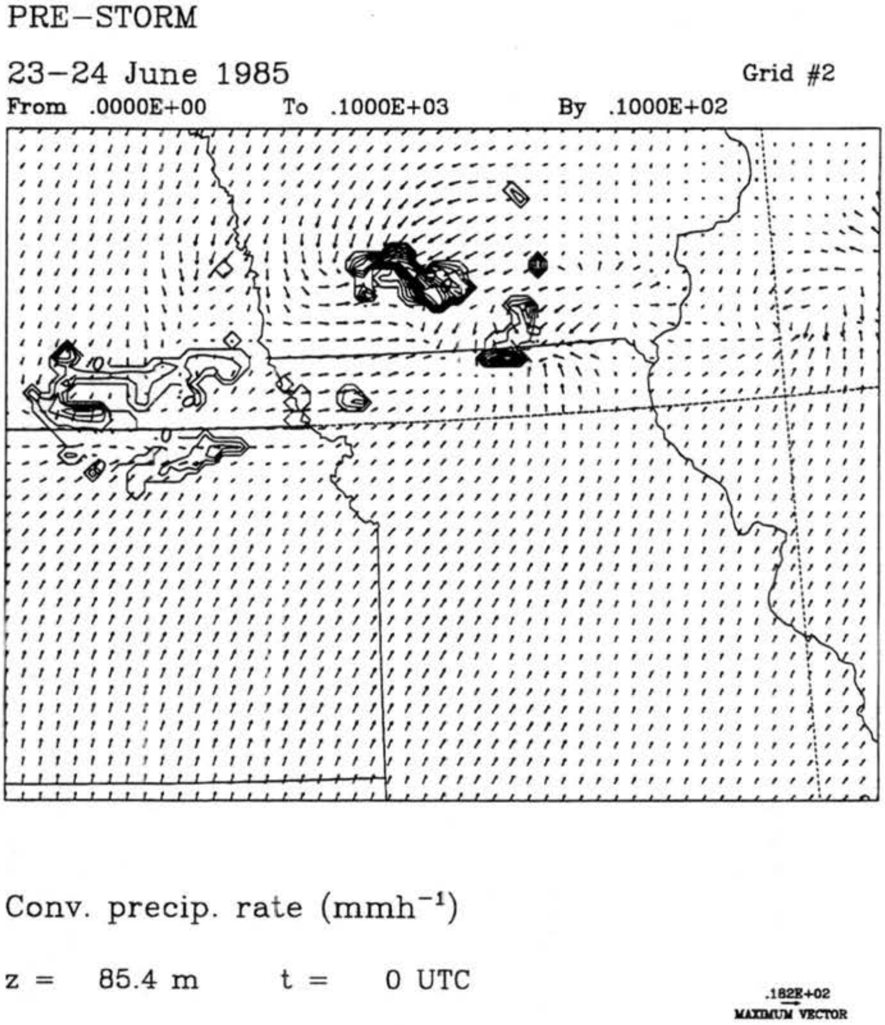

Fig. 3.25: Simulated convective precipitation rate and horizontal wind vectors at the lowest model level on Grid #2 at 0000 UTC 24 June.

(a)

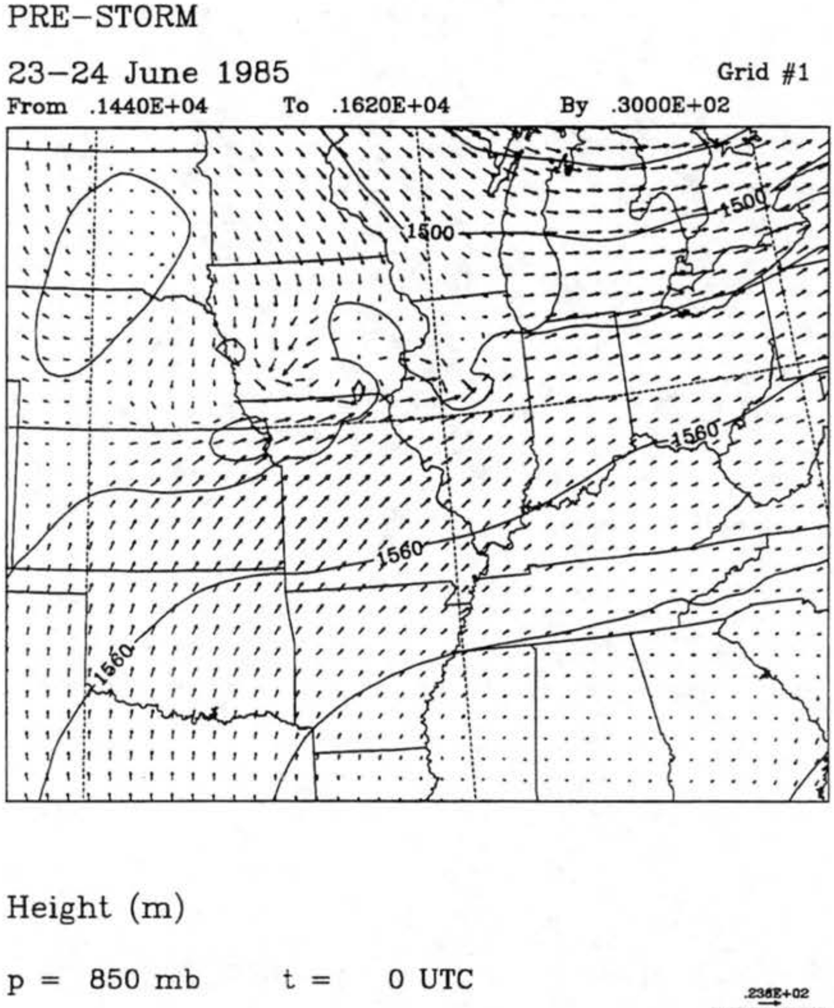
PRE-STORM
23-24 June 1985
Grid #1
From .1440E+04 To .1620E+04 By .3000E+02
1500
1500
1560
1560
1560
Height (m)
p = 850 mb t = 0 UTC
.236E+02
MAXIMUM VECTOR

(b)

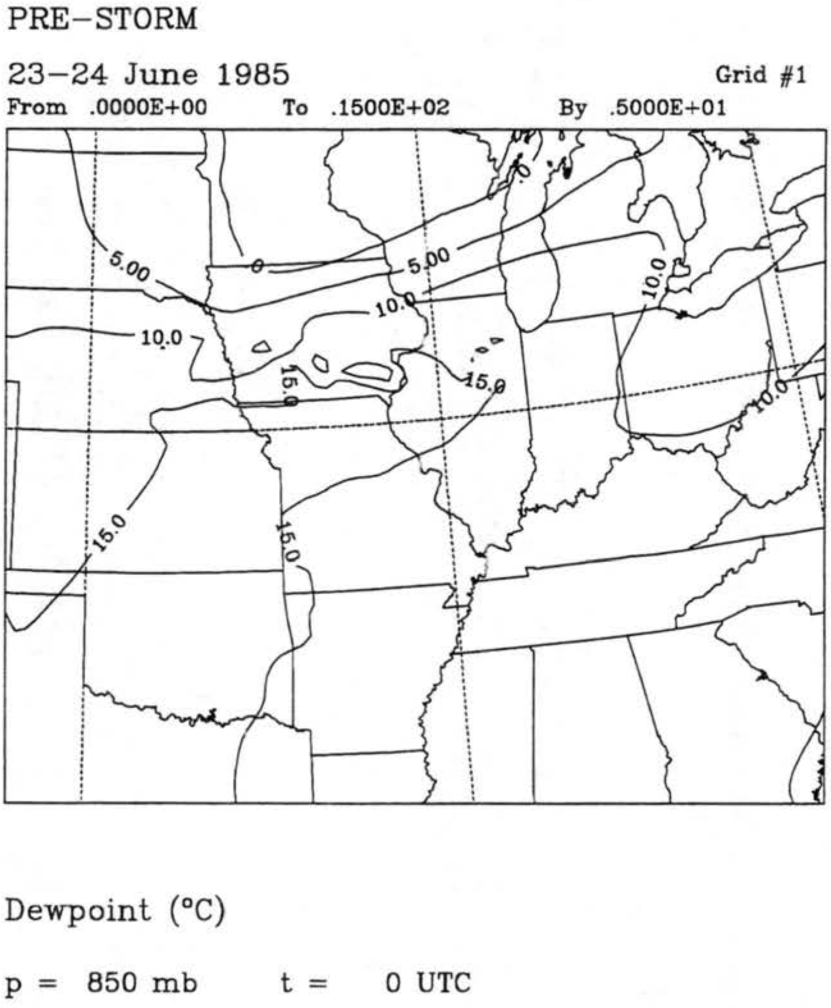

Fig. 3.26: Simulated 850 mb (a) wind vectors and height, and (b) dewpoint temperature on Grid #1 at 0000 UTC 24 June.

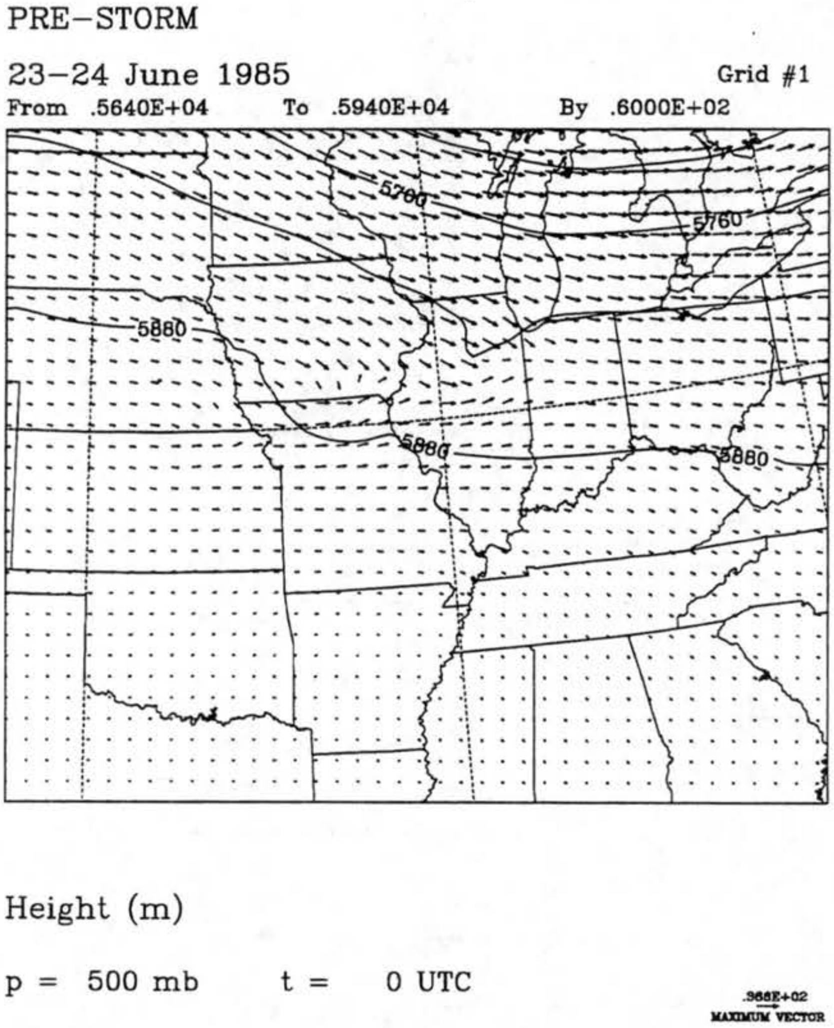

Fig. 3.27: Simulated 500 mb wind vectors and height field on Grid #1 at 0000 UTC 24 June.

positive vertical velocities trail the convective elements.

Three-dimensional plots provide another perspective of the simulated PRE-STORM convection. Fig. 3.30 shows the 0.5 gkg^{-1} surface of condensate mixing ratio on Grid #3 at 0130, 0230, and 0330 UTC. Although deep convection is confined to the northern part of the grid at 0130 UTC a thin leading anvil stretches southward across most of the grid. By 0330 UTC the deep convection is in the southern portion of the grid and a stratiform cloud with a middle-level cloud base extends all the way back to the north edge of the grid.

Fig. 3.31 shows vertical cross-sections of the convection along a north-south line bisecting Grid #3 at 0200 UTC. The condensate cross-section shows that the deep convection penetrates to the top of the troposphere with a stratiform cloud extending both ahead of and behind the convection. The vertical velocity cross section shows convective drafts which have maximum magnitudes at varying altitudes between 4 and 12 km. The upper-level updrafts and downdrafts between 8 and 12 km appear similar to those simulated for EMEX9. Here, draft magnitudes vary between -8 and +10 ms^{-1} although more extreme values can be found elsewhere (e.g., Fig. 3.29). The meridional wind cross section shows a front-to-rear slantwise ascending flow branch which appears to carry southerly momentum up to levels between 8 and 15 km. Strong northerlies appear at the surface behind of the leading edge of convection and in the upper troposphere ahead of the convection. The cross-section of perturbation Exner function (where the perturbations are from a Grid #3 mean at each altitude) shows that the upper-tropospheric northerlies are consistent with a north-to-south directed

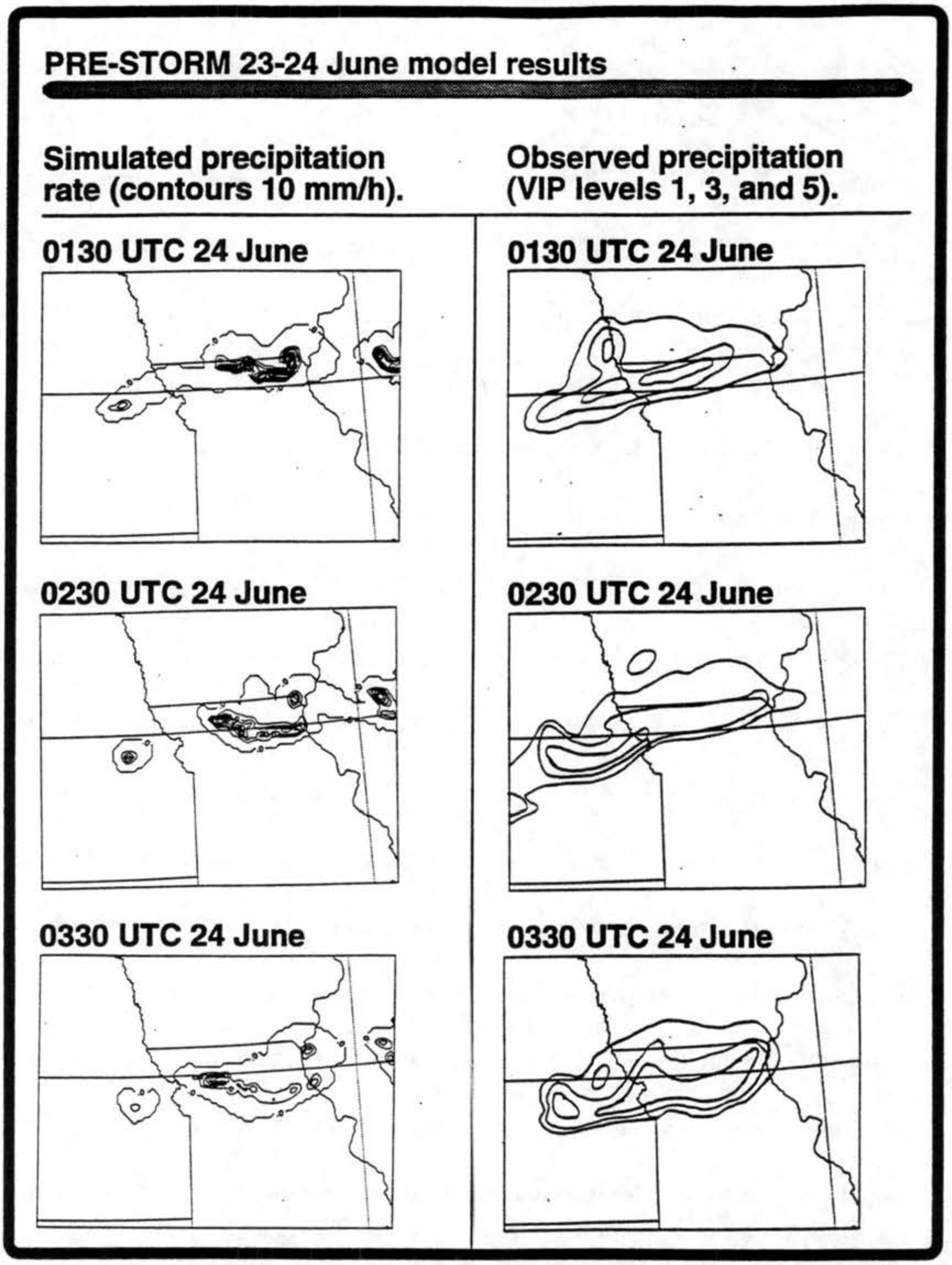

Fig. 3.28: Simulated surface precipitation rate (contours are 10 mmh^{-1}) on Grid #2 at 0130 UTC, 0230 UTC, and 0330 UTC 24 June 1985 compared with contemporaneous WSR-57 observed radar echoes (contours are VIP levels 1, 3, and 5, corresponding to approximately 30, 40, and 50 dBZ respectively).

(a)

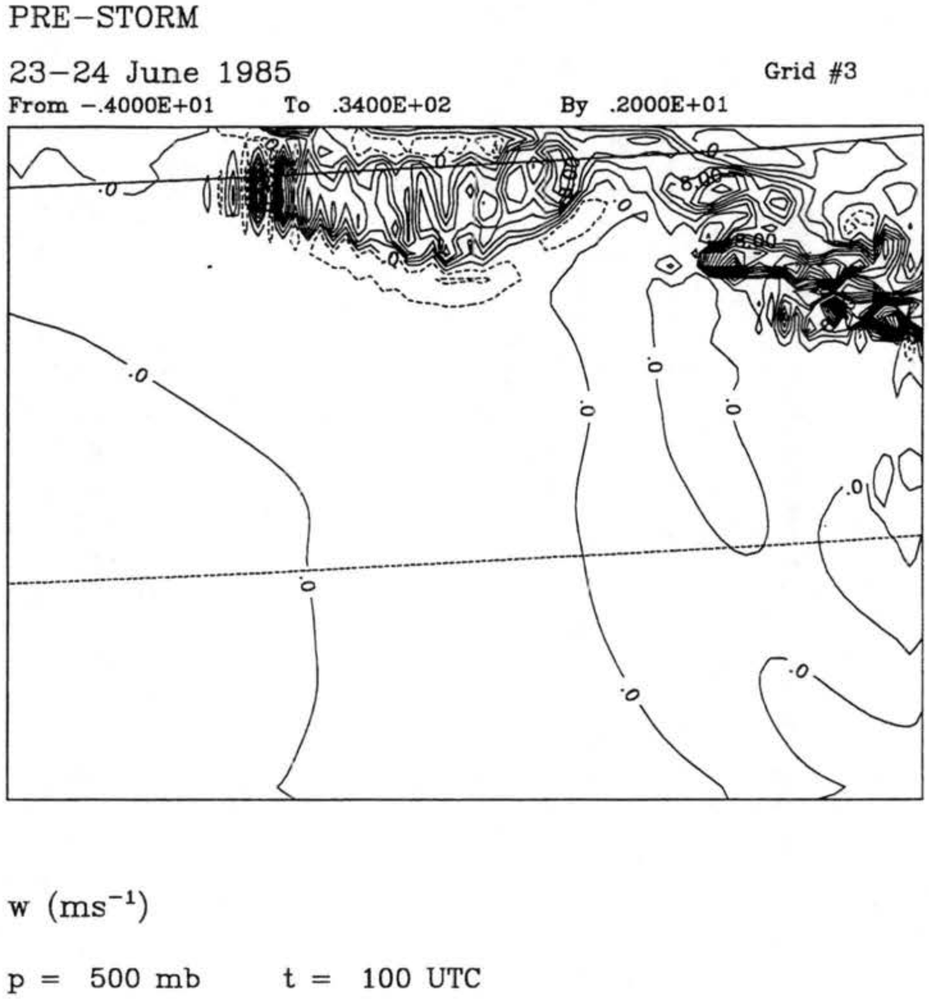
PRE-STORM
23-24 June 1985
Grid #3
From -.4000E+01 To .3400E+02 By .2000E+01
0
8.00
w (ms^{-1})
p = 500 mb t = 100 UTC

(b)

PRE−STORM

23−24 June 1985 Grid #3

From −.8000E+01 To .2000E+02 By .2000E+01

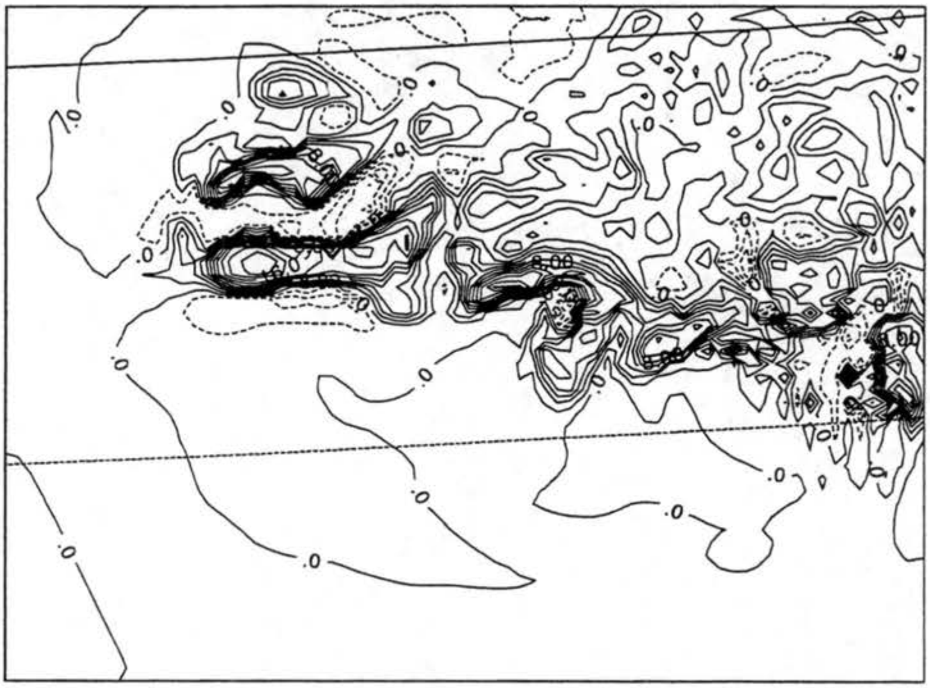

w (ms^{-1})

p = 500 mb t = 200 UTC

(c)

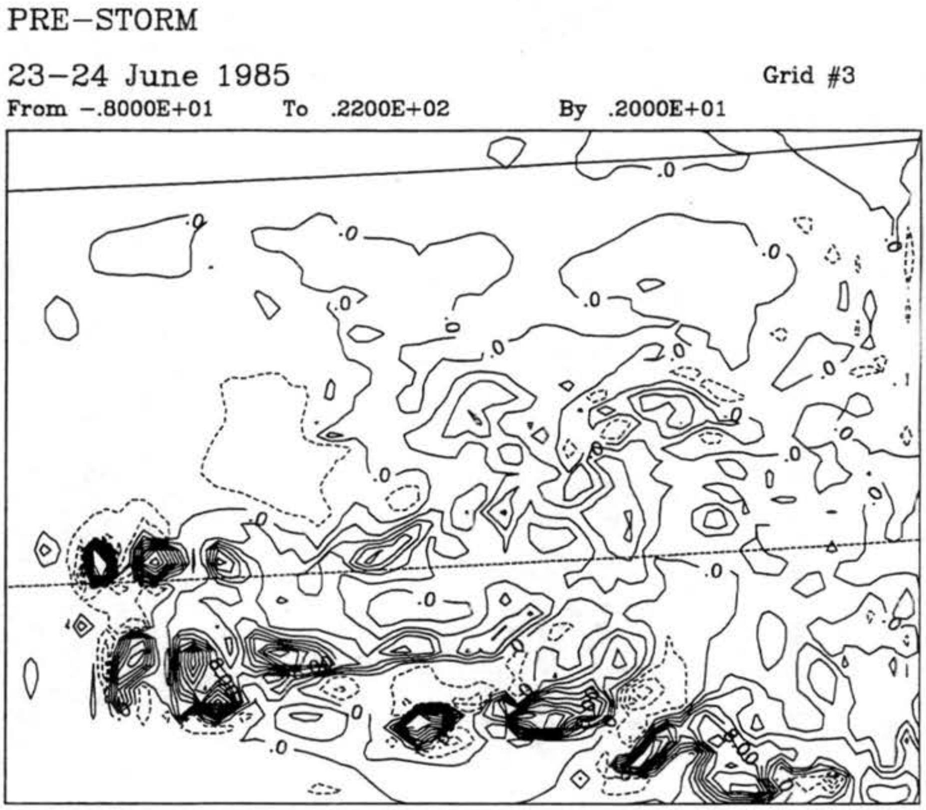

w (ms^{-1})

p = 500 mb t = 300 UTC

(d)

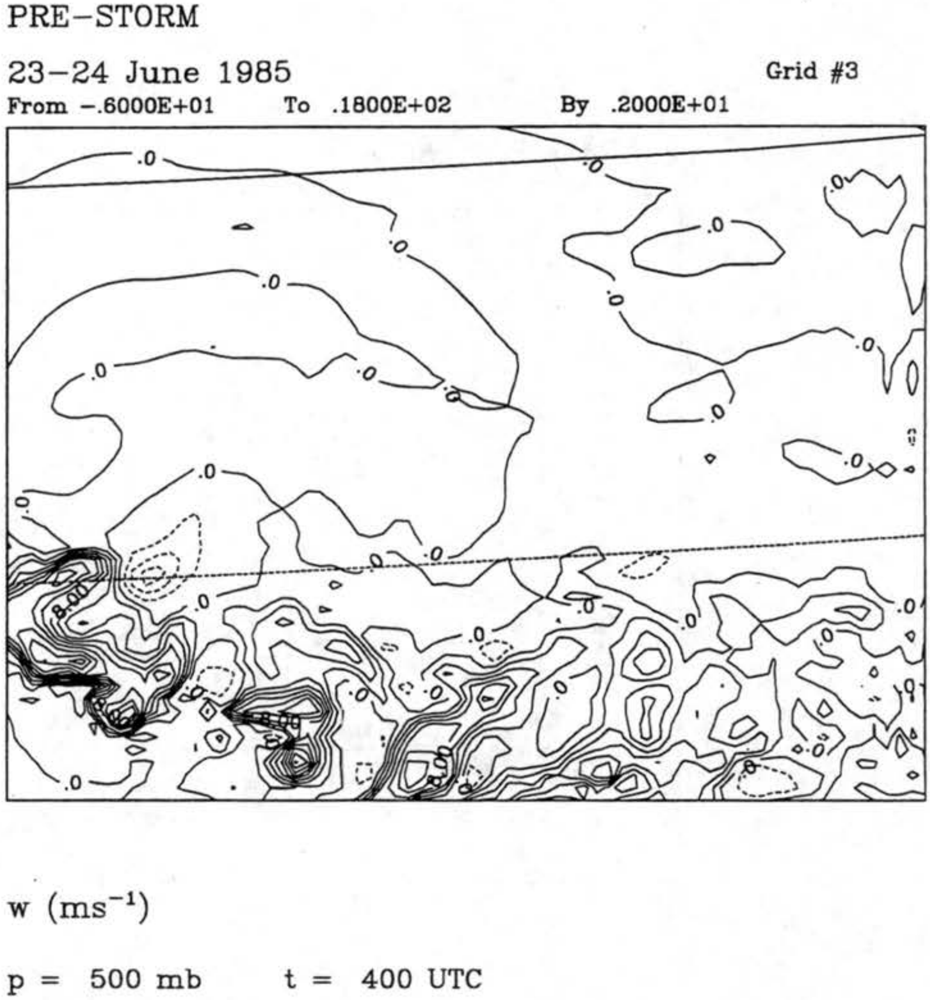

Fig. 3.29: Vertical velocity at 500 mb on Grid #3 at (a) 0100 UTC, (b) 0200 UTC, (c) 0300 UTC, and (d) 0400 UTC.

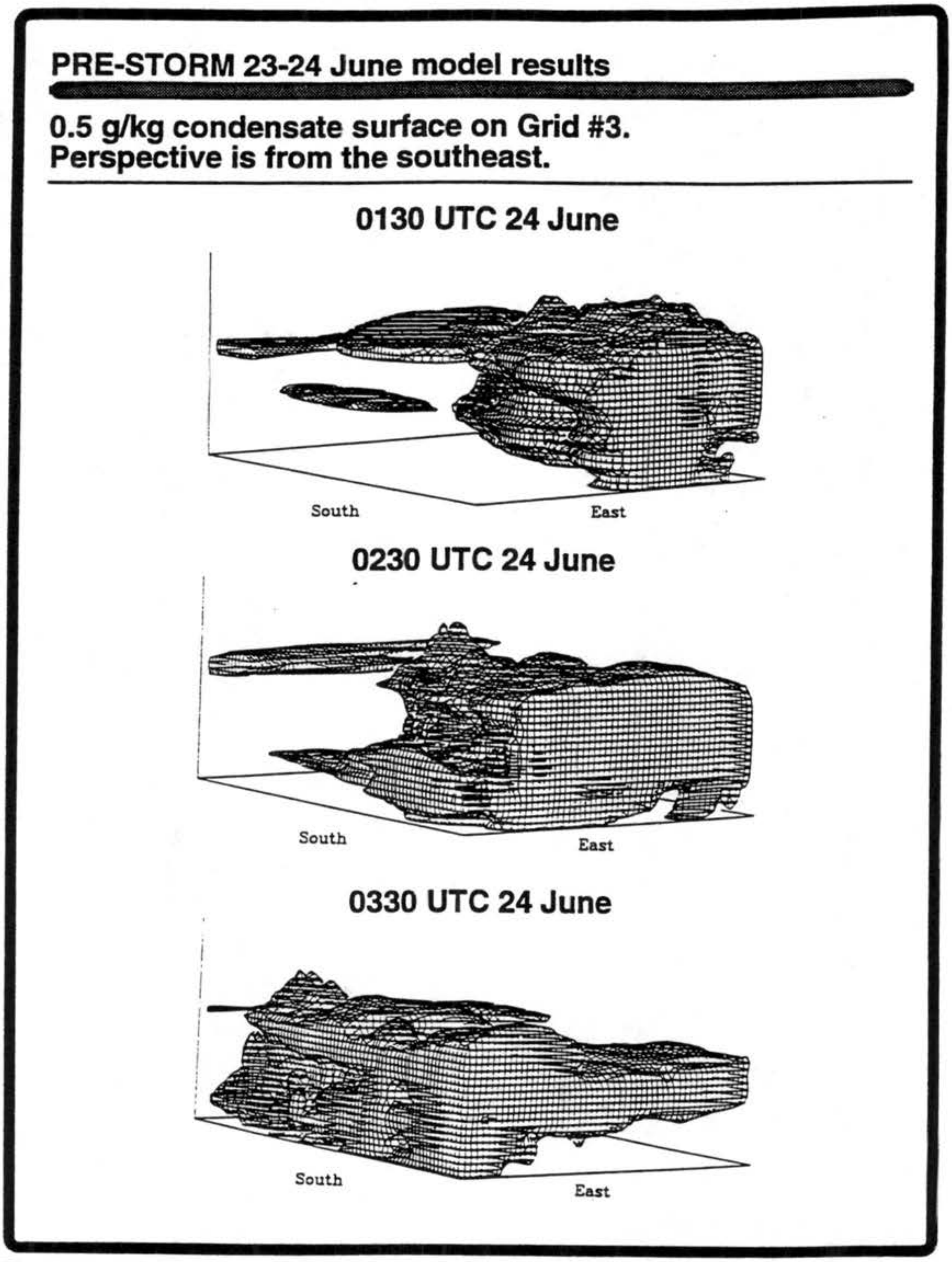

Fig. 3.30: The 0.5 gkg^{-1} condensate surface on Grid #3 at 0130 UTC, 0230 UTC, and 0330 UTC 24 June. The vertical line on the southwest corner of the grid extends from the surface to 20 km. Perspective is from the southeast.

meridional component of the perturbation pressure gradient force above 8 km in the vicinity of the convection. Below 8 km, the meridional component of the perturbation pressure gradient force is directed from south to north across the convective line (with flanking areas of north-to-south acceleration). A surface mesohigh is located between y=222 km and y=232 km with a wake low extending behind it.

Examination of precipitation rates on Grid #3 shows that we have captured the 23-24 June MCS as it grows to its mature stage. The total precipitation rate on Grid #3 steadily increases from $\sim 1.5 \times 10^7$ kgs^{-1} to $\sim 6.5 \times 10^7$ kgs^{-1} between 0100 and 0200 UTC before dropping off to $\sim 3\times 10^7$ kgs^{-1} at 0300 UTC (Fig. 3.32). The precipitation rate remains relatively constant from then until 0400 UTC. In Chapter 4, the partitioning of this precipitation between the convective and stratiform regions is discussed.

(a)

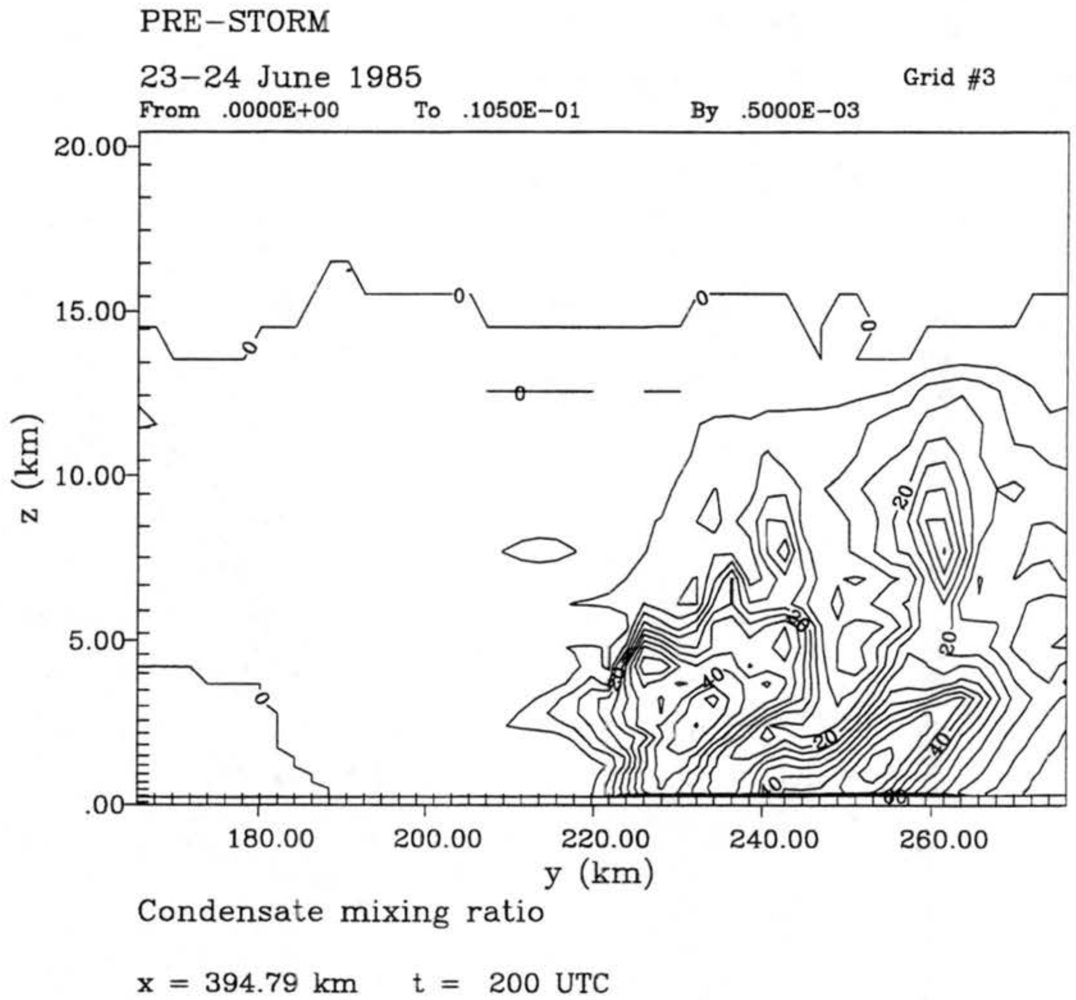
PRE-STORM
23-24 June 1985
Grid #3
From .0000E+00
To .1050E-01
By .5000E-03
20.00
15.00
10.00
5.00
.00
z (km)
180.00
200.00
220.00
240.00
260.00
y (km)
0
20
40
60
Condensate mixing ratio
x = 394.79 km t = 200 UTC

(b)

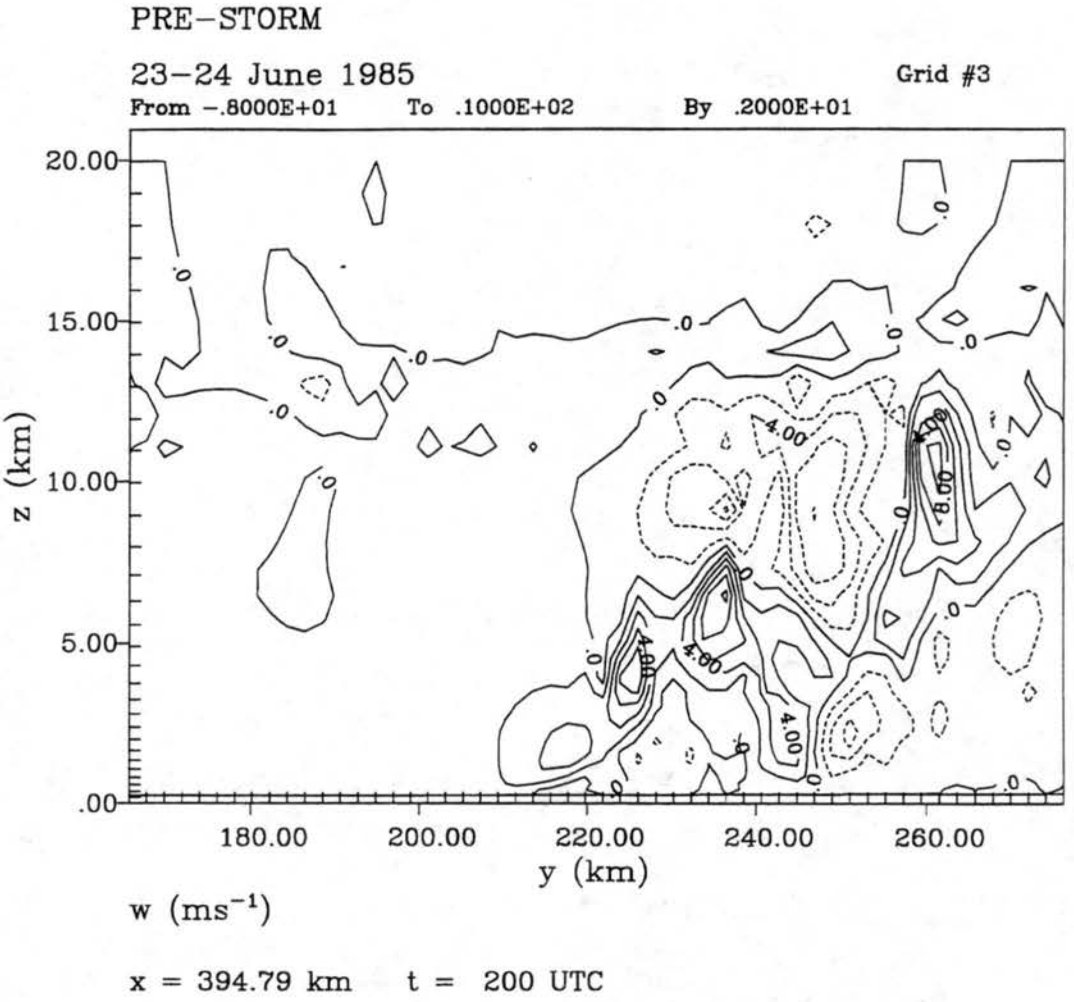

PRE−STORM

23−24 June 1985 Grid #3

From −.8000E+01 To .1000E+02 By .2000E+01

w (ms^{-1})

x = 394.79 km t = 200 UTC

(c)

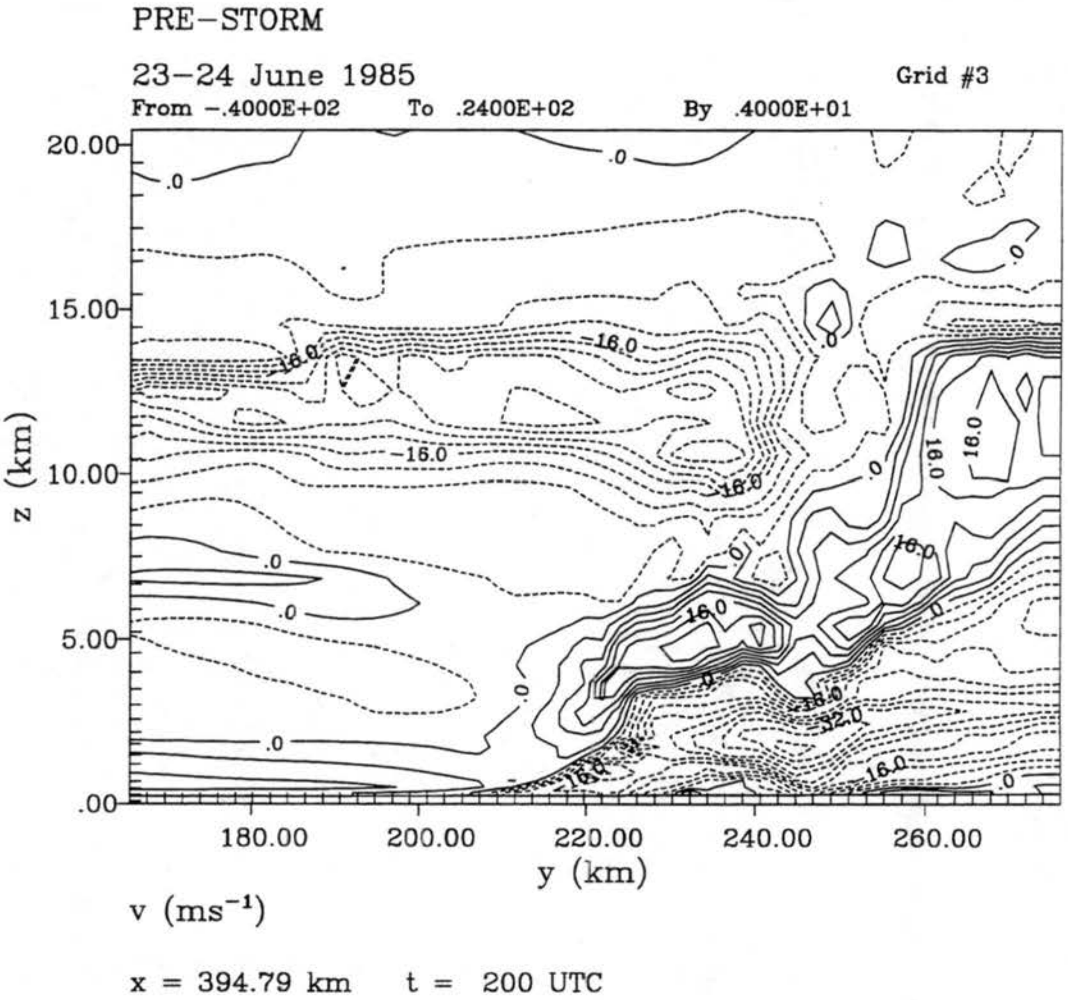
PRE-STORM
23-24 June 1985
Grid #3
From -.4000E+02 To .2400E+02 By .4000E+01
20.00
15.00
10.00
5.00
.00
z (km)
180.00
200.00
220.00
240.00
260.00
y (km)
.0
-16.0
16.0
-32.0
v (ms⁻¹)
x = 394.79 km t = 200 UTC

(d)

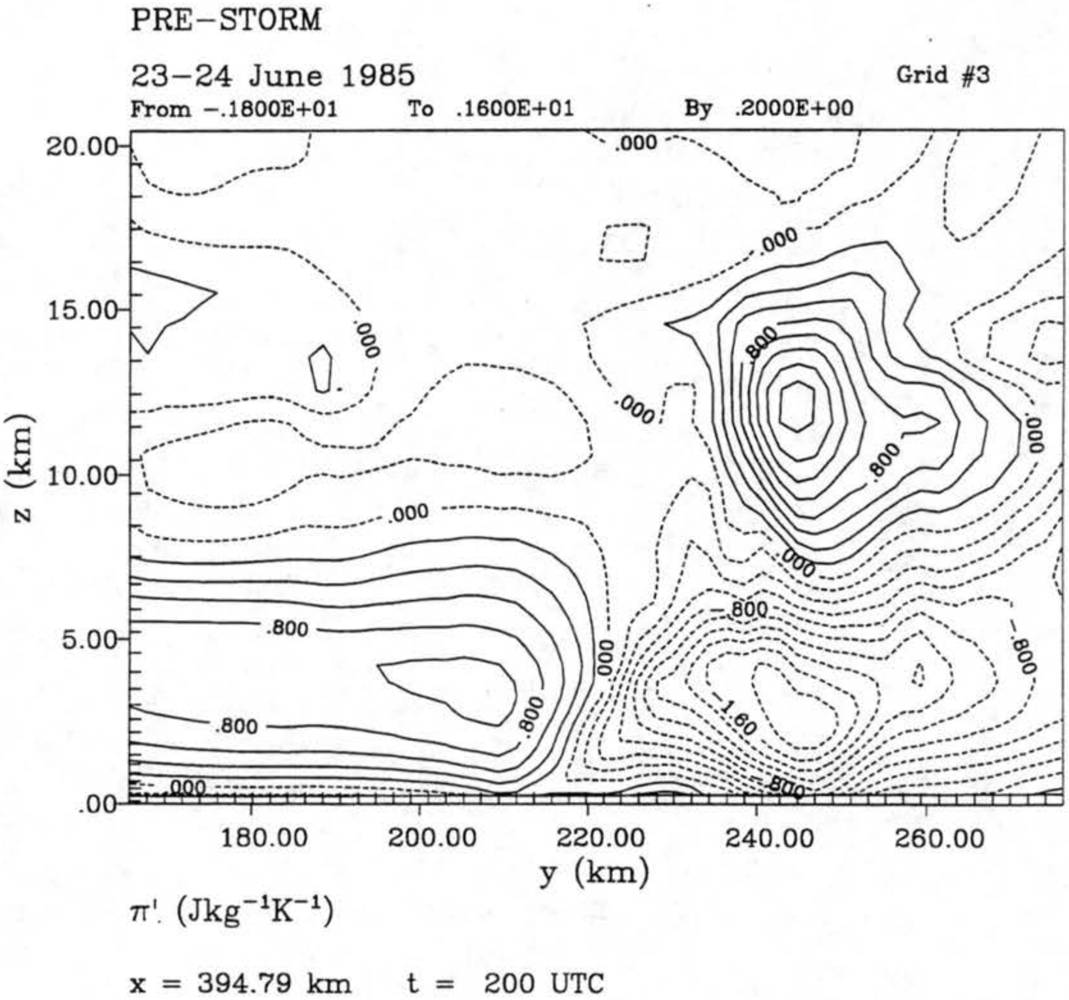

Fig. 3.31: Vertical cross-section along a north-south line bisecting Grid #3 at 0200 UTC 24 June 1985 for (a) condensate mixing ratio, (b) vertical velocity, (c) meridional velocity, (d) perturbation Exner function.

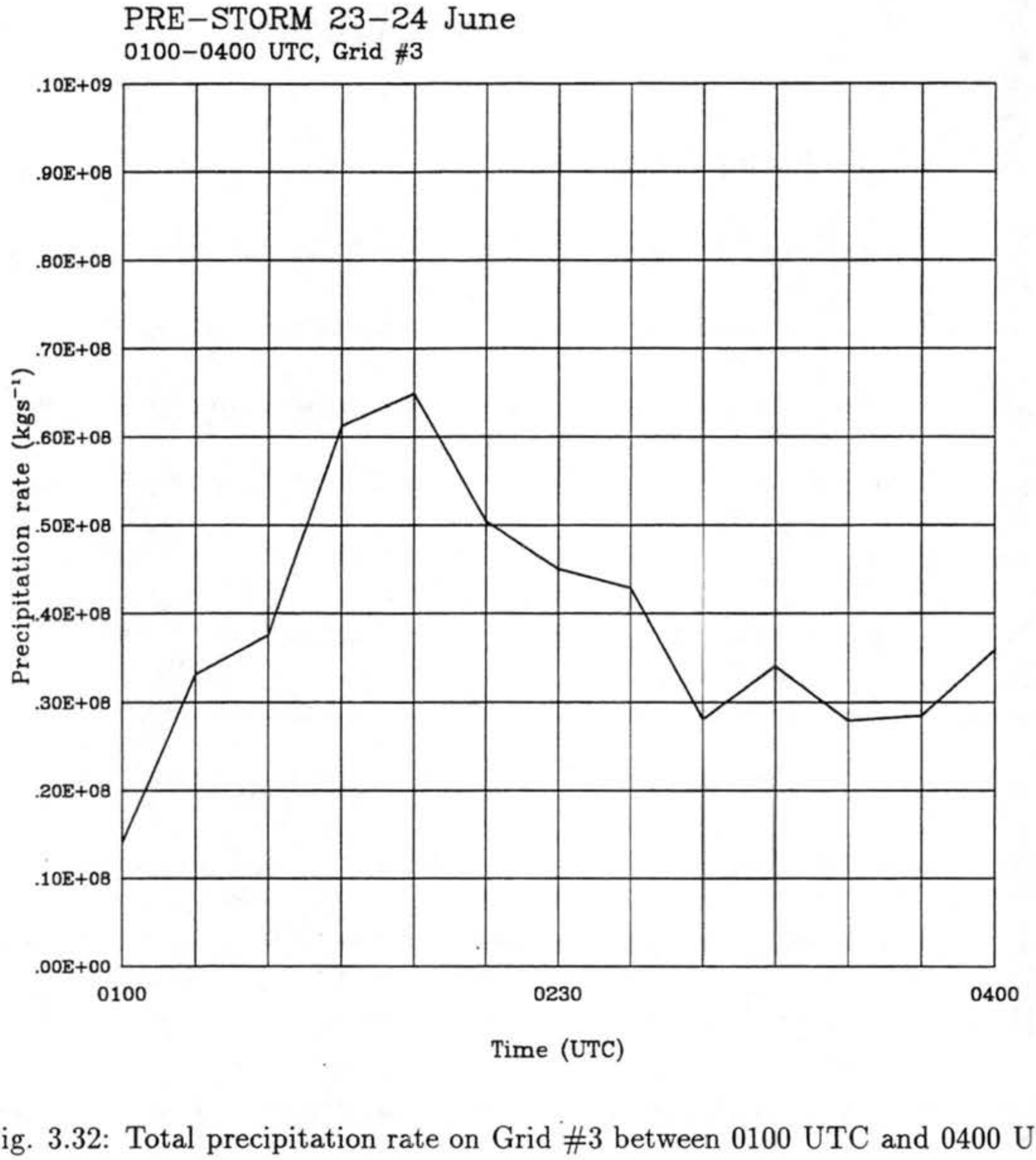

Fig. 3.32: Total precipitation rate on Grid #3 between 0100 UTC and 0400 UTC.

Chapter 4

SCHEME CONSTRUCTION

4.1 Conditional sampling strategy

Chapter 2 discussed the philosophy of how the explicit parameterizations discussed in Chapter 3 will be used to build an MCS parameterization scheme. Obtaining vertical profiles of the phase transformation processes and other needed quantities in mesoscale updrafts and mesoscale downdrafts regions requires conditionally sampling these regions in the stratiform regions of the cloud-resolving grids of the synthetic dataset. To be considered a part of a mesoscale updraft or mesoscale downdraft, a point must reside within the stratiform region. In the past, objective criteria for separating the convective and stratiform regions have been based on the horizontal distribution of maximum cloud draft strength below the melting level (e.g., Xu 1995) or on the horizontal distribution of surface precipitation rate (e.g., Churchill and Houze 1984, Tao et al. 1993).

In the Tao et al. (1993) separation technique, model grid columns exhibiting a surface precipitation rate twice as large as the average value taken over the surrounding grid columns are identified as convective cells. For each core grid column, all adjacent grid columns are also taken to be convective. In addition, any grid column with a rain rate in excess of 25 $\mathrm{mmh^{-1}}$ is considered as convective regardless of the above criteria, and any grid column with no surface precipitation is considered convective if the maximum updraft exceeds 5 ms^{-1}. All other precipitating grid columns are considered to be stratiform.

The Xu (1995) separation technique is primarily based on $|w_{max}|$, the maximum draft strength below the melting level. Here, a convective core must satisfy at least one of the following three criteria: (1) $|w_{max}|$ is twice as large as the average over four adjacent grid columns, (2) $|w_{max}|$ is greater than 3 ms^{-1}, or (3) the precipitation rate exceeds 25 mmh^{-1}. As in the Tao et al. (1993) method, for each core grid column, all adjacent grid columns are also taken to be convective. The stratiform region then consists of all remaining grid columns in which the total liquid water path exceeds 0.2 kgm^{-2}. This differs from the Tao et al. (1993) method, in that here, it is possible for nonprecipitating grid columns to be included in the stratiform region.

For the purposes of this study, the convective-stratiform separation technique used by Tao et al. (1993) is more preferable because here, it is not necessary to conditionally sample nonprecipitating grid columns which may nevertheless contain the "anvil" cloud. Another component of the parameterization scheme, described in Nebuda (1995), accounts for the feedback of these nonprecipitating anvils on the large-scales. Nonetheless, the two techniques yield very similar results for the MCSs simulated here. Fig. 4.1, for instance, shows a comparison of the Tao et al. (1993) and Xu (1995) convective-stratiform partitioning techniques for the fine grid of the EMEX9 simulation at 1800 UTC. Although the Xu (1995) criteria do identify a slightly greater number of convective grid points, the spatial distributions of the convective and stratiform regions are about the same. The Xu (1995) criteria identify a number of outlying points as being convective in regions which would not ordinarily be subjectively identified as such.

Fig. 4.2 shows the time evolution of the number of grid points in the convective and stratiform regions of the EMEX9 and PRE-STORM MCS simulations. In both simulations, the number of grid points in the stratiform region far exceeds the number of grid points in the convective region. For EMEX9 (Fig. 4.2a), the stratiform region grows rapidly between 1400 and 1600 UTC and then remains about the same size from then until 1800 UTC. The EMEX9 convective region grows steadily in size throughout the simulation. For PRE-STORM (Fig. 4.2b), the stratiform region grows until 0215 UTC before gradually shrinking. The PRE-STORM convective region behaves similarly except that it achieves its maximum area 15 minutes earlier.

Fig. 4.3 shows the time evolution of the precipitation rate in the convective and stratiform regions of the EMEX9 and PRE-STORM MCS simulations. For EMEX9 (Fig. 4.3a), the precipitation falling from the stratiform region gradually increases, and overtakes the convective precipitation at 1715 UTC. The convective precipitation remains steady between 1600 and 1800 UTC. For PRE-STORM (Fig. 4.3b), the stratiform precipitation exceeds the convective precipitation only at 0300 UTC.

After two-dimensionally separating the MCS into convective and stratiform regions, the mesoscale updrafts and mesoscale downdrafts are isolated within the stratiform region. The aims here are one, to ensure that the mesoscale updrafts or downdrafts are spatially coherent, and two, to allow the mesoscale updrafts and downdrafts

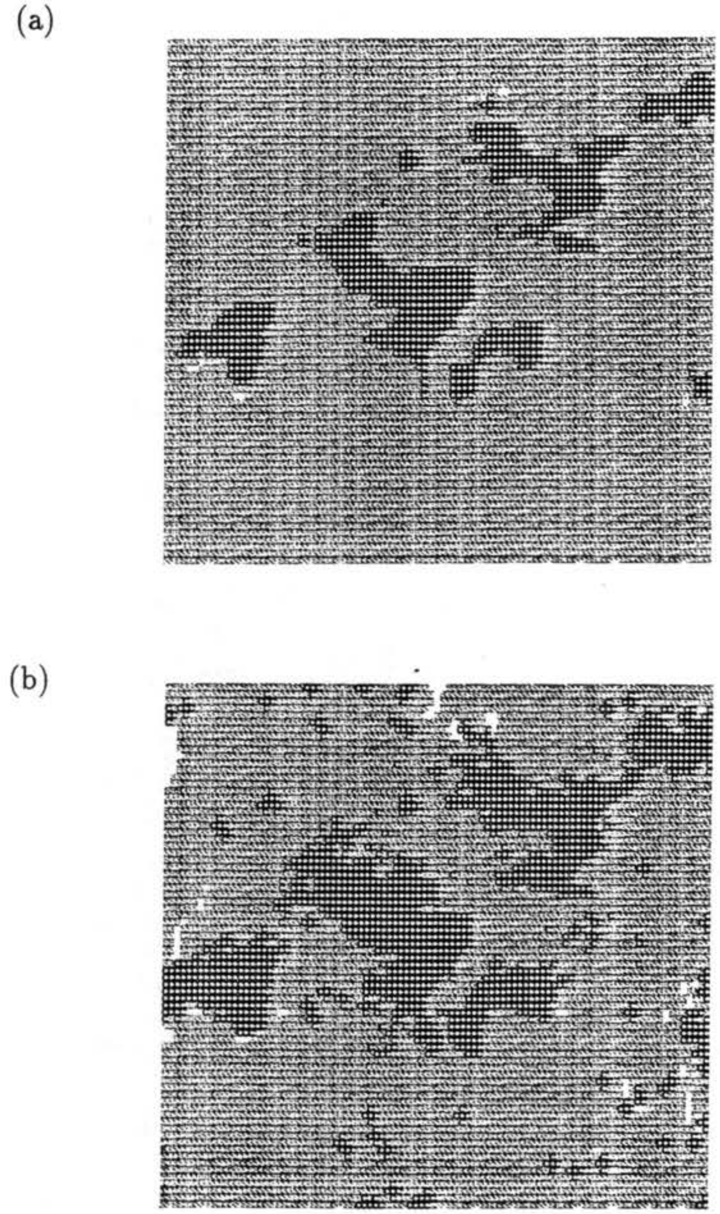

Fig. 4.1: Spatial distribution of the convective and stratiform regions on Grid #3 of the EMEX9 simulation at 1800 UTC using the (a) Tao et al. (1993) and (b) Xu (1995) partitioning criteria. Convective grid points are denoted by a black "C". Stratiform grid points are denoted by a grey "S". The 500 mb vertical velocity field on Grid #3 at 1800 UTC is shown in Fig. 3.11d.

(a)

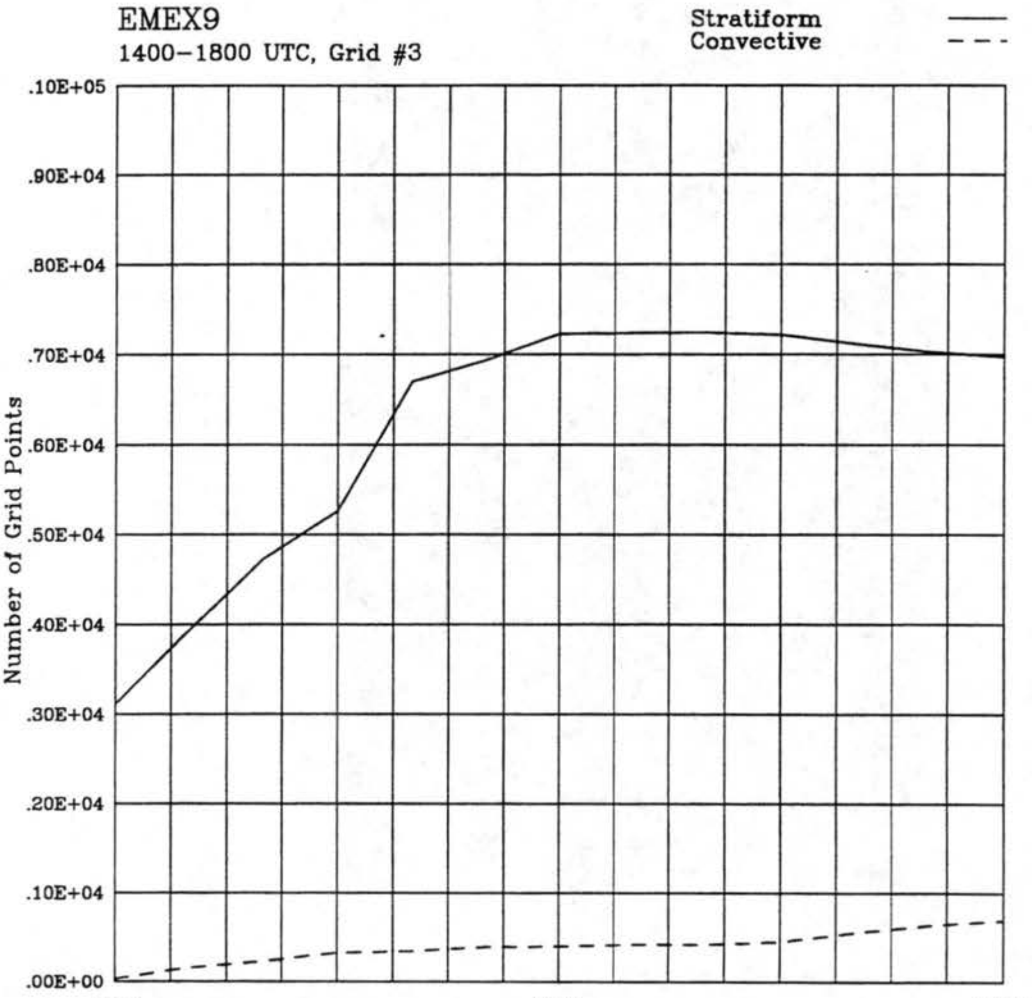
EMEX9
1400–1800 UTC, Grid #3
Stratiform
Convective
.10E+05
.90E+04
.80E+04
.70E+04
.60E+04
.50E+04
.40E+04
.30E+04
.20E+04
.10E+04
.00E+00
Number of Grid Points
1400
1600
1800
Time (UTC)

(b)

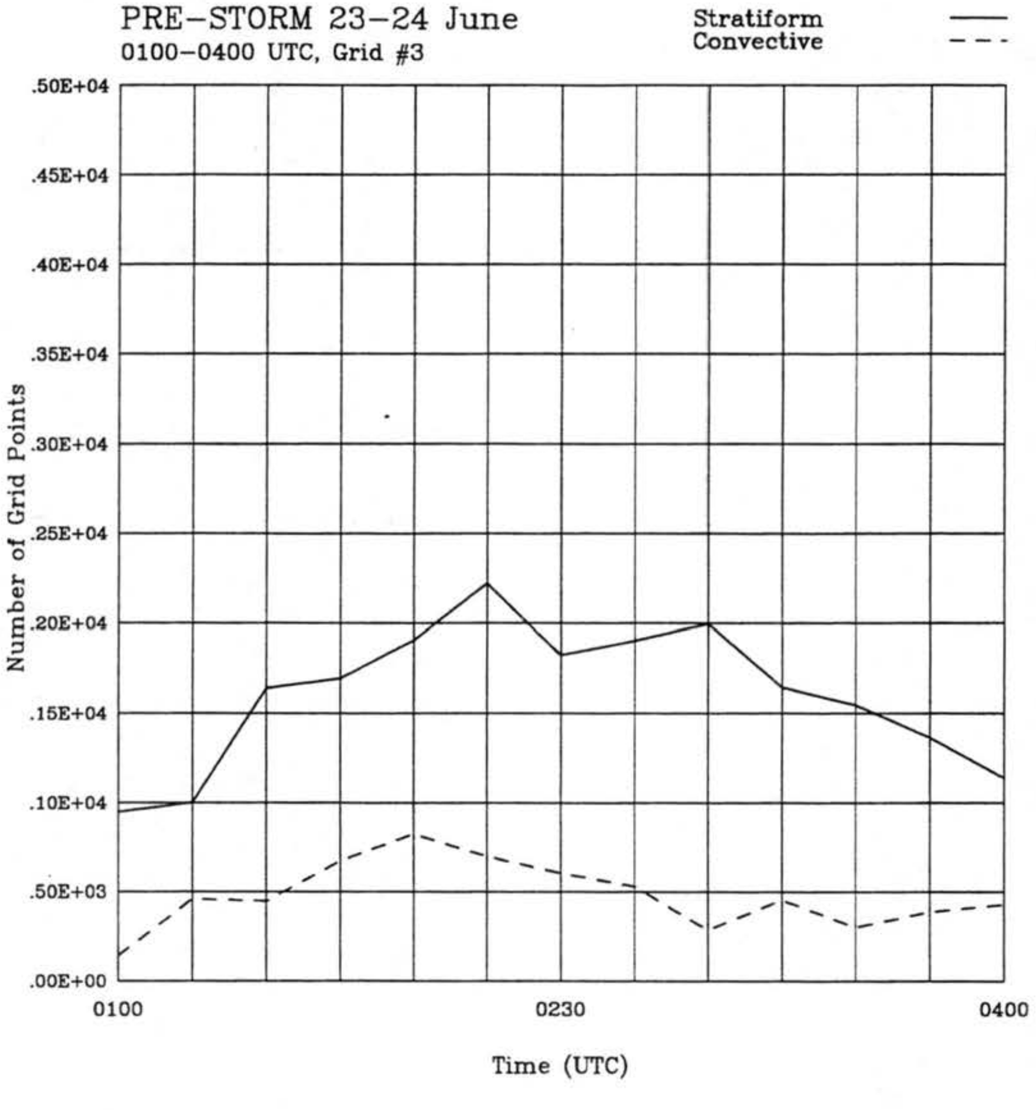

Fig. 4.2: Time evolution of the number of grid points in the convective and stratiform regions of the (a) EMEX9 and (b) PRE-STORM 23-24 June MCS simulations.

(a)

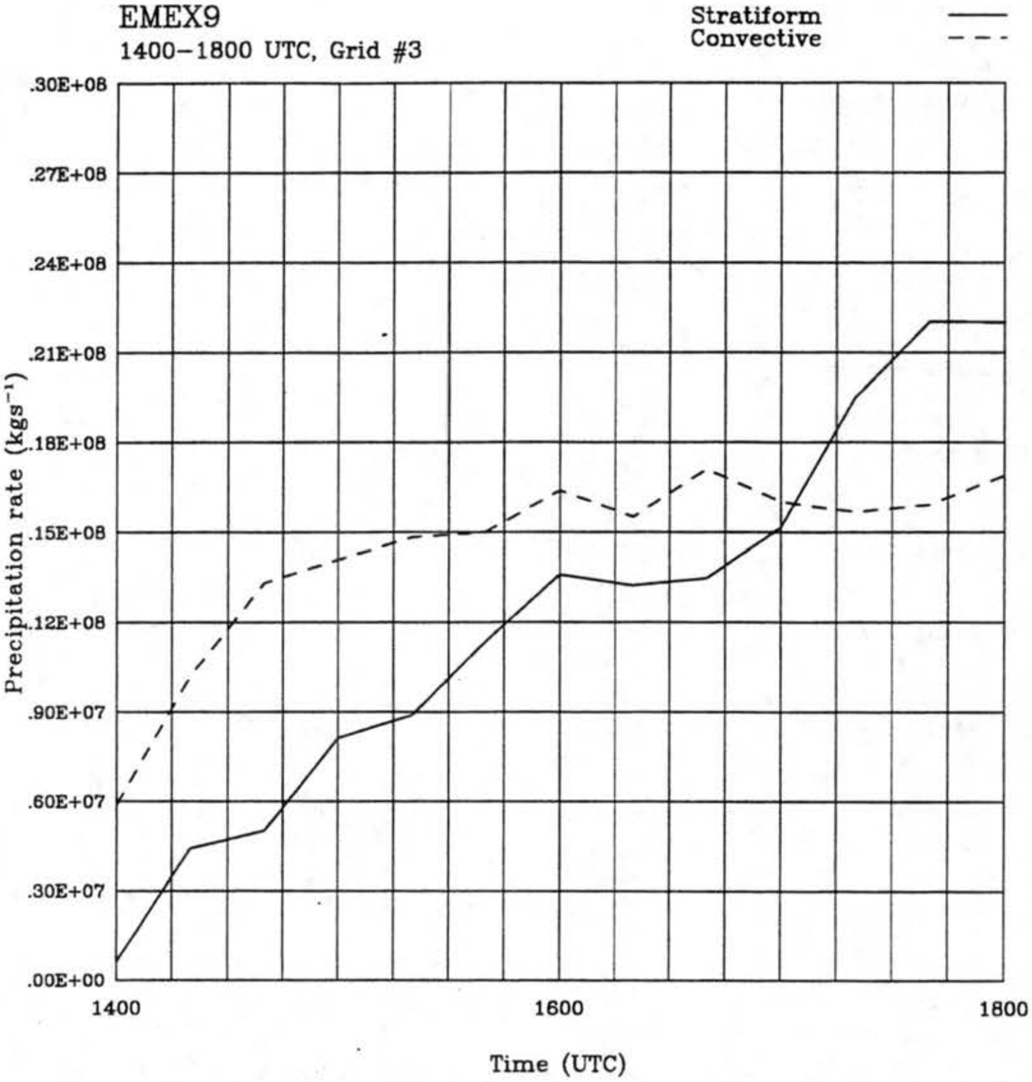
EMEX9
1400–1800 UTC, Grid #3
Stratiform
Convective
Precipitation rate (kgs^{-1})
.30E+08
.27E+08
.24E+08
.21E+08
.18E+08
.15E+08
.12E+08
.90E+07
.60E+07
.30E+07
.00E+00
1400
1600
1800
Time (UTC)

(b)

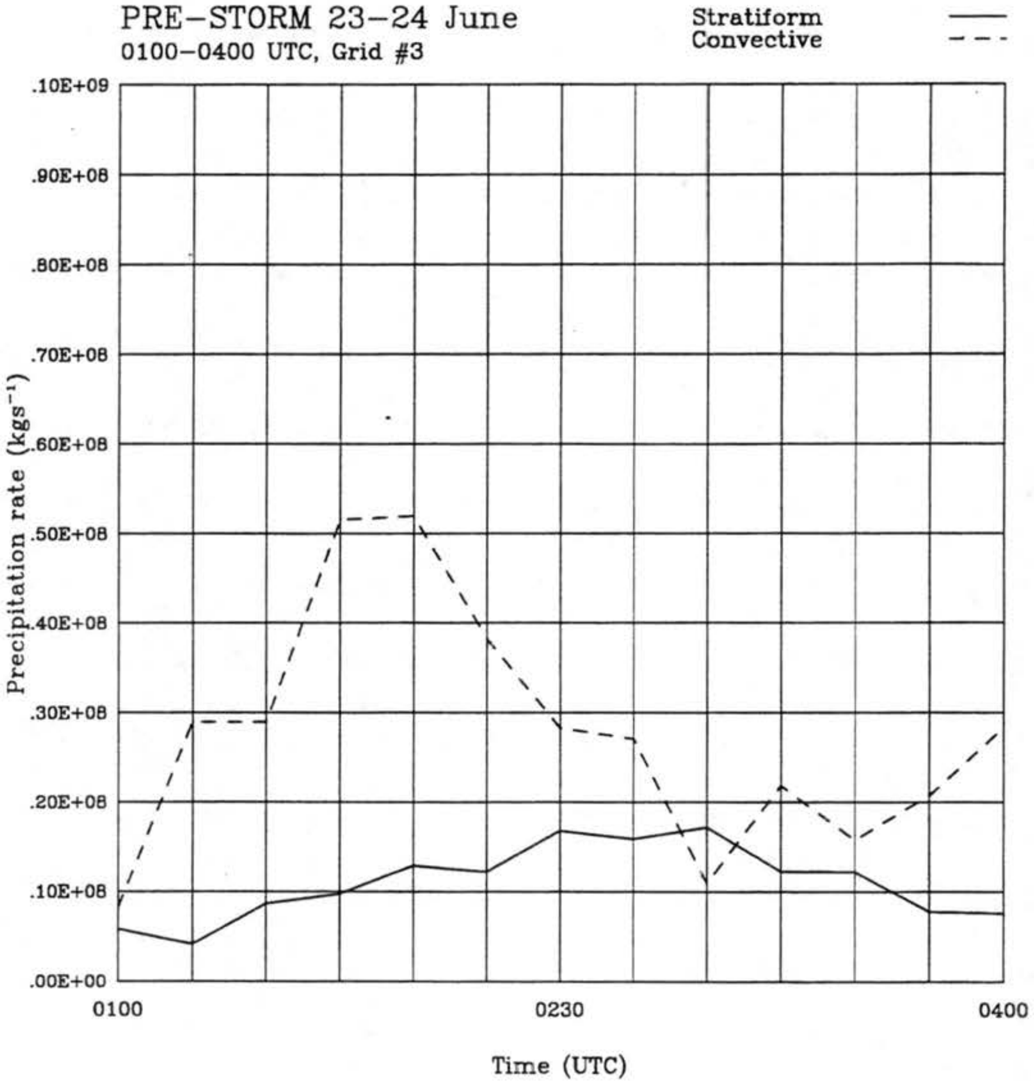

Fig. 4.3: Time evolution of precipitation rate in the convective and stratiform regions of the (a) EMEX9 and (b) PRE-STORM 23-24 June MCS simulations.

to have some vertical structure. In light of these requirements, the conditional sampling is done on a gridpoint-by-gridpoint basis (not a column-by-column basis as above). A stratiform region grid point is considered to be within a mesoscale updraft if (1) there is condensate present, (2) the vertical velocity is upward, (3) conditions (1) and (2) are satisfied at *all* adjacent grid points, and (4) the grid point is located above the 0°C level. A stratiform region grid point is considered to be within a mesoscale downdraft if (1) the vertical velocity is downward, (2) condition (1) is satisfied at *all* adjacent grid points, (3) the grid point is located below the 0°C level. Although the simulations show that some mesoscale updrafts occur below the freezing level and that some mesoscale downdrafts occur above the freezing level, conditional sampling of these drafts reveals that their net heating and drying rates are small; they are neglected here. Vertical profiles of physical processes in these conditionally-sampled mesoscale updrafts and downdrafts will be used to determine the shapes of vertical profiles of various physical processes as well as relationships between various components of an MCS's water budget. To build the MCS parameterization, EMEX9 simulation data are examined for 1700-1800 UTC and the PRE-STORM simulation data for 0300-0400 UTC.

4.2 Shape and depth of parameterized curves

The conditionally-sampled data are used, in part, to provide insight into the shape and depth of the vertical profiles of various parameterized physical processes. To a first approximation, all of the curves are symmetric with a sinusoidal form. Occasionally, however, the departure from symmetry may be significant. For instance, the vertical profiles of freezing rates in the conditionally-sampled mesoscale updrafts of each MCS indicate that the peak freezing rate is located much closer to the bottom of the mesoscale updraft than to the top of the mesoscale updraft (see Fig. 4.6). To describe the precise shape of a curve, each curve is given a shape parameter. The shape parameter may range between 0 and 1, with a value of 0 indicating a vertical profile which has a maximum value at its bottom side, a value of 1 indicating a vertical profile which has a maximum value at its top side, and a value of 0.5 indicating a vertical profile which is perfectly symmetric. A depth parameter completes the description of the vertical profile. The depth parameter also may range between 0 and 1, with a value of 0 indicating that the profile has no depth and a value of 1 indicating that the profile extends fully through the extent of the mesoscale updraft or downdraft. All profiles for parameterized mesoscale downdrafts have a top at the top of the mesoscale downdraft; all profiles for parameterized mesoscale updrafts have a base at the base of the mesoscale updraft.

Consider then, a vertical profile of a process q with shape parameter S and depth parameter D, which is placed within a mesoscale updraft which extends from pressure level p_{zm} (bottom of the mesoscale updraft) to pressure level p_{ztm} (top of the mesoscale updraft). The vertical profile of q extends from p_{bq} (bottom of curve q) to p_{pq} (top of curve q), where p_{bq} and p_{tq} are

$$p_{bq} = p_{zm} \tag{4.1}$$

and

$$p_{tq} = p_{zm} - D(p_{zm} - p_{ztm}), \tag{4.2}$$

respectively. Then, if the quantity x varies from 0 at p=p_{tq} to 1 at p=p_{bq} as

$$x = \frac{p - p_{tq}}{p_{bq} - p_{tq}}, \tag{4.3}$$

the normalized value of q at pressure p is

$$q(p) = sin(\frac{\pi}{2}\frac{x}{S}) \tag{4.4}$$

for $x \leq S$ and

$$q(p) = sin[\frac{\pi}{2(1-S)}(x + 1 - 2S)] \tag{4.5}$$

for $x > S$.

The vertical profile of each phase transformation process is assigned a shape and depth parameter. The conditionally-sampled data provide guidance as to appropriate values. In practice, of course, one would not know exactly which values to use for these parameters—the numbers given in the following sections simply represent a reasonable range. The sensitivity of the parameterization to the prescribed values of these shape and depth parameters is examined in Chapter 5.

4.3 Phase transformation rates

The bulk microphysics scheme used in the two MCS simulations is discussed in detail by Flatau et al. (1989). Here, we are particularly interested in conversions between the microphysical categories (cloud water, rain, pristine crystals, snow, graupel, and aggregates). Parameterized conversion processes include collection, vapor deposition/evaporation, melting, and ice nucleation (sorption/deposition, phoretic contact, and splintering).

4.3.1 Deposition and condensation in mesoscale updrafts

Section 2.2.3 discusses how the magnitude of the vertically-integrated vapor deposition plus condensation in the mesoscale updraft is parameterized. To complete the parameterization it is necessary to know (1) the ratio of the vertically-integrated condensation to the vertically-integrated deposition, and (2) the shapes of the vertical profiles of deposition and condensation individually.

Fig. 4.4 shows the ratio of vertically-integrated condensation to vertically-integrated deposition $(\frac{\int C_{mu}dp}{\int D_{mu}dp})$in the conditionally-sampled mesoscale updrafts for each MCS simulation. The values of $\frac{\int C_{mu}dp}{\int D_{mu}dp}$ range from about 0.1 to 0.3 for EMEX9 and 0.8 to 2.6 for PRE-STORM. Thus, the parameter varies significantly between simulations. Still, within the extreme values given here, the results of the parameterization are not particularly sensitive to the value of this parameter.

Fig. 4.5 shows a time-height plot of the deposition rate in the conditionally-sampled mesoscale updrafts for the EMEX9 (1700-1800 UTC) and PRE-STORM (0300-0400 UTC) simulations. Based on the character of the vertical profiles in Fig.

(a)

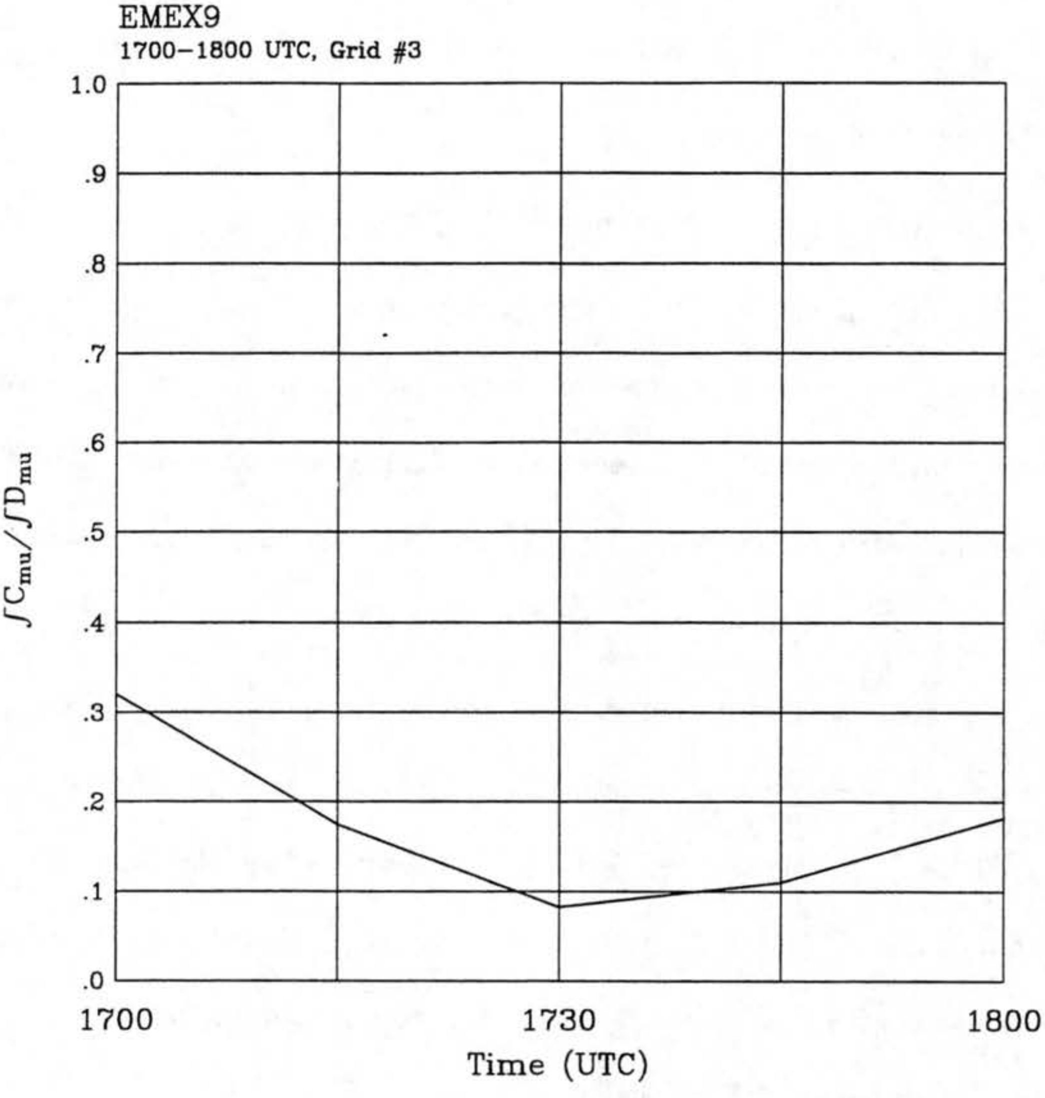
EMEX9
1700–1800 UTC, Grid #3
1.0
.9
.8
.7
.6
.5
.4
.3
.2
.1
.0
$\int C_{mu} / \int D_{mu}$
1700
1730
1800
Time (UTC)

(b)

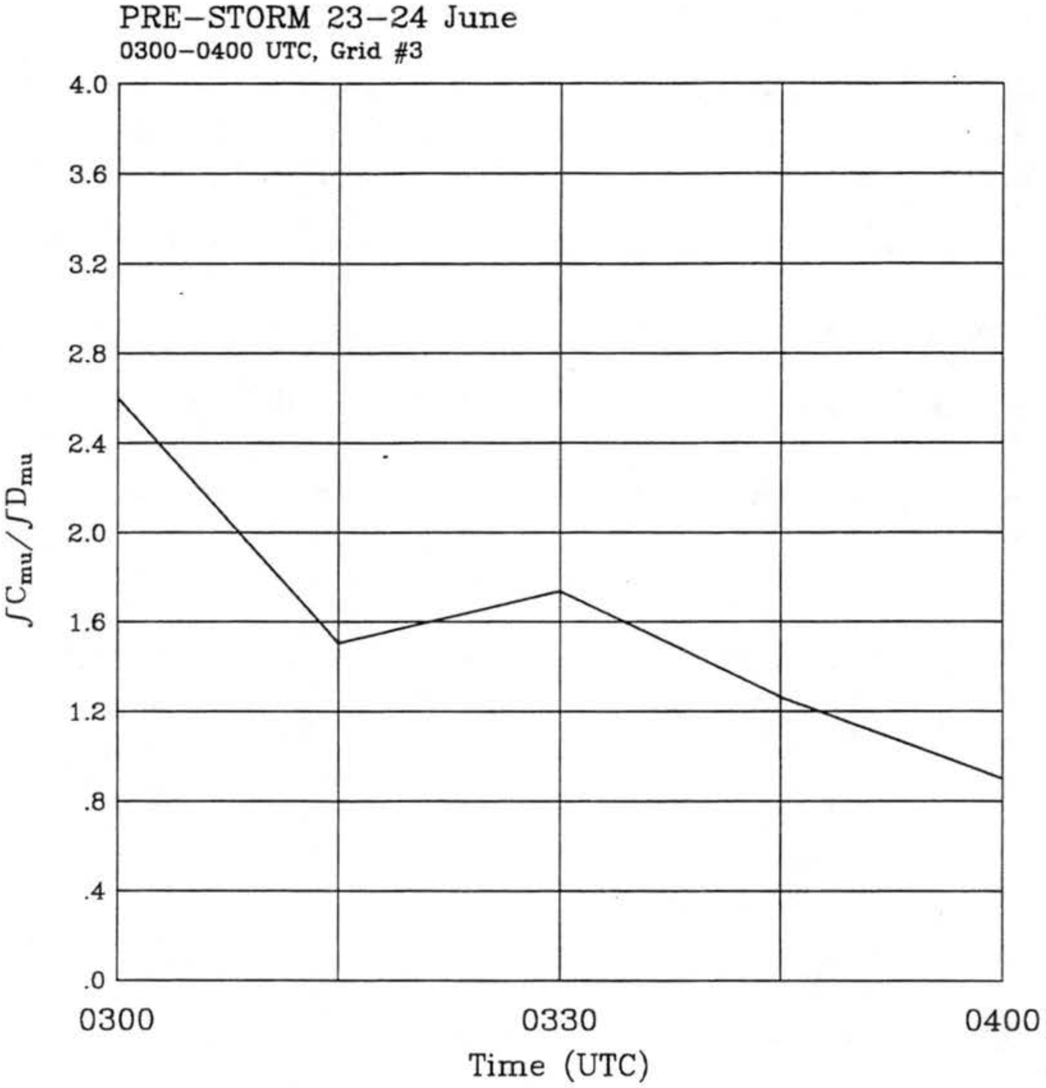

Fig. 4.4: Time evolution of the ratio of the vertically integrated condensation rate to the vertically-integrated deposition rate in the conditionally-sampled mesoscale updrafts for (a) EMEX9 and (b) PRE-STORM.

4.4, the parameterized vertical profile of deposition rate in the mesoscale updraft is assumed to have a shape parameter of 0.85 for EMEX and 0.50 for PRE-STORM and a depth parameter of 0.80 for both EMEX and PRE-STORM.

Fig. 4.6 shows a time-height plot of the condensation rate in the conditionally-sampled mesoscale updrafts for the EMEX9 (1700-1800 UTC) and PRE-STORM (0300-0400 UTC) simulations. Based on the character of the vertical profiles in Fig. 4.4, the parameterized vertical profile of condensation rate in the mesoscale updraft is assumed to have a depth parameter of 0.40 for EMEX and 0.70 for PRE-STORM and a shape parameter of 0.85 for both EMEX and PRE-STORM.

Deposition and condensation in mesoscale downdrafts are not included in the parameterization, as conditional sampling shows each quantity to be very small. For PRE-STORM, in fact, the deposition and condensation in mesoscale downdrafts is essentially zero. For EMEX9, the values are a little larger, but still negligible. For instance, for the 1700-1800 UTC mean profile, the peak value of heating due to condensation in mesoscale downdrafts is 0.04 Kd^{-1} compared to a peak value of 0.60 Kd^{-1} for heating due to condensation in mesoscale updrafts, while the peak value of heating due to deposition in mesoscale downdrafts is 0.05 Kd^{-1} compared to a peak value of 0.50 Kd^{-1} in mesoscale updrafts.

4.3.2 Freezing in mesoscale updrafts

The magnitude of freezing in the parameterized mesoscale updraft is determined as discussed in Section 2.2.4. The shape of the freezing profile is determined through conditional sampling of the explicit MCS simulations. Fig. 4.7 shows a time-height

(a)

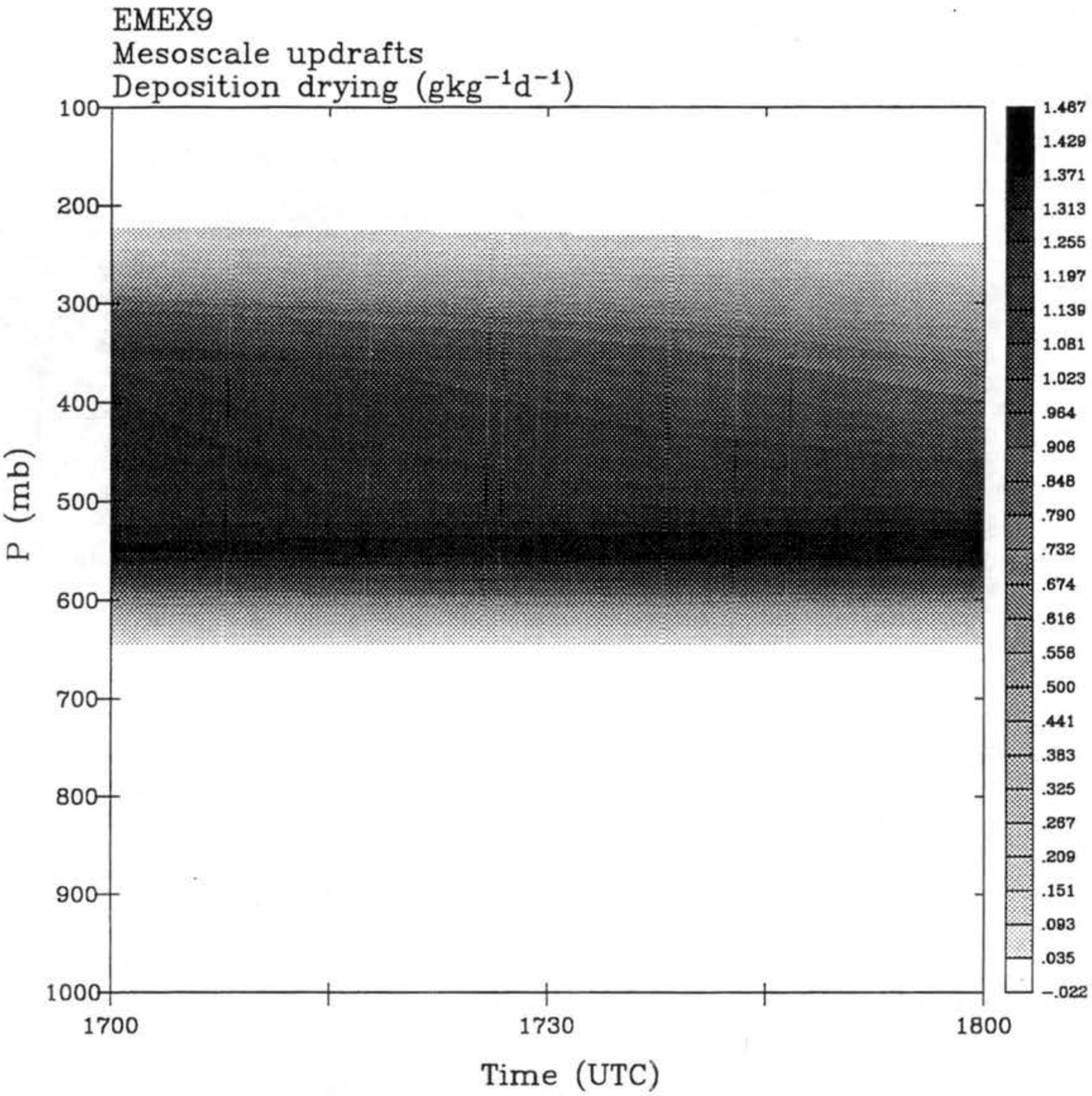
EMEX9
Mesoscale updrafts
Deposition drying $(gkg^{-1}d^{-1})$
P (mb)
100
200
300
400
500
600
700
800
900
1000
1700
1730
1800
Time (UTC)
1.487
1.429
1.371
1.313
1.255
1.197
1.139
1.081
1.023
.964
.906
.848
.790
.732
.674
.616
.558
.500
.441
.383
.325
.267
.209
.151
.093
.035
-.022

(b)

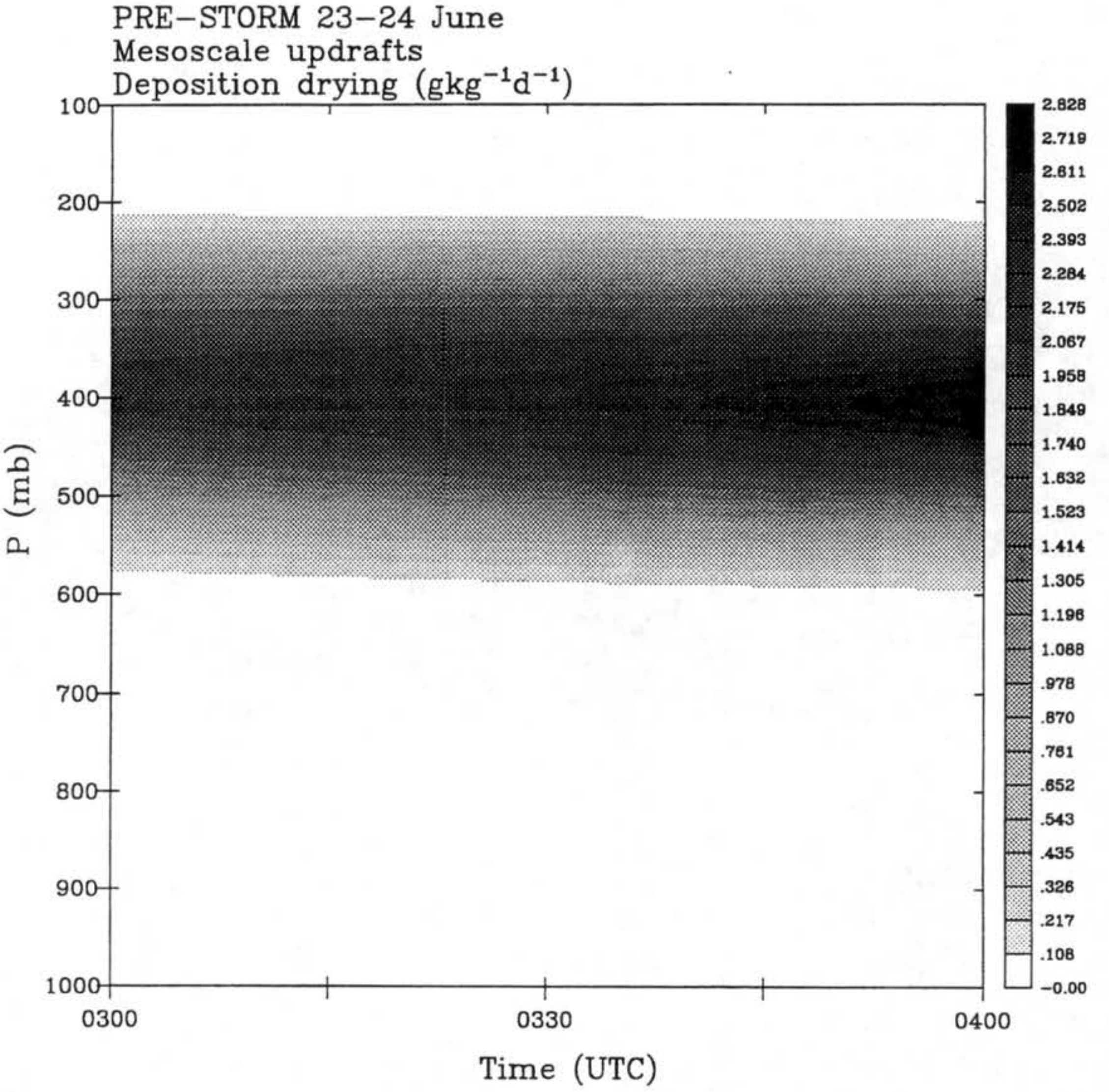

Fig. 4.5: Time evolution of the deposition rate in the conditionally-sampled mesoscale updrafts for (a) EMEX9 and (b) PRE-STORM.

(a)

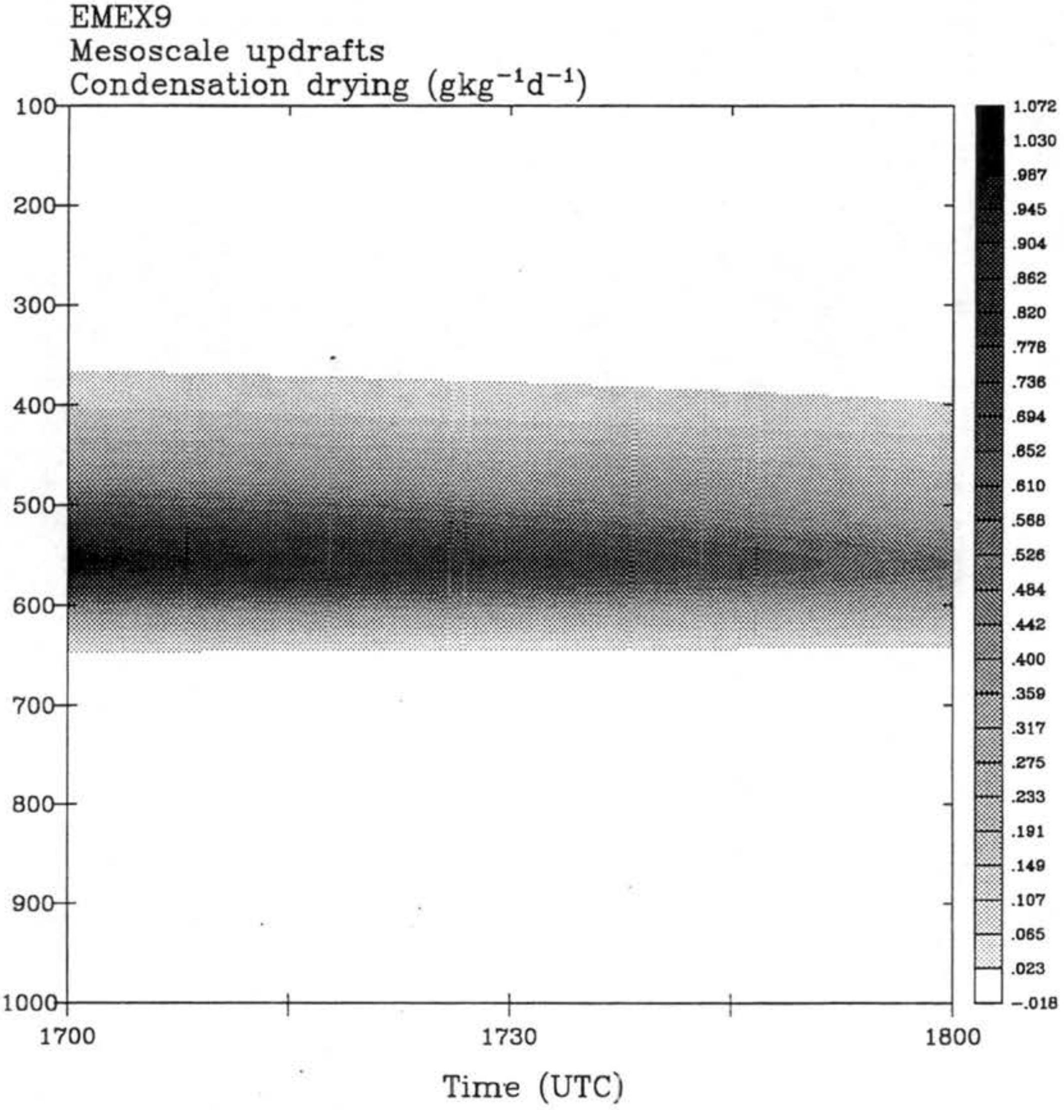
EMEX9
Mesoscale updrafts
Condensation drying ($gkg^{-1}d^{-1}$)
P (mb)
100
200
300
400
500
600
700
800
900
1000
1700
1730
1800
Time (UTC)
1.072
1.030
.987
.945
.904
.862
.820
.778
.736
.694
.652
.610
.568
.526
.484
.442
.400
.359
.317
.275
.233
.191
.149
.107
.065
.023
-.018

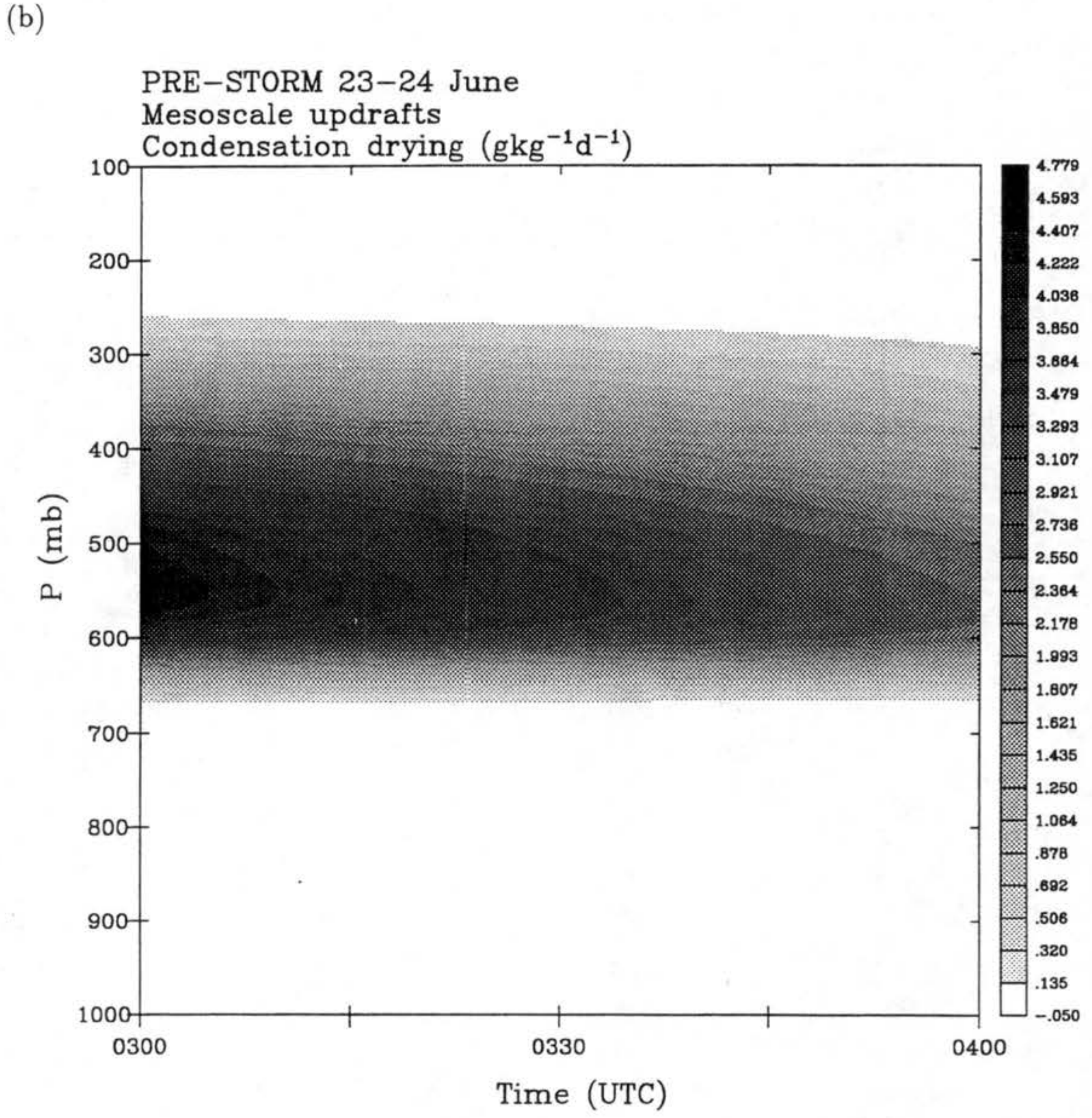

Fig. 4.6: Time evolution of the condensation rate in the conditionally-sampled mesoscale updrafts for (a) EMEX9 and (b) PRE-STORM.

plot of the freezing rate for the EMEX9 and PRE-STORM simulations. Based on these vertical profiles, the shape parameter has a value of 0.75 for EMEX and 0.65 for PRE-STORM; the depth parameter is 0.6 for EMEX and 0.5 for PRE-STORM. Freezing, of course, only serves to modify the shape of the parameterized vertical profile of $\frac{d\overline{\theta}}{dt}$ and will have no effect on the parameterized vertical profile of $\frac{d\overline{q}}{dt}$. Freezing in mesoscale downdrafts is not parameterized. In the explicit simulations, conversions from liquid to ice beneath the freezing level were, in fact, allowed when unmelted ice particles collected liquid particles (see Flatau et al. 1989). In each simulation, however, the magnitude of freezing through this process is negligible compared to freezing in conditionally-sampled mesoscale updrafts.

4.3.3 Sublimation in mesoscale updrafts

Sublimation in mesoscale downdrafts is a *very* small quantity compared to, say, deposition in mesoscale updrafts (e.g., compare Figs. 4.9 and 4.5) and can therefore probably be excluded from a parameterization. However, it was considered in Leary and Houze (1980) and Donner (1993), and therefore will be included here for completeness. As Leary and Houze (1980) point out, physically, this process can occur along the edge of a stratiform cloud as ice is evaporated into the larger scale enviroment (see their Fig. 2, for instance). The magnitude of sublimation is determined as discussed in Section 2.2.5. As discussed in Chapter 2, the budget of condensed water in the mesoscale region of an MCS may be described by

$$R_m + \frac{1}{g}\int_0^{p_g} E_{me} dp + \frac{1}{g}\int_0^{p_g} E_{md} dp = \frac{1}{g}\int_0^{p_g} C_{mu} dp + C_A, \qquad (4.6)$$

(a)

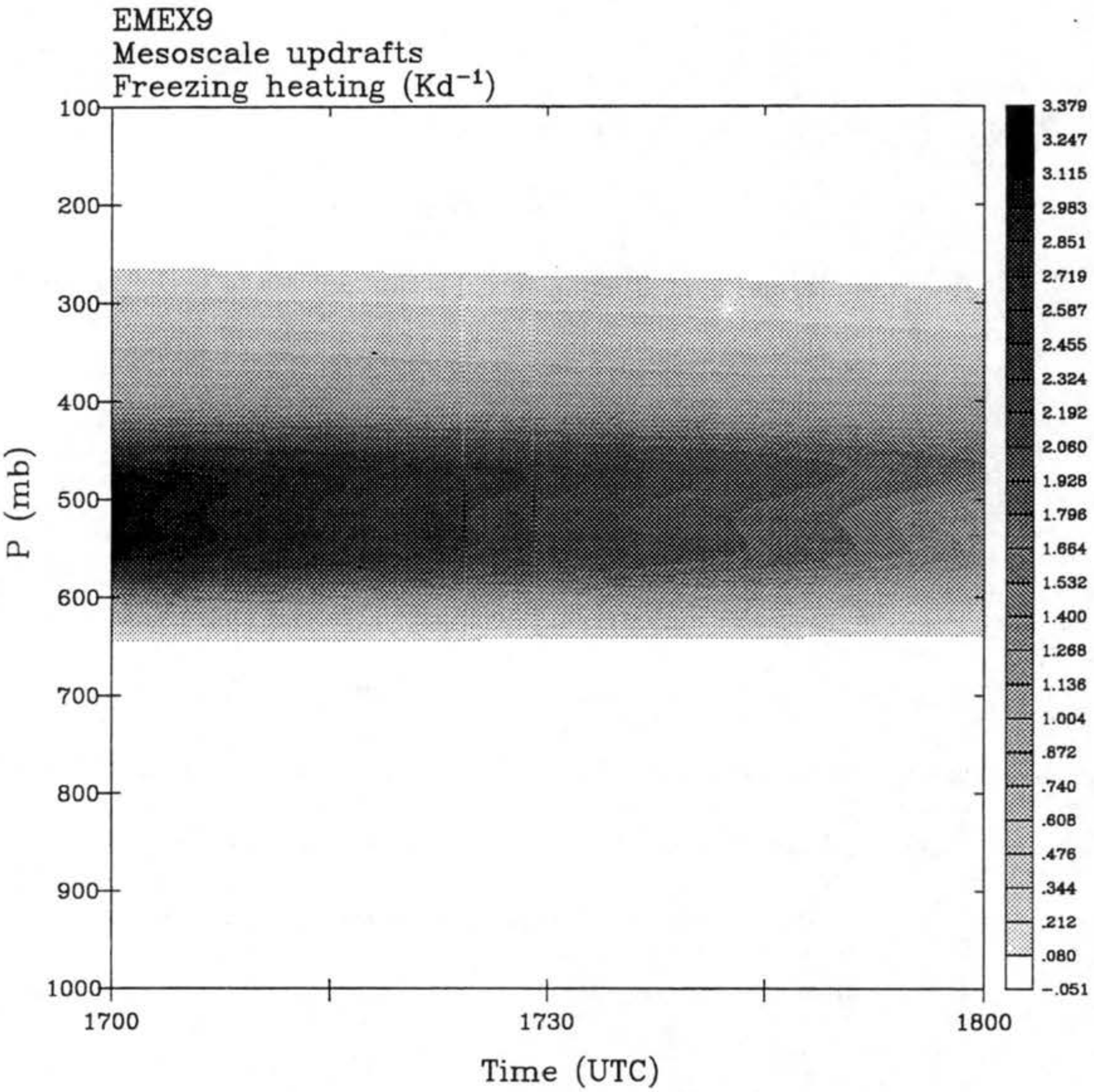
EMEX9
Mesoscale updrafts
Freezing heating (Kd^{-1})
P (mb)
100
200
300
400
500
600
700
800
900
1000
1700
1730
1800
Time (UTC)
3.379
3.247
3.115
2.983
2.851
2.719
2.587
2.455
2.324
2.192
2.060
1.928
1.796
1.664
1.532
1.400
1.268
1.136
1.004
.872
.740
.608
.476
.344
.212
.080
-.051

(b)

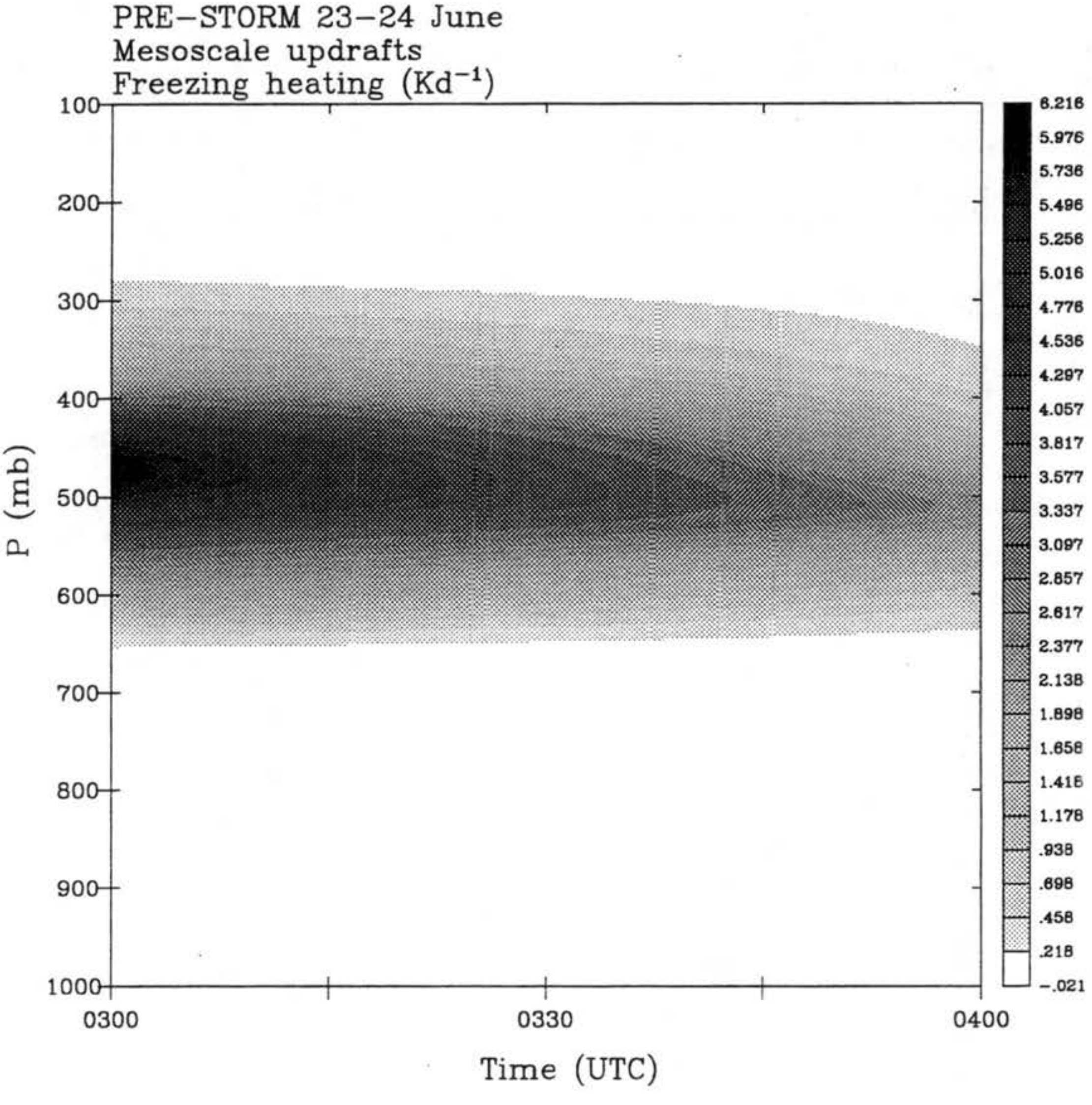

Fig. 4.7: Time evolution of the heating rate due to freezing in the conditionally-sampled mesoscale updrafts for (a) EMEX9 and (b) PRE-STORM.

where R_m is the mesoscale rainfall, E_{me} is the sublimation in mesoscale updrafts, E_{md} is the sublimation plus evaporation in mesoscale downdrafts, C_{mu} is the deposition plus condensation in mesoscale updrafts, and C_A is the condensate transferred from the convective region into the mesoscale region. The first term on the right side of (4.6) is determined as described in section 2.2.3; the second term on the right side of (4.6) is provided by the convective parameterization. To complete the water budget, we need the ratios among the three terms on the left side of (4.6). Equation (4.6) may be rewritten as

$$a + b + c = 1, \tag{4.7}$$

where

$$a = \frac{R_m}{\frac{1}{g}\int_0^{p_g} C_{mu} dp + C_A}, \tag{4.8}$$

$$b = \frac{\frac{1}{g}\int_0^{p_g} E_{me} dp}{\frac{1}{g}\int_0^{p_g} C_{mu} dp + C_A}, \tag{4.9}$$

and

$$c = \frac{\frac{1}{g}\int_0^{p_g} E_{me} dp}{\frac{1}{g}\int_0^{p_g} C_{mu} dp + C_A}. \tag{4.10}$$

Thus, the magnitude of vertically-integrated sublimation in mesoscale updrafts is given by

$$\frac{1}{g}\int_0^{p_g} E_{md}dp = b[\frac{1}{g}\int_0^{p_g} C_{mu}dp + C_A], \tag{4.11}$$

where c is a constant whose value may be approximated by evaluating the terms in equation (4.10) in conditionally-sampled mesoscale updrafts and downdrafts in the explicit MCS simulations. Fig. 4.8 shows the value of a, b, and c in the EMEX (1700-1800 UTC) and PRE-STORM (0300-0400 UTC) simulations. For EMEX, a ranges between 0.91 and 0.93, b ranges between 0.05 and 0.06, and c ranges between 0.02 and 0.03. For PRE-STORM, a ranges between 0.80 and 0.92, b ranges between 0.07 and 0.14, and c ranges between 0.02 and 0.05. Table 4.1 lists values of a, b, and c determined by other investigators for various MCSs in the midlatitudes and tropics. The studies summarized in Table 4.1 use widely varying techniques to evaluate these quantities and therefore directly comparing one to another may be dubious. Methodology aside, it is expected that there will also be physical differences in these quantities from one MCS to the next which will be particularly dependent on which stage of the MCS's life cycle is sampled.

Once the magnitude of vertically-integrated sublimation in the parameterized mesoscale updraft is determined, all that remains is to determine how to vertically distribute this sublimation vertically. Fig. 4.9 shows a time-height plot of the deposition rate for the EMEX9 and PRE-STORM simulations. Based on these profiles, both EMEX9's and PRE-STORM's mesoscale updraft sublimation profiles have a shape parameter of 0.80 and a depth parameter of 0.80.

(a)

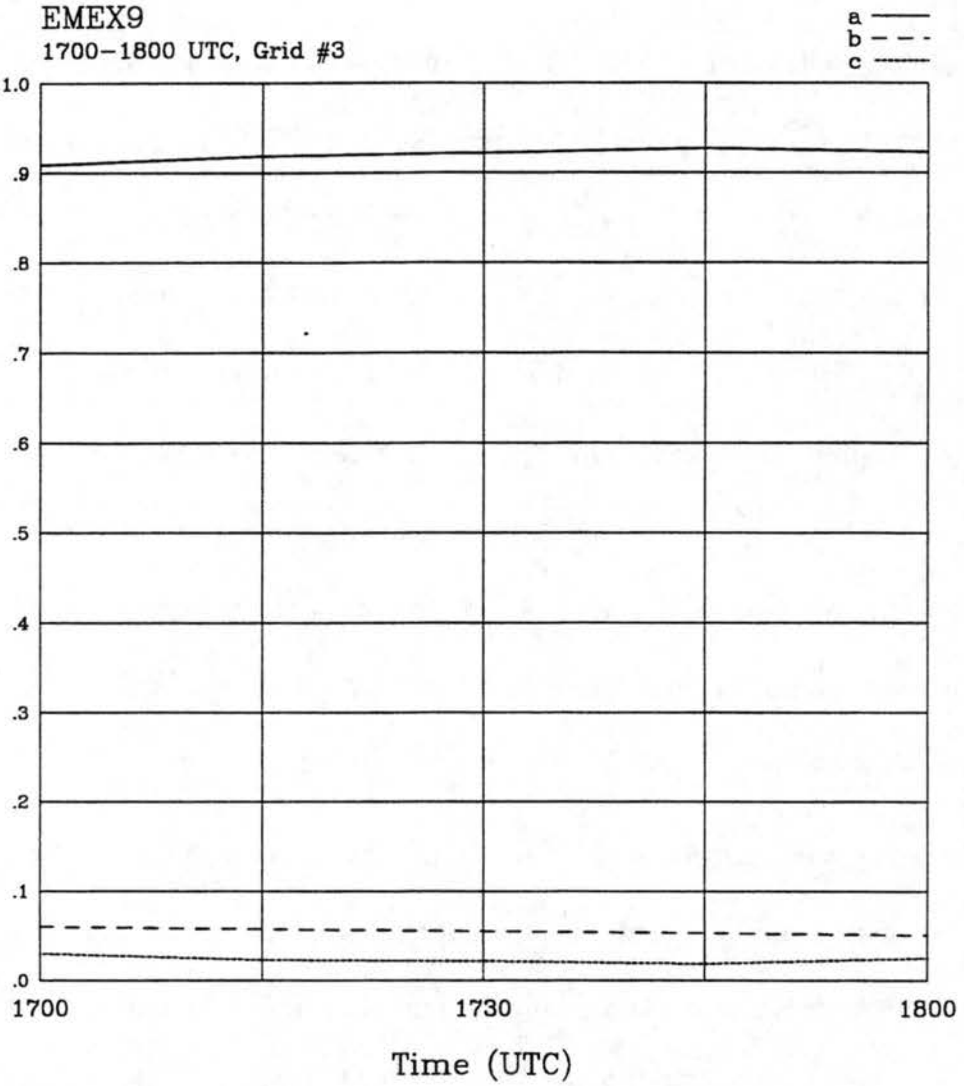
EMEX9
1700–1800 UTC, Grid #3
a
b
c
1.0
.9
.8
.7
.6
.5
.4
.3
.2
.1
.0
1700
1730
1800
Time (UTC)

(b)

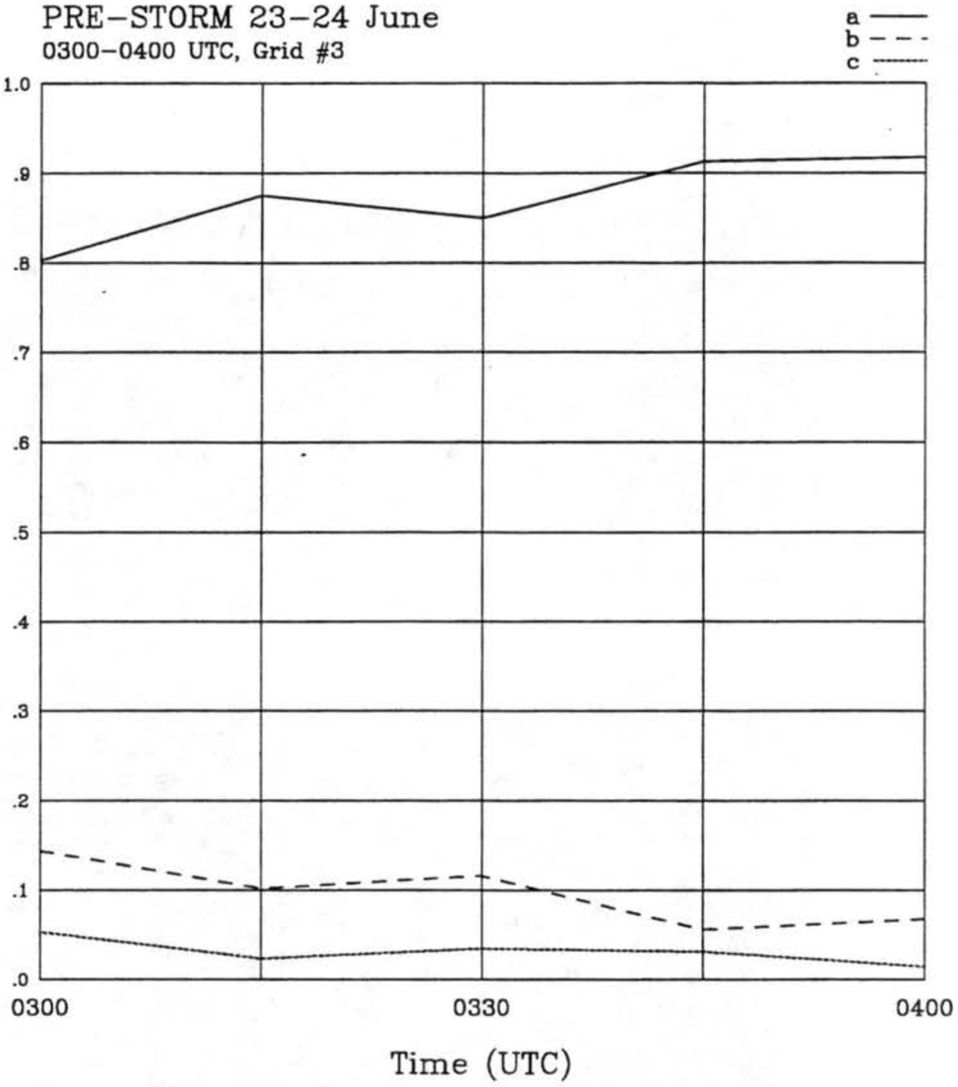

Fig. 4.8: Time evolution of the MCS water budget parameters a, b, and c in the conditionally-sampled mesoscale updrafts and downdrafts for (a) EMEX9 and (b) PRE-STORM. The quantities a, b, and c are defined in the text.

(a)

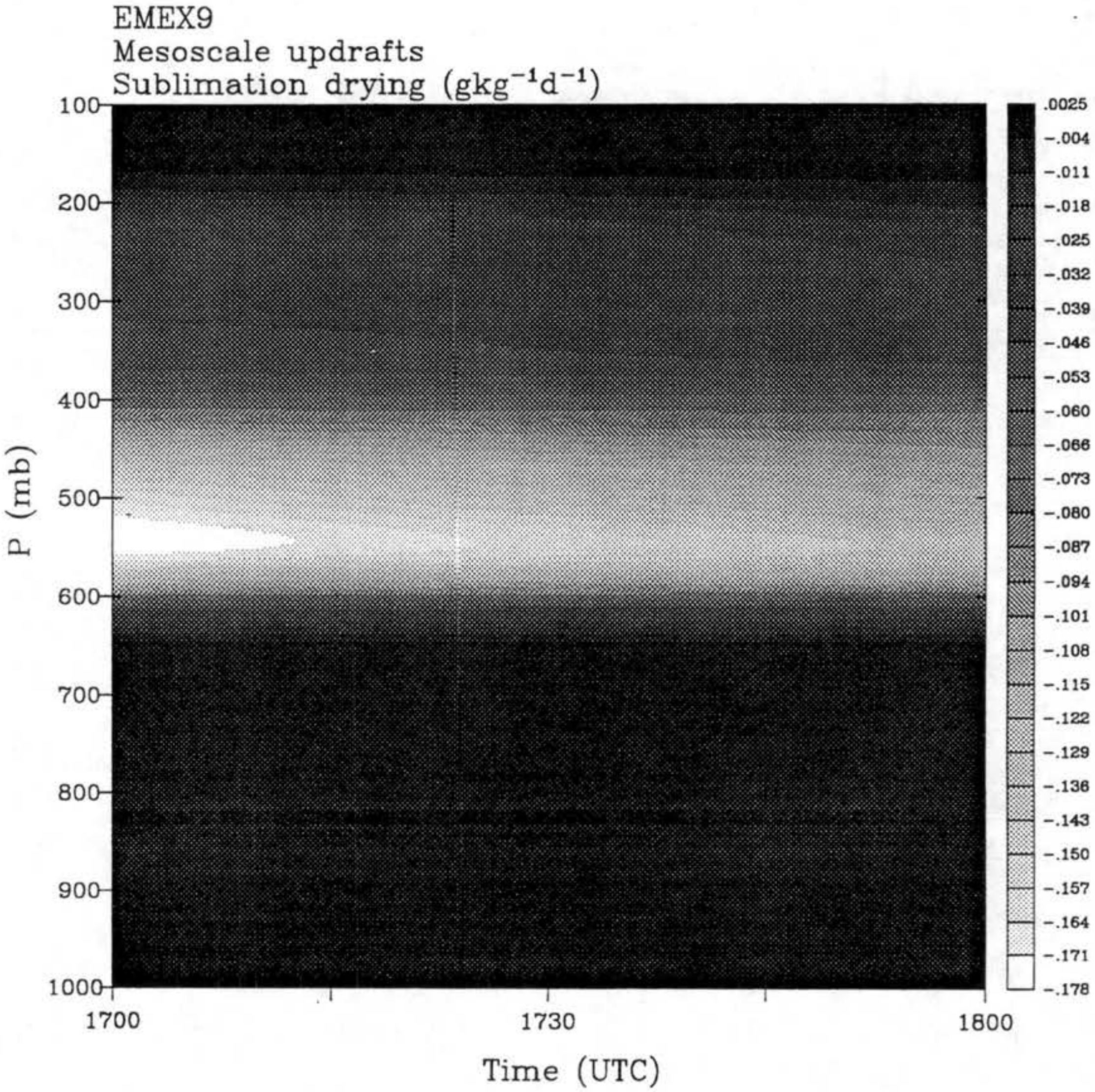
EMEX9
Mesoscale updrafts
Sublimation drying ($gkg^{-1}d^{-1}$)
P (mb)
100
200
300
400
500
600
700
800
900
1000
Time (UTC)
1700
1730
1800
.0025
-.004
-.011
-.018
-.025
-.032
-.039
-.046
-.053
-.060
-.066
-.073
-.080
-.087
-.094
-.101
-.108
-.115
-.122
-.129
-.136
-.143
-.150
-.157
-.164
-.171
-.178

(b)

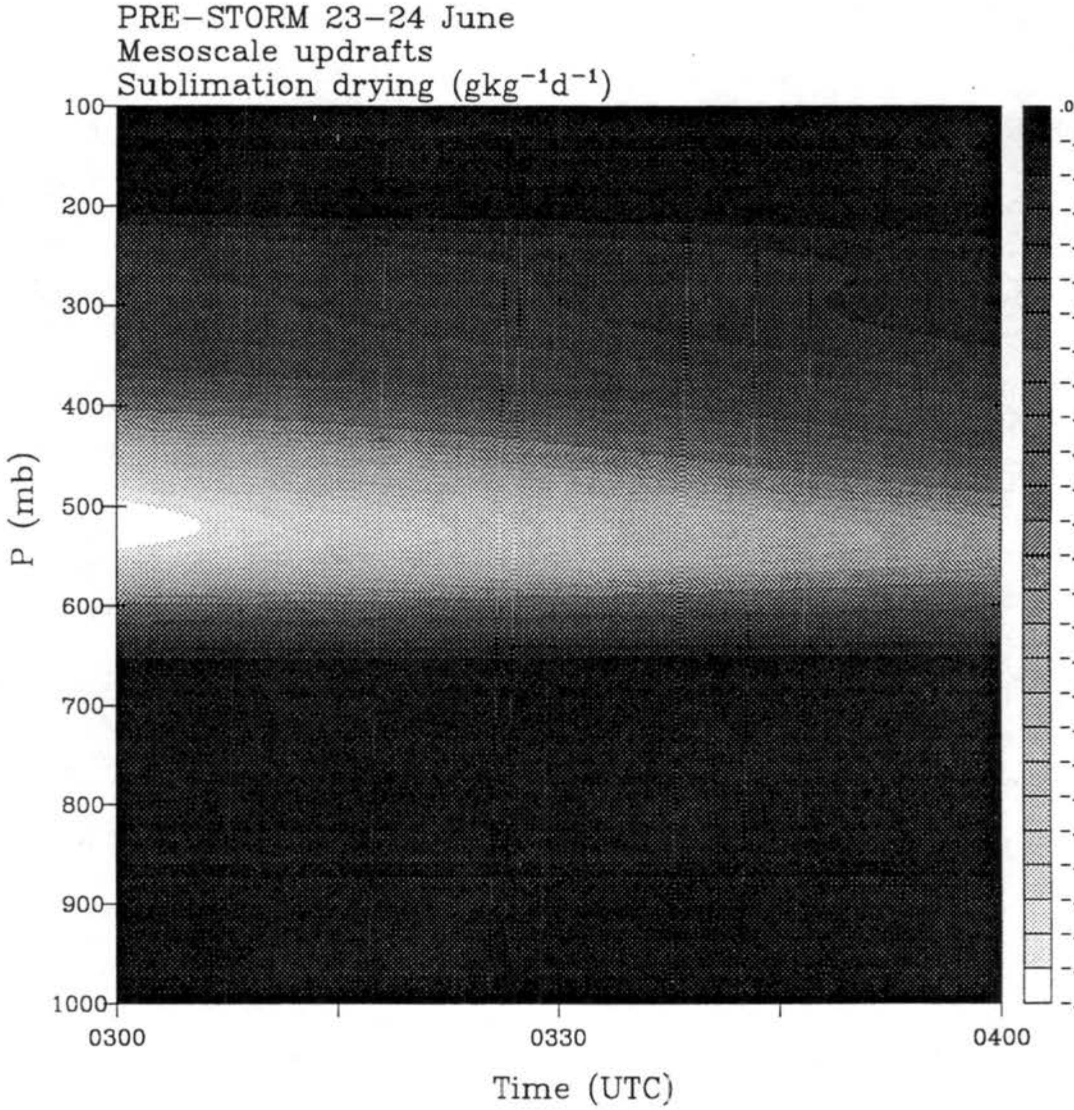

Fig. 4.9: Time evolution of the sublimation rate in the conditionally-sampled mesoscale updrafts for (a) EMEX9 and (b) PRE-STORM.

Case	LH-A	LH-B	LH-C	GH-I	GH-II	CH	RJ	GJ	E9	PS
a	0.91	0.50	0.50	0.64	0.64	0.52	0.61	0.54	0.92	0.87
b	0.09	0.10	0.10	0.16	0.16	0.16	0.11	0.20	0.06	0.10
c	0.00	0.40	0.40	0.20	0.27	0.38	0.28	0.27	0.02	0.13

Table 4.1: Values of MCS water budget parameters a, b, and c for cases A, B, and C of Leary and Houze (1980; LH), cases I and II of Gamache and Houze (1983; GH), Chong and Hauser (1989; CH), Roux and Ju (1990; RJ), Gallus and Johnson (1991; GH), EMEX9 (1700-1800 UTC mean; E9), and PRE-STORM 23-24 June (0300-0400 UTC mean; PS).

4.3.4 Sublimation and evaporation in mesoscale downdrafts

The magnitude of the vertical integral of sublimation plus evaporation in mesoscale downdrafts is given by

$$\frac{1}{g}\int_0^{p_g} E_{md}dp = c[\frac{1}{g}\int_0^{p_g} C_{mu}dp + C_A], \tag{4.12}$$

where c is as defined in (4.10). To determine how to partition this quantity into vertically-integrated sublimation and vertically-integrated evaporation individually, we look at the ratio between these quantities in the conditionally-sampled downdrafts of the explicit simulations. Fig. 4.10 shows the ratio of the vertically-integrated evaporation in conditionally-sampled mesoscale downdrafts to the vertically-integrated sublimation in conditionally-sampled mesoscale downdrafts for both EMEX9 and PRE-STORM. In each case, the vertically-integrated evaporation rate far exceeds the vertically integrated sublimation rate with the ratio ranging from 10 to 16 for EMEX9 and from 3 to 11 for PRE-STORM.

Fig. 4.10 shows a time-height plot of the evaporation rate in the conditionally-sampled mesoscale downdrafts for the EMEX9 (1700-1800 UTC) and PRE-STORM (0300-0400 UTC) simulations. Based on the character of the vertical profiles in Fig. 4.11, the vertical profile of evaporation rate in the parameterized mesoscale downdraft is assumed to have a shape parameter of 0.25 for EMEX and 0.85 for PRE-STORM. The depth parameter is 1.0 for each case.

Fig. 4.12 shows a time-height plot of the sublimation rate in the conditionally-sampled mesoscale downdrafts for the EMEX9 (1700-1800 UTC) and PRE-STORM

(a)

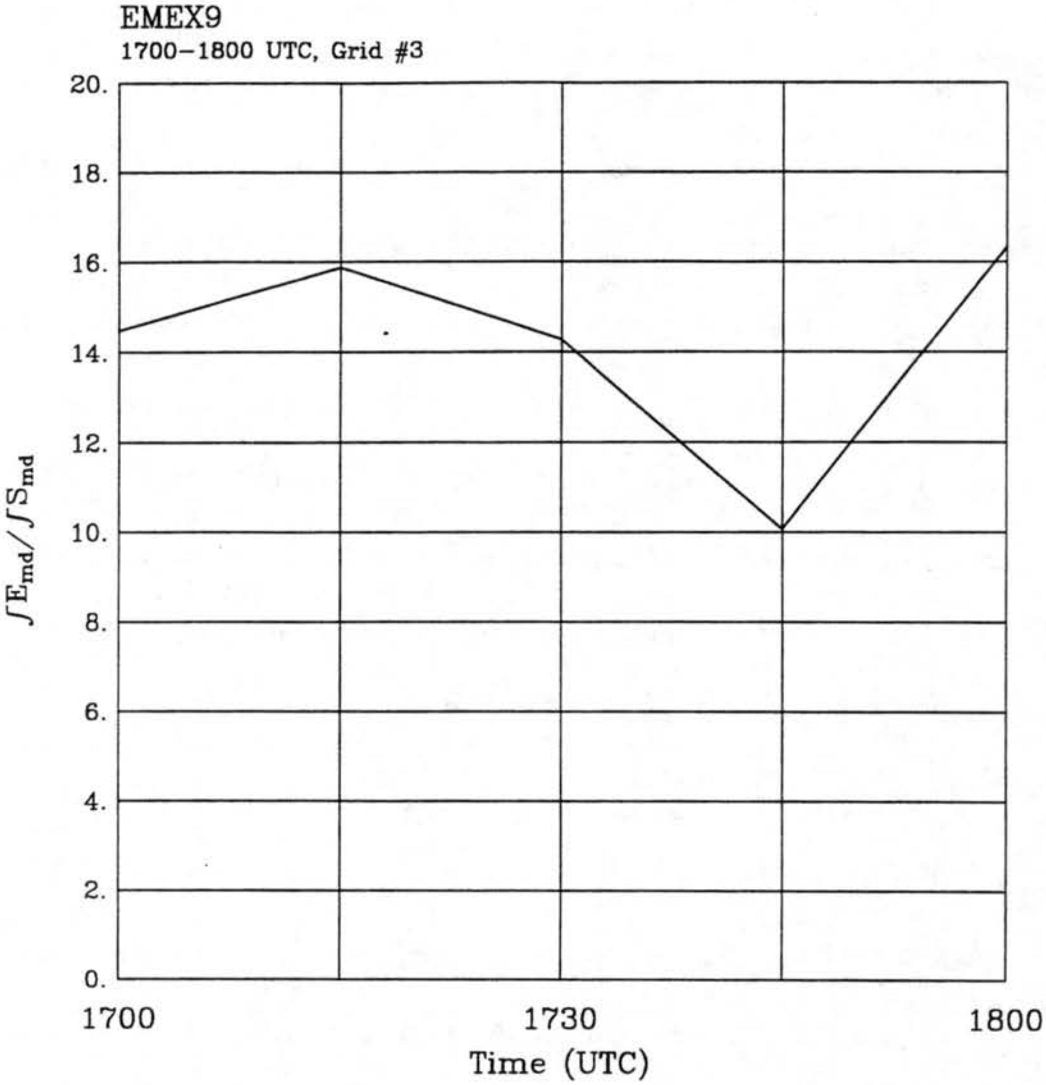
EMEX9
1700–1800 UTC, Grid #3
20.
18.
16.
14.
12.
10.
8.
6.
4.
2.
0.
$\int E_{md} / \int S_{md}$
1700
1730
1800
Time (UTC)

(b)

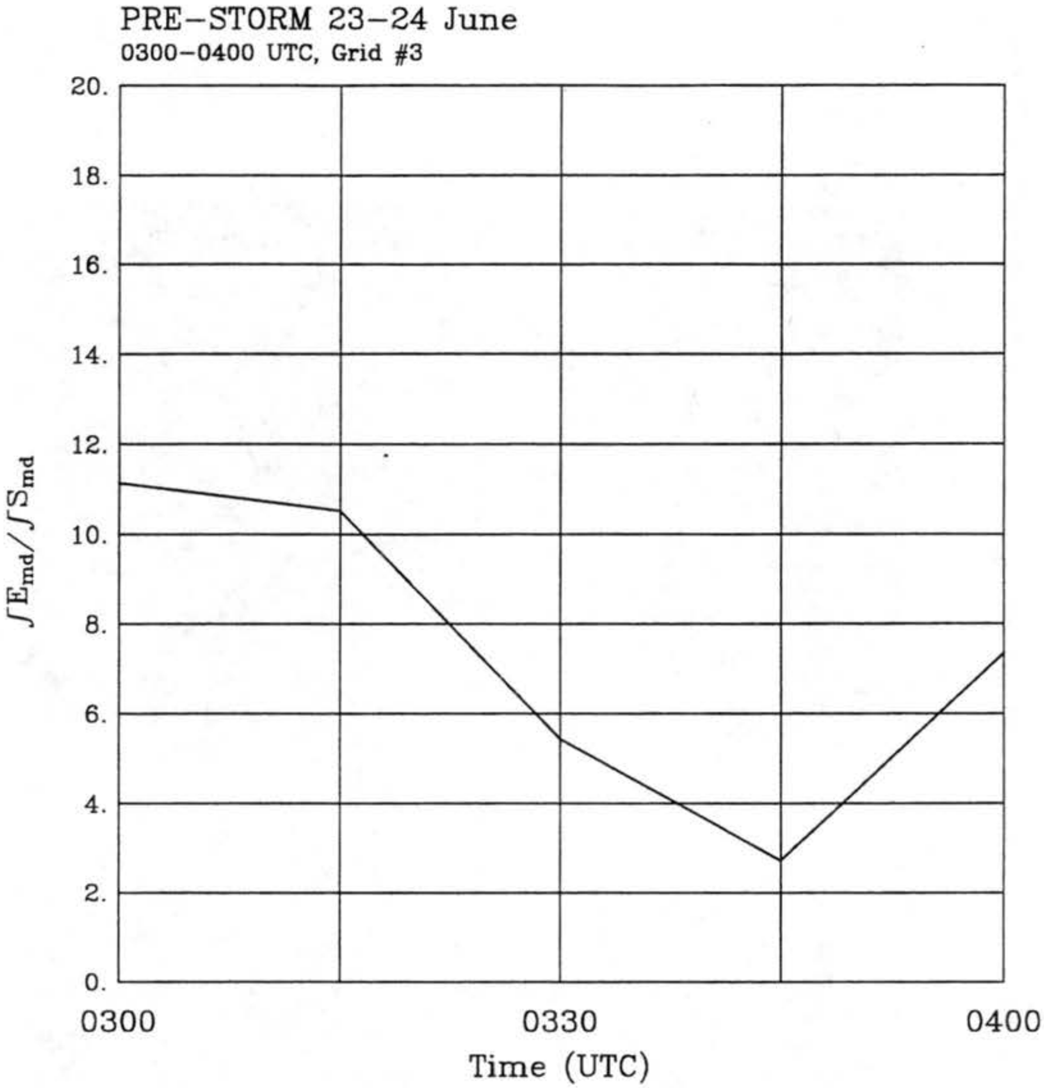

Fig. 4.10: Time evolution of the ratio of the vertically integrated evaporation rate to the vertically-integrated sublimation rate in conditionally-sampled mesoscale downdrafts for (a) EMEX9 and (b) PRE-STORM.

(a)

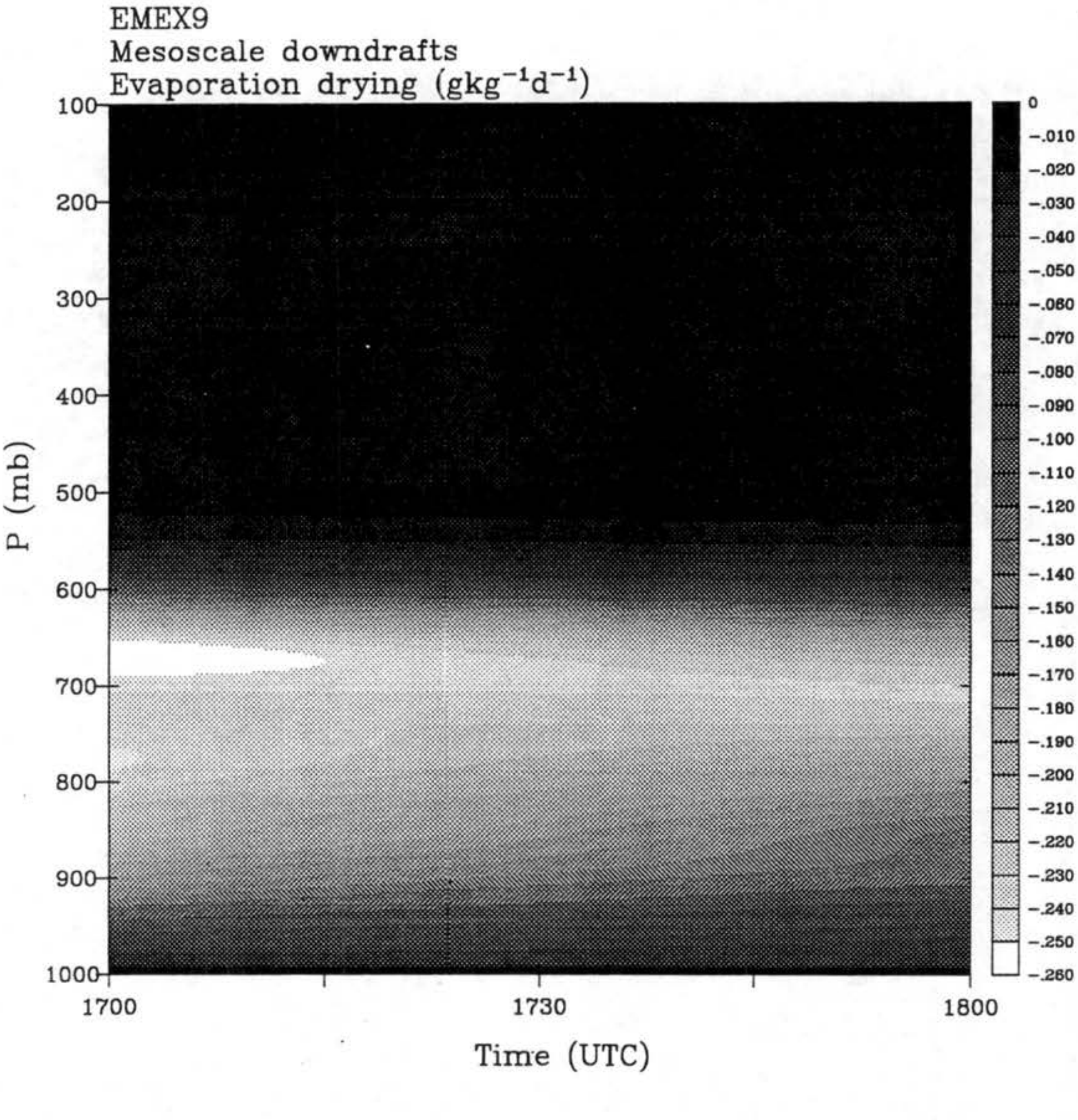
EMEX9
Mesoscale downdrafts
Evaporation drying ($gkg^{-1}d^{-1}$)
P (mb)
100
200
300
400
500
600
700
800
900
1000
Time (UTC)
1700
1730
1800
0
-.010
-.020
-.030
-.040
-.050
-.060
-.070
-.080
-.090
-.100
-.110
-.120
-.130
-.140
-.150
-.160
-.170
-.180
-.190
-.200
-.210
-.220
-.230
-.240
-.250
-.260

(b)

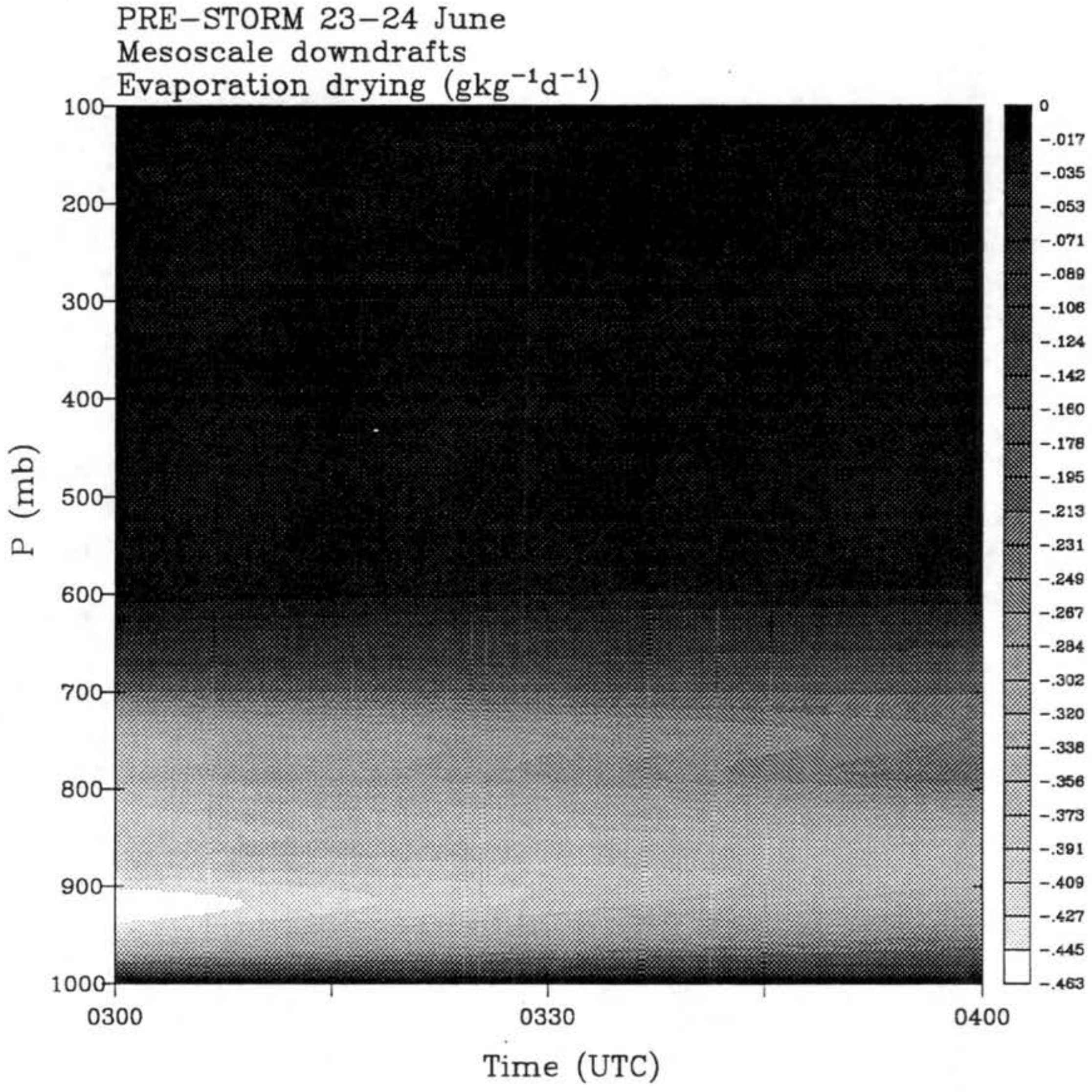

Fig. 4.11: Time evolution of the evaporation rate in the conditionally-sampled mesoscale downdrafts for (a) EMEX9 and (b) PRE-STORM.

(0300-0400 UTC) simulations. The vertical profiles in Fig. 4.11 yield a shape parameter of 0.50 for EMEX and 0.65 for PRE-STORM for sublimation in the parameterized mesoscale downdraft. The depth parameter is 0.20 for both EMEX and PRE-STORM.

4.3.5 Melting

The magnitude of the vertically-integrated melting in mesoscale downdrafts is computed as discussed in Section 2.2.7. That is, the melting depends on the magnitude of the parameter a, as defined in equation (4.8). Melting profiles for the conditionally-sampled mesoscale downdrafts of each MCS are shown in Fig. 4.13. These profiles of melting in conditionally-sampled mesoscale downdrafts yield a depth parameter of 0.60 for EMEX and 0.80 for PRE-STORM and yield a shape parameter of 0.45 for EMEX and 0.40 for PRE-STORM. Flatau et al. (1989) acknowledge that it is possible for the microphysics parameterization to produce melting at sub-zero ambient temperatures if there is an error in the calculated thermodynamic budget of the ice particle. In the MCS simulations, the magnitude of such melting is negligible and therefore melting in parameterized mesoscale updrafts is not considered.

4.4 Eddy flux convergences

The mesoscale eddy flux convergences of entropy $(-\frac{\partial}{\partial p}\overline{\omega'\theta'})$ and water vapor $(\frac{\partial}{\partial p}\overline{\omega' \mathrm{q}'})$ are the final terms needed to parameterize mesoscale heating and drying, respectively. There have been conflicting assessments as to the significance of these terms. Cheng and Yanai (1989), for instance, argued that the convergence of eddy fluxes can be *neglected* in stratiform regions compared to condensation and evapo-

(a)

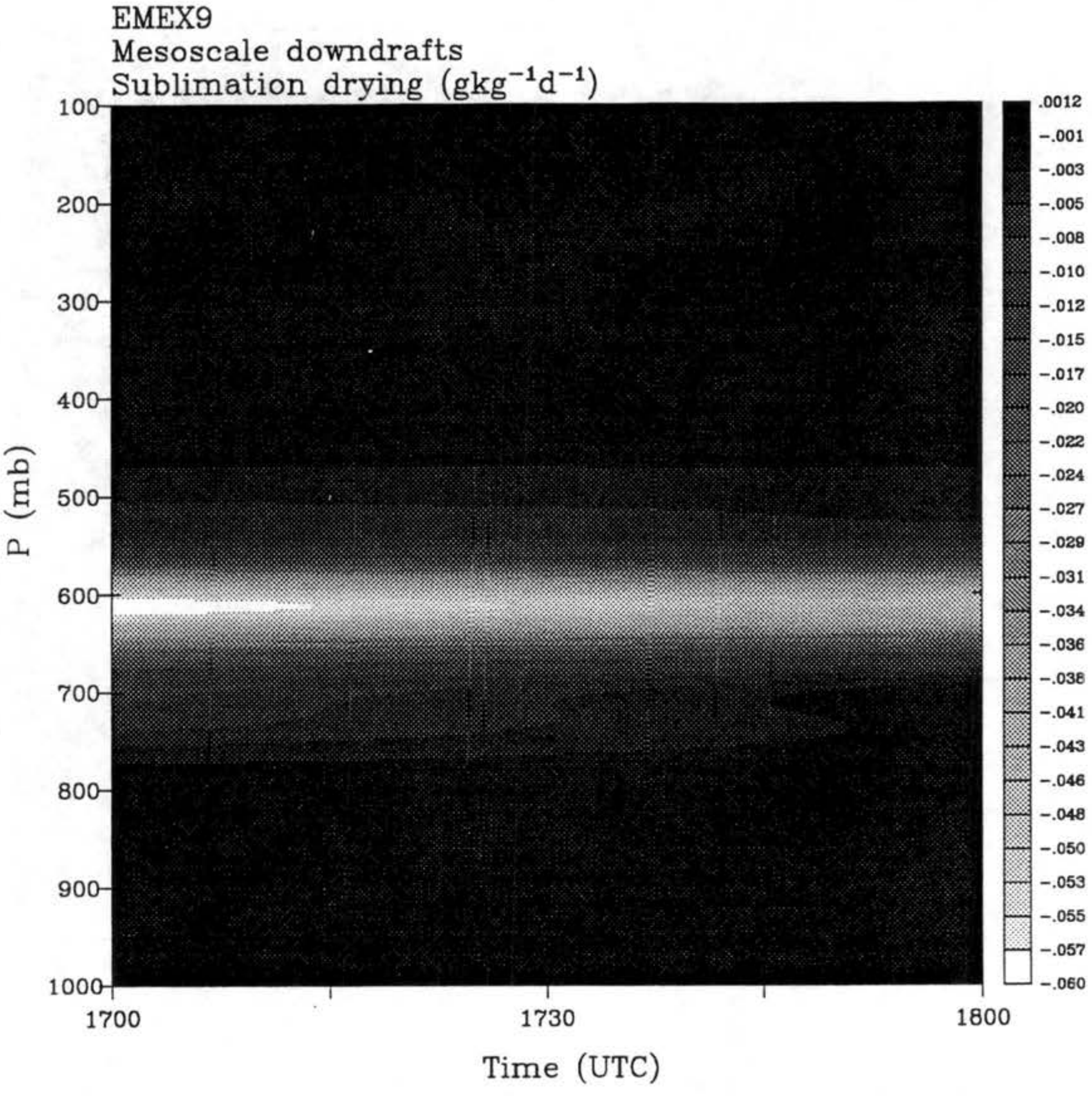
EMEX9
Mesoscale downdrafts
Sublimation drying ($gkg^{-1}d^{-1}$)
P (mb)
100
200
300
400
500
600
700
800
900
1000
1700
1730
1800
Time (UTC)
.0012
-.001
-.003
-.005
-.008
-.010
-.012
-.015
-.017
-.020
-.022
-.024
-.027
-.029
-.031
-.034
-.036
-.038
-.041
-.043
-.046
-.048
-.050
-.053
-.055
-.057
-.060

(b)

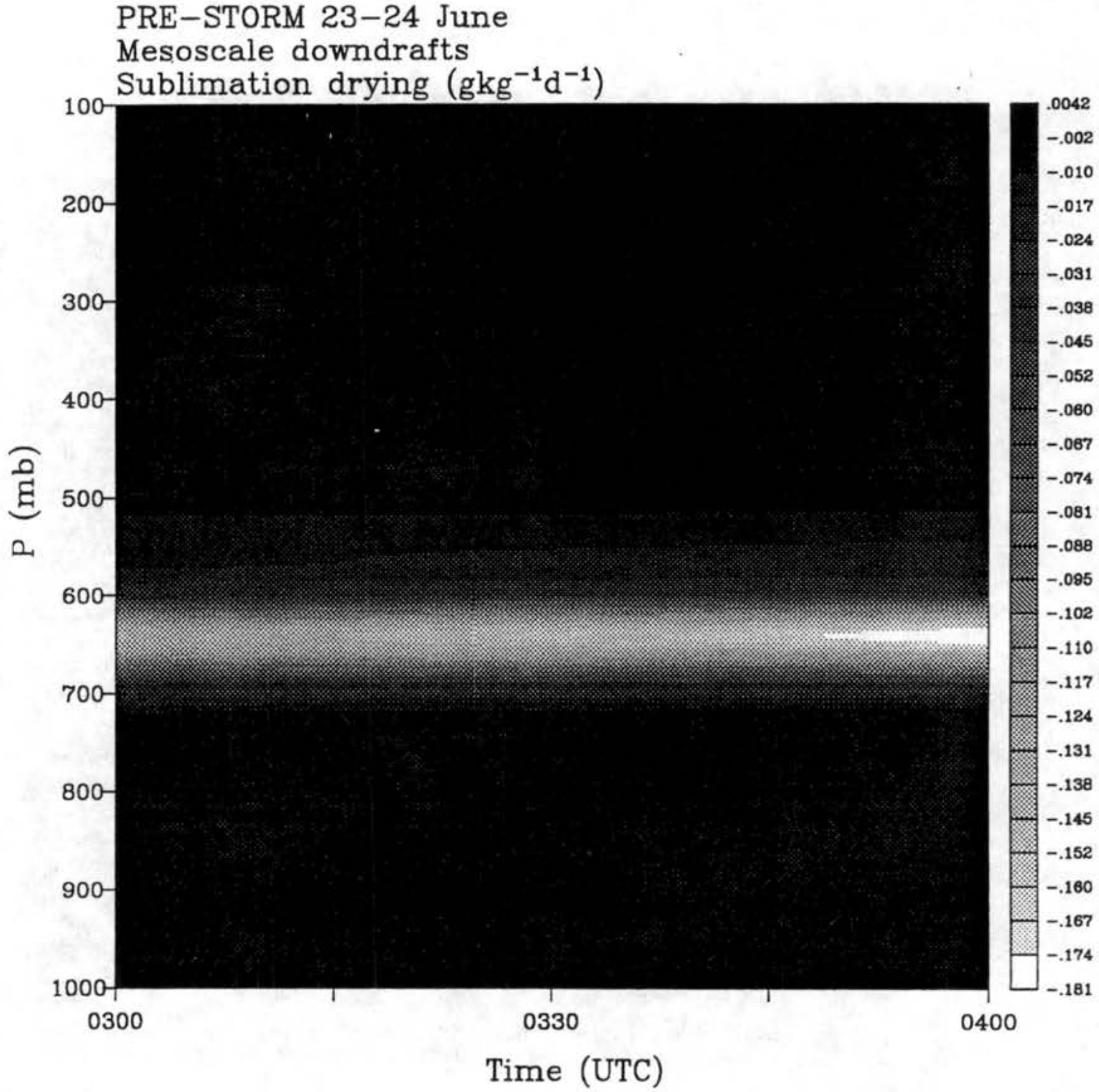

Fig. 4.12: Time evolution of the sublimation rate in the conditionally-sampled mesoscale downdrafts for (a) EMEX9 and (b) PRE-STORM.

(a)

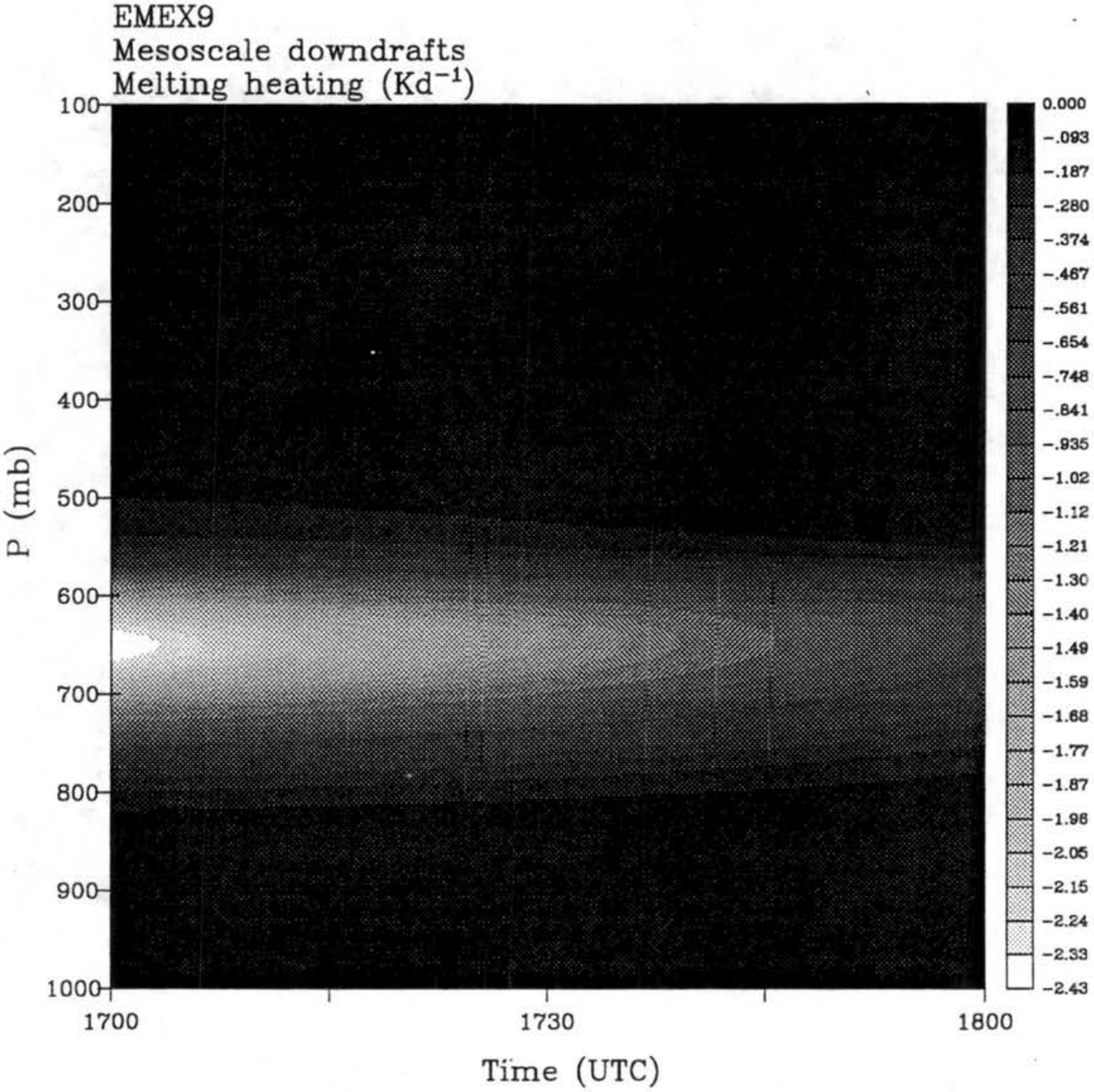
EMEX9
Mesoscale downdrafts
Melting heating (Kd^{-1})
P (mb)
100
200
300
400
500
600
700
800
900
1000
1700
1730
1800
Time (UTC)
0.000
-.093
-.187
-.280
-.374
-.467
-.561
-.654
-.748
-.841
-.935
-1.02
-1.12
-1.21
-1.30
-1.40
-1.49
-1.59
-1.68
-1.77
-1.87
-1.96
-2.05
-2.15
-2.24
-2.33
-2.43

(b)

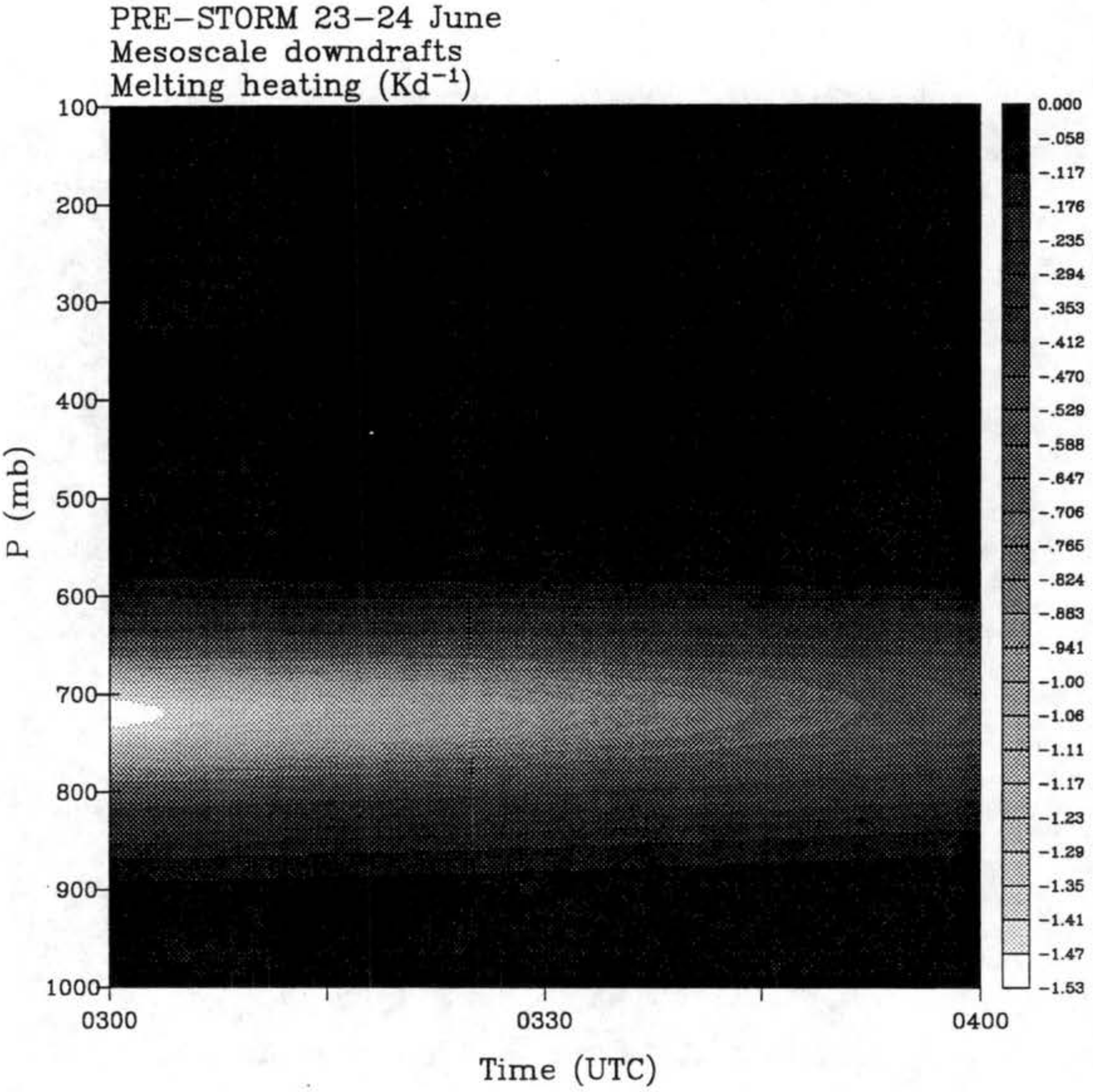

Fig. 4.13: Time evolution of the melting rate in the conditionally-sampled mesoscale downdrafts for (a) EMEX9 and (b) PRE-STORM.

ration. The analyses of Gallus and Johnson (1991) and Johnson and Young (1983) support this argument for MCSs in the midlatitudes (PRE-STORM 10-11 June squall line) and tropics (December 1978 Winter Monsoon Experiment systems), respectively. Houze (1982) evaluated terms in the heat budget of an idealized tropical cloud cluster and surmised that in the mesoscale updraft, the heating resulting from eddy flux convergence of entropy had a maximum magnitude one-fifth that of the heating resulting from condensation. In the mesoscale downdraft, the heating resulting from eddy flux convergence of entropy had a maximum magnitude only one-eighth of that resulting from melting and evaporation. On the other hand, Tao et al. (1993), in two-dimensional modeling studies of a tropical MCS (EMEX9) and a midlatitude MCS (PRE-STORM 10-11 June) evaluated the magnitude of the eddy moisture flux convergence in the stratiform region and found this term to be a significant component of the water budget of each MCS. For example, in their EMEX9 simulation, the maximum magnitude of apparent heating due to the eddy flux convergence of moisture in the mesoscale updraft (0.1 Kh^{-1}) was one-fifth the maximum magnitude of the heating due the eddy flux convergence of moisture (0.5 Kh^{-1}) in the mesoscale updraft. In their EMEX9 mesoscale downdraft, the maximum magnitude of the heating due to the eddy flux convergence of moisture (0.2 Kh^{-1}) was about half the maximum magnitude of the total heating due to the eddy flux convergence of moisture (0.4 Kh^{-1}). Xu's (1995) cumulus ensemble model simulations also demonstrated that the eddy flux convergences of heat and moisture can contribute significantly to the heat and moisture budgets of the stratiform region. Fig. 4.14, for instance, compares the magnitude of the phase change component of his stratiform heat budget to the magnitudes of the stratiform eddy flux convergences of heat and moisture. The heating resulting from eddy flux of moisture appears to be particularly important, reaching maximum magnitudes of over 2 Kd^{-1}, compared to about 6 Kd^{-1} for the phase change terms.

For the present simulations, the vertical profile of the eddy flux entropy convergence show features analogous to those in Fig. 4.14. A time series of heating resulting from the eddy flux convergence of entropy for conditionally-sampled updrafts and downdrafts in EMEX9 (Fig. 4.15a) shows that the important features of the profile are heating at the top of the troposphere and cooling of similar magnitude just beneath there. In the lower troposphere, particularly after 0345 UTC, there is a layer of cooling sandwiched between two layers of heating, as in Xu (1995). The PRE-STORM 0300-0400 UTC mean of the vertical profile of heating due to eddy flux convergence of entropy (Fig. 4.15b) shows similar features to EMEX9 and Xu (1995). In both cases, the magnitude of heating from the eddy flux convergence term is relatively small in comparison to that by the phase change terms, except perhaps in the upper troposphere where the phase change terms are small. The magnitude of the eddy heat flux convergences presented here are comparable to those found by Xu (1995). For EMEX9, the heating ranges from approximately -0.60 to +0.75 Kd^{-1}; for PRE-STORM, the heating ranges from -1.40 to +0.75 Kd^{-1}.

The vertical profiles of the eddy moisture convergence in the conditionally-sampled regions also show features similar to those in Fig. 4.13. For EMEX9 (Fig. 4.16a) the mesoscale updrafts effect upper tropospheric moistening and midtropospheric drying.

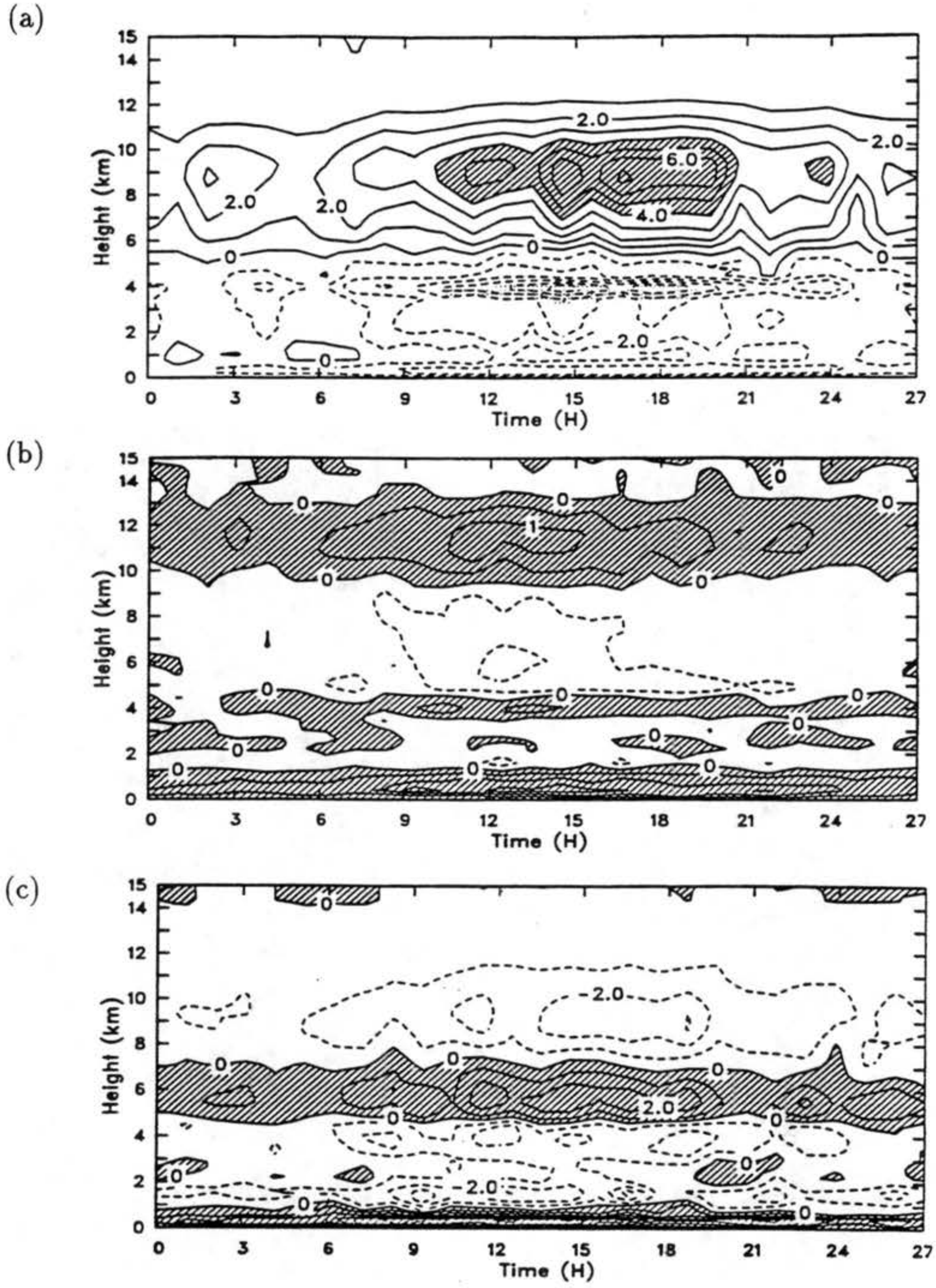

Fig. 4.14: Time evolution of the ensemble mean of the (a) the apparent heat source due to the phase change component of stratiform heat/moisture budget (contour interval 1 Kd^{-1}), (b) the apparent heat source due to the stratiform eddy heat flux convergence (contour interval 0.5 Kd^{-1}), and (c) the apparent moisture sink due to the stratiform eddy moisture flux convergence (contour interval 1 Kd^{-1}). From Xu (1995).

(a)

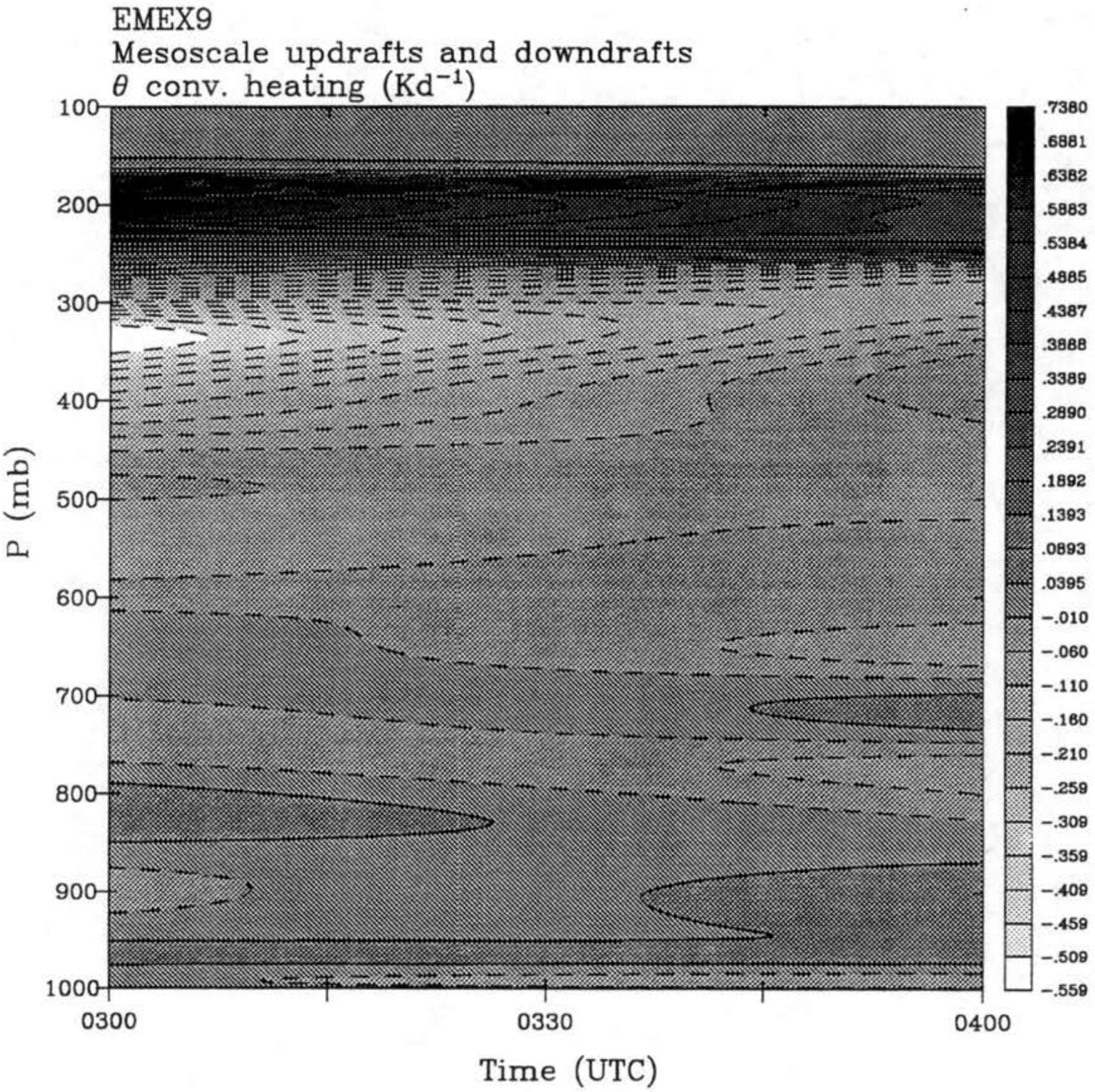
EMEX9
Mesoscale updrafts and downdrafts
θ conv. heating (Kd^{-1})
P (mb)
100
200
300
400
500
600
700
800
900
1000
0300
0330
0400
Time (UTC)
.7380
.6881
.6382
.5883
.5384
.4885
.4387
.3888
.3389
.2890
.2391
.1892
.1393
.0893
.0395
-.010
-.060
-.110
-.160
-.210
-.259
-.309
-.359
-.409
-.459
-.509
-.559

(b)

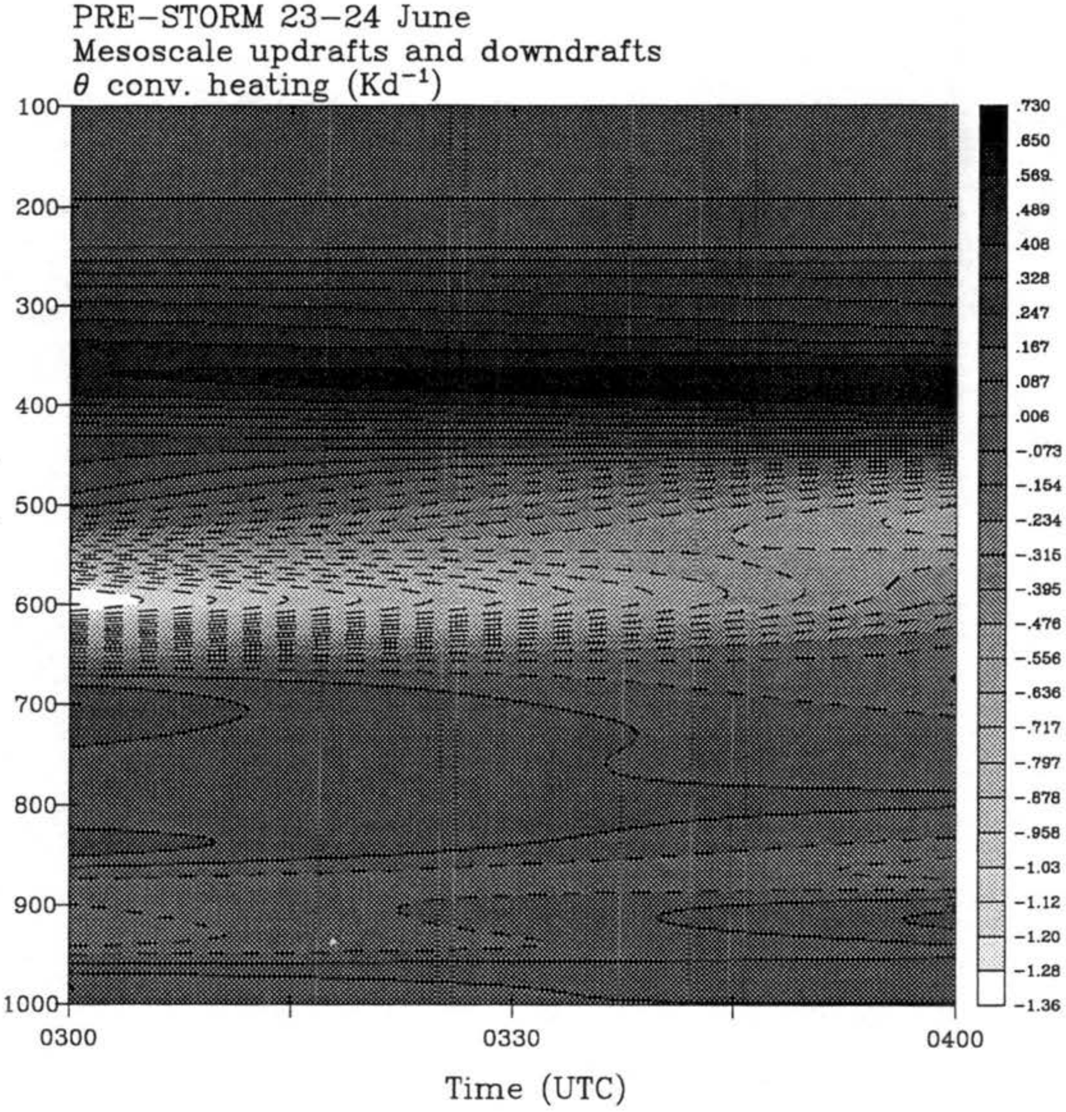

Fig. 4.15: Time evolution of the vertical profiles of the heating resulting from the eddy flux convergence of entropy for the conditionally-sampled stratiform region of (a) EMEX9 (1700-1800 UTC), and (b) PRE-STORM 23-24 June (0300-0400 UTC). Dashed lines indicate negative contour values.

In mesoscale downdrafts, the strongest feature is drying below 950 mb, which reaches a magnitude of about 0.75 $gkg^{-1}d^{-1}$. For PRE-STORM (Fig. 4.16b), the features are similar. Mesoscale updrafts effect upper tropospheric moistening and midtropospheric drying. In mesoscale downdrafts, moistening also overlies drying, with evidence of a secondary drying layer around 850 mb, as seen in Fig. 4.14.

The mesoscale eddy flux convergence of a variable χ (where here χ is either θ or q) is parameterized as specified in equation (2.6), except a_i is replaced by a_m, the parameterized fractional coverage of the stratiform region. That is,

$$\frac{\partial \overline{\omega' \chi'}}{\partial p} = -\frac{a_m \omega'_m \chi'_m}{1 - a_m}. \tag{4.13}$$

Thus, to parameterize eddy flux convergence profiles the shapes and magnitudes of vertical profiles of w', θ', and q' are specified according to the results of conditiional sampling of mesoscale updrafts and downdrafts. The shape and depth parameters and maximum magnitudes of these profiles are summarized in Tables 4.2-4.4.

Fractional coverage of the stratiform region is parameterized based on observational evidence, following Leary and Houze (1980) and Donner (1993), who both assumed that the stratiform region's fractional area is 5 times that of the convective region fractional area. This ratio of stratiform fractional area to convective fractional area is based on observations and is meant to represent a storm lifetime mean value. One could argue whether this ratio should actually be 3, 5, 7, or whatever—with all the other approximations and uncertainties in the parameterization of eddy flux

(a)

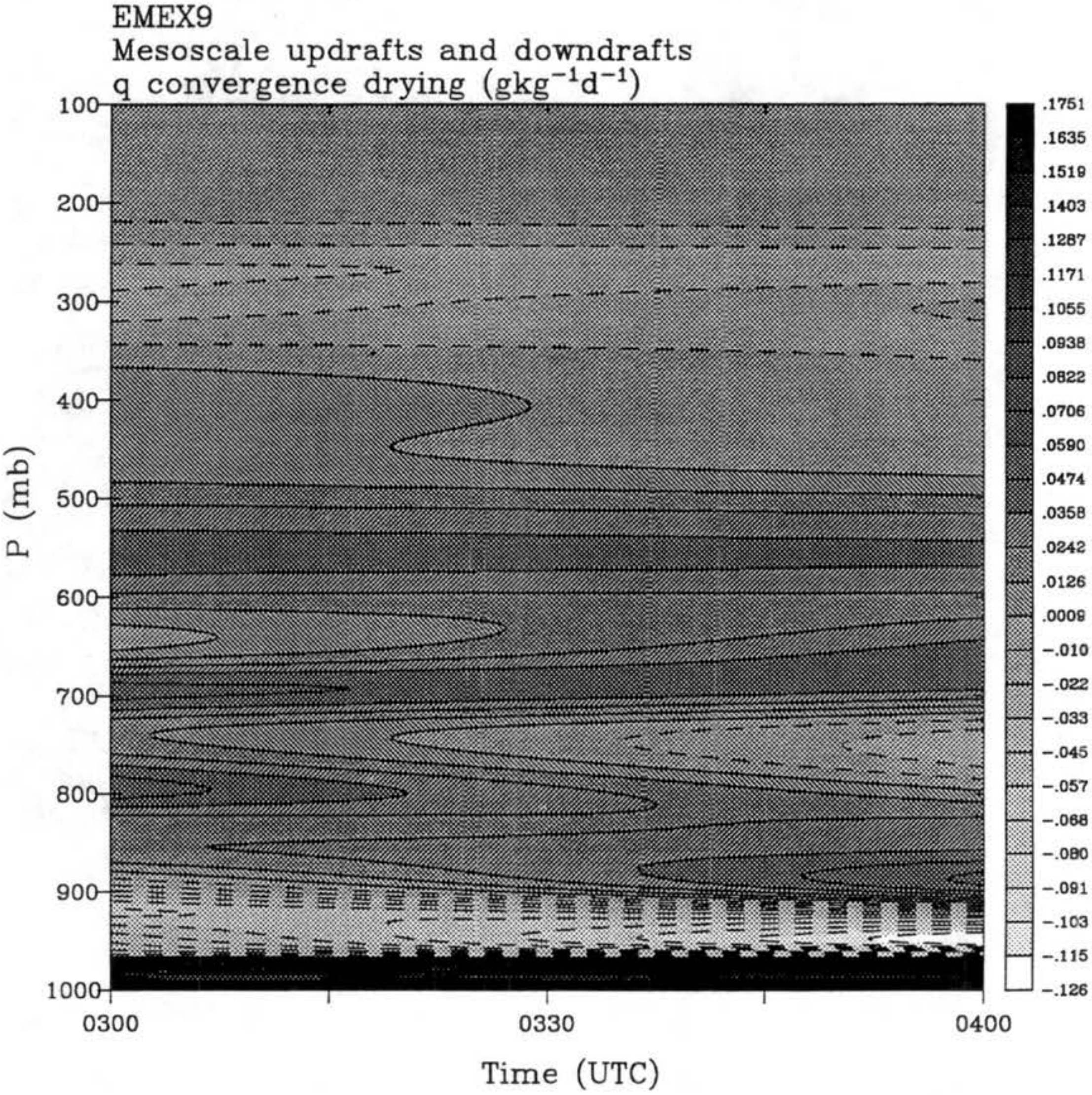
EMEX9
Mesoscale updrafts and downdrafts
q convergence drying (gkg^{-1}d^{-1})
P (mb)
100
200
300
400
500
600
700
800
900
1000
0300
0330
0400
Time (UTC)
.1751
.1635
.1519
.1403
.1287
.1171
.1055
.0938
.0822
.0706
.0590
.0474
.0358
.0242
.0126
.0009
−.010
−.022
−.033
−.045
−.057
−.068
−.080
−.091
−.103
−.115
−.126

(b)

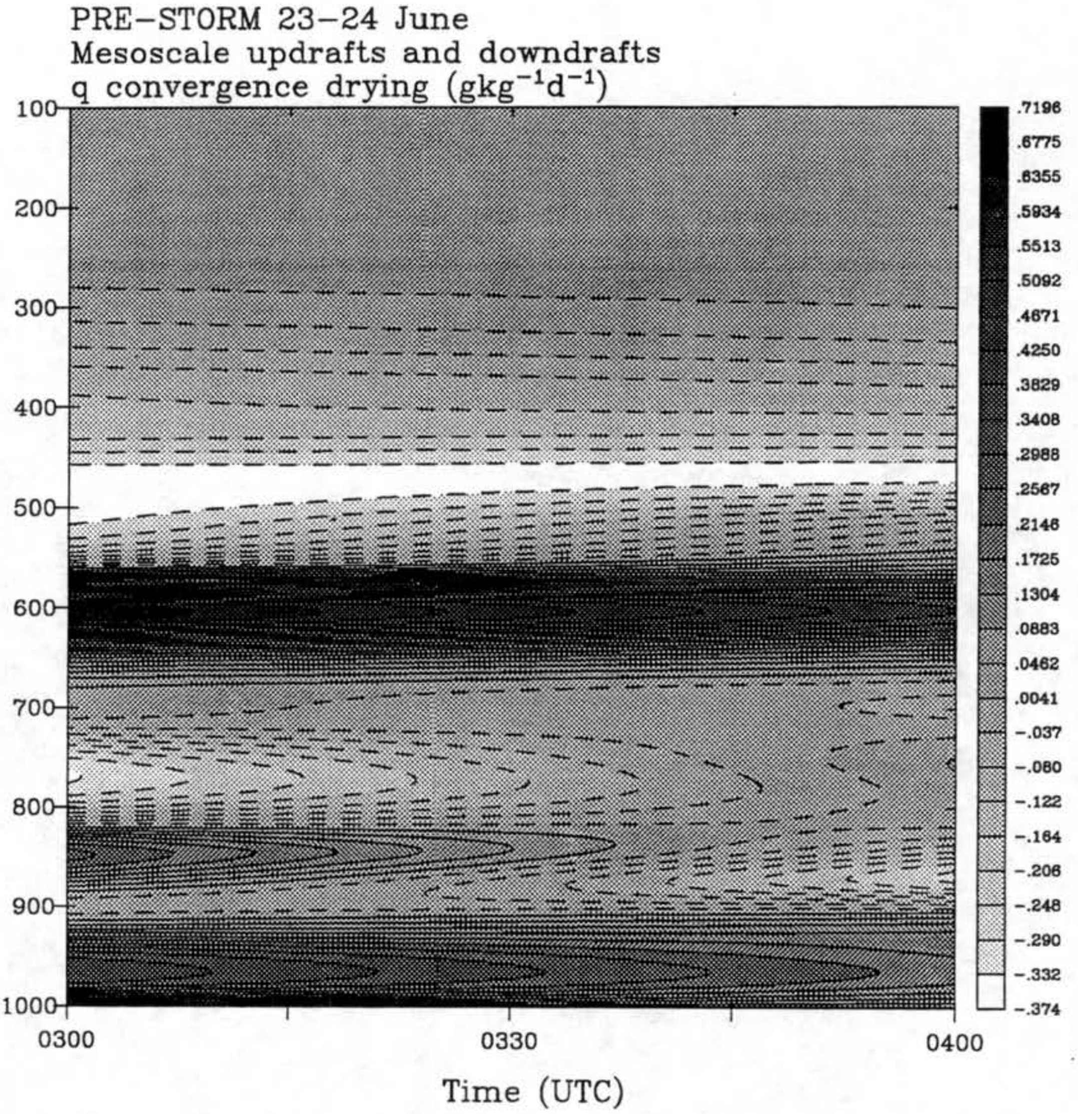

Fig. 4.16: Time evolution of the vertical profiles of drying resulting from the eddy flux convergence of water vapor for the conditionally-sampled stratiform region of (a) EMEX9 (1700-1800 UTC), and (b) PRE-STORM 23-24 June (0300-0400 UTC). Dashed lines indicate negative contour values.

w′	Depth par.	Shape par.	Max. value (ms^{-1})
EMEX9 meso. updrafts	1.0	0.20	0.30
EMEX9 meso. downdrafts	1.0	0.20	-0.20
PRE-STORM meso. updrafts	1.0	0.50	1.40
PRE-STORM meso. downdrafts	1.0	0.20	-0.30

Table 4.2: Values of shape parameter, depth parameter, and maximum magnitudes of w' in conditionally-sampled mesoscale updrafts and downdrafts of the EMEX9 and PRE-STORM 23-24 June simulations.

θ'	Depth par.	Shape par.	Max. value (K)
EMEX9 meso. updrafts	1.0	0.20	0.30
EMEX9 meso. downdrafts	1.0	0.50	0.60
PRE-STORM meso. updrafts	1.0	0.50	0.05
PRE-STORM meso. downdrafts	1.0	0.50	-0.10

Table 4.3: Values of shape parameter, depth parameter, and maximum magnitudes of θ' in conditionally-sampled mesoscale updrafts and downdrafts of the EMEX9 and PRE-STORM 23-24 June simulations.

q'	Depth par.	Shape par.	Max. value (gkg^{-1})
EMEX9 meso. updrafts	1.0	0.40	0.07
EMEX9 meso. downdrafts	1.0	0.30	-0.07
PRE-STORM meso. updrafts	1.0	0.80	0.50
PRE-STORM meso. downdrafts	1.0	0.80	-0.50

Table 4.4: Values of shape parameter, depth parameter, and maximum magnitudes of q' in conditionally-sampled mesoscale updrafts and downdrafts of the EMEX9 and PRE-STORM 23-24 June simulations.

convergences, however, 5 seems as reasonable a number as any. For the simulated EMEX9 MCS the 1700-1800 UTC mean value of this ratio is 4.1; for the simulated PRE-STORM MCS the 0300-0400 mean value of the ratio is 2.5.

Because the Arakawa-Schubert scheme does not predict cumulus fractional area, this is parameterized following Weissbluth and Cotton (1993). Here, cumulus updraft fractional coverage is parameterized based on observational evidence of the diameter of the updraft core and its associated environment (which is assumed to comprise weaker updrafts as well as any compensating subsidence around the cloud). The area of the core and its associated environment (η) is stratified according to a bulk Richardson number (Weisman and Klemp 1982). The Richardson number, Ri, depends on the convective available potential energy and the mean shear in the lower troposphere:

$$Ri = \frac{g \int \frac{\theta_u - \overline{\theta}}{\overline{\theta}} dz}{\frac{1}{2}\left(\frac{1}{\overline{\rho}\Delta z} \int_0^{6km} \rho \overline{U} dz - \frac{1}{\overline{\rho}\Delta z} \int_0^{0.5km} \rho \overline{U} dz\right)^2}. \tag{4.14}$$

So the maximum fractional updraft core coverage is represented by

$$\sigma_c = \frac{A_{up}}{\eta}, \tag{4.15}$$

where

$$\eta = \frac{2 \times 10^{10}}{Ri} [m^2]. \tag{4.16}$$

The area of the updraft core itself, is parameterized assuming an inverse relationship between cloud radius (r_{up}) and Ri, following Cotton and Anthes (1989):

$$r_{up} = \frac{5 \times 10^3}{\log Ri} [m]. \tag{4.17}$$

Another fairly simple parameterization of cumulus and stratiform cloud fractional coverage is presented by Tiedtke (1993), who develops prognostic equations for the fractional coverage of each cloud type. The fractional area of cumulus clouds and associated anvil cloudiness is parameterized as being proportional to the detrainment of mass from cumulus updrafts. The fractional area of stratiform clouds (assumed to be those formed by non-convective processes) depends on how much of the cloud-free area exceeds saturation in a time step, which in turn depends on the moisture distribution in the cloud-free area and how fast saturation is approached. A similar parameterization for fractional area could be implemented into the present scheme in the future.

Now, having described the construction of the parameterization scheme, in Chapter 5 we turn to evaluation of the scheme.

Chapter 5

SCHEME EVALUATION

5.1 EMEX9 simulation

5.1.1 Thermodynamic

The scheme described in Chapter 3 requires an input sounding of pressure, temperature, moisture, and winds, and then provides as output the vertical profiles of the mesoscale heating rate (shown here as Kd^{-1}), the mesoscale drying rate (shown as $gkgd^{-1}$), and the momentum forcing (shown as ms^{-2}). The scheme will be tested by comparing its output with the diagnosed heating and drying resulting from phase transformations and eddy flux convergences in conditionally-sampled mesoscale updrafts and downdrafts. For EMEX9, the input sounding will be the mean Grid #2 sounding at a given time.

As discussed in Chapter 4, the scheme has been built using conditionally-sampled data from Grid #3 data of the EMEX simulation from 1700-1800 UTC. The scheme, therefore, would be expected to perform very well during this time if we specify the scheme's free parameters based on guidance given by the EMEX9 simulation. Fig. 5.1, then, shows a test of the scheme with an input sounding from 1700 UTC (tests from all times between 1400 and 1800 UTC are shown later in this section). Fig. 5.2 shows the resulting vertical profiles of the diagnosed and parameterized mesoscale heating and drying rates at 1700 UTC. The mesoscale heating and drying rates have the familiar profiles: positive above the freezing level and negative below the freezing level. The maximum heating rate in the parameterized mesoscale updraft is about 8 Kd^{-1}; the maximum cooling rate in the parameterized mesoscale downdraft is about 3 Kd^{-1}. The maximum drying rate in the parameterized mesoscale updraft is 2 $gkgd^{-1}$; the maximum moistening rate in the parameterized mesoscale downdraft is 0.5 $gkgd^{-1}$. By comparison, the maximum parameterized convective heating rate is 55 Kd^{-1} and the maximum parameterized convective drying rate is 36 $gkgd^{-1}$ at this time (not shown). Agreement between the diagnosed and parameterized heating and drying rate profiles is generally very good, although the maximum heating is slightly underpredicted in the parameterized mesoscale updraft and the maximum cooling is slightly overpredicted in the parameterized mesoscale downdraft. Examination of the individual terms reveals that the main source of error in the updraft is the parameterized freezing rate, which reaches a maximum value of only 1 Kd^{-1} in the mesoscale updraft as compared to the diagnosed value of ~ 3.5 Kd^{-1}. However, there are no systematic errors in parameterized freezing rates—at some times the agreement is nearly perfect; at other times freezing is overpredicted.

It is acknowledged that all of the parameters discussed in Chapter 4 vary from one MCS to the next, and even during the life cycle of a particular MCS. These parameters include the depth and shape parameters for the vertical profiles of all phase transformations, the values of water budget parameters a, b, and c given in Table 4.1, and the ratios of (1) the vertically-integrated evaporation to the vertically-integrated

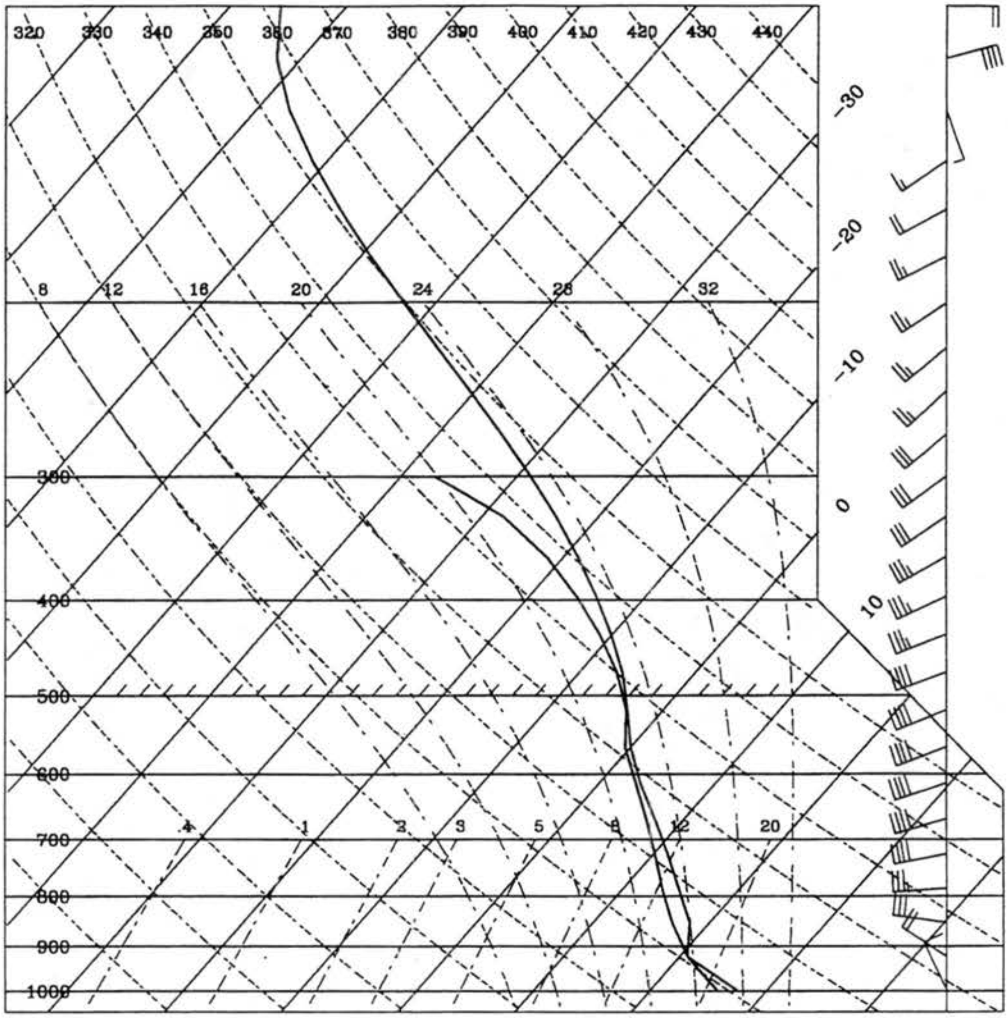

Fig. 5.1: Mean Grid #2 sounding for the EMEX9 simulation at 1700 UTC.

(a)

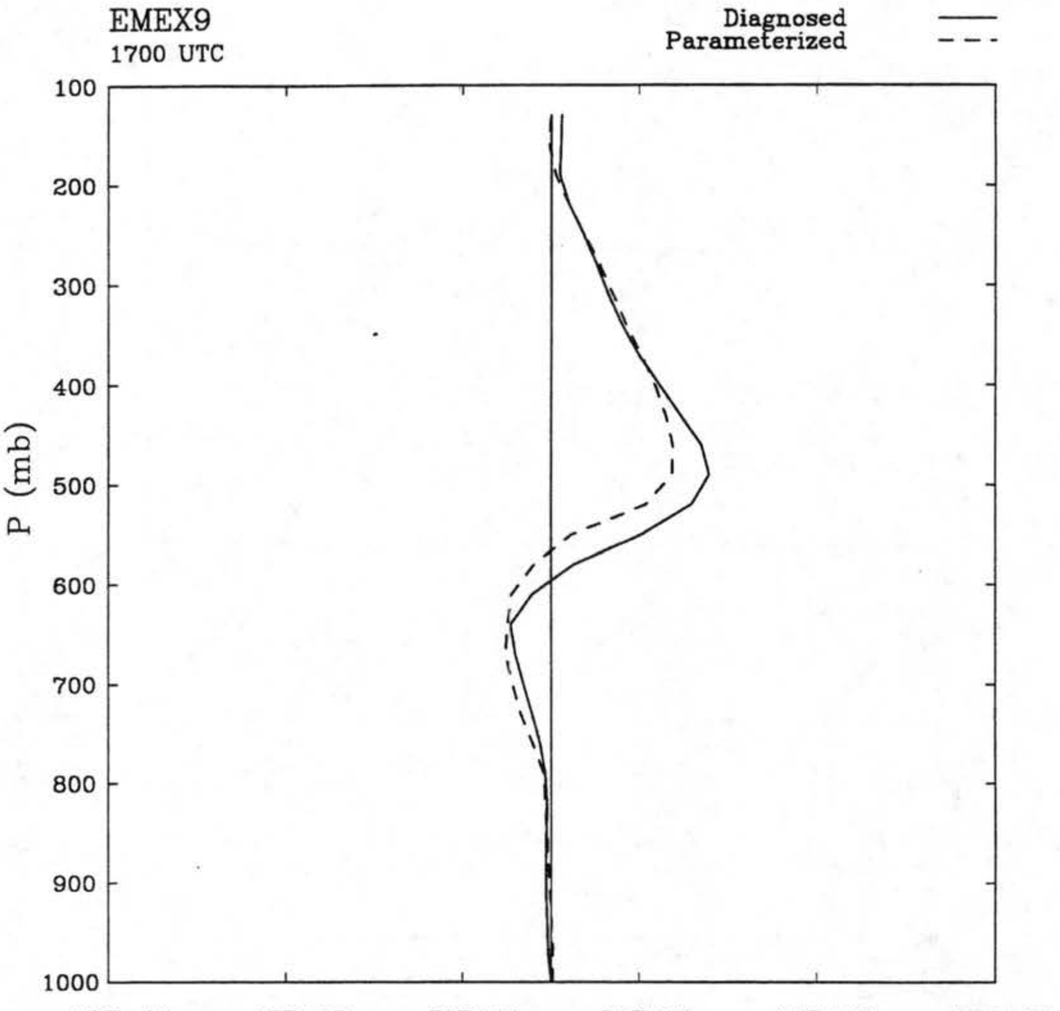
EMEX9
1700 UTC
Diagnosed
Parameterized
P (mb)
100
200
300
400
500
600
700
800
900
1000
−.25E+02
−.15E+02
−.50E+01
.50E+01
.15E+02
.25E+02
Heating (Kd^{-1})

(b)

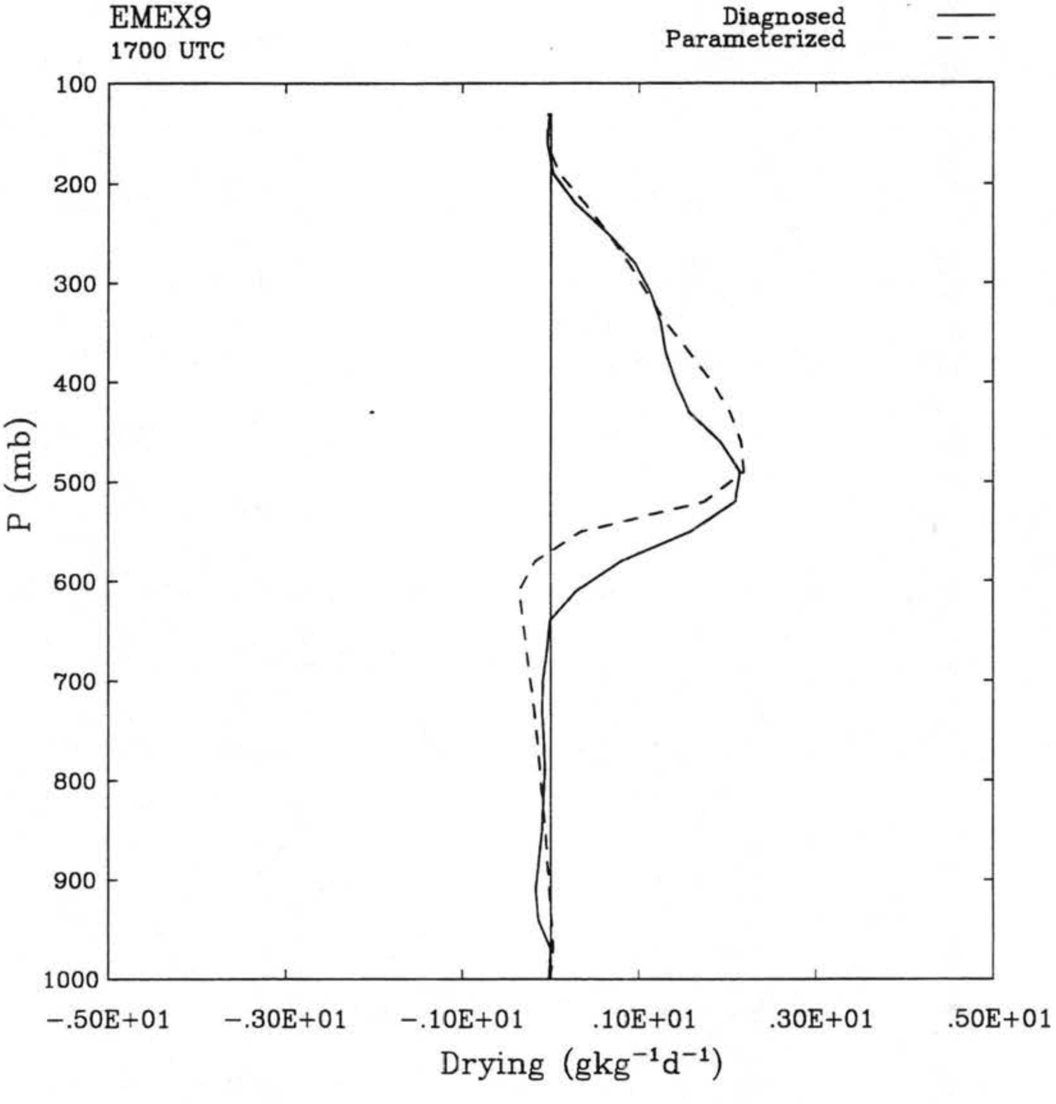

Fig. 5.2: The parameterized and diagnosed (a) heating and (b) drying rates for the EMEX9 simulation at 1700 UTC.

sublimation in mesoscale downdrafts and (2) the vertically-integrated condensation to the vertically-integrated deposition in mesoscale updrafts.

Because the values of all the parameters discussed in Chapter 4 were chosen by examing EMEX9 model output from 1700-1800 UTC, a more rigorous test of the scheme is to use input data from times *other* than 1700-1800 UTC (a *still* more rigorous test is discussed in section 5.2.1). Figs. 5.3 and 5.4 show a comparison of diagnosed and parameterized heating and drying rates, respectively, for 1400-1800 UTC. These results show that the parameterization performs well for the entire four hour period. In particular, the parameterization is able to reproduce the maximum values of heating and drying diagnosed at 1400, 1700, and 1745 UTC. The only systematic errors which appear in Figs. 5.3 and 5.4 are slightly overestimated cooling and moistening in mesoscale downdrafts. Although the magnitude of the errors is quite small ($\sim$ 0.5 $\mathrm{Kd^{-1}}$ too much cooling and $\sim$ 0.1-0.2 $\mathrm{gkg^{-1}d^{-1}}$ too much moistening), these errors appear over a layer about 200 mb deep in the mesoscale downdraft (see Fig. 5.2, for instance).

5.1.2 Momentum

The input momentum sounding to the parameterization is also the mean Grid #2 sounding. The parameterization is tested with and without the convective-scale horizontal pressure gradient force. Wu and Yanai (1994) show that the pressure gradient force can be important if the convection is linear. In that case, the pressure gradient force can impact the line-normal component of the momentum budget. The results of the parameterization are then compared with the diagnosed momentum

(a)

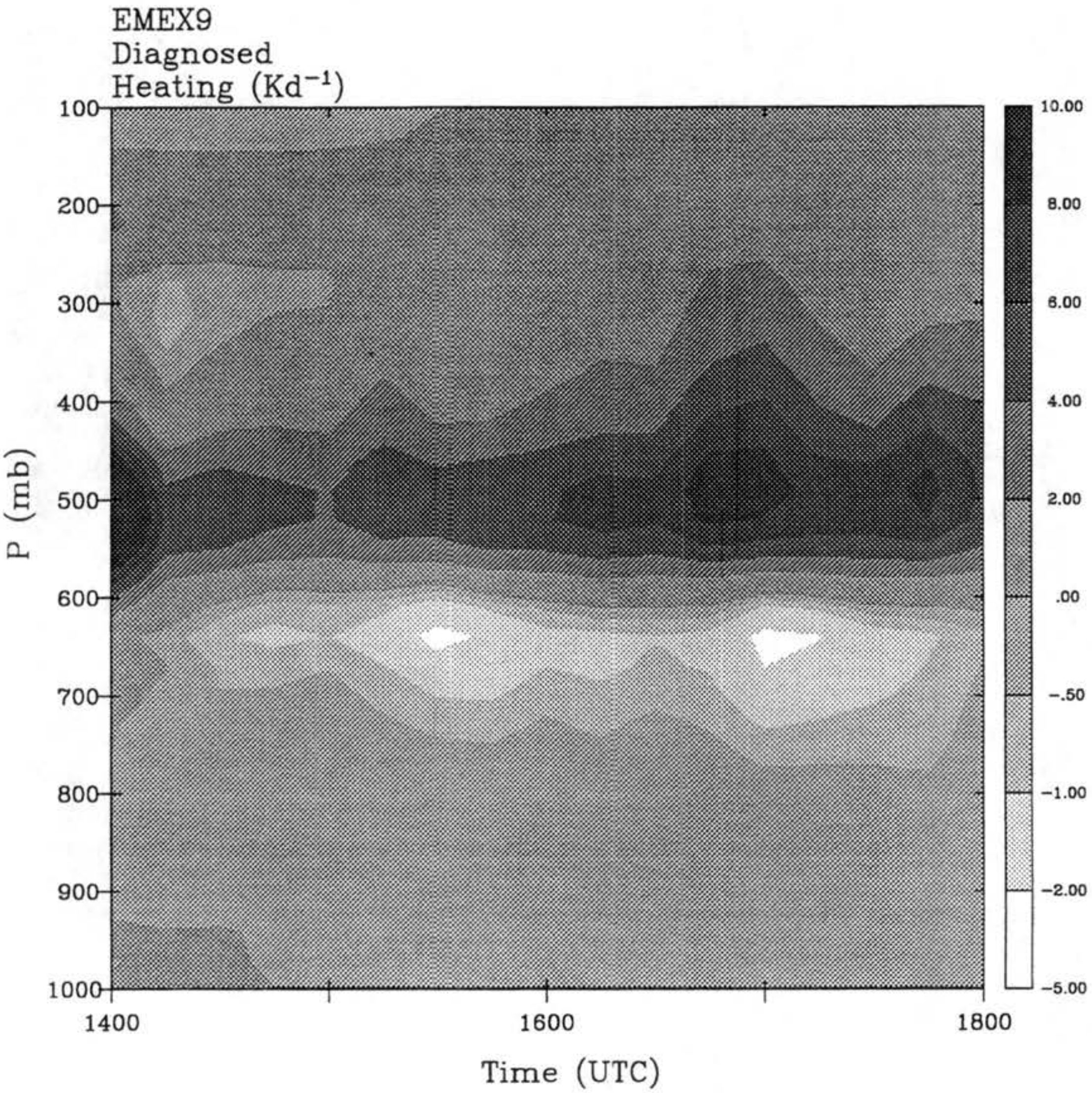
EMEX9
Diagnosed
Heating (Kd^{-1})
100
200
300
400
500
600
700
800
900
1000
P (mb)
1400
1600
1800
Time (UTC)
10.00
8.00
6.00
4.00
2.00
.00
-.50
-1.00
-2.00
-5.00

(b)

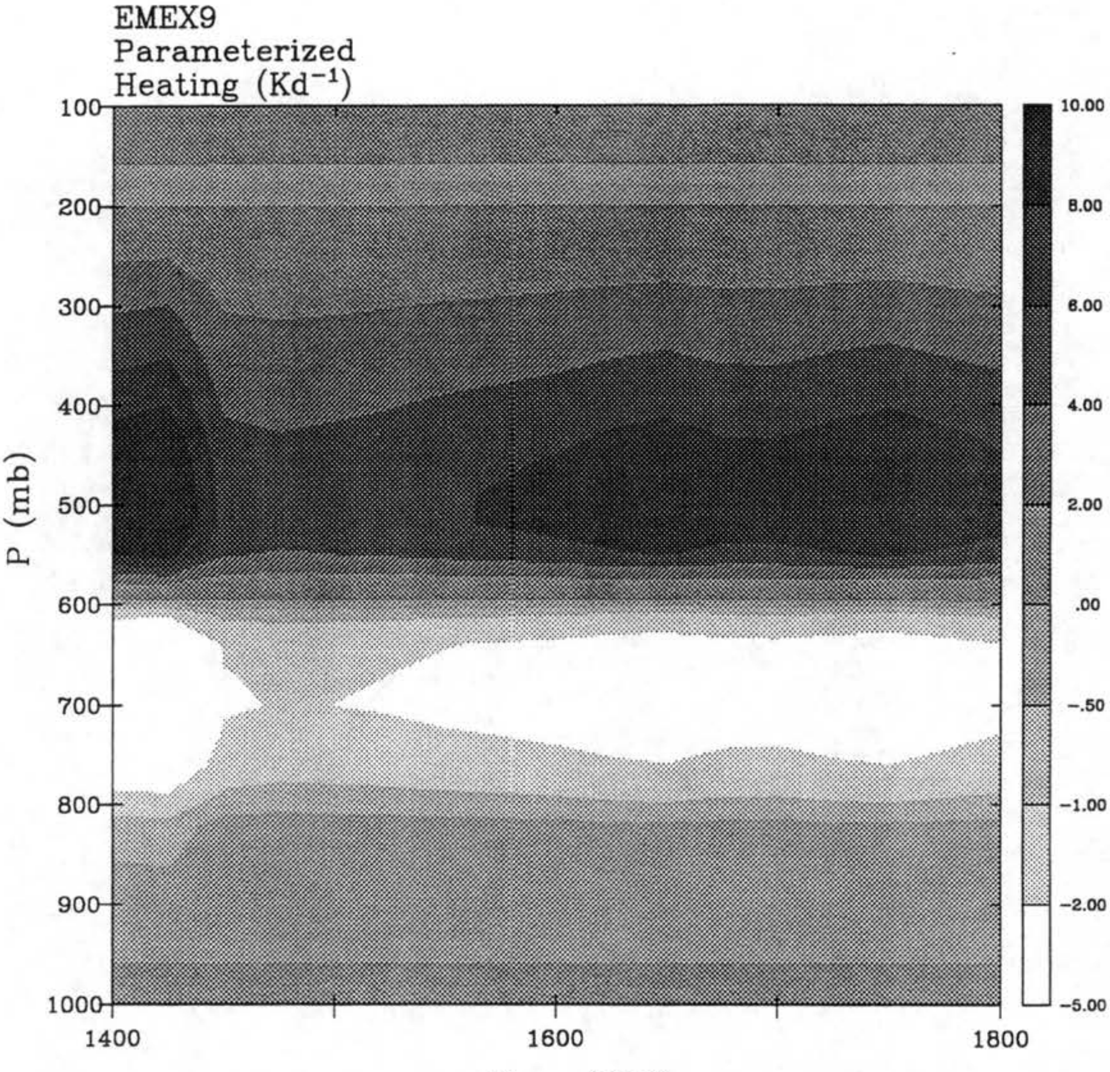

Fig. 5.3: The (a) diagnosed and (b) parameterized heating rates for the EMEX9 simulation between 1400 and 1800 UTC.

(a)

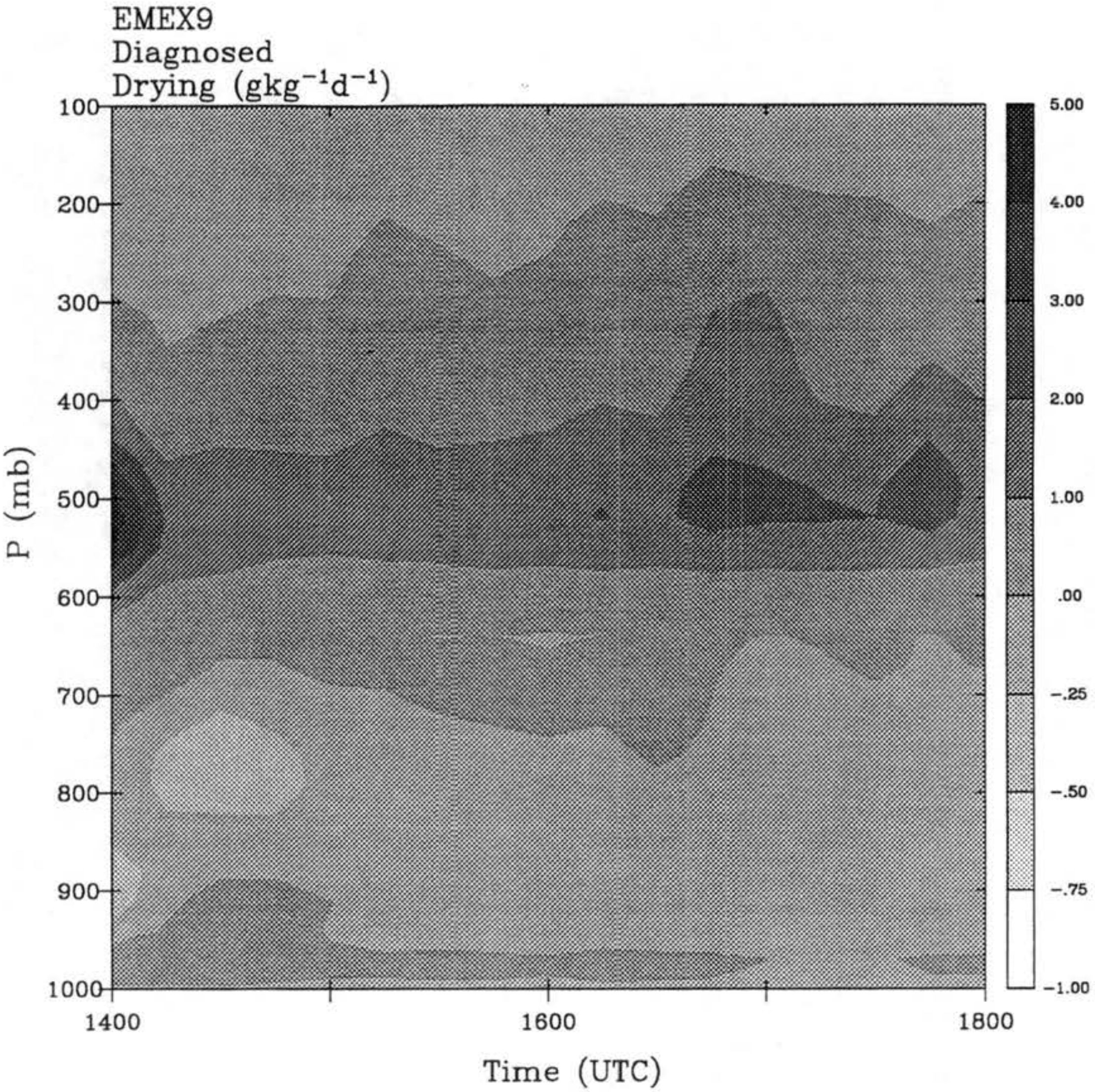
EMEX9
Diagnosed
Drying ($gkg^{-1}d^{-1}$)
100
200
300
400
500
600
700
800
900
1000
P (mb)
1400
1600
1800
Time (UTC)
5.00
4.00
3.00
2.00
1.00
.00
-.25
-.50
-.75
-1.00

(b)

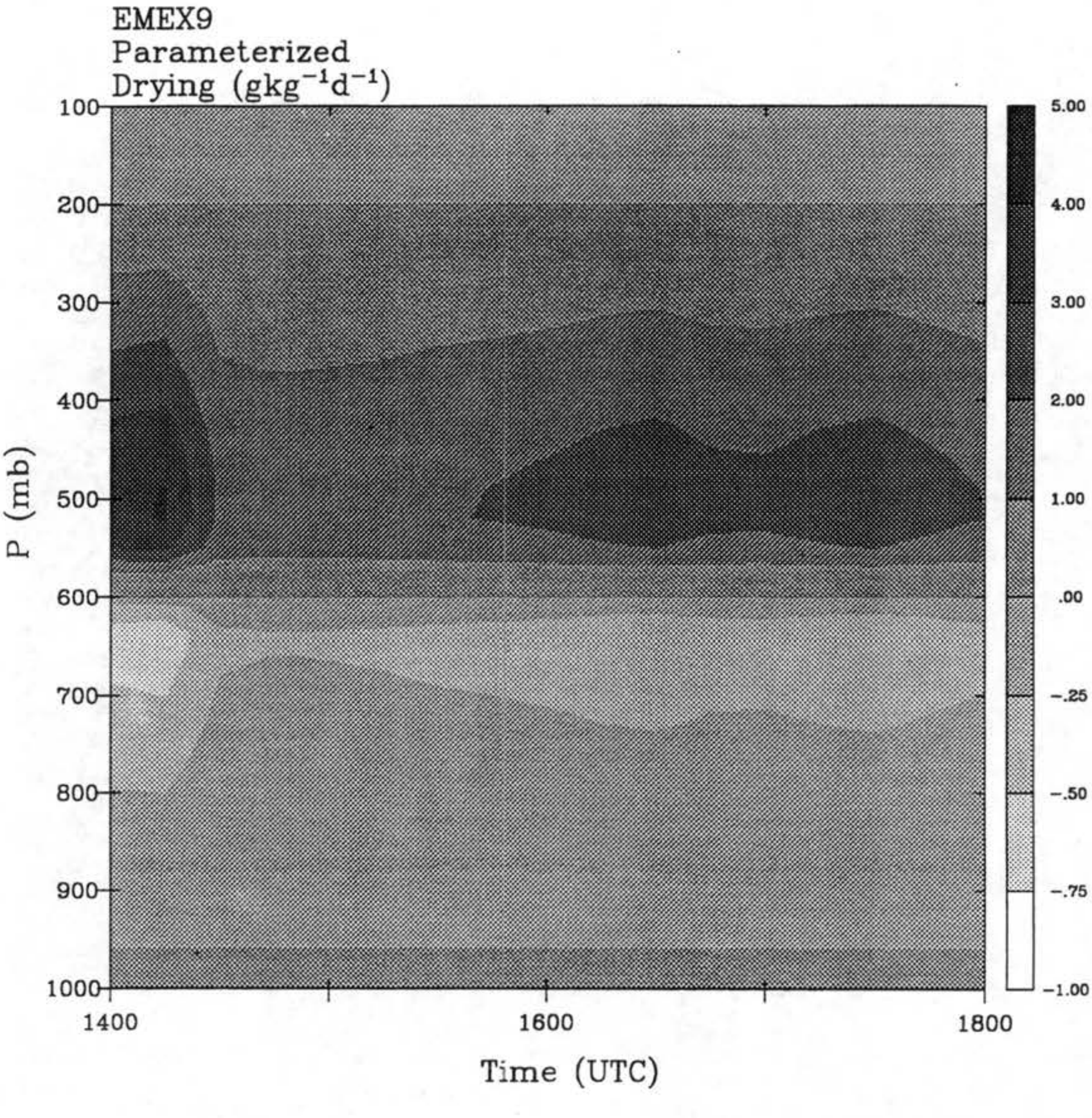

Fig. 5.4: The (a) diagnosed and (b) parameterized drying rates for the EMEX9 simulation between 1400 and 1800 UTC.

budget residual, **F**, which represents the acceleration of the mean flow due to the eddy correlation terms. Following Wu and Yanai (1994), the momentum budget equation for the mean flow may be written as

$$\mathbf{F} \equiv \frac{\partial \overline{\mathbf{v}}}{\partial \mathbf{t}} + \overline{\mathbf{v}} \cdot \nabla \overline{\mathbf{v}} + \overline{\omega} \frac{\partial \overline{\mathbf{v}}}{\partial \mathbf{p}} + \nabla \overline{\phi} + \mathbf{fk} \times \overline{\mathbf{v}} = -\nabla \cdot \overline{\mathbf{v}'\mathbf{v}'} - \frac{\partial}{\partial \mathbf{p}} \overline{\mathbf{v}'\omega'}, \qquad (5.1)$$

where **v** is the horizontal velocity, ω is the vertical p velocity, ϕ the geopotential, and f the Coriolis parameter. An overbar denotes resolvable (or mean) components and a prime expresses unresolvable (or eddy) components. The two terms on the right-hand side of (5.1) may be computed for the MCS simulations to obtain a value for the momentum budget residual **F**. The momentum budget residual will be computed for Grid #2, with the perturbation quantities computed as perturbations from Grid #2 means.

As discussed in Chapter 2, the momentum budget residual resulting from convective drafts far exceeds that resulting from mesoscale drafts. For example, for Grid #3 of the EMEX9 simulation for 1700-1800 UTC, the maximum magnitude of the zonal momentum budget residual for mesoscale drafts at any level is $\sim 0.10 \times 10^{-3}$ ms^{-2} compared to a maximum magnitude of $\sim 0.60 \times 10^{-3}$ ms^{-2} for convective drafts (Fig. 5.5). Note, however, that there is still a significant portion of the momentum budget residual that is unexplained by either convective drafts or the mesoscale flow branches. This residual is especially large above 300 mb. A similar result holds for the PRE-STORM simulation. Thus, it appears that circulations separate from either convective drafts or mesoscale flow branches, such as gravity waves, are responsible for significant momentum accelerations in MCSs. Previous studies have shown the importance of convectively-triggered gravity waves to the redistribution of heat and moisture (e.g., Bretherton and Smolarkiewicz 1989); it appears they same may be true for momentum.

The momentum of all predicted convective subensembles is needed to parameterize horizontal momentum tendencies, as shown in equation (2.12). Each component of momentum is computed by applying equations (2.17) and (2.18) to each subensemble. Fig. 5.6 shows the resulting cloud momentum for all of the predicted subensemble updrafts computed by the parameterization at 1700 UTC along with the zonal and meridional components of the observed environmental wind. The deepest subensembles nearly maintain the cloud base momentum through their depth whereas the shallower subensembles approach the environmental momentum.

The momentum parameterization may be run with or without the pressure gradient force acceleration term (see Section 2.3). First, the results are shown for no pressure gradient force acceleration (i.e., entrainment-detrainment only). For this case, Fig. 5.7 shows the parameterized momentum acceleration and the diagnosed momentum budget residual at 1700 UTC. The parameterization predicts virtually no momentum acceleration below 500 mb. In the cloud model used here, detrainment occurs only at cloud top, and the shallowest cloud predicted by the cloud model has a cloud top at 540 mb. As a result, the cloud-top detrainment term is zero below 540 mb. Although the term that accounts for the subsidence of environmental air which compensates convective mass flux is not zero below 500 mb, it is nonetheless

(a)

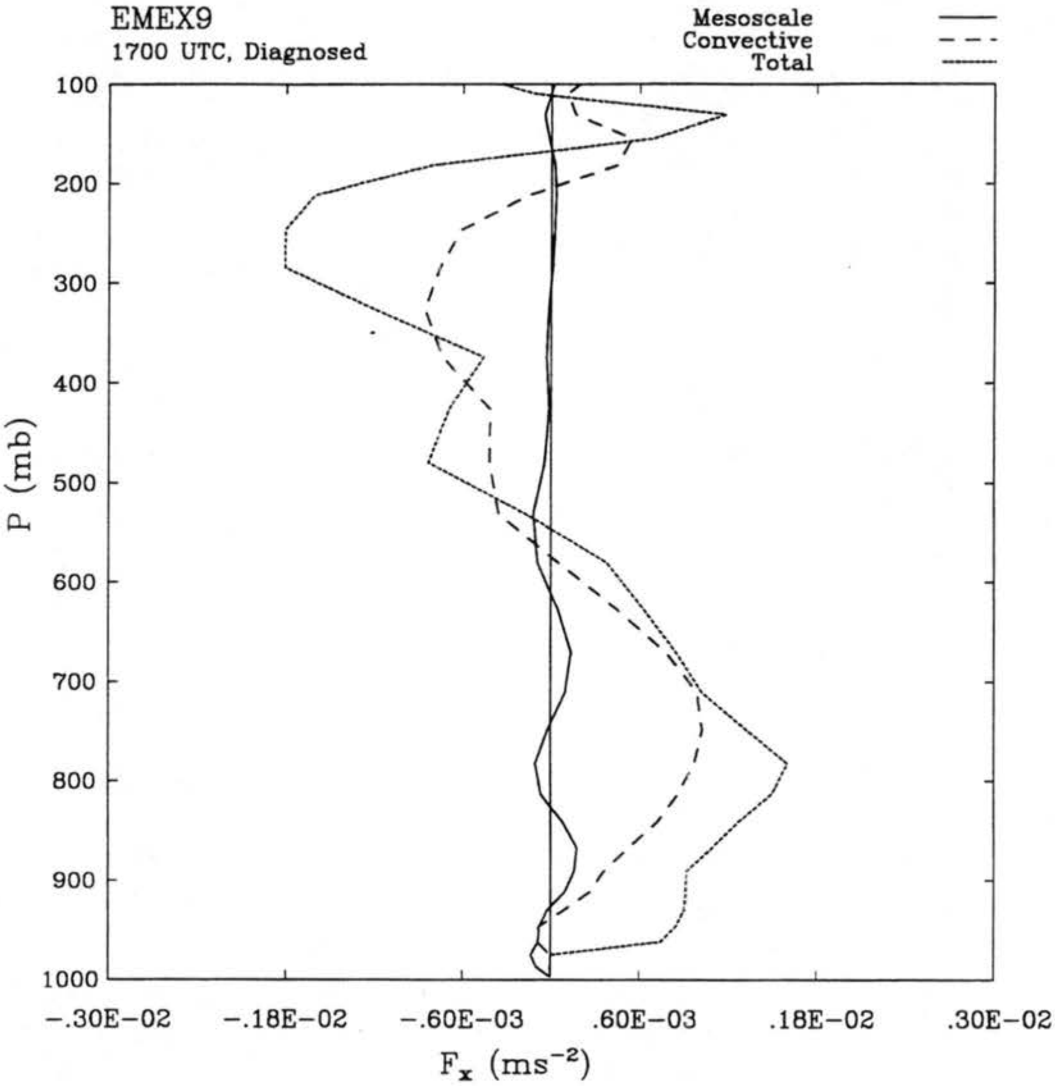
EMEX9
1700 UTC, Diagnosed
Mesoscale
Convective
Total
100
200
300
400
500
600
700
800
900
1000
P (mb)
−.30E−02
−.18E−02
−.60E−03
.60E−03
.18E−02
.30E−02
F_x (ms^-2)

(b)

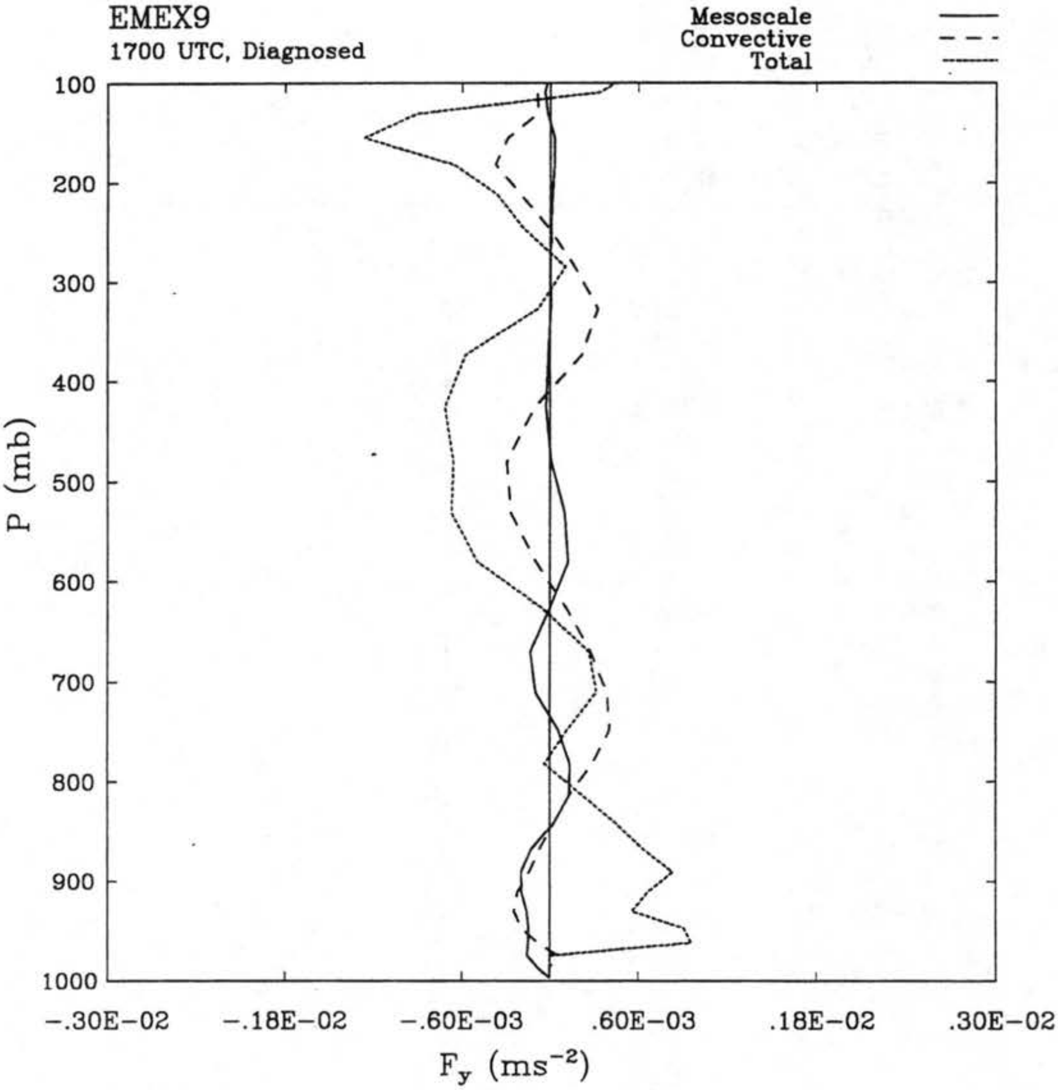

Fig. 5.5: Vertical profiles of the diagnosed (a) zonal and (b) meridional momentum budget residual on Grid #3 of the EMEX9 simulation at 1700 UTC for conditionally sampled convective drafts, mesoscale drafts, and for all grid points.

(a)

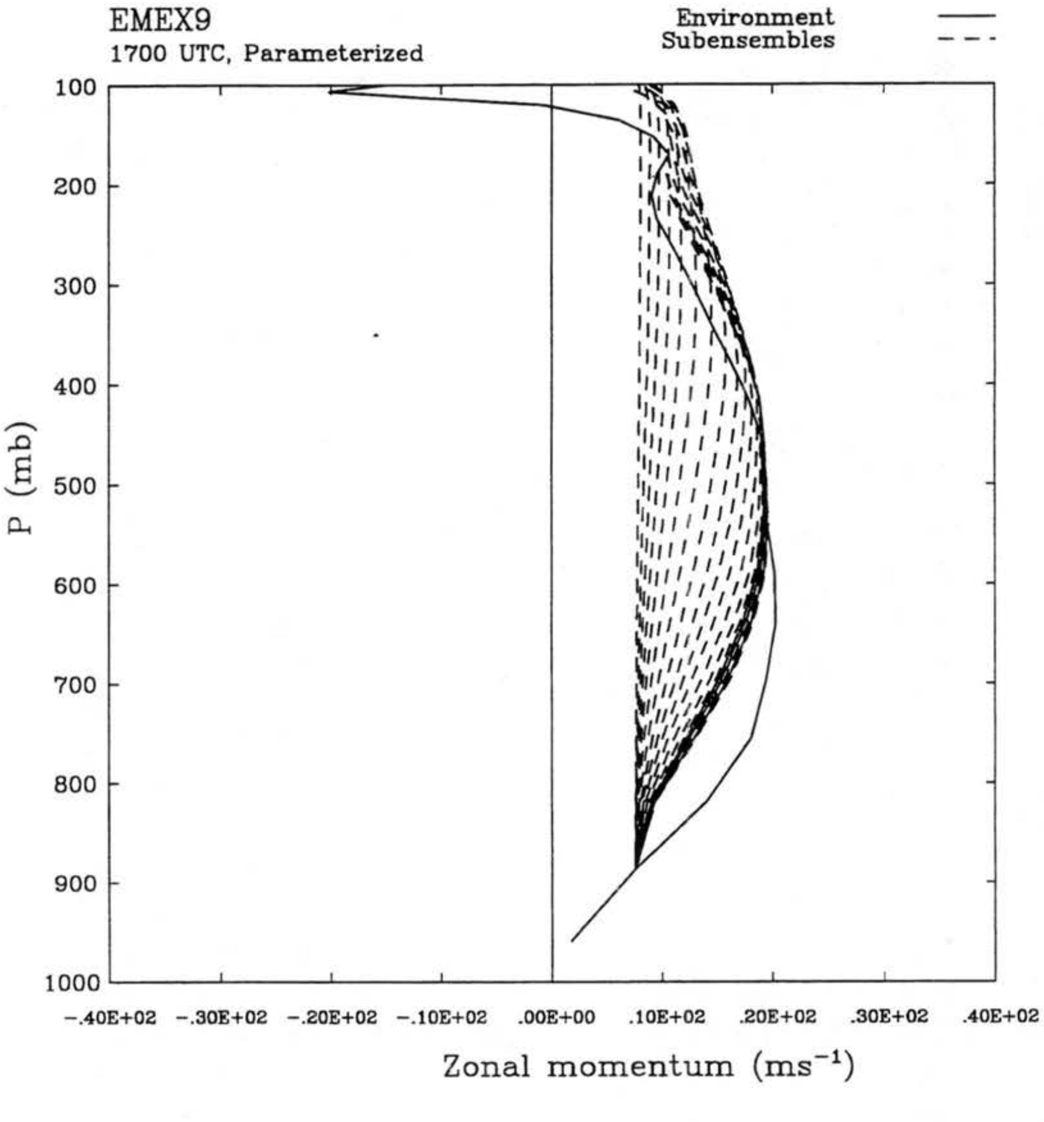
EMEX9
1700 UTC, Parameterized
Environment
Subensembles
100
200
300
400
500
600
700
800
900
1000
P (mb)
-.40E+02
-.30E+02
-.20E+02
-.10E+02
.00E+00
.10E+02
.20E+02
.30E+02
.40E+02
Zonal momentum (ms^{-1})

(b)

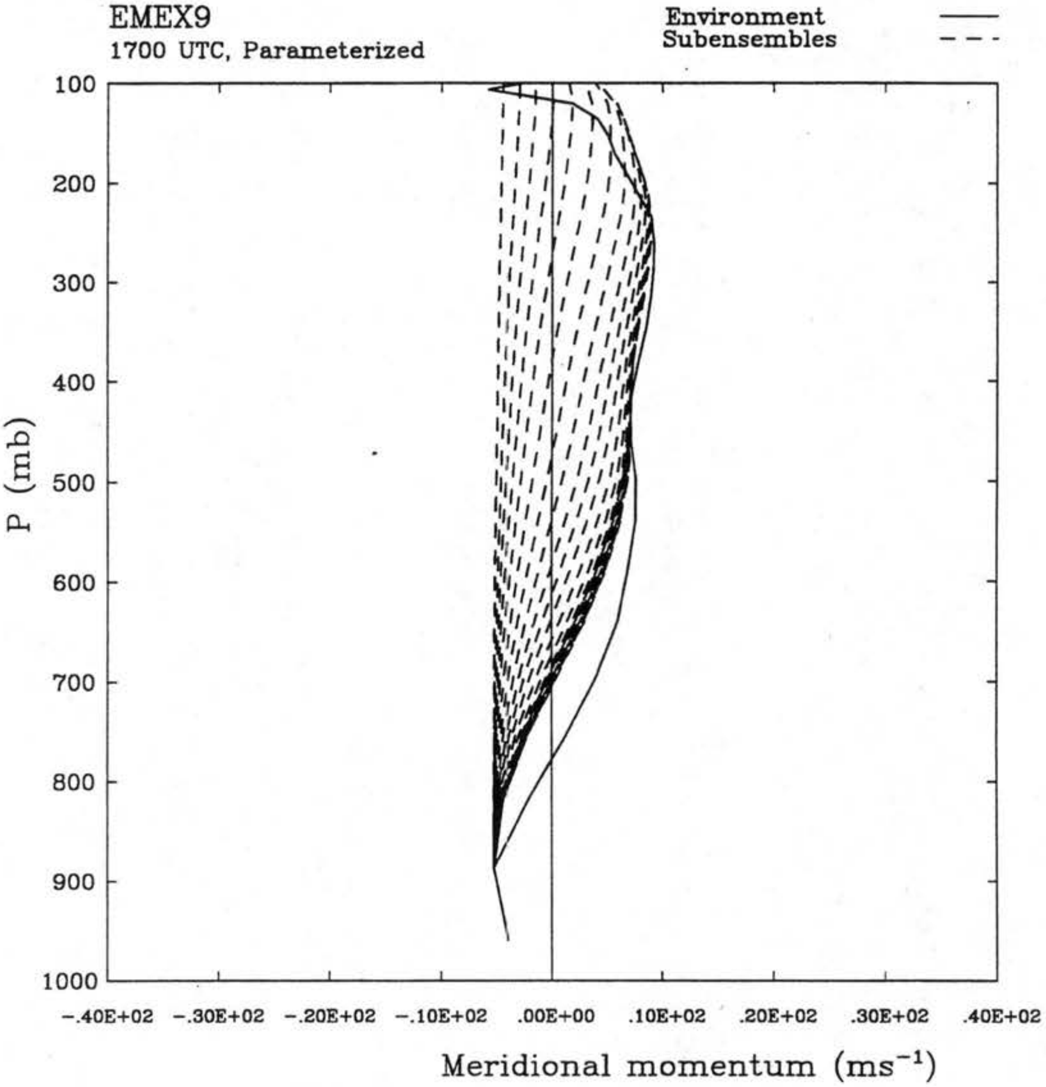

Fig. 5.6: Vertical profiles of environmental wind (solid) and the cloud momentum of all subensembles (dashed) as predicted by the momentum parameterization at 1700 UTC for (a) zonal momentum and (b) meridional momentum.

an order of magnitude smaller than any of the terms in the upper troposphere. The diagnosed momentum budget residuals below 500 mb suggest that the momentum parameterization has performed poorly here. Above 500 mb, however, the momentum parameterization performs much more satisfactorily. The parameterized zonal wind decelerates between 500 and 250 mb and accelerates between 250 and 200 mb. The parameterized meridional wind accelerates between 400 and 300 mb and decelerates between 300 and 200 mb. All of these features are reproduced in the diagnosed budget residuals. The maximum magnitudes of the wind accelerations depicted in Fig. 5.6 are $\sim 10^{-3}$ $\mathrm{ms^{-2}}$, or about 100 $\mathrm{ms^{-1}d^{-1}}$.

Convection in the EMEX9 MCS initially maintains a quasi-linear structure (see Fig. 3.11), suggesting that including the pressure-gradient acceleration term in the momentum parameterization may improve the results. This is not the case, however. Although, as shown in Fig. 3.13, there *is* a strong front-to-rear directed pressure gradient force across the convective line in the upper troposphere, its spatial scale is small enough that it is nearly cancelled out by two flanking regions of rear-to-front directed pressure gradient accelerations. A vertical profile of the Grid #2 mean line-normal pressure gradient force at 1700 UTC shows it to be very small ($\sim 2 \times 10^{-4}$ $\mathrm{ms^{-2}}$) compared to the observed line-normal momentum budget residual on Grid #2 (Fig. 5.8a). In fact, at 1800 UTC, when the convection has essentially lost its linear orientation, the Grid #2 mean line-normal pressure gradient force is nearly zero through almost all of the troposphere (Fig. 5.8b). Figs. 3.13 and 5.8b both indicate that the simulated MCS fails to develop a dipole pressure perturbation field on a

(a)

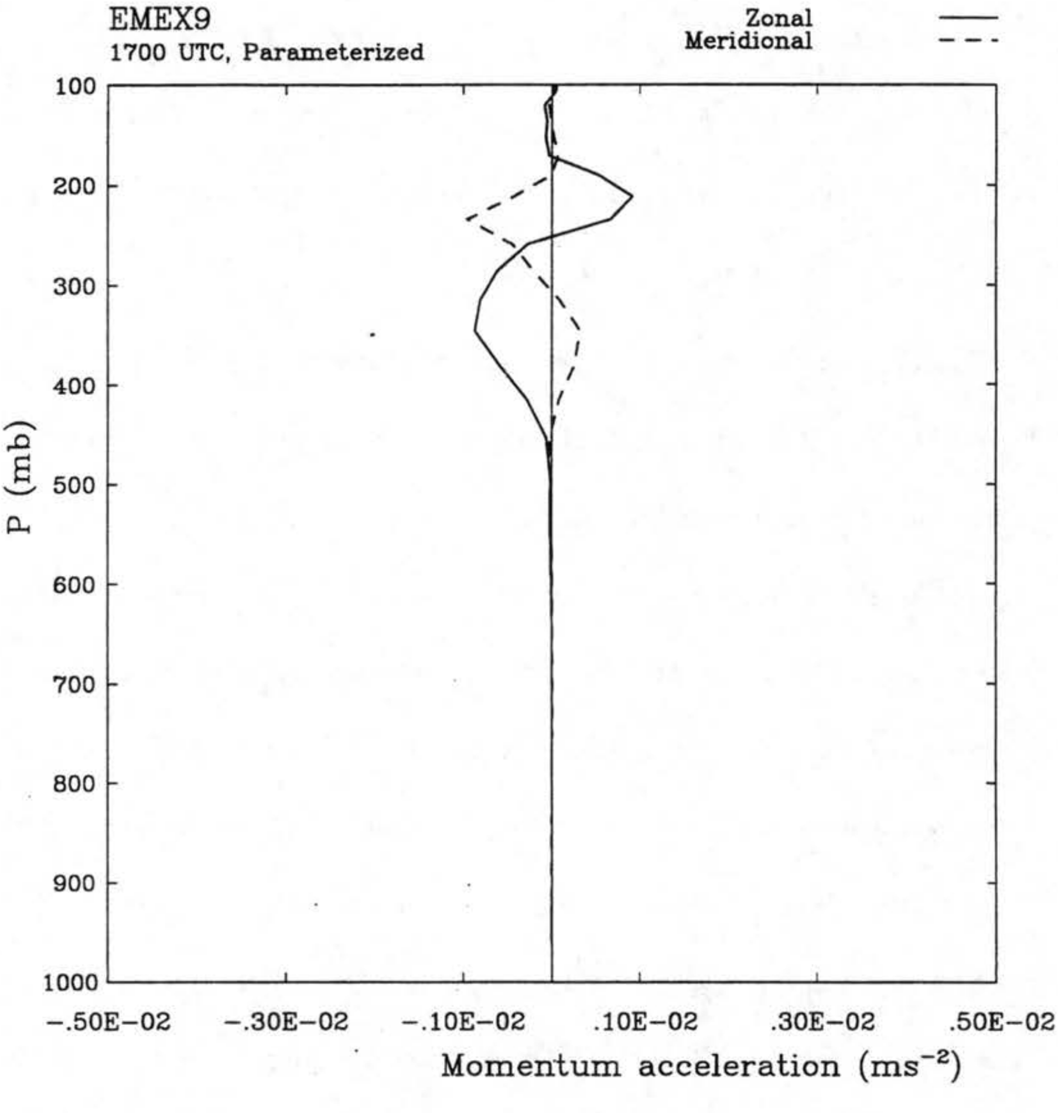

EMEX9
1700 UTC, Parameterized
Zonal
Meridional
100
200
300
400
500
600
700
800
900
1000
P (mb)
-.50E-02
-.30E-02
-.10E-02
.10E-02
.30E-02
.50E-02
Momentum acceleration (ms^{-2})

(b)

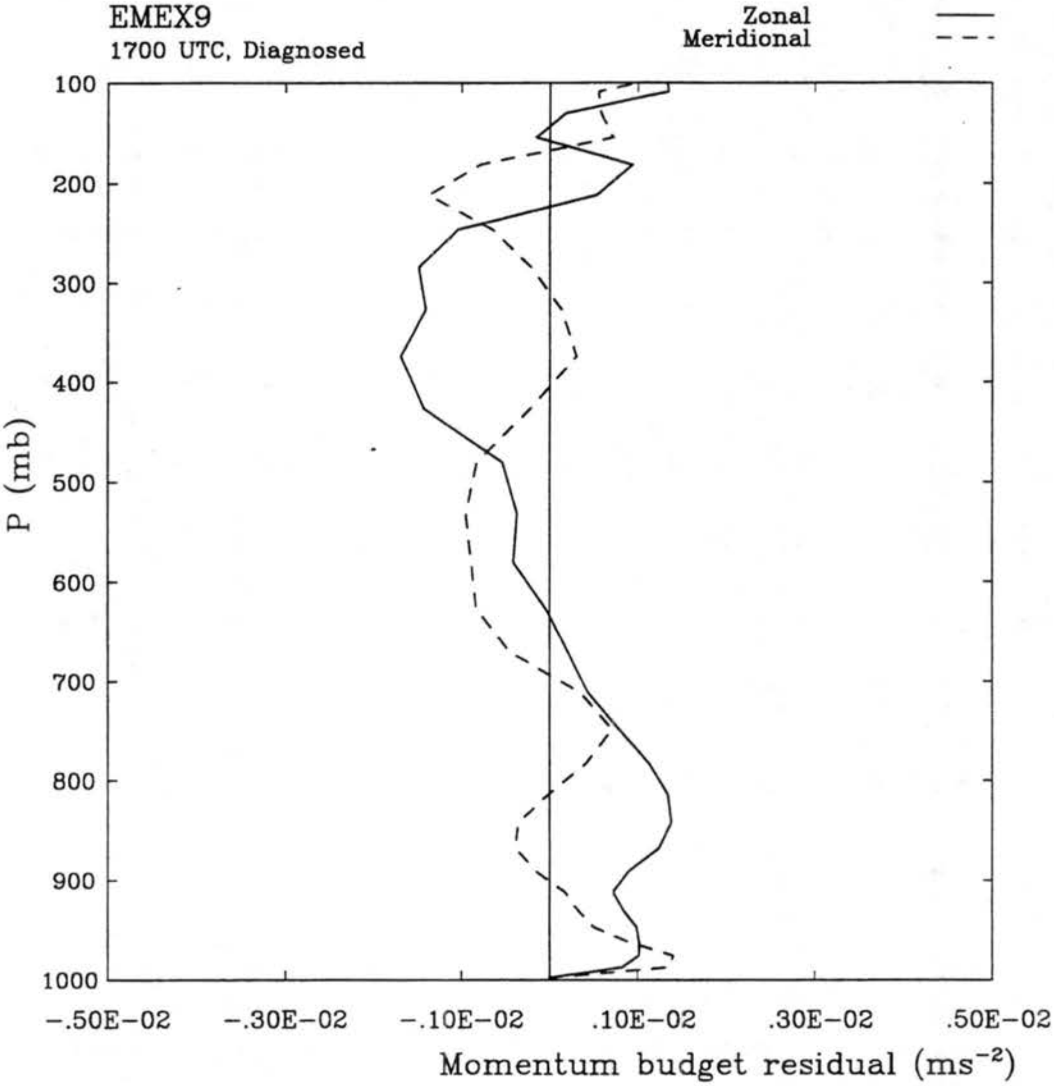

Fig. 5.7: Vertical profiles of (a) the parameterized zonal and meridional momentum acceleration and (b) the diagnosed momentum budget residual of zonal and meridional momentum at 1700 UTC.

spatial scale larger than the analysis grid (Grid #2). Thus, for EMEX9, including the convective-scale pressure gradient acceleration term in the momentum parameterization yields spurious accelerations in the upper troposphere. The results above suggest that in a situation in which the perturbation pressure field associated with an MCS is of a small enough scale compared to a GCM grid box, the pressure gradient force directed across the system could be effectively cancelled out *in the mean* by a corresponding region of oppositely-directed pressure gradient force. In practice, then, the pressure gradient acceleration term should be parameterized with caution. Still, in some cases (e.g., the PRE-STORM 23-24 June MCS, as described below), including the pressure gradient term does improve the results of the momentum parameterization. The differing behavior of the two simulated MCSs in this regard can be interpreted in the context of their spatial scale relative to the Rossby radius of deformation (see discussion in Section 6.1).

5.2 PRE-STORM simulation

5.2.1 Thermodynamic

For PRE-STORM, as for EMEX9, the input sounding for each time will be the mean Grid #2 sounding. The scheme has been built using conditionally-sampled data from Grid #3 data of the PRE-STORM simulation from 0300-0400 UTC. We first test the scheme with an input sounding from 0400 UTC (Fig. 5.9). Fig. 5.10 shows the resulting vertical profiles of the parameterized mesoscale heating and drying rates at 0400 UTC. The agreement between the parameterized and diagnosed profiles is generally good. In the mesoscale updraft, the parameterized heating and drying are

(a)

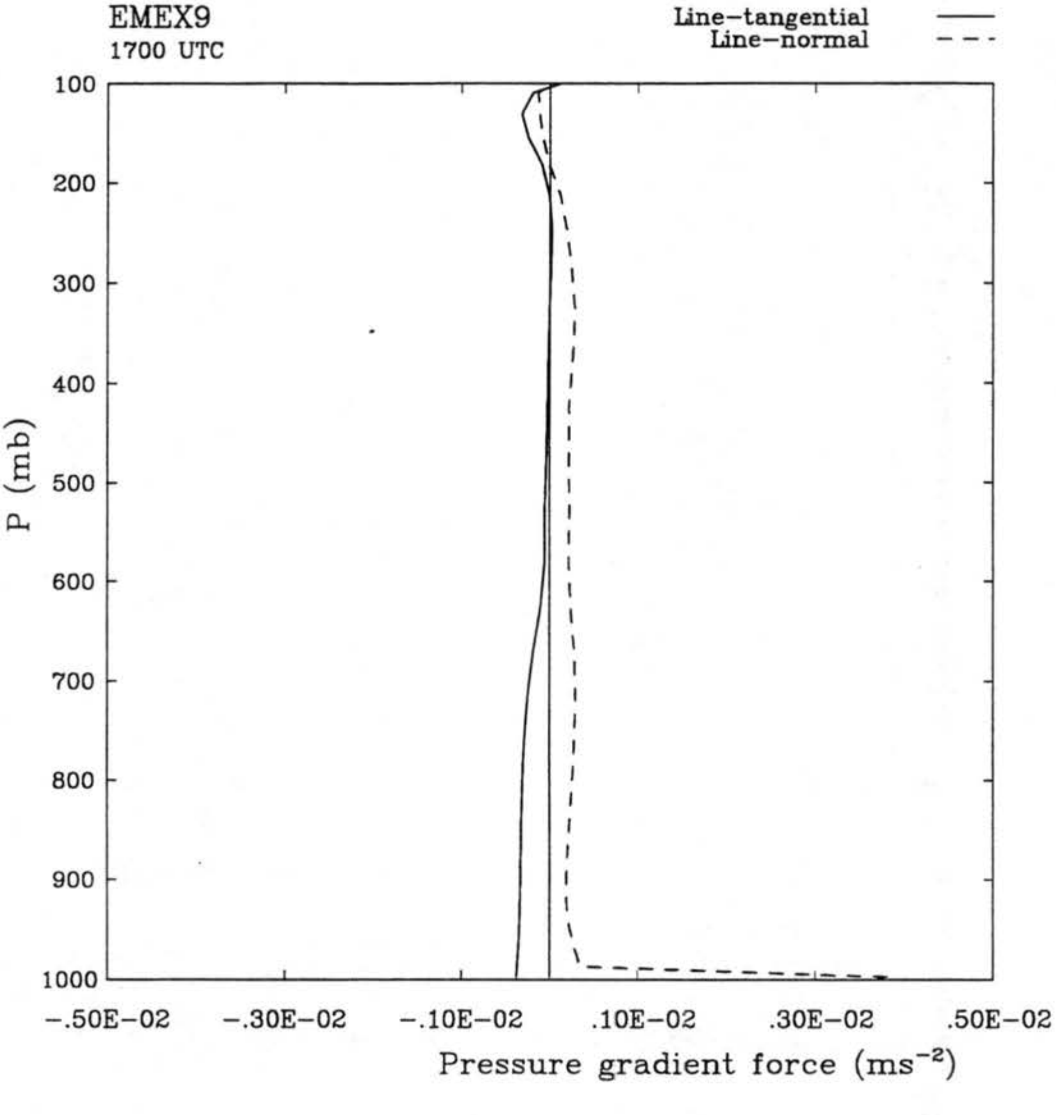
EMEX9
1700 UTC
Line–tangential
Line–normal
P (mb)
100
200
300
400
500
600
700
800
900
1000
–.50E–02
–.30E–02
–.10E–02
.10E–02
.30E–02
.50E–02
Pressure gradient force (ms^{-2})

(b)

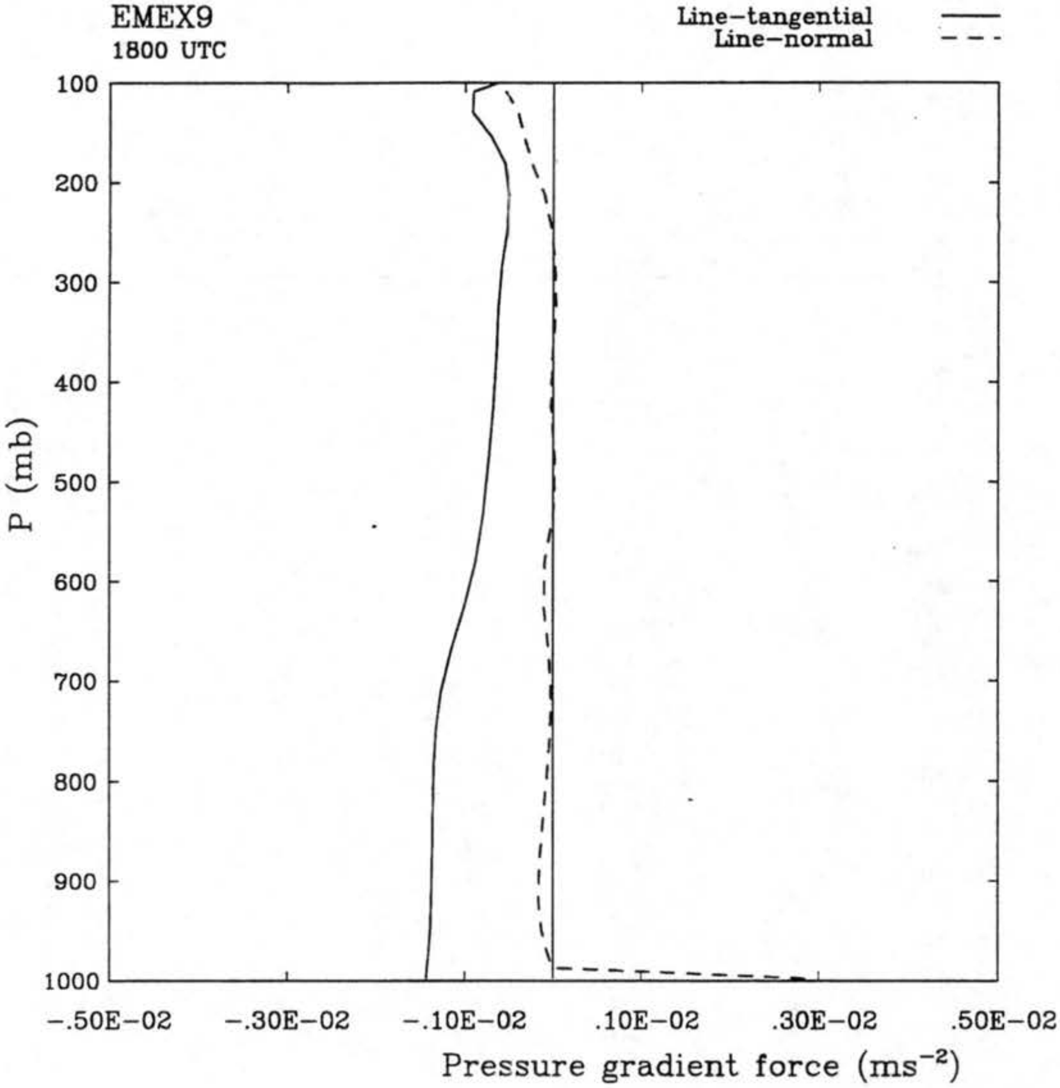

Fig. 5.8: Vertical profiles of the EMEX9 Grid #2 mean line-normal and line-tangential pressure gradient force at (a) 1700 UTC and (b) 1800 UTC. A positive line-normal pressure gradient force represents acceleration from front-to-rear. A positive line-tangential pressure gradient force represents acceleration from left-to-right as seen from ahead of the line.

both slightly underpredicted. This error results primarily from the deposition rate being underpredicted. In the mesoscale downdraft, the cooling is slightly overpredicted and the moistening is displaced too high. Both of the latter errors result primarily from an overestimation of the melting rate in the mesoscale downdraft.

The parameterized mesoscale heating and drying tendencies for the PRE-STORM simulation account for a smaller fraction of the total heating and drying tendencies than for EMEX9. The maximum heating rate in the parameterized mesoscale updraft is about 10 Kd^{-1}; the maximum cooling rate in the parameterized mesoscale downdraft is about 3.8 Kd^{-1}. The maximum drying rate in the parameterized mesoscale updraft is 5.0 $gkgd^{-1}$; the maximum moistening rate in the parameterized mesoscale downdraft is 1.0 $gkgd^{-1}$. By comparison, the maximum parameterized convective heating rate is 165 Kd^{-1} and the maximum parameterized convective drying rate is 34 $gkgd^{-1}$ at this time (not shown). Thus, although the absolute magnitudes of the mesoscale heating and drying are about the same for EMEX9 and PRE-STORM, their magnitudes relative to the convective heating and drying are greater for EMEX9. These results are consistent with those of Wu (1993). He found for instance, that for six PRE-STORM observation times, the maximum magnitude of mesoscale heating was about 17 Kd^{-1} compared to a maximum magnitude of convective heating of about 125 Kd^{-1} (his Figs. 21-23). For six GATE observation times, on the other hand, Wu (1993) found a maximum mesoscale heating rate of 4 Kd^{-1} versus a maximum convective heating rate of 15 Kd^{-1}.

As for EMEX9, the scheme is also tested for times prior to the hour for which the

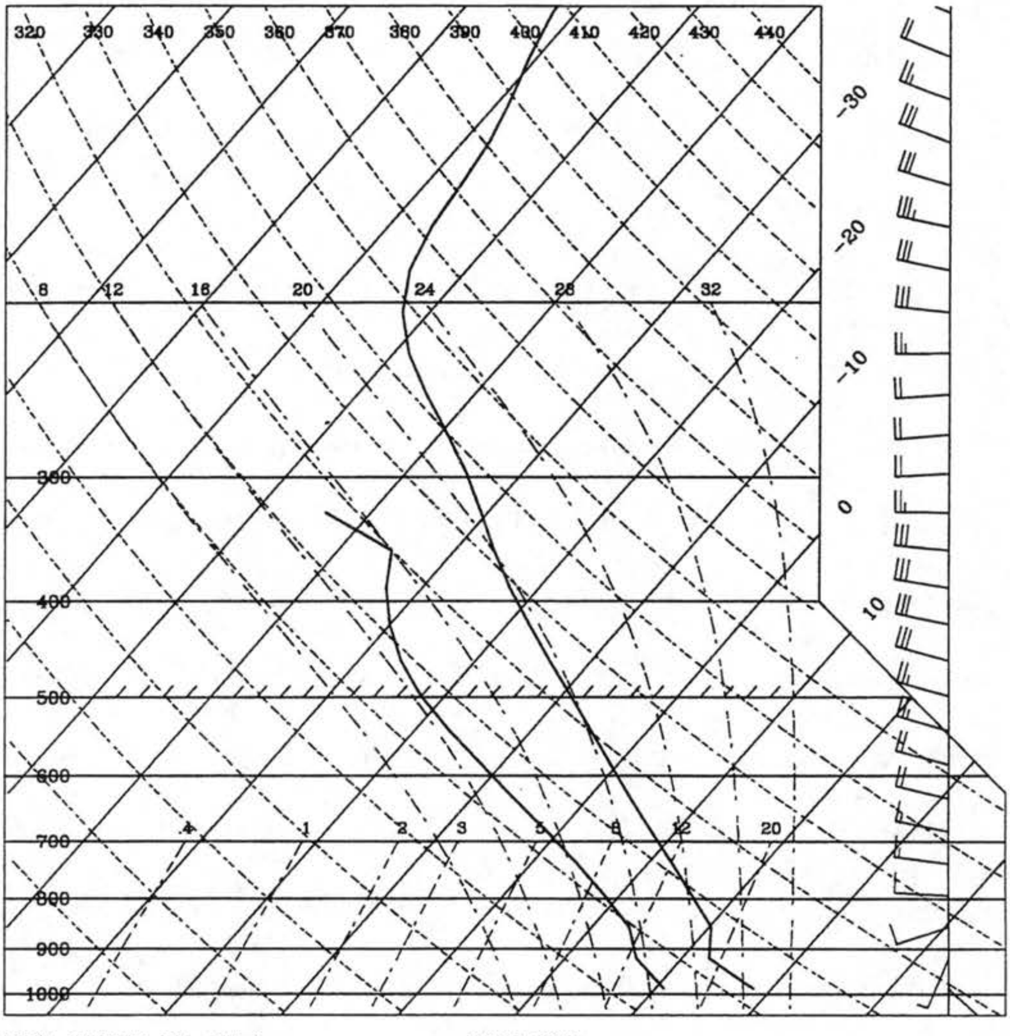

Fig. 5.9: Mean Grid #2 sounding for the PRE-STORM 24-24 June simulation at 0400 UTC.

(a)

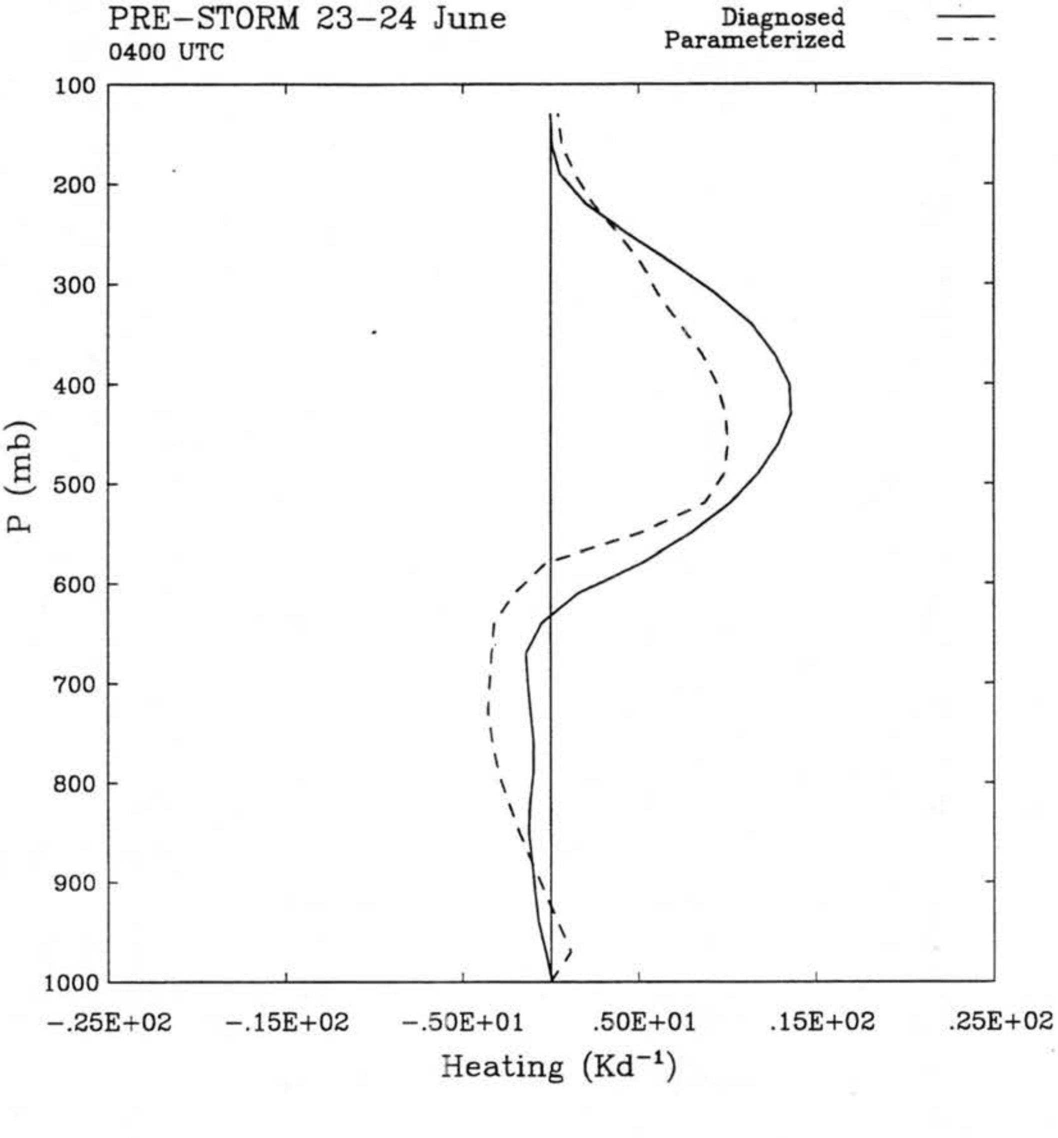
PRE-STORM 23-24 June
0400 UTC
Diagnosed
Parameterized
P (mb)
100
200
300
400
500
600
700
800
900
1000
-.25E+02
-.15E+02
-.50E+01
.50E+01
.15E+02
.25E+02
Heating (Kd^{-1})

(b)

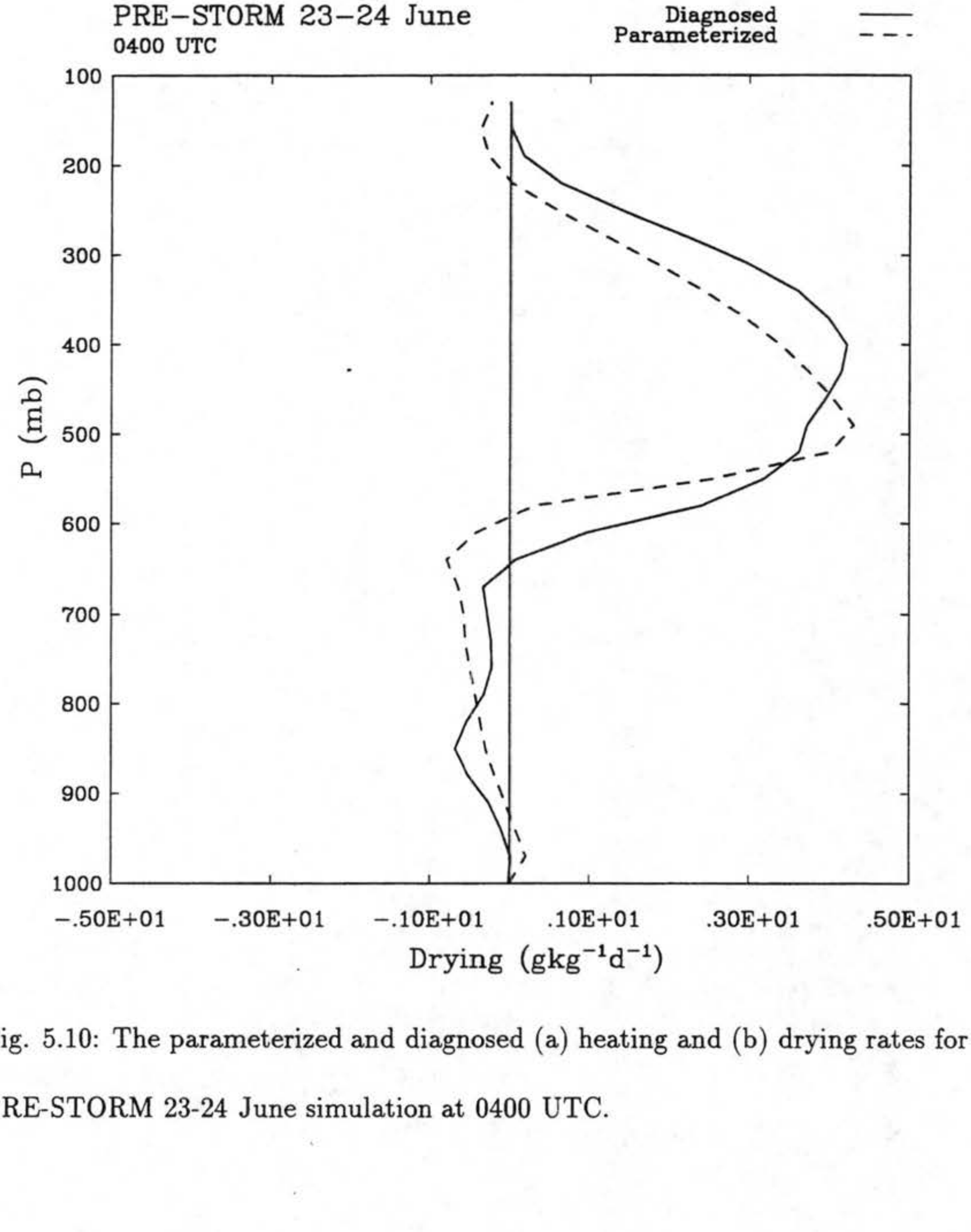

Fig. 5.10: The parameterized and diagnosed (a) heating and (b) drying rates for the PRE-STORM 23-24 June simulation at 0400 UTC.

parameters described in Chapter 4 were determined. Fig. 5.11 shows the diagnosed and parameterized heating rates for the PRE-STORM simulation for between 0100 and 0400 UTC. Fig. 5.12 shows the diagnosed and parameterized drying rates for the PRE-STORM simulation for between 0100 and 0400 UTC. Compared to EMEX9, the parameterized heating and drying rates show relatively little variation with time.

As discussed above, the values of all parameters determined through conditional sampling would be expected to vary among different MCSs, and throughout the life cycle of a single MCS. So far we have seen how sensitive the scheme is to the variation of these parameters through an MCS's life cycle. What happens if we now *completely* change these parameters, but still maintain "reasonable" values? To answer this question, we will run the parameterization using (1) the PRE-STORM soundings for 0100 to 0400 UTC, and (2) the EMEX9 parameters (all water budget parameters, depth and shape parameters for phase transformations). This could be viewed as a "worst case" scenario, and there is certainly no question that the parameters have been derived using an independent dataset. The parameterized heating and drying tendencies for this situation are compared to the PRE-STORM diagnosed heating and drying in Fig. 5.13, for 0400 UTC, and in Figs. 5.14 and 5.15 for 0100-0400 UTC. Naturally, the results are not as accurate as before, but are at least reasonable. At 0400 UTC, the maximum parameterized heating in the mesoscale updraft is underestimated by ~ 4 Kd^{-1}, with the maximum value displaced about 100 mb too low. The maximum parameterized heating in the mesoscale downdraft at 0400 UTC is overestimated by about a factor of two. For the 0400 UTC drying

(a)

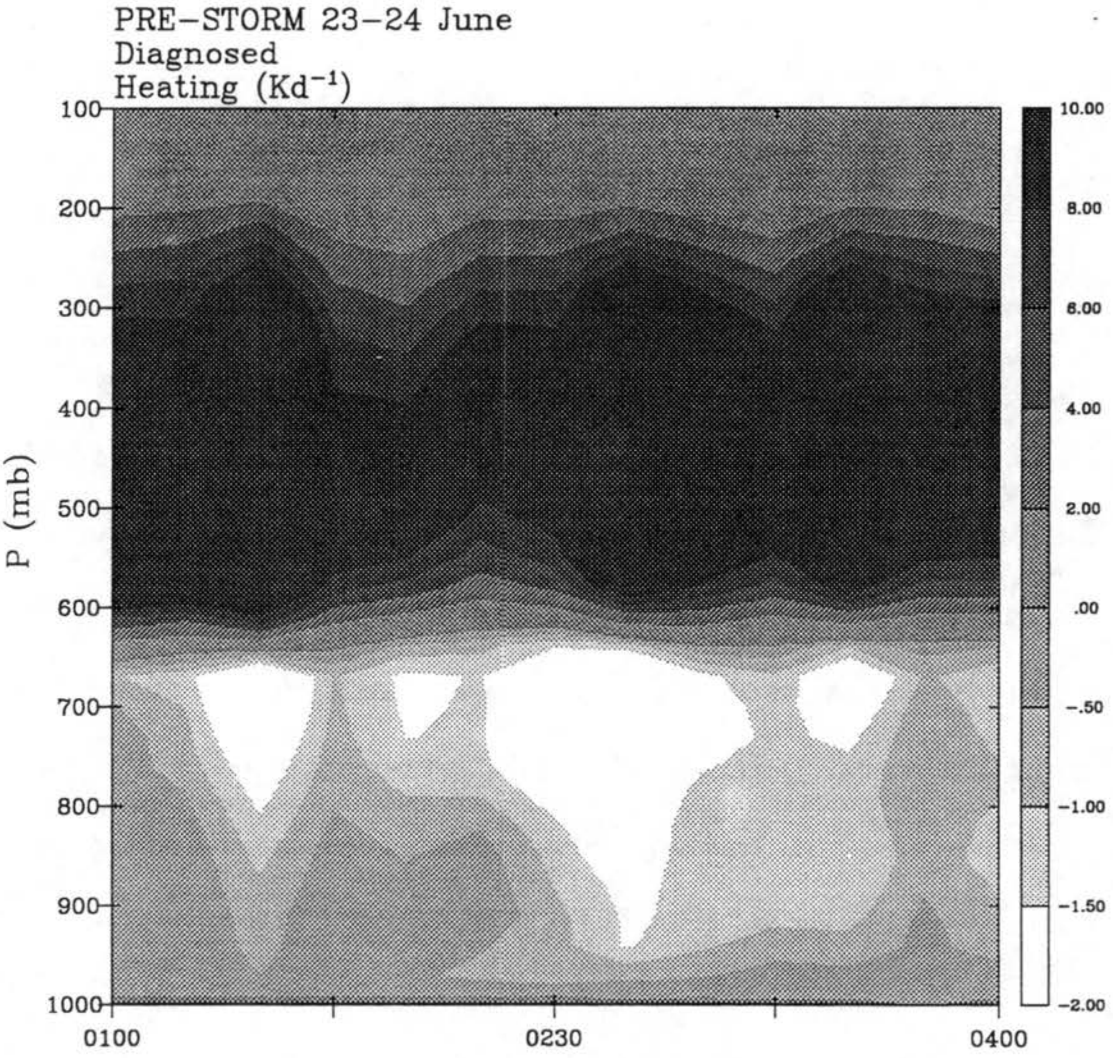
PRE–STORM 23–24 June
Diagnosed
Heating (Kd^{-1})
100
200
300
400
500
600
700
800
900
1000
P (mb)
0100
0230
0400
Time (UTC)
10.00
8.00
6.00
4.00
2.00
.00
–.50
–1.00
–1.50
–2.00

(b)

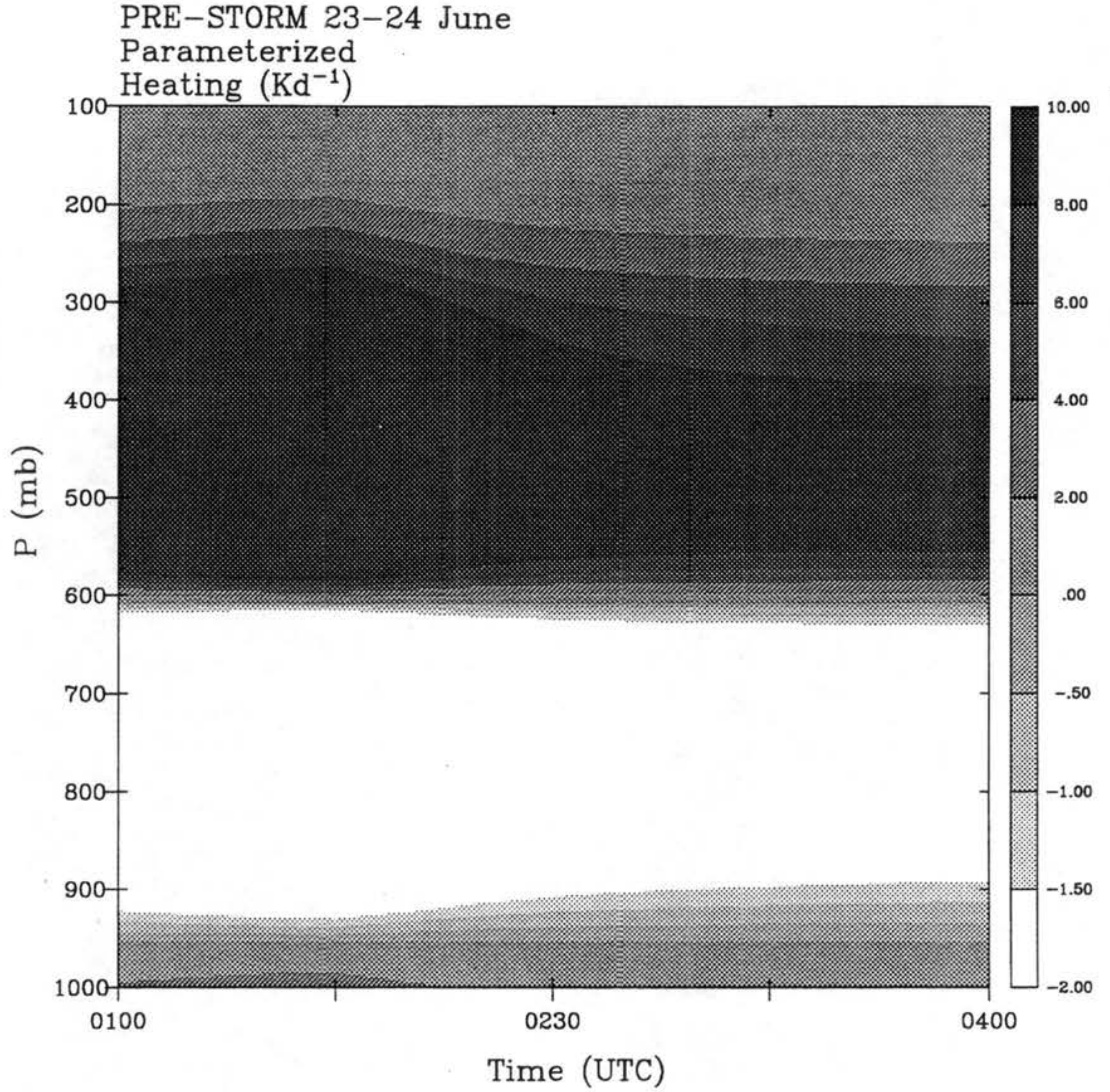

Fig. 5.11: The (a) diagnosed and (b) parameterized heating rates for the PRE-STORM simulation between 0100 and 0400 UTC.

(a)

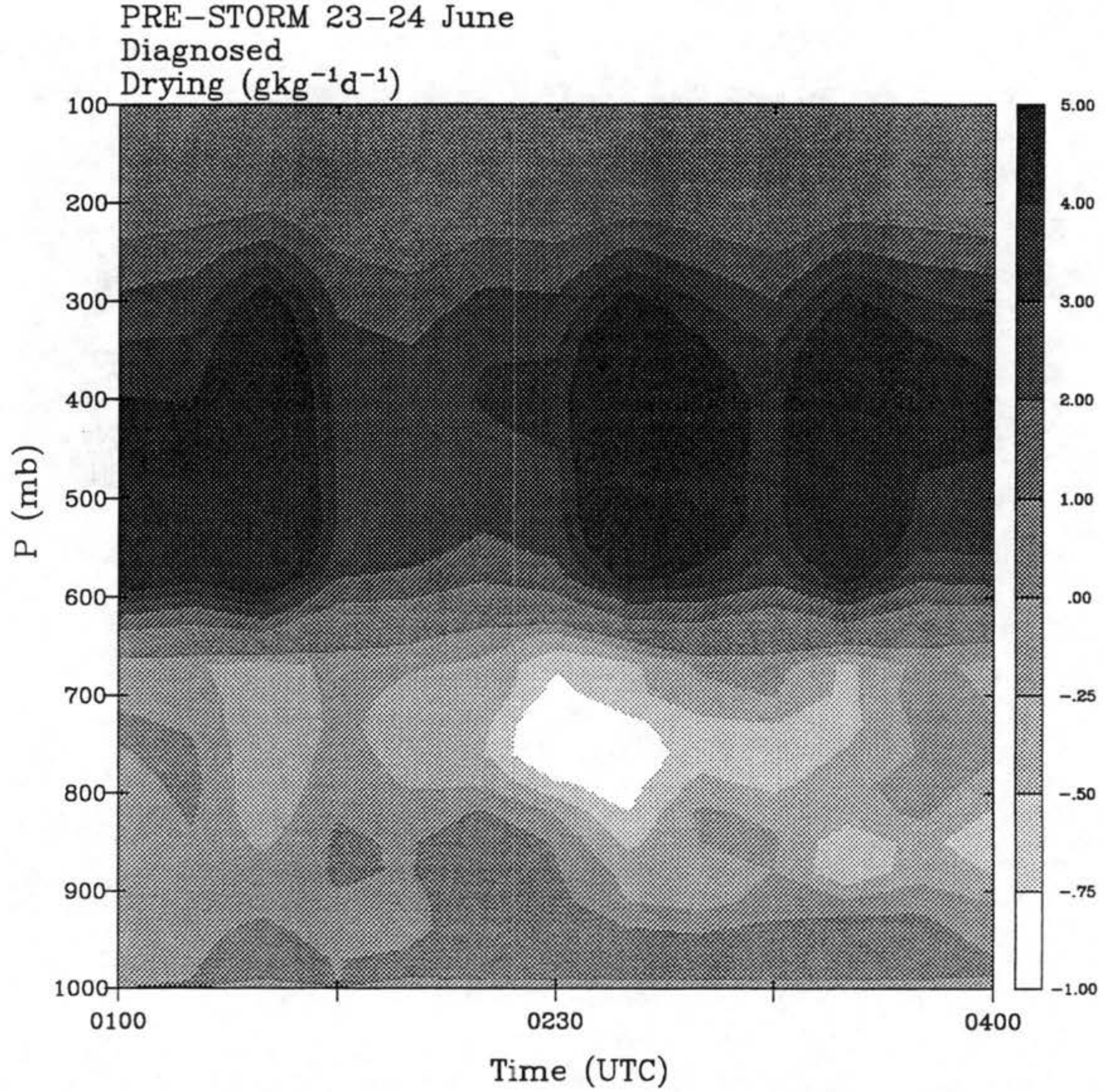
PRE−STORM 23−24 June
Diagnosed
Drying (gkg⁻¹d⁻¹)
100
200
300
400
500
600
700
800
900
1000
P (mb)
0100
0230
0400
Time (UTC)
5.00
4.00
3.00
2.00
1.00
.00
−.25
−.50
−.75
−1.00

(b)

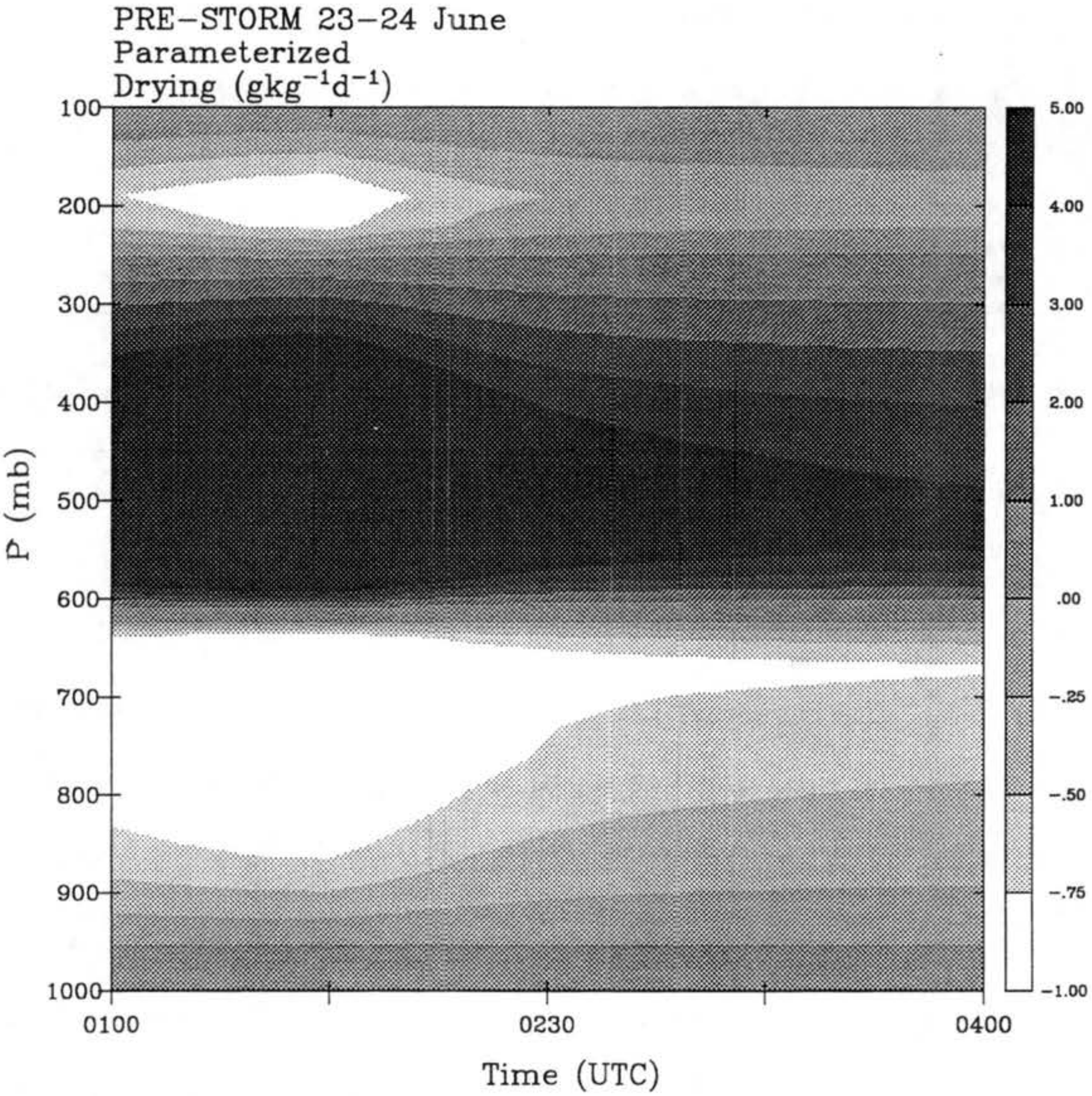

Fig. 5.12: The (a) diagnosed and (b) parameterized drying rates for the PRE-STORM simulation between 0100 and 0400 UTC.

profiles, the nature of the errors is similar, with errors of 1-2 gkgd^{-1} in the mesoscale updraft, and < 0.5 gkgd^{-1} in the mesoscale downdraft.

5.2.2 Momentum

Again, the parameterization is fed a Grid #2 mean sounding. First, we examine the results for the case in which the term accounting for the effect of convective-scale pressure gradient force is not included. Fig. 5.16 shows the vertical profiles of the environmental momentum along with the momentum of each of the predicted subensembles at 0400 UTC in this case. Again, the deepest subensembles maintain their cloud-base momentum values whereas the shallower subensembles approach the environmental momentum as they rise toward their respective cloud tops.

The 0400 UTC parameterized zonal and meridional momentum acceleration is compared with the 0400 UTC diagnosed momentum budget residual on Grid #2 in Fig. 5.17. The meridional (i.e., nearly line-tangential) component of the momentum is parameterized quite well, with the following features correctly predicted: deceleration between 100 and 200 mb, acceleration between 200 and 300 mb, deceleration between 300 and 450 mb, and acceleration between 450 and 850 mb. For the line-normal component of momentum, the parameterization does not perform as well, especially above 300 mb. The momentum parameterization does not (and *cannot*) predict any momentum acceleration or deceleration below cloud base, and therefore here it does not capture the features of the momentum budget residual.

Unlike for EMEX9, for PRE-STORM the performance of the momentum parameterization improves when the convective-scale pressure gradient acceleration term is

(a)

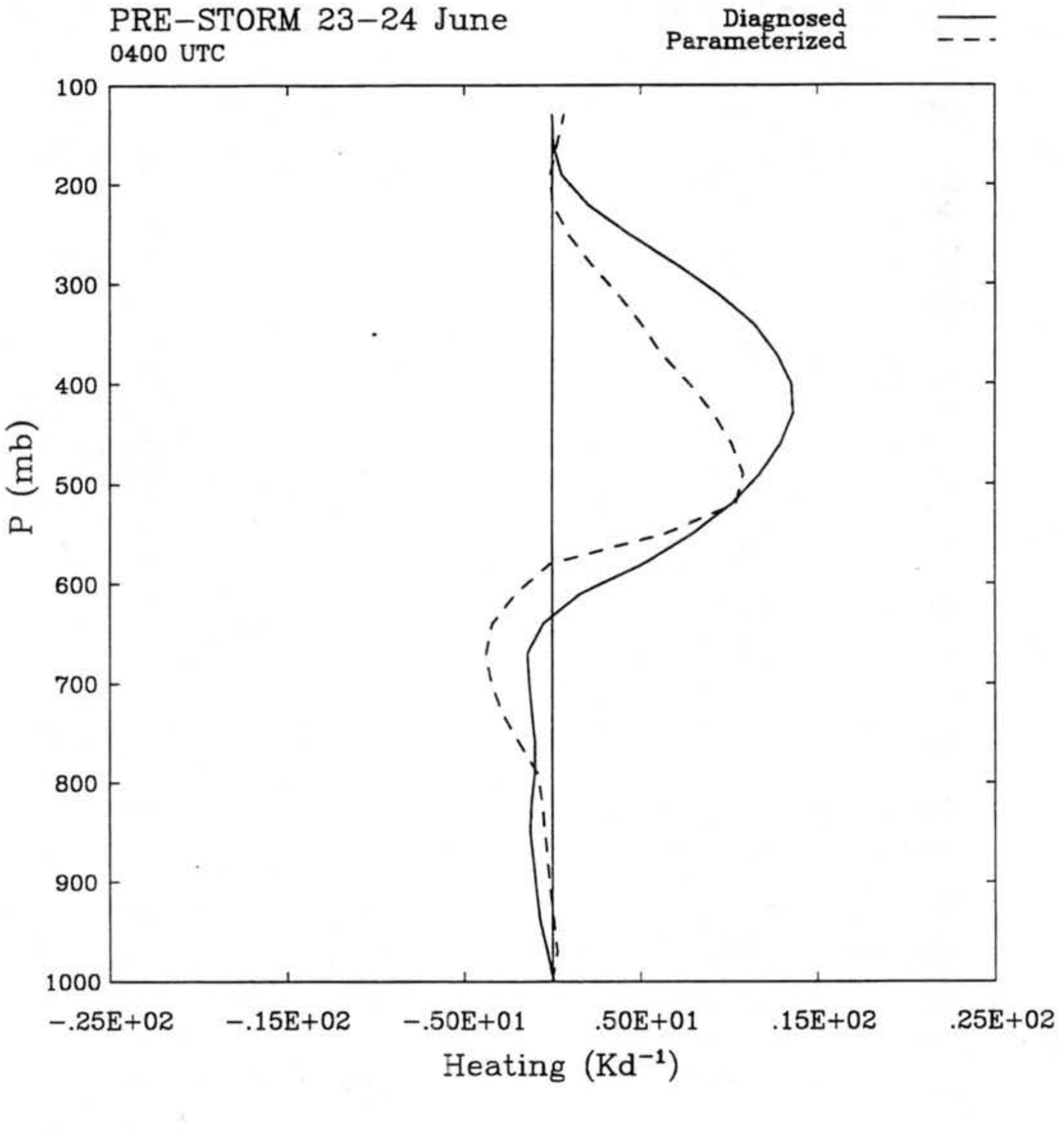
PRE–STORM 23–24 June
0400 UTC
Diagnosed
Parameterized
100
200
300
400
500
600
700
800
900
1000
P (mb)
–.25E+02
–.15E+02
–.50E+01
.50E+01
.15E+02
.25E+02
Heating (Kd⁻¹)

(b)

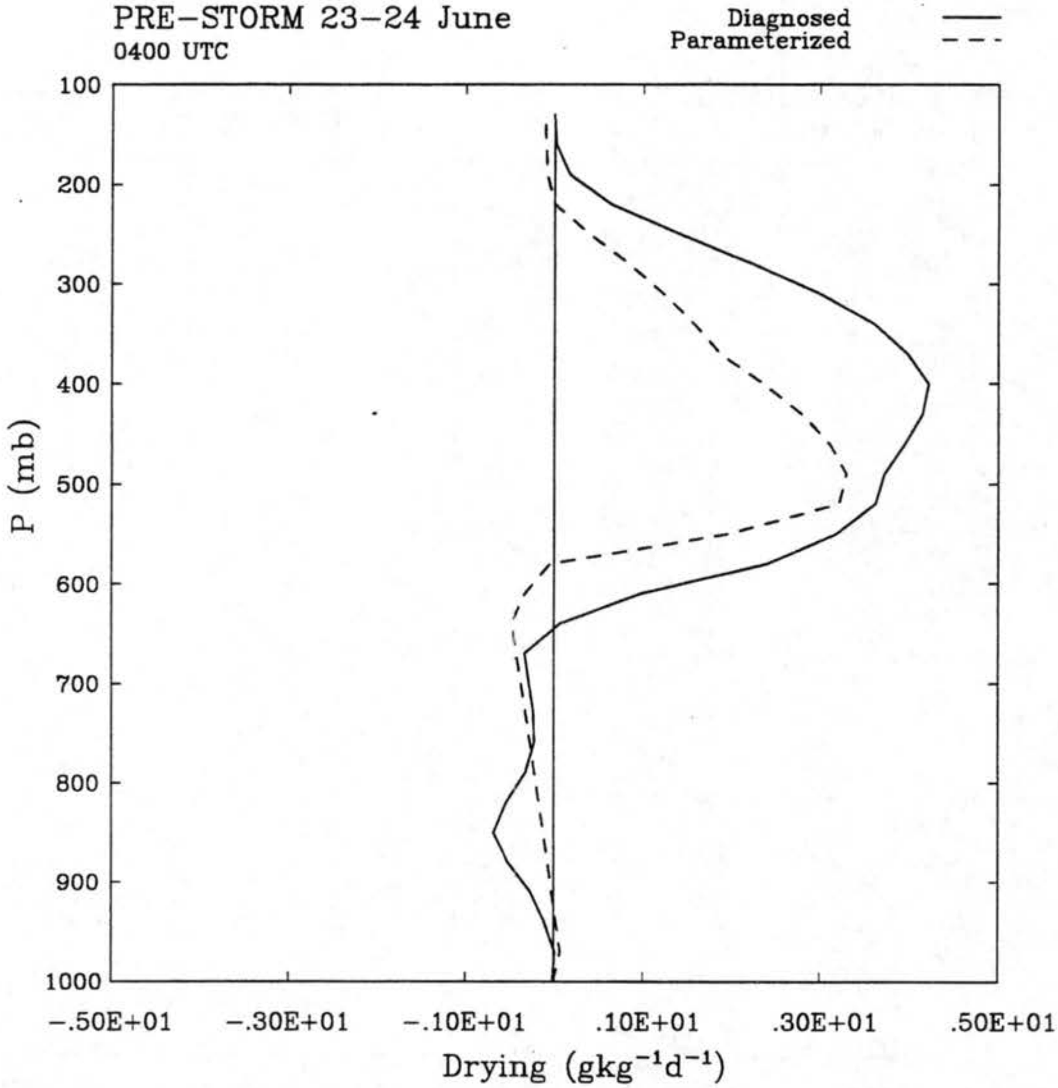

Fig. 5.13: The parameterized and diagnosed (a) heating and (b) drying rates for the PRE-STORM 23-24 June simulation at 0400 UTC.

(a)

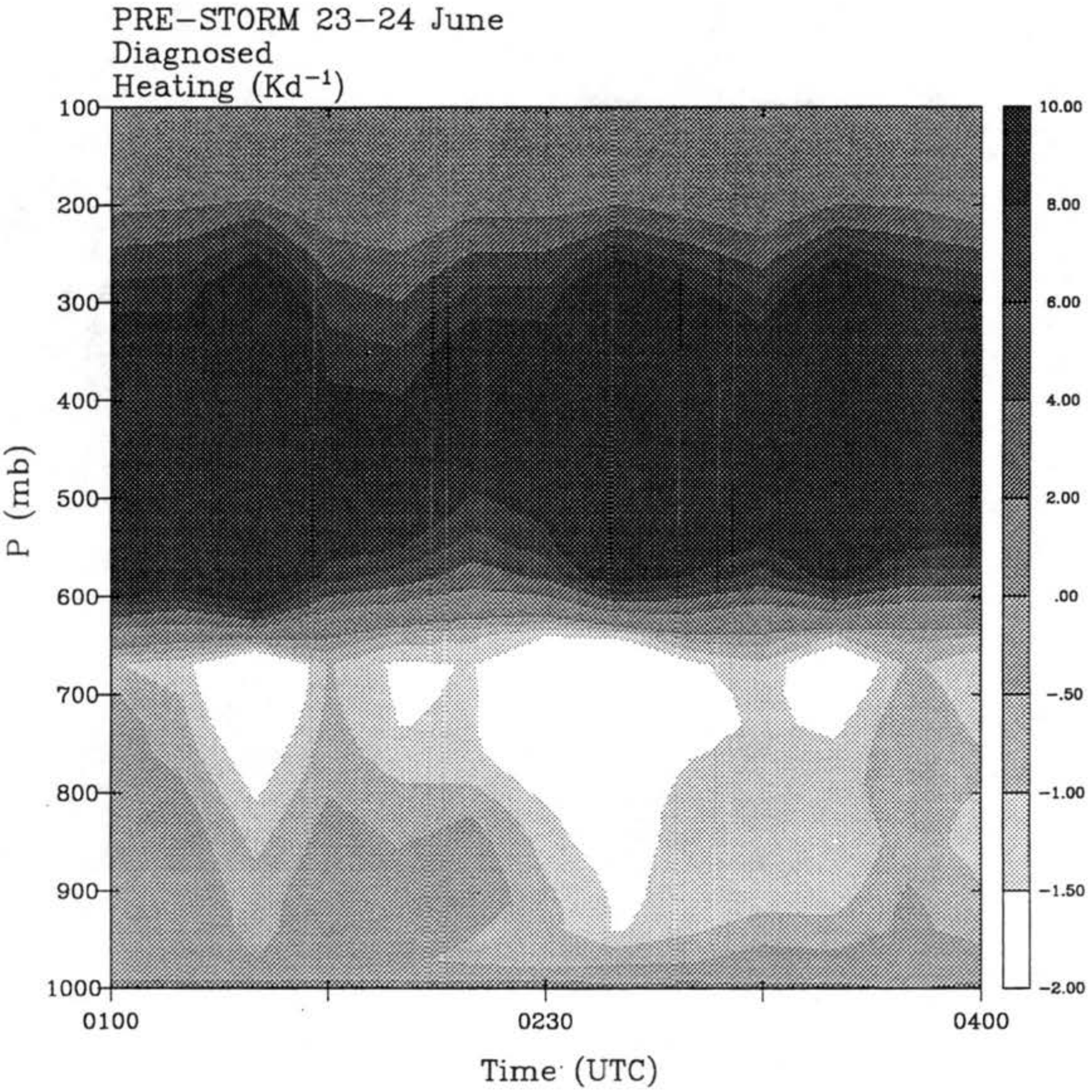
PRE–STORM 23–24 June
Diagnosed
Heating (Kd^{-1})
100
200
300
400
500
600
700
800
900
1000
P (mb)
0100
0230
0400
Time (UTC)
10.00
8.00
6.00
4.00
2.00
.00
-.50
-1.00
-1.50
-2.00

(b)

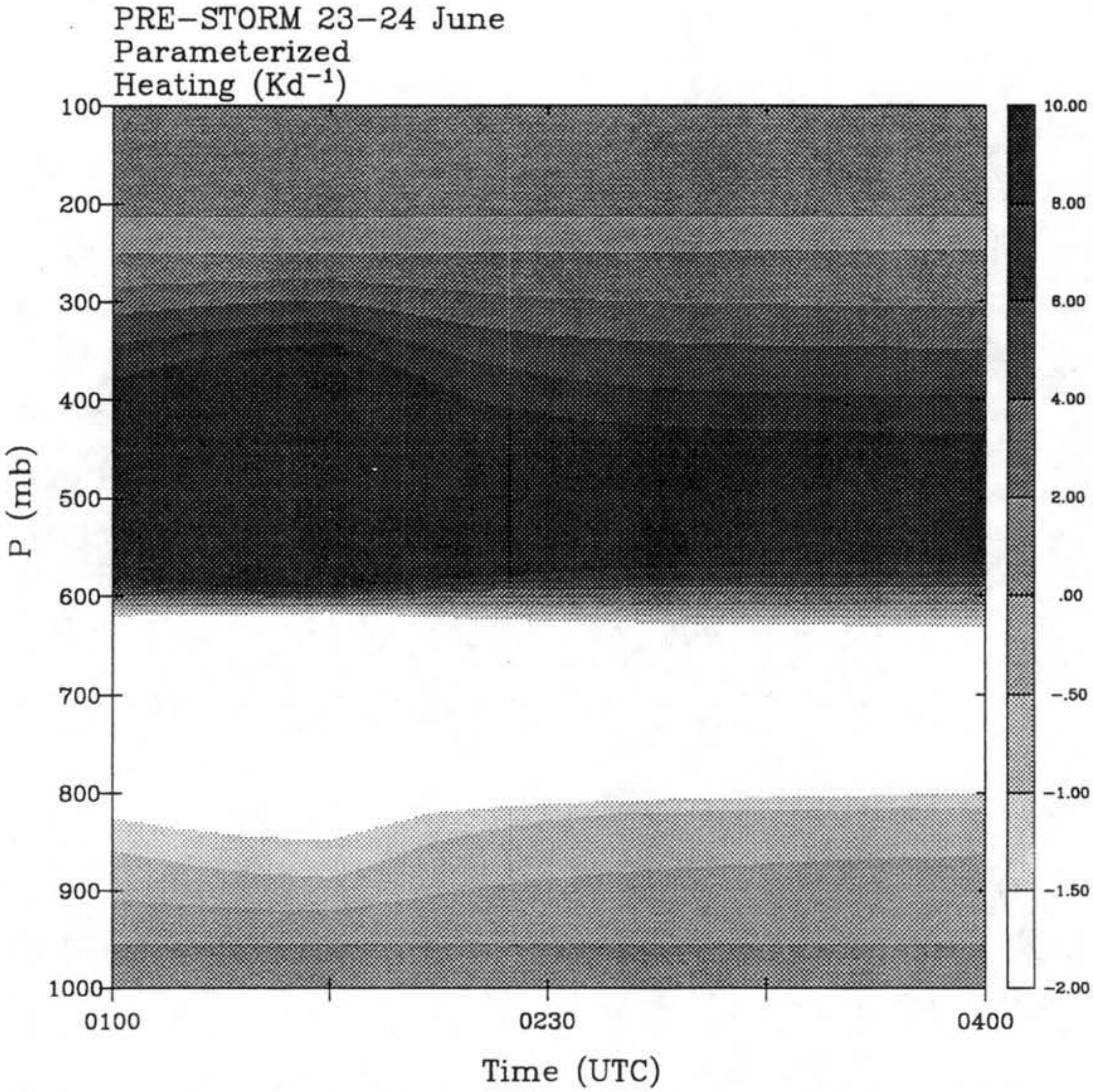

Fig. 5.14: The (a) diagnosed and (b) parameterized heating rates for the PRE-STORM simulation between 0100 and 0400 UTC, where PRE-STORM parameters are replaced with the EMEX9 parameters (see text).

(a)

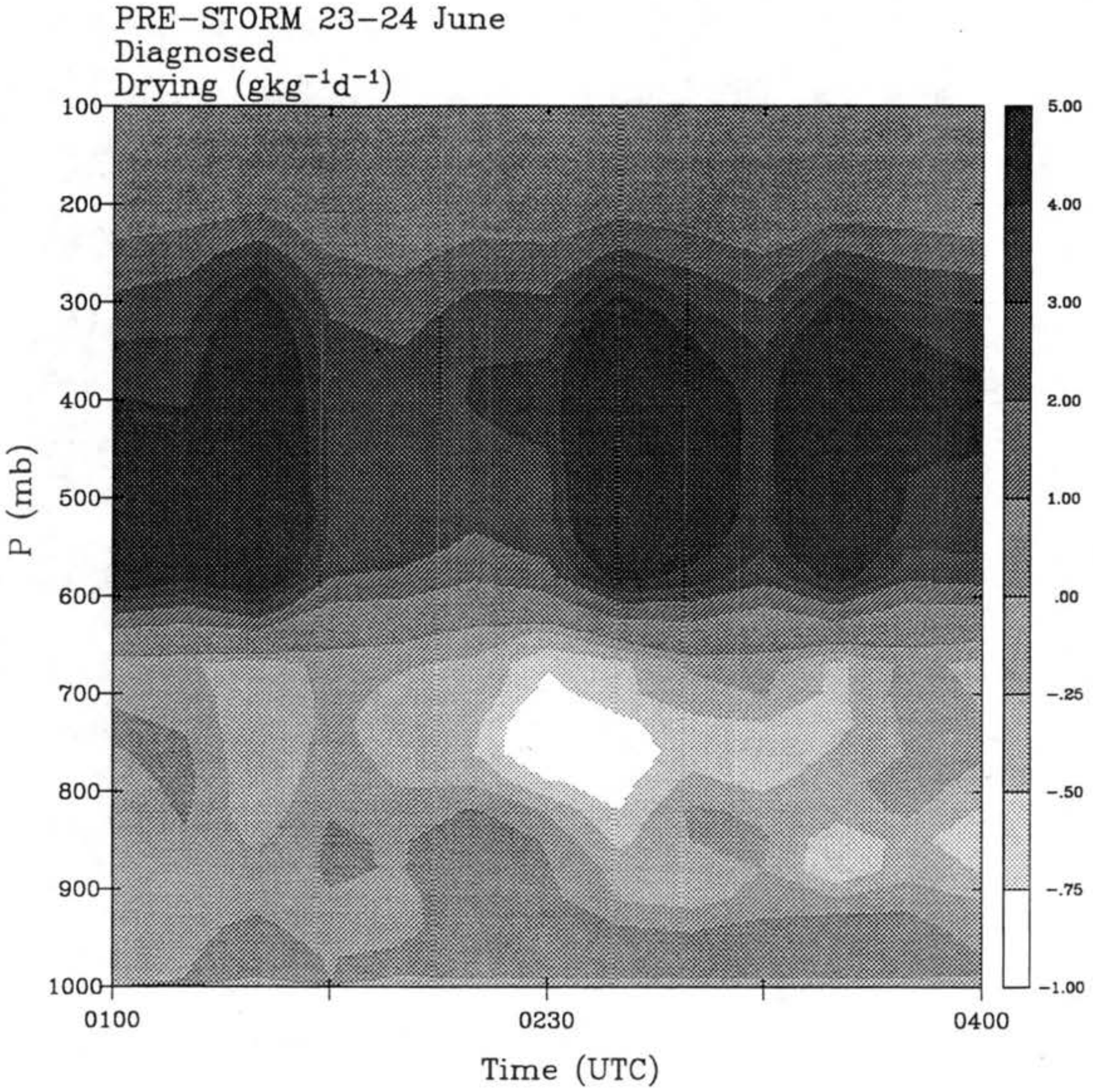
PRE–STORM 23–24 June
Diagnosed
Drying ($gkg^{-1}d^{-1}$)
P (mb)
100
200
300
400
500
600
700
800
900
1000
0100
0230
0400
Time (UTC)
5.00
4.00
3.00
2.00
1.00
.00
–.25
–.50
–.75
–1.00

(b)

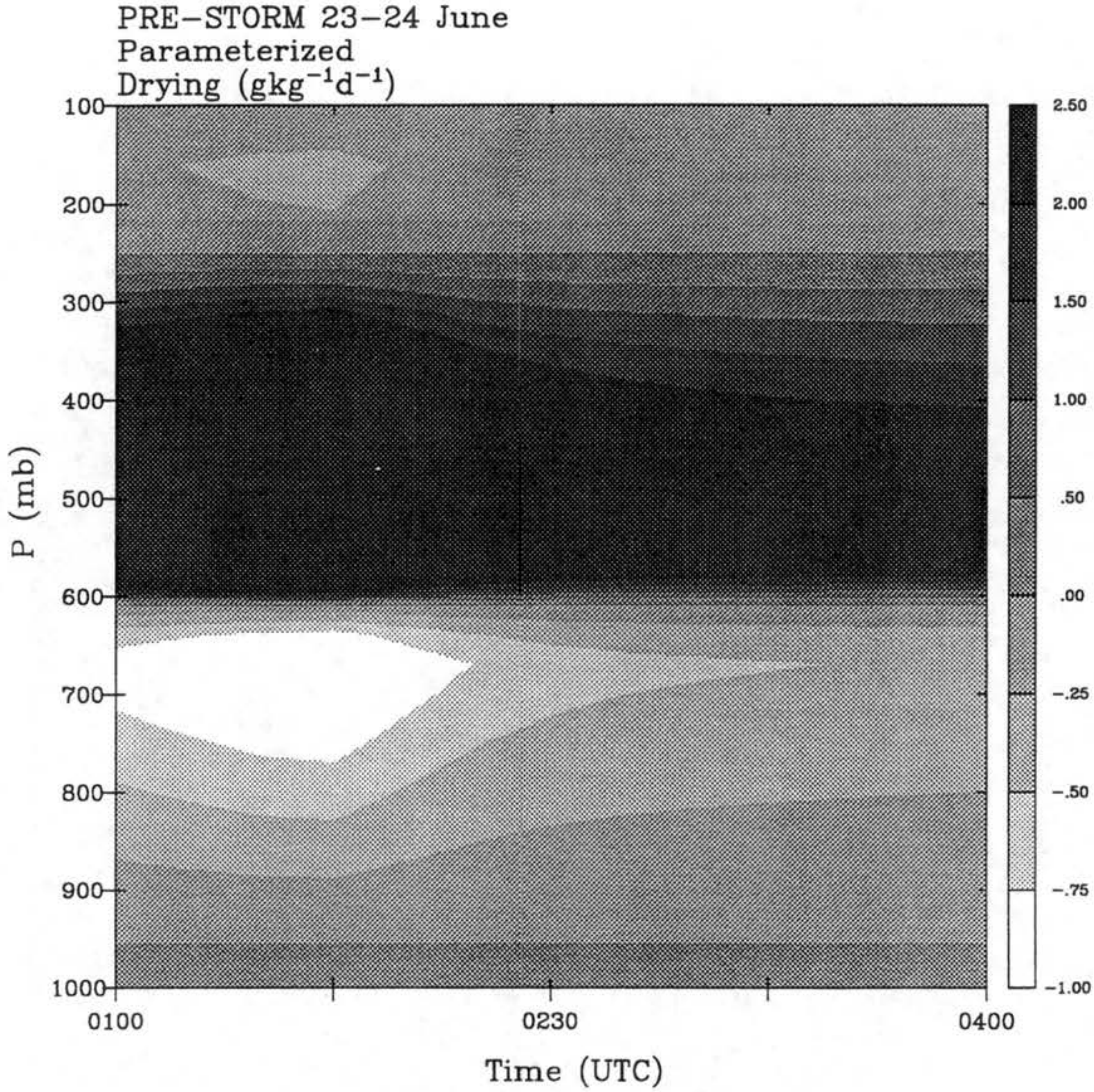

Fig. 5.15: The (a) diagnosed and (b) parameterized drying rates for the PRE-STORM simulation between 0100 and 0400 UTC, where PRE-STORM parameters are replaced with the EMEX9 parameters (see text).

(a)

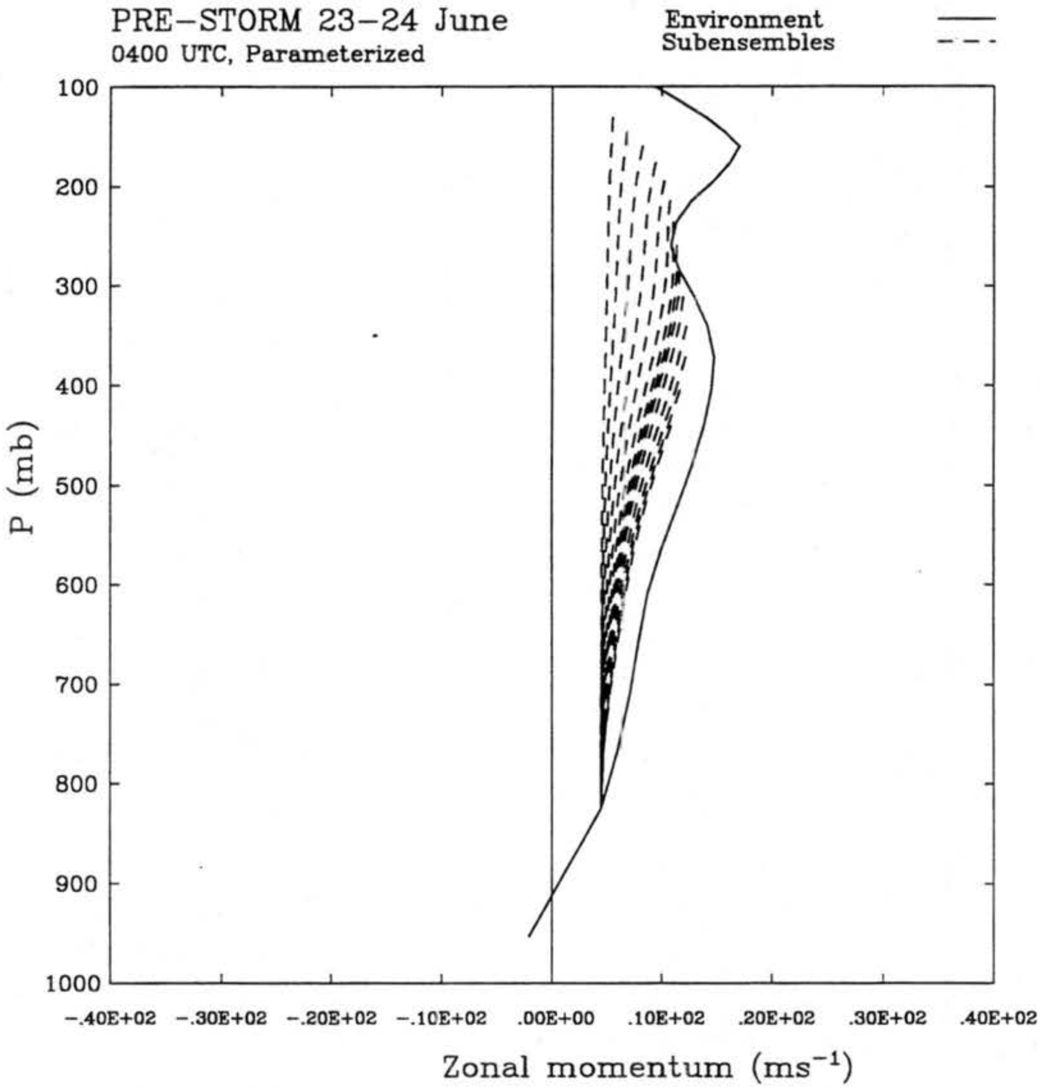
PRE–STORM 23–24 June
0400 UTC, Parameterized
Environment
Subensembles
100
200
300
400
500
600
700
800
900
1000
P (mb)
–.40E+02
–.30E+02
–.20E+02
–.10E+02
.00E+00
.10E+02
.20E+02
.30E+02
.40E+02
Zonal momentum (ms⁻¹)

(b)

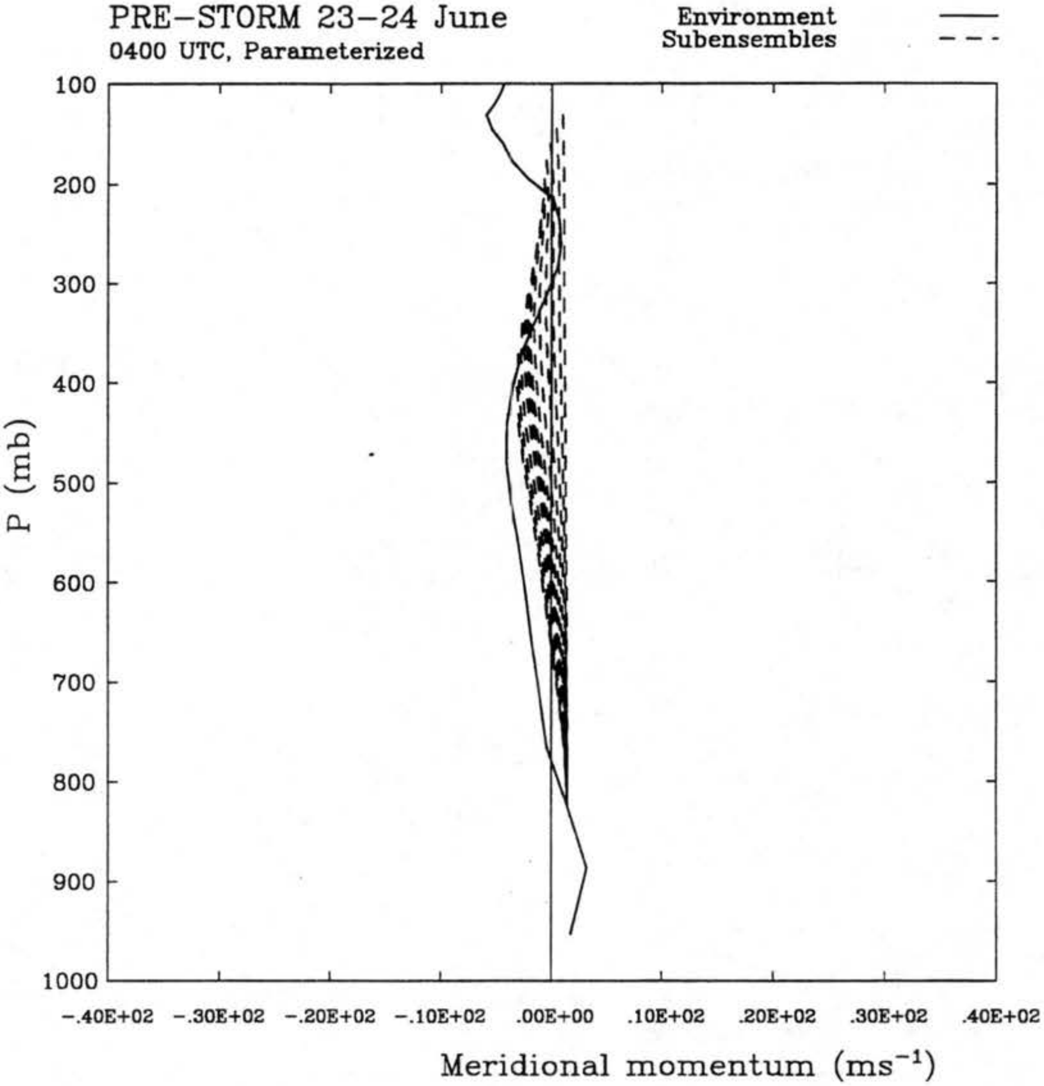

Fig. 5.16: Vertical profiles of environmental wind (solid) and the cloud momentum of all subensembles (dashed) as predicted by the momentum parameterization at 0400 UTC for (a) zonal momentum and (b) meridional momentum.

(a)

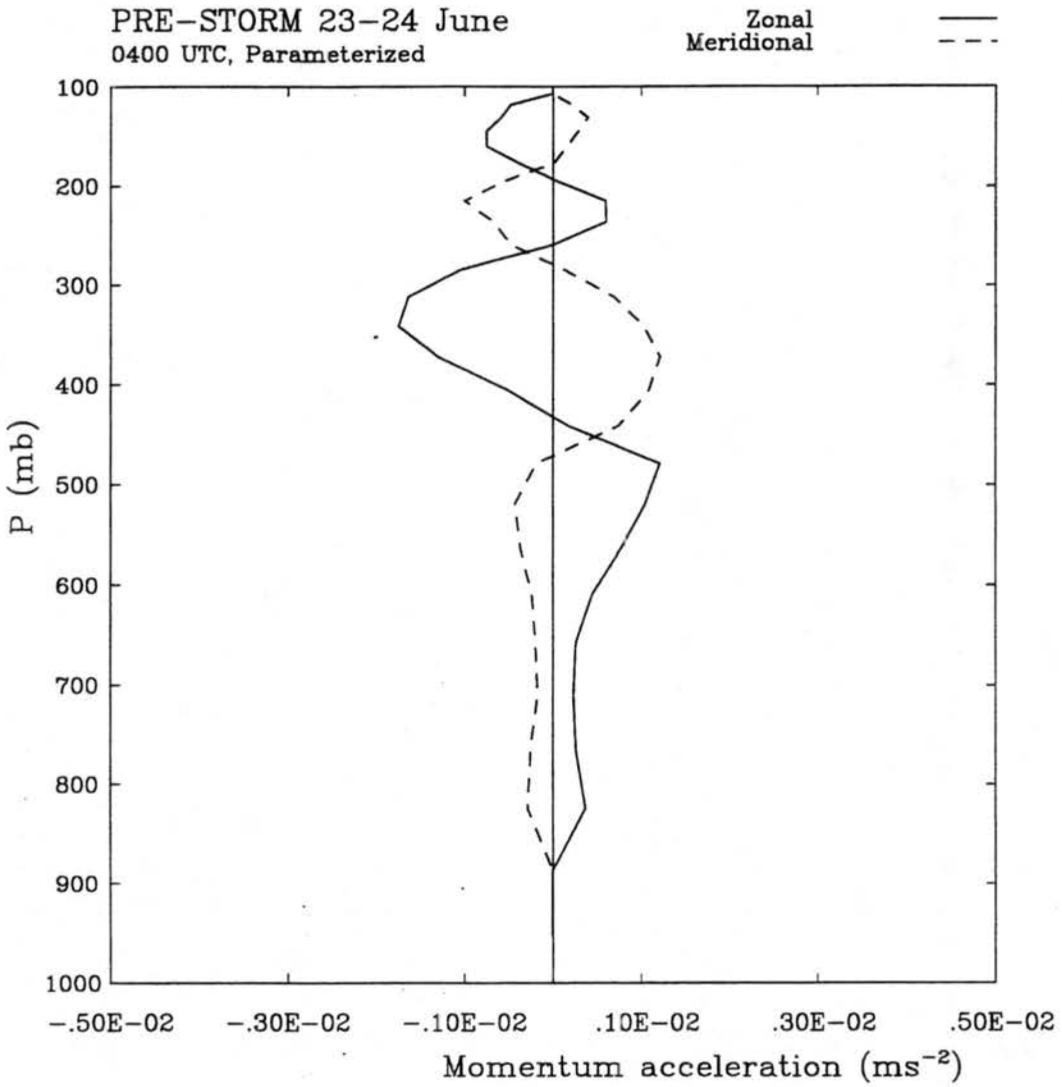
PRE–STORM 23–24 June
0400 UTC, Parameterized
Zonal
Meridional
100
200
300
400
500
600
700
800
900
1000
P (mb)
–.50E–02
–.30E–02
–.10E–02
.10E–02
.30E–02
.50E–02
Momentum acceleration (ms^{-2})

(b)

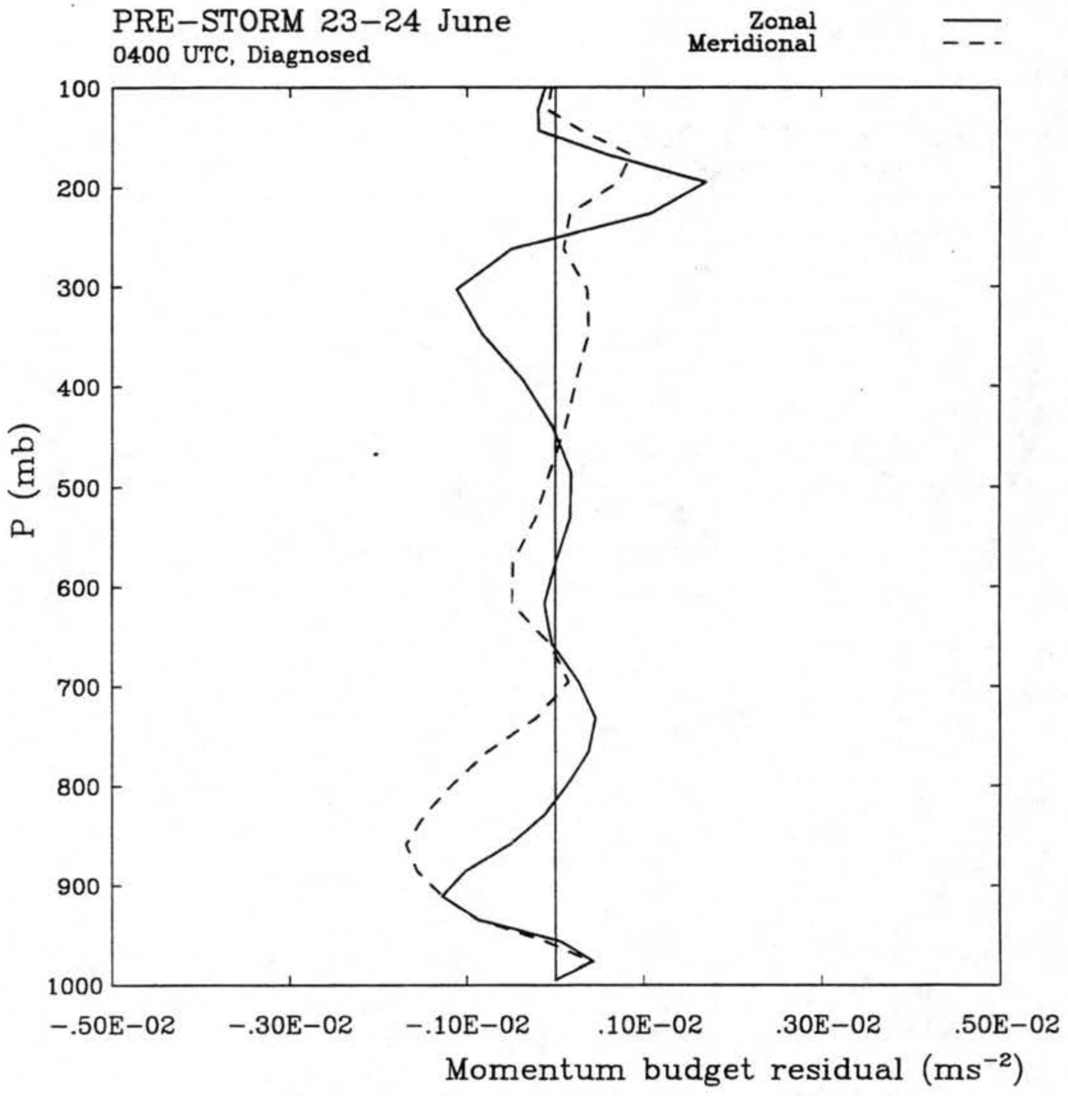

Fig. 5.17: Vertical profiles of (a) the parameterized zonal and meridional momentum acceleration and (b) the diagnosed momentum budget residual of zonal and meridional momentum at 0400 UTC.

considered. In order to include this term in the parameterization, we must specify a line orientation as well as values of γ_k and γ_l (see Section 2.3). Examination of the vertical velocity fields throughout the simulations indicates a predominant WNW-ESE line orientation throughout the simulation. Specifying appropriate values of γ_k and γ_l is a bit more difficult, as it requires assumptions about the line-normal, line-tangential, and vertical "scale-lengths" of the convective updrafts. Examination of the vertical velocity fields suggest that for the PRE-STORM 23-24 June MCS, reasonable values for each of these quantities are 20 km, 200 km, and 20 km, for the line-normal, line-tangential, and vertical scale-lengths, respectively. If we take the x-direction to be parallel to the line and the y-direction to be normal to the line, these assumptions yield a value of γ_k of 0.02 and a value of γ_l of 2.0. Again, these parameters simply enable the momentum parameterization to "feel" the observed spatial orientation of the convective updrafts.

We now apply the momentum parameterization as above, except now including the term involving the convective-scale horizontal pressure gradient force along with the aforementioned values of line-orientation, γ_k, and γ_l. Because the value of γ_l is so small, the parameterized line-tangential momentum of the convective subensembles (Fig. 5.19a) is essentially the same as with the entrainment-detrainment model (Fig. 5.18a). However, the parameterized line-normal momentum of the convective subensembles (Fig. 5.19b) behaves quite differently than before (Fig. 5.18b). In particular, below 500 mb, the line-normal momentum of the convective subensembles is directed in a rear-to-front direction rather than a front-to-rear direction, whereas above 500 mb, the line-normal momentum of the convective subensembles has a larger front-to-rear component that before. Both of these differences are effected by a parameterized horizontal convective-scale pressure gradient force which results from inferring lower perturbation pressure on the downshear side of convective updrafts.

Including the horizontal convective-scale pressure gradient force in the parameterization improves the predicted acceleration of the line-normal component of momentum. Fig. 5.20 shows the parameterized acceleration of the line-normal and line-tangential momentum components at 0400 UTC along with the diagnosed momentum budget residual for each of these components at 0400 UTC for this case. For comparison purposes, Fig. 5.21 shows the parameterized and diagnosed line-normal and line-tangential momentum accelerations for the entrainment-detrainment model only. With the inclusion of the horizontal convective-scale pressure gradient force, the parameterization correctly predicts the front-to-rear momentum acceleration between 300 and 100 mb. The prediction of the line-tangential momentum remains essentially unchanged. The improved performance of the momentum parameterization with the inclusion of the horizontal pressure gradient force terms seems reasonable in light of the simulated Grid #2 mean line-normal pressure gradient force (Fig. 5.22). For the PRE-STORM MCS, there is a significant mean pressure jump across the system from front-to-rear, especially in the upper troposphere. This plot also suggests why the parameterization with convective-scale horizontal pressure gradient force still failed in the middle troposphere. The parameterization predicted that the pressure gradient force would effect a rear-to-front acceleration in the layer between $\sim$ 310 and $\sim$

(a)

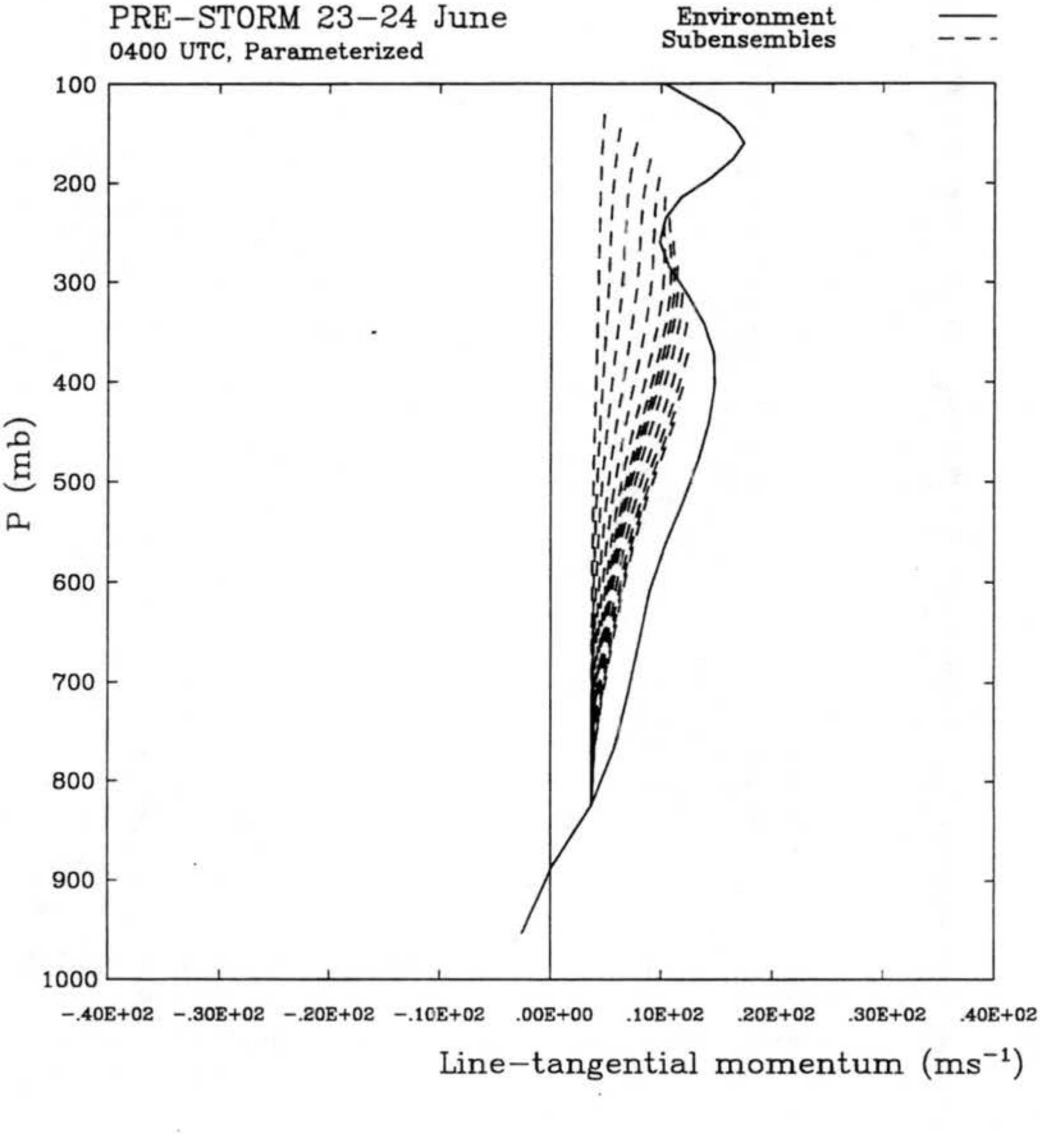
PRE–STORM 23–24 June
0400 UTC, Parameterized
Environment
Subensembles
100
200
300
400
500
600
700
800
900
1000
P (mb)
-.40E+02
-.30E+02
-.20E+02
-.10E+02
.00E+00
.10E+02
.20E+02
.30E+02
.40E+02
Line–tangential momentum (ms⁻¹)

(b)

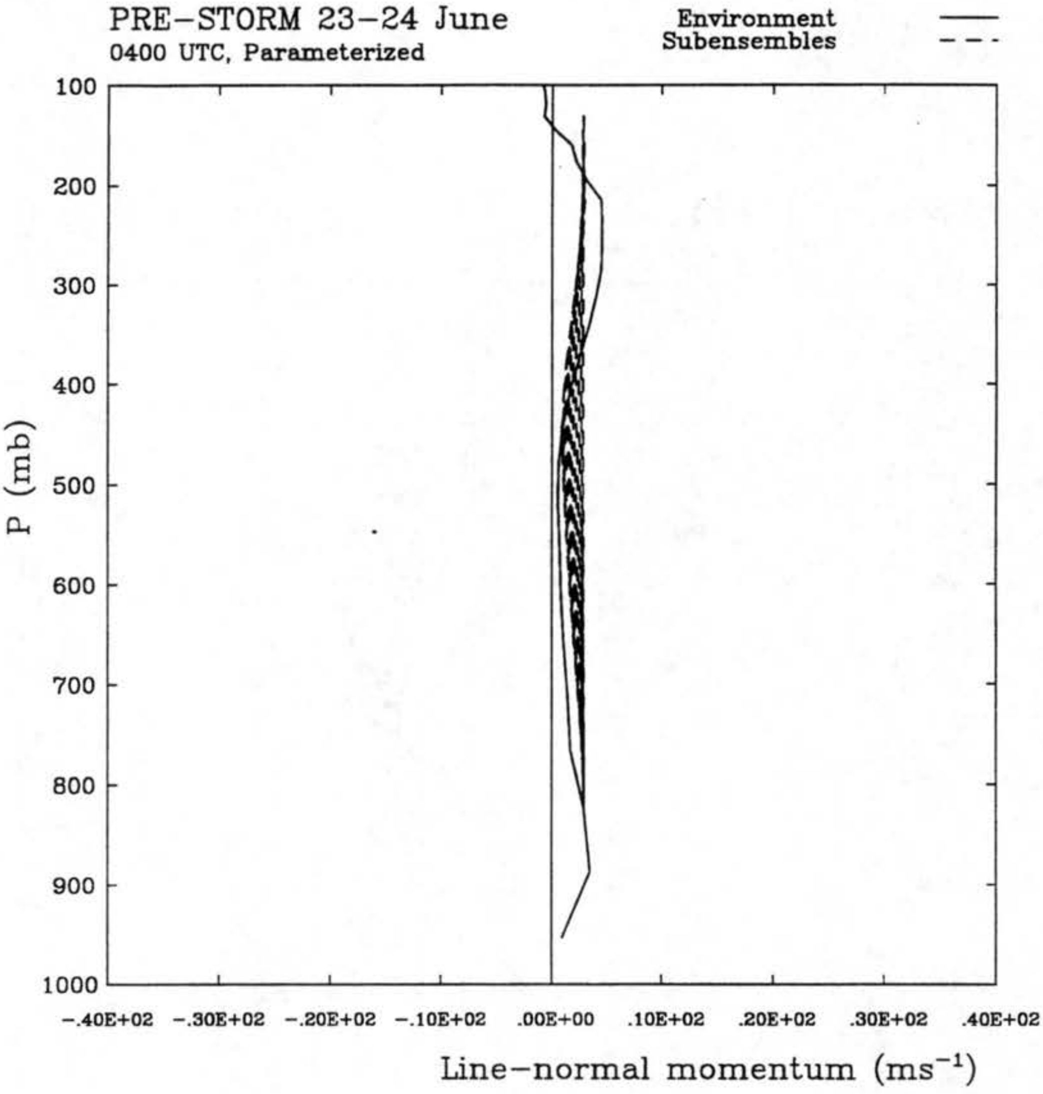

Fig. 5.18: Vertical profiles of environmental wind (solid) and the cloud momentum of all subensembles (dashed) as predicted by the momentum parameterization at 0400 UTC for (a) line-tangential momentum and (b) line-normal momentum when the momentum parameterization is applied using the entrainment-detrainment terms only.

(a)

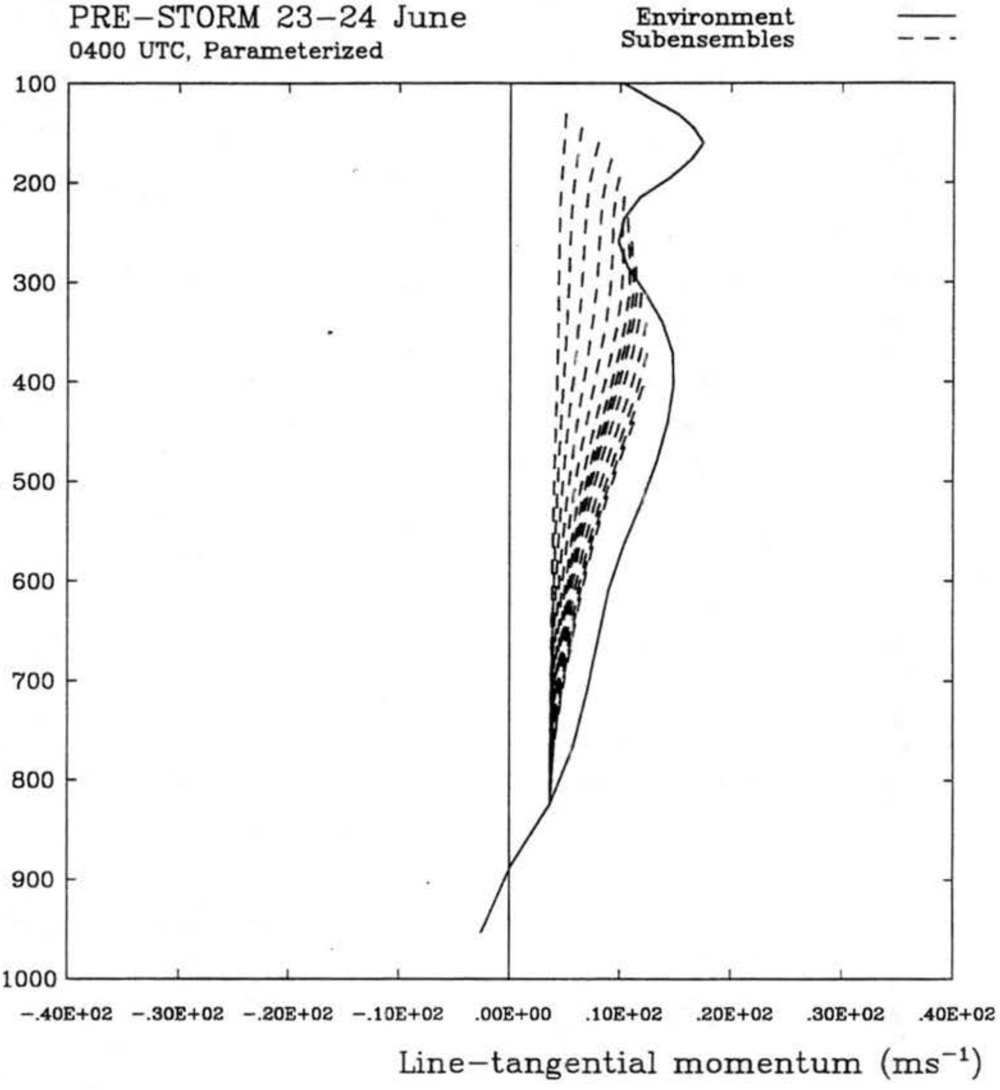
PRE−STORM 23−24 June
0400 UTC, Parameterized
Environment
Subensembles
100
200
300
400
500
600
700
800
900
1000
P (mb)
−.40E+02
−.30E+02
−.20E+02
−.10E+02
.00E+00
.10E+02
.20E+02
.30E+02
.40E+02
Line−tangential momentum (ms−1)

(b)

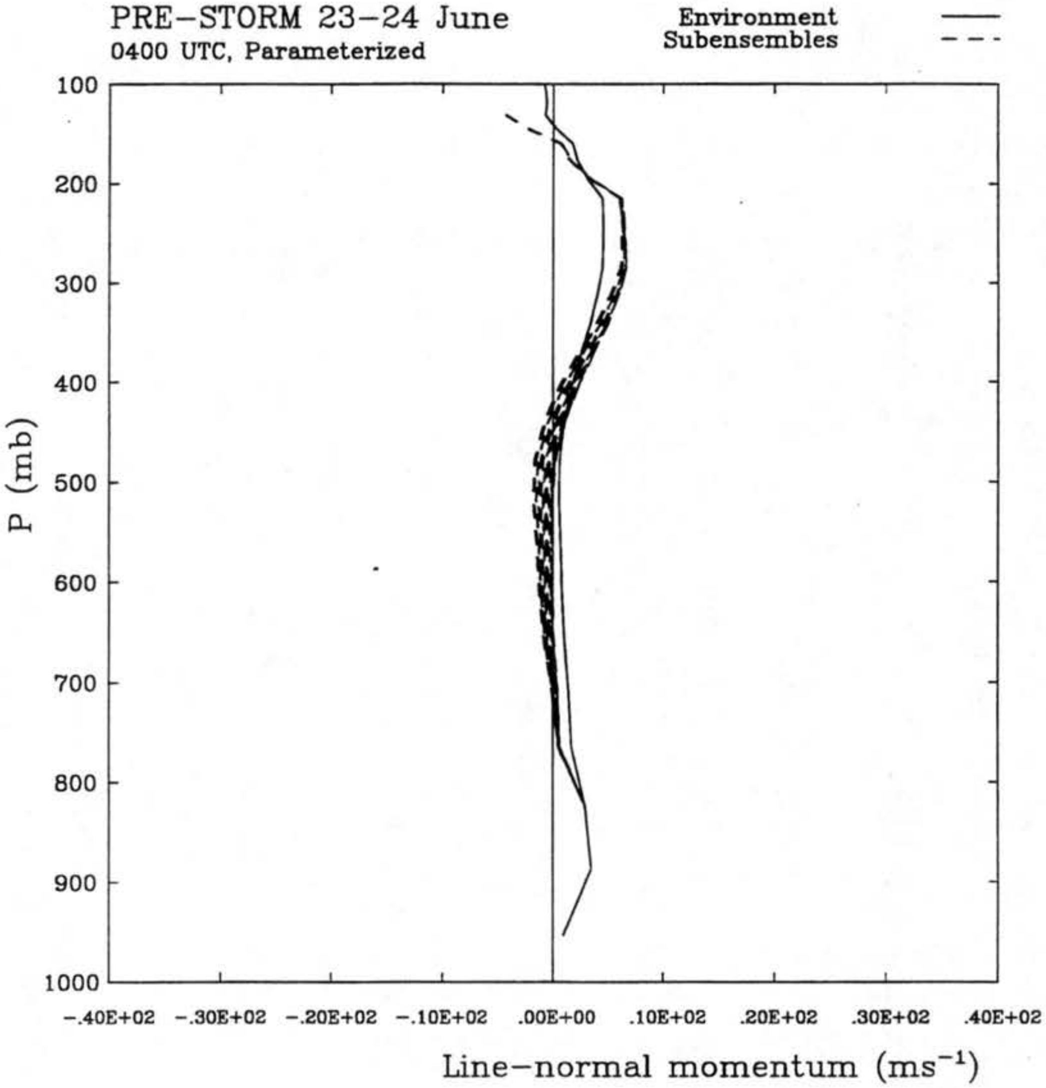

Fig. 5.19: Vertical profiles of environmental wind (solid) and the cloud momentum of all subensembles (dashed) as predicted by the momentum parameterization at 0400 UTC for (a) line-tangential momentum and (b) line-normal momentum when the momentum parameterization is applied using the entrainment-detrainment terms along with the term which accounts for the momentum acceleration by the horizontal convective-scale pressure gradient force.

480 mb at 0400 UTC; this rear-to-front pressure gradient force acceleration was not diagnosed in the Grid #2 mean model results. The parameterization did correctly predict a front-to-rear acceleration elsewhere in the troposphere, however.

(a)

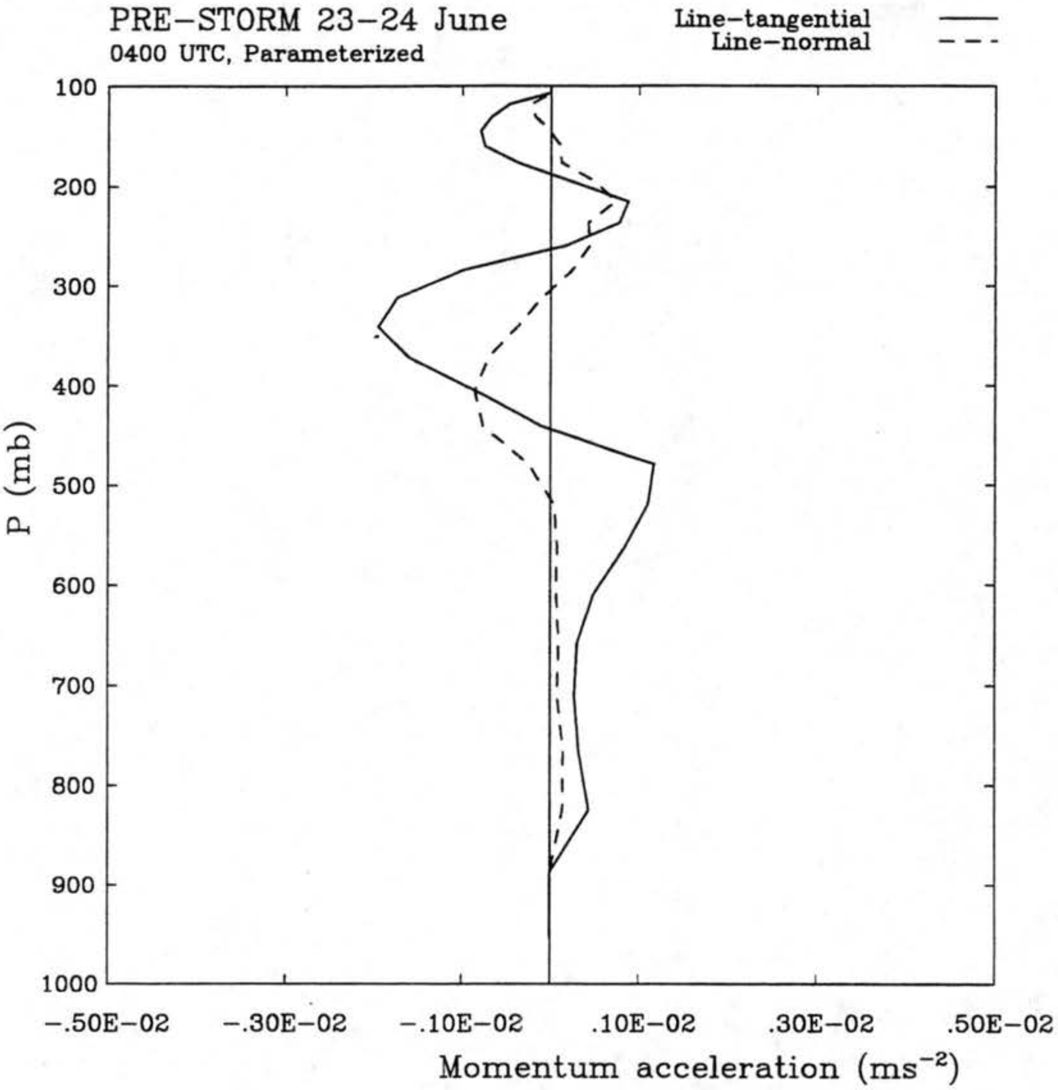
PRE-STORM 23-24 June
0400 UTC, Parameterized
Line-tangential
Line-normal
100
200
300
400
500
600
700
800
900
1000
P (mb)
-.50E-02
-.30E-02
-.10E-02
.10E-02
.30E-02
.50E-02
Momentum acceleration (ms^{-2})

(b)

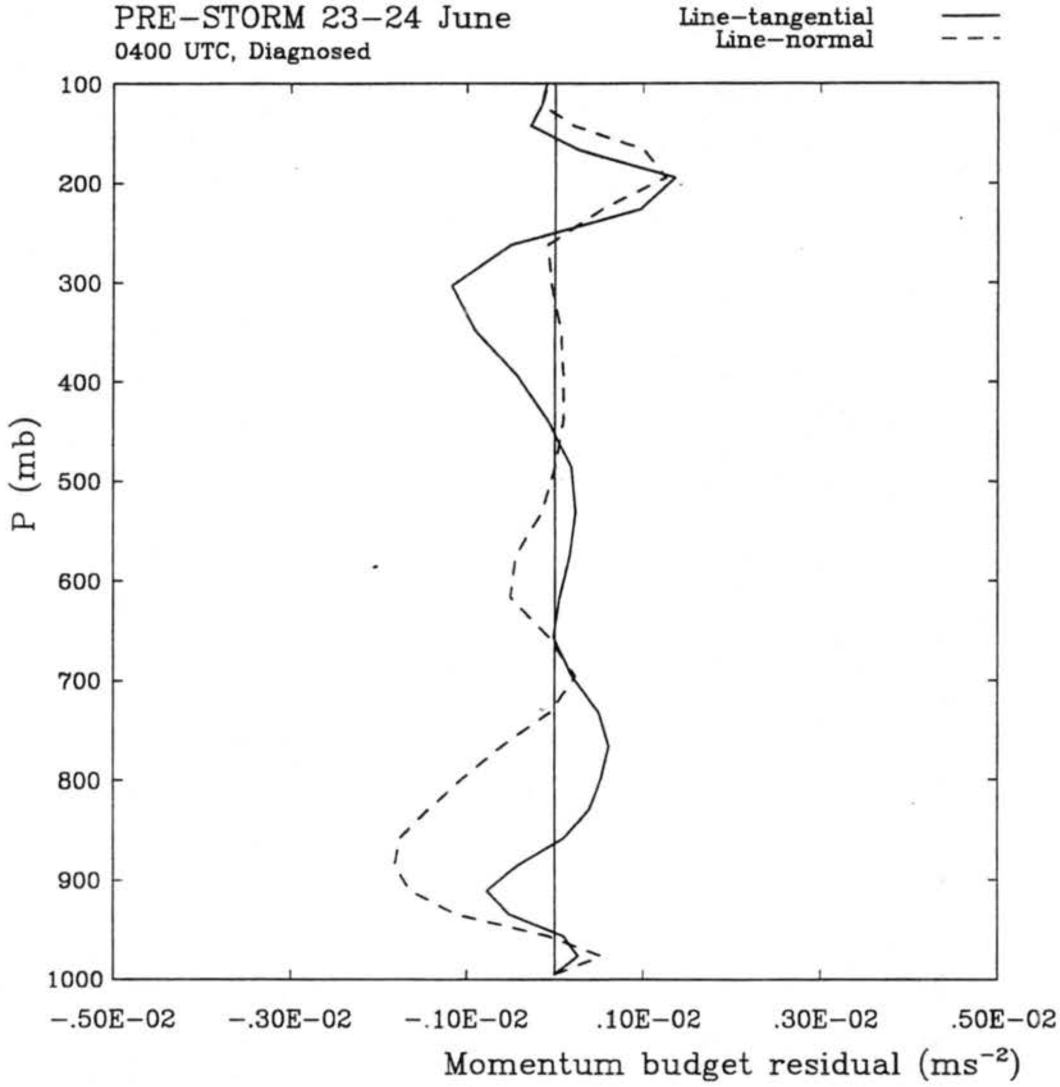

Fig. 5.20: Vertical profiles of (a) the parameterized line-tangential and line-normal momentum acceleration and (b) the momentum budget residual of line-tangential and line-normal momentum at 0400 UTC for when the momentum parameterization is applied using the entrainment-detrainment terms along with the term which accounts for the momentum acceleration by the horizontal convective-scale pressure gradient force.

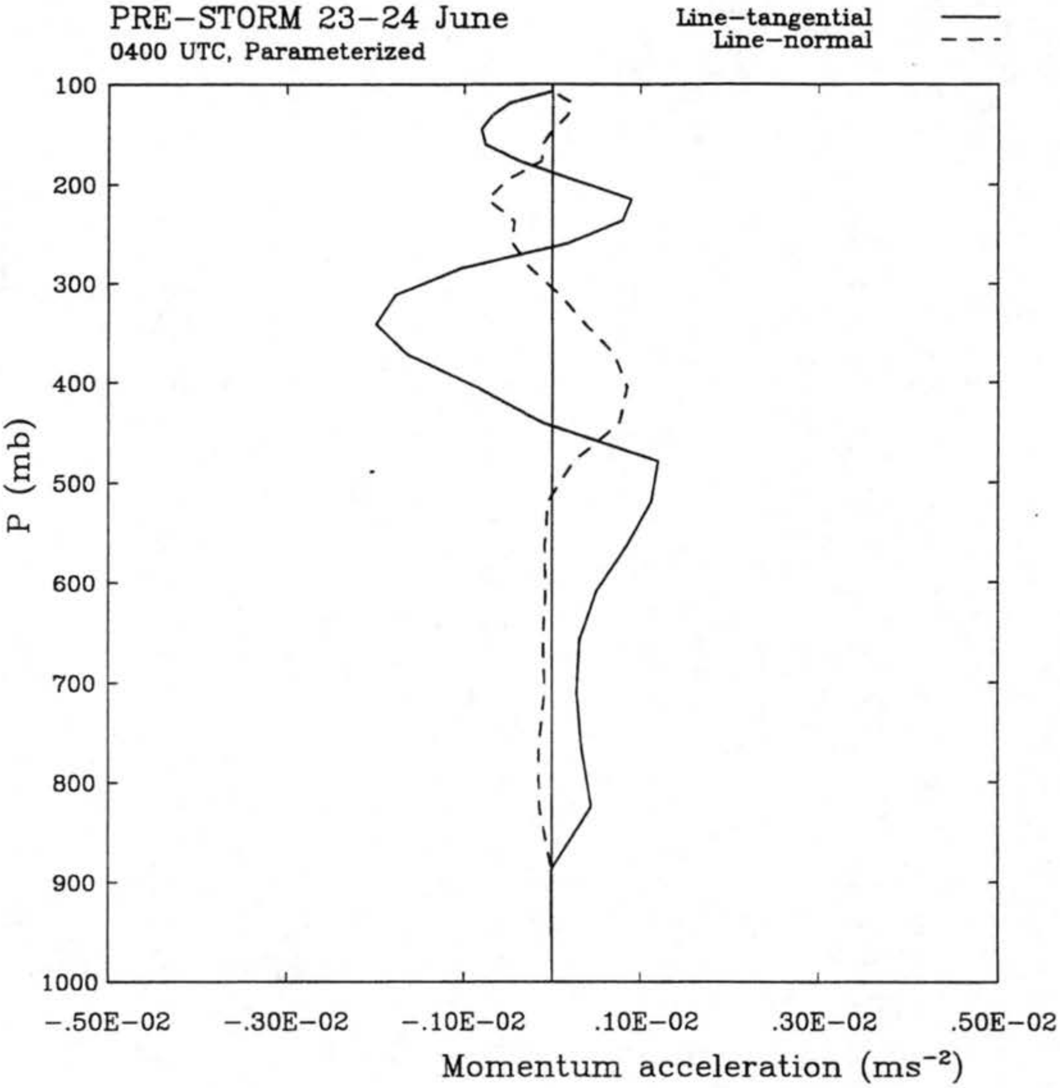

Fig. 5.21: Vertical profiles of the parameterized line-tangential and line-normal momentum acceleration at 0400 UTC for when the momentum parameterization is applied using the entrainment-detrainment terms only.

(a)

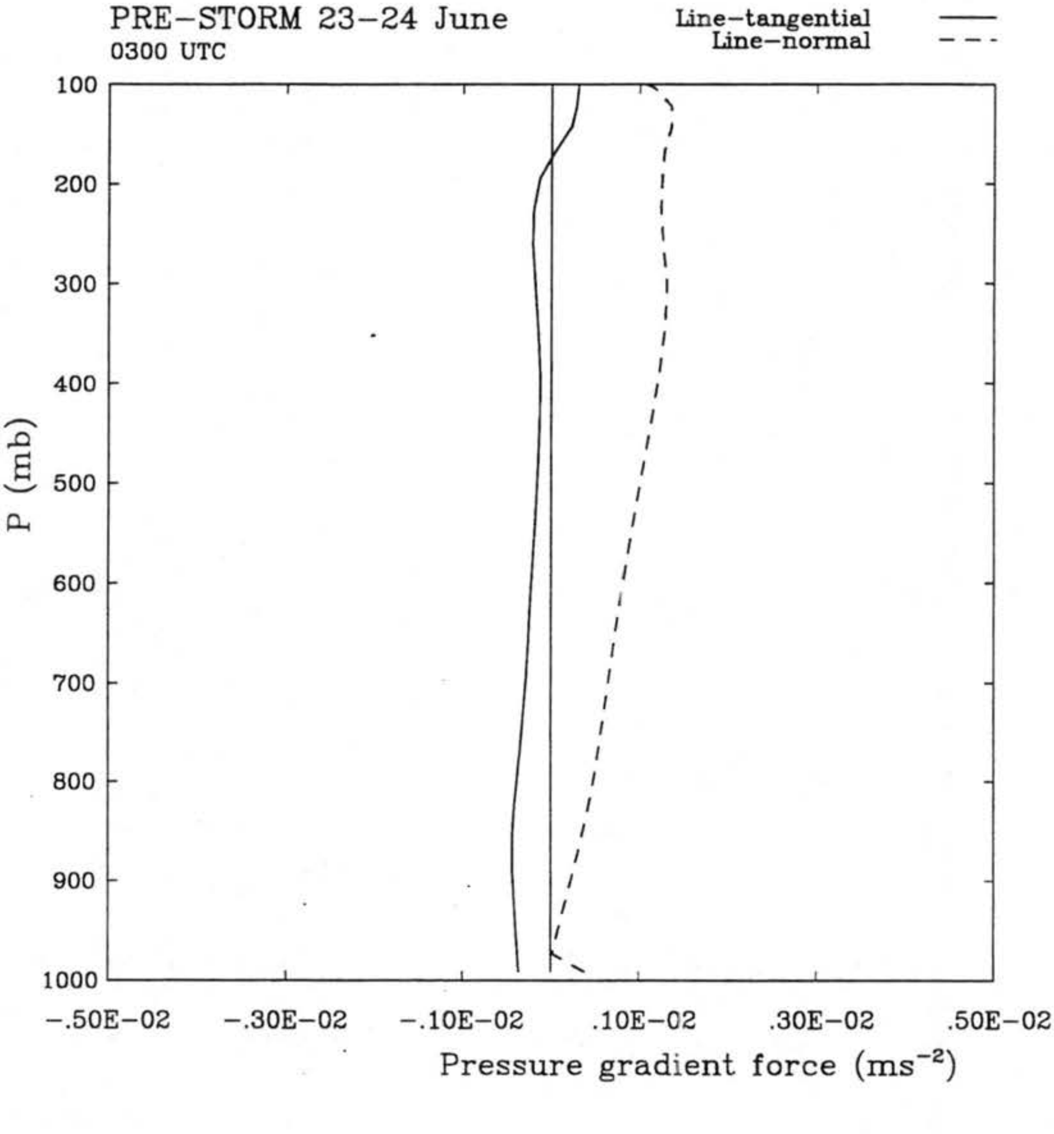
PRE–STORM 23–24 June
0300 UTC
Line–tangential
Line–normal
P (mb)
100
200
300
400
500
600
700
800
900
1000
–.50E–02
–.30E–02
–.10E–02
.10E–02
.30E–02
.50E–02
Pressure gradient force (ms⁻²)

(b)

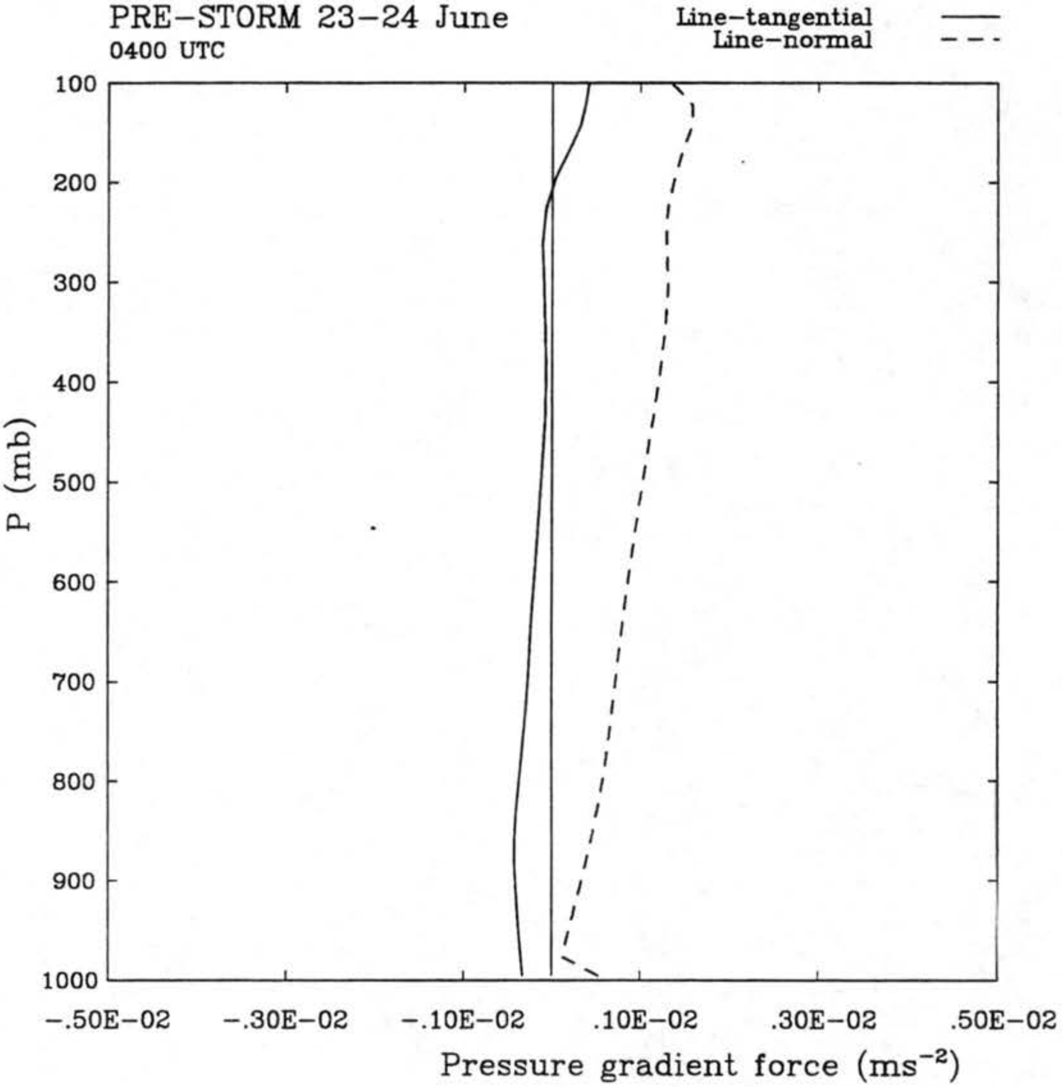

Fig. 5.22: Vertical profiles of the Grid #2 mean line-normal and line-tangential pressure gradient force at (a) 0300 UTC and (b) 0400 UTC. A positive line-normal pressure gradient force represents acceleration from front-to-rear. A positive line-tangential pressure gradient force represents acceleration from left-to-right as seen from ahead of the line.

Chapter 6

CONCLUSIONS

6.1 Summary

A framework has been described for parameterizing the mesoscale flow branches of MCSs in models with resolution too coarse to resolve these flow branches. The thermodynamic part of the parameterization is analogous to the formulation of Donner (1993), with improvements of a more sophisticated convective driver (the Arakawa-Schubert convective scheme with convective downdrafts) and inclusion of the vertical distribution of various physical processes obtained through conditional sampling of two cloud-resolving MCS simulations. The Wu and Yanai (1994) convective momentum parameterization has also been included as a separate component of the parameterization scheme. The mesoscale parameterization is tied to a version of the Arakawa-Schubert convective parameterization scheme which is modified to employ a prognostic closure, as described by Randall and Pan (1993). The parameterized Arakawa-Schubert cumulus convection provides condensed water, ice, and water vapor which drives the parameterization for the large-scale effects of mesoscale circulations associated with the convection.

The mesoscale thermodynamic parameterization is developed with the idea that determining thermodynamic forcing of the large scale depends on knowing the vertically-integrated values and the vertical distributions of the following quantities: (1) deposition and condensation in mesoscale updrafts, (2) freezing in mesoscale updrafts, (3) sublimation in mesoscale updrafts, (4) sublimation and evaporation in mesoscale downdrafts, (5) melting in mesoscale downdrafts, and (6) mesoscale eddy fluxes of entropy and water vapor. The relative magnitudes of these quantities are constrained by assumptions made about the relationships between various quantities in an MCS's water budget deduced from three-dimensional cloud-resolving MCS simulations

The MCS simulations presented here include one of a tropical MCS observed during the 1987 Australian monsoon season (EMEX9), and one of a midlatitude MCS observed during a 1985 field experiment in the central Plains of the U.S. (PRE-STORM 23-24 June). For both simulations, the grid spacing on the finest grid is fine enough (1500 m for EMEX9, 2083 m for PRE-STORM) that no convective parameterization scheme is required. In each case, the finest grid covers an area on the order of tens of thousands square kilometers ($\sim$ 18,000 km^2 for EMEX9, $\sim$ 17,300 km^2 for PRE-STORM). Each simulation is run for several hours using all grids and no convective parameterization (4.5 hours for EMEX9, 3.5 hours for PRE-STORM 23-24 June). Each simulation yields a data set that can only be described as monstrous (40 variables every 15 minutes on 454,860 grid points for EMEX9 and on 543,136 grid points for PRE-STORM). In both cases, the model simulates organized convection and an adjacent stratiform region which closely resemble the observed system. The analysis of these data then focuses on conditional sampling of the stratiform region of each system.

The conditional sampling of the fine grid data of each MCS simulation attempts to identify mesoscale updrafts and mesoscale downdrafts within the stratiform region of each system. Convective/stratiform partitioning criteria are those used by Tao et al. (1993), which are based primarily on surface precipitation rate. These criteria require the stratiform region to be raining, which eliminates columns containing nonprecipitating anvil clouds. After two-dimensionally separating the MCS into convective and stratiform regions, mesoscale updrafts and mesoscale downdrafts are isolated within the stratiform region. Here, the conditional sampling is done on a gridpoint-by-gridpoint basis (not column-by-column) to allow the updrafts and downdrafts to have vertical structure or slant. Spatial coherence of mesoscale drafts is also required, however, with the core grid point and all contiguous grid points required to have vertical velocity of the same sign to be considered a mesoscale draft. Once these mesoscale updraft and downdrafts are identified, vertical profiles of physical processes in these conditionally-sampled mesoscale updrafts and downdrafts are used to determine the shapes of vertical profiles of various physical processes as well as relationships between various components of an MCS's water budget.

The scheme is then tested by comparing the heating and drying tendencies produced by feeding it mean soundings from the simulations with tendencies diagnosed from the conditional sampling of the simulations. As designed, the scheme is of course going to be sensitive to values of the parameters deduced from the conditional sampling. These parameters include:

(1) the depth and shape parameters for the vertical profiles of all phase transforma-

tions,

(2) the ratios among the vertically-integrated values of

(a) the sublimation in mesoscale updrafts,

(b) the evaporation plus sublimation in mesoscale downdrafts, and

(c) the mesoscale precipitation, and

(3) the ratios of

(a) the vertically-integrated evaporation to the vertically-integrated sublimation in mesoscale downdrafts and

(b) the vertically-integrated condensation to the vertically integrated deposition in mesoscale updrafts.

All of the quantities listed above are determined using one hour of fine grid data from each simulation. However, the parameterization is tested on four hours of data for the EMEX9 simulation and three hours of data for the PRE-STORM simulation. Agreement between parameterized and diagnosed heating and drying tendencies is very good for both cases. As an additional test of the sensitivity of the scheme to specified values of the quantities listed above, we use the EMEX9 values of these parameters for a parameterization of PRE-STORM tendencies. As expected, the parameterization does not do quite as good a job of reproducing the exact shapes of the tendency profiles, but the agreement is at least reasonable. In practice, it would be difficult to decide on appropriate values of these "tunable" parameters. The values presented here, along with those presented elsewhere in published literature, suggest a reasonable range for each parameter, however.

The convective momentum parameterization is tested in much the same way as is the thermodynamic parameterization. That is, the output of the parameterized momentum tendencies computed by feeding the scheme grid mean soundings are compared with the diagnosed momentum budget residuals on the fine grid of each simulation. For each MCS, an effort is made to see whether including the convective-scale pressure gradient force term improves the performance of the momentum parameterization. This pressure gradient term might be expected to be particularly important for mesoscale convective systems whose convection is arranged linearly. It is found that for EMEX9, taking this pressure gradient term into account does not improve the results of the momentum parameterization. On the other hand, for the PRE-STORM 23-24 June MCS, including this term does improve the results. It is hypothesized that the fundamental difference between the two simulations is that the simulated EMEX9 MCS does not develop a broad-scale organized pressure perturbation field whereas the PRE-STORM MCS does. Intuitively, this makes sense, as the EMEX9 convection evolves from almost perfect linearity to a more scattered mesoscale organization as the simulation proceeds whereas the PRE-STORM 23-24 June MCS maintains its linearity. This intuition is supported by an analysis of the vertical profile of the line-normal component of the pressure gradient force on Grid #2 of each simulation. For EMEX9, this quantity starts out small and eventually becomes nearly zero throughout most of the troposphere. For PRE-STORM, a cross-line pressure gradient force maintains its magnitude for the entire simulation. It seems reasonable that the two simulated MCSs should differ in their degree of balance, as their scale relative to the local Rossby radius of deformation is quite different. Cotton et al. (1989) discussed the importance of an MCS's scale relative to the Rossby radius. The PRE-STORM 23-24 June MCS, as a midlatitude system, is much more likely to evolve into a balanced MCS as convective heating projects its energy into the balanced flow.

In light of these results, it is suggested that the parameterization of the acceleration of large-scale momentum by the convective-scale pressure gradient force should be handled with caution. It certainly seems possible that there will be occasions when, even for linear convection, the spatial scale of the pressure perturbation field will be small enough that there will be plenty of room for corresponding areas of oppositely-directed pressure gradient acceleration in the same grid box. Thus, even if we are confident that we can determine line-orientation, do we really want to parameterize its effects?

6.2 Unresolved issues

6.2.1 Activation of scheme

A key issue which has not been addressed in this study is how the mesoscale parameterization scheme should be activated. Although, the Arakawa-Schubert scheme can tell us whether deep convection is expected, it does not tell us whether it will be organized on the mesoscale or not. This problem is the subject of ongoing research by another member of the CSU cloud dynamic group, Hongli Jiang, and is discussed briefly here.

The means by which convection becomes organized are complex—there are many ways it can happen. Convection, by its very nature, tends to promote new convection around it. For instance, convection that is initially "randomly" scattered may organize itself, as moisture detrained from initial convective cells creates an environment around the cells which promotes additional cell development (e.g., Randall and Huffman 1980; Simpson et al. 1980). The theory advanced by Nicholls et al. (1991) and Mapes (1993) describes another way convection may organize itself. Here, an MCS-like heat source promotes, through inviscid gravity wave dynamics, upward displacements at low levels in a mesoscale region surrounding the heat source. Another theory suggests that a main organizing mechanism of convection in MCSs is that the pool of cold downdraft air at the surface triggers new convective cells (e.g., Mapes and Houze 1992).

In the absence of vorticity sources and sinks, shear is typically detrimental to organized convection (e.g., Asai 1964). Otherwise, however, the opposite may be true. Two- and three-dimensional modeling studies suggest that environmental wind shear critically governs if and how organized convection evolves. For instance, Rotunno et al. (1988) presented numerical simulations which showed that there is an optimal condition for producing uplift at a gust front (the front leading the cold pool). They showed that this optimal condition occurs when the import of vorticity associated with low-level environmental shear balances the circulation induced by the cold outflow. Weisman (1992) elucidated on the Rotunno et al. theory, describing how organized convection evolves systematically in response to the development and intensification of a convectively generated cold pool (Fig. 6.1). Early on, the convective cells lean downshear in response to the environmental shear. As the cold pool strengthens, the cells become more upright. Finally, the convection tilts upshear in response to negative horizontal vorticity generated at the cold pool's leading edge. During this upshear-tilting phase, the stratiform region and rear-to-front descending flow branch gradually evolve. The time period over which the whole sequence unfolds (and if, indeed, it does) depends on both the strength of the cold pool and the strength of the low-level ambient wind shear.

The degree to which convection is organized also appears to depend on the thermodynamic structure of the environment. Cheng (1989) showed, for instance, that the degree of mesoscale convective organization for GATE MCSs was closely related to a thermodynamically diagnosed updraft tilting angle. Cheng diagnosed the tilting angle by using a cumulus ensemble model which considered the vertical momentum and rainwater budgets of cumulus updrafts. For GATE convection, horizontal distributions of this tilting angle exhibited local maxima in areas of organized convection. The distributions were more uniform, however, when only scattered convection was present. The tilting angle's importance is tied to its role in the updraft rainwater budget. Cheng's cumulus ensemble model considers that convective-scale downdrafts are dynamical phenomena resulting from rainwater falling through the subsaturated cloud environment. Because the rainwater originates in the updraft, the amount of tilt of the updraft will dictate how much rainwater can separate from the updraft—tilted updrafts can successfully unload their rainwater whereas upright updrafts may

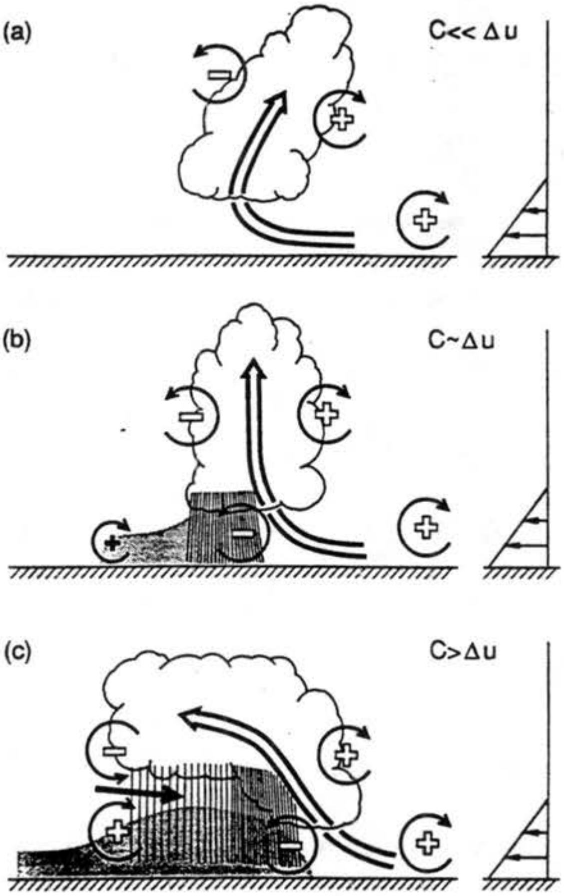

Fig. 6.1: Three stages in the evolution of a convective system. The system tilt evolves through a (a) downshear, (b) vertical, and (c) upshear orientation over time. From Weisman (1992).

suffer a perilous fate as water loading kills their buoyancy. Thus, the thermodynamically diagnosed tilting angle is essentially the mean angle required for a statistically steady updraft subensemble to maintain its buoyancy against water loading.

The role of tilting angle and low-level shear in maintaining organized convection are closely coupled. Consider why for a moment. A larger tilting angle typically yields a larger downdraft mass flux relative to the updraft mass flux. The larger downdraft mass flux maintains a more robust cold pool. And, as discussed above, it is the interaction of the vorticity of the cold pool and that of low-level flow that creates conditions ripe for organized convection. So the updraft tilt and low-level shear work in concert with one another, with organized convection generally needing both. Cheng and Yanai (1989), for example, evaluated both the low-level shear ($S \equiv |\mathbf{v}(700\text{mb}) - \mathbf{v}(950\text{mb})|$) and the updraft tilting angle for deep clouds for about three weeks during GATE. The two quantities are remarkably correlated with maxima in vertical wind shear generally lagging those in diagnosed tilting angle (Fig. 6.2), and the diagnosed tilting angle typically increasing simultaneously with the mass flux of deep clouds associated with squall clusters.

Ideally, an MCS parameterization could consider both the environmental low-level shear *and* the updraft tilting angle, with MCSs likely to be triggered where the former is sufficiently large and the latter exhibit local maxima. Obtaining the low-level shear is trivial: the host model provides it. Obtaining the updraft tilting angle requires a sophisticated updraft/downdraft model such as the one described by Cheng and Yanai (1989).

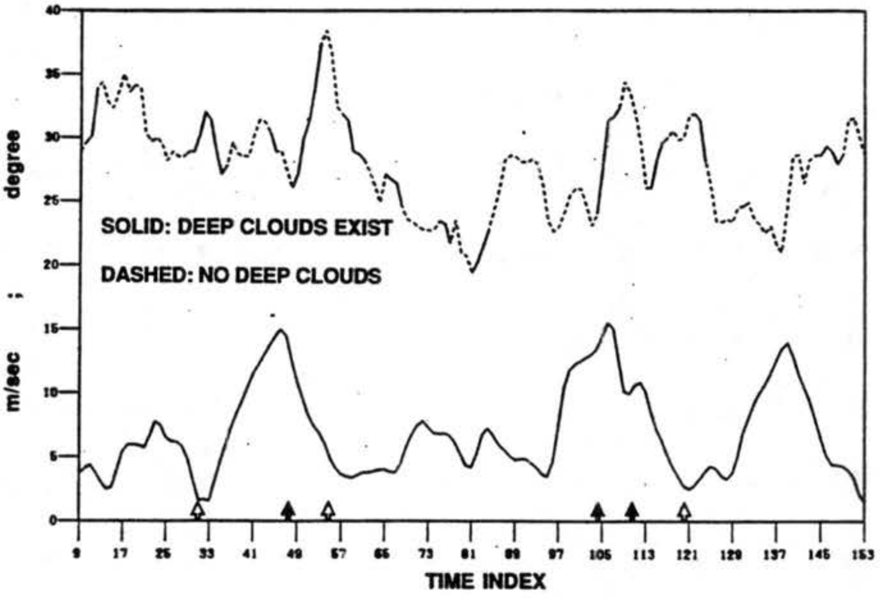

Fig. 6.2: Time series of the diagnosed updraft tilting angle (upper; degrees) and the vertical wind shear between 700 and 950 mb (lower; ms^{-1}) at the center of the GATE network form 0000 UTC 31 August 1974 (Time index 9) to 0000 UTC 18 September 1974 (Time index 153). From Cheng and Yanai (1989).

In practice, a simple way to activate the mesoscale component of the scheme could be to track a quantity dubbed "mesoscale kinetic energy" (MKE) by another member of our research group, Scot Rafkin. Actually, the term MKE has been used previously in the context of mesoscale circulations which develop in response to land surface heteorogeneities (Avissar and Chen 1993). The MKE is an extension of the concept of cumulus kinetic energy (CKE) discussed by Lord and Arakawa (1980) and Randall and Pan (1993), among others. An equation for subgrid-scale MKE can be developed in a way analogous to Randall and Pan's equation for subgrid-scale CKE (as Avissar and Chen have done). The mesoscale parameterization could then either be turned on or off if the MKE exceeds a certain threshold or could have its tendencies modulated by the magnitude of the MKE. This is consistent with the concept that an MCS represents a more balanced form of convection (Olsson 1995). That is, a signature of a balanced MCS would be the amount of kinetic energy residing in the mesoscale flow branches.

The MKE would have two fundamental sources/sinks. The first would be a source/sink from CKE and the second would be an internal source/sink due to the parameterized mesoscale circulation itself. The direct pathway between CKE and MKE is simply based on our observations and intuition that the mesoscale region is driven by convection. The CKE could evolve upscale to produce MKE or could evolve downscale to destroy MKE. The internal source of MKE could be a function of the mesoscale heating itself, among other things; the internal sink of MKE would probably be tied to a simple dissipation term like the one in the Randall and Pan

CKE equation. The appropriate way to parameterize each term in an equation for MKE is a difficult question and is a subject of ongoing research in our group.

6.2.2 Convection: Linear or not?

If it is determined that the mesoscale portion of the scheme should be activated, an additional question whose answer would be useful to the momentum scheme is whether the convection will be arranged in a line. Wu and Yanai's parameterization shows that momentum forcing resulting from accelerations by the convective-scale horizontal pressure gradient force depends on the arrangement of convection, thus the values of γ_k and γ_l should be adjusted accordingly. Can large-scale variables be used to determine whether convection will be linear? Observations indicate that, more often than not, organized convection *is* oriented in lines. But not always. For instance, Houze et al. (1990) estimated that between $\frac{2}{3}$ and $\frac{3}{4}$ of the MCSs they studied were organized in linear convective bands during some part of their life cycle. How, then, do large-scale properties tell us whether we'll get a line or not?

In the previous section, it is suggested that to get MCSs, the low-level shear needs to exceed a critical threshold. Observational evidence indicates that to get linear rather than nonlinear convection, the low-level wind profile is also important. However, it is not so much the magnitude of the shear that's important as it is the presence of a low-level jet (as we'll see, the two are not identical). Consider, for instance, observations from GATE. Houze and Betts (1981) noticed two main regimes of mesoscale organization in GATE—so-called squall and nonsquall clusters. Squall clusters are characterized by fast-moving convective lines trailed by large areas of stratiform precipitation. Nonsquall clusters, on the other hand, have more chaotically placed convective elements (still accompanied by large areas of stratiform precipitation) and typically move slower than squalls. Frank (1978) investigated the question of which large-scale factors modulate the type of mesoscale organization (squall or nonsquall). He found that the vertical wind shear in the lower troposphere was the distinguishing difference in the environments—squall cluster environments had about twice as much easterly shear between the surface and 650 mb than did nonsquall environments (13 ms^{-1} as compared to 6 ms^{-1}). This shear threshold essentially identifies the presence of an easterly jet over the east Atlantic. Barnes and Sieckman (1984) also noted that squall clusters in GATE were closely related to the appearance of a low-level easterly jet near 650 mb whereas nonsquall clusters there were not.

Houze et al. (1990) examined the mesoscale structure of MCSs over Oklahoma and again showed that the low-level jet's strength was critical in determining whether convection was linear or not. However, their observations also made it clear that looking at the speed shear between two given levels (say, the surface and 500 mb) is not sufficient. This can be understood by realizing that a jet can be confined completely in-between two arbitrary levels. Houze et al. considered MCSs to be "classifiable" if they strongly resembled the leading-line/trailing stratiform structure and "unclassifiable" if the convection was chaotically organized. After examining environmental soundings, Houze et al. concluded that as MCSs progressed from being unclassifiable to classifiable the hodograph *curvature* below 500 mb increased significantly. Through the same layer, however, the magnitude of the speed shear actually decreased. The sharp hodograph curvature associated with linear convection was associated with the Great Plains southerly low-level jet, suggesting that a stronger low-level jet promotes the organization of convective cells into a line.

Wu and Yanai (1994) also show the importance of a low-level jet in determining whether convection will be linear. Because they only consider low-level *speed* shear, however, one must scrutinize their plots carefully to see this. Their scatter diagrams of the cloud work function (essentially the convective available potential energy) and the low-level vertical shear for SESAME, PRE-STORM, and GATE show that large low-level vertical shear of the horizontal wind is a key environmental factor separating squall lines and squall clusters from MCCs and nonsquall clusters (Fig. 6.3). However, looking carefully at the PRE-STORM and SESAME plots (both experiments were in the south-central U.S), you can see that many of the *weakest* speed shear cases are actually squall lines rather than MCCs. The southerly jet could still have been strong for these weak shear cases—we don't know for sure though. The GATE plot, on the other hand, shows an almost perfect speed shear cutoff between squall lines and chaotic convection. These plots also show that mesoscale organization is apparently not very sensitive to the convective available potential energy.

Numerical results support observations that a curved low-level hodograph (i.e., low-level jet) supports linear convection. Balaji and Clark (1988) and Hauf and Clark (1989), for instance, simulated the initiation and growth of deep convection in a disturbed boundary layer using differing shear profiles. For a curved hodograph, veering 90° through the low-level mixed layer and exhibiting speed shear alone

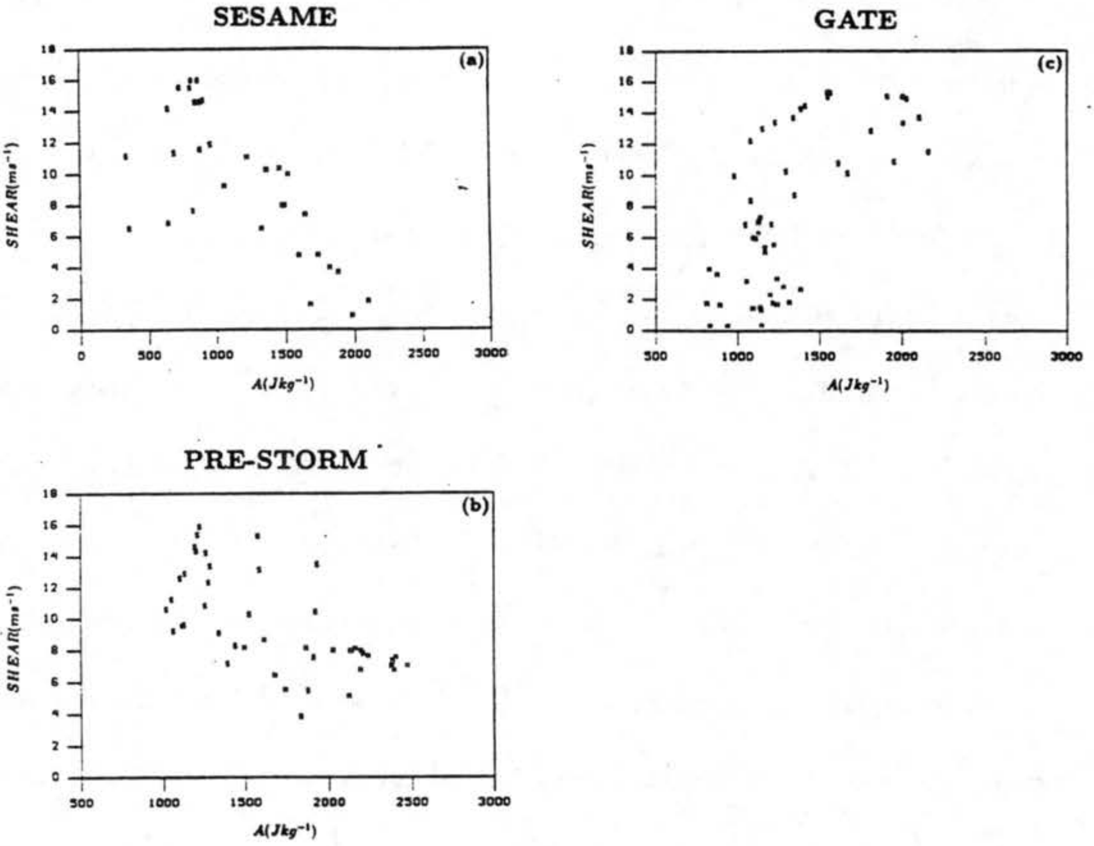

Fig. 6.3: Scatter diagrams of the cloud work function (A) of deep clouds versus the low-level vertical wind shear for grid points in the convective region during (a) SESAME, (b) PRE-STORM, and (c) GATE. The low-level vertical wind shear is defined by $|\mathbf{v}(900\text{mb}) - \mathbf{v}(700\text{mb})|$ in SESAME, $|\mathbf{v}(900\text{mb}) - \mathbf{v}(750\text{mb})|$ in PRE-STORM, and $|\mathbf{v}(950\text{mb}) - \mathbf{v}(700\text{mb})|$ in GATE. "M" represents an MCC or a non-squall cloud cluster; "s" represents a squall line or squall cloud cluster. From Wu and Yanai (1994).

above the inversion, the resulting convection was oriented in bands parallel to the mid-tropospheric shear vector. On the other hand, simulations with a straight-line hodograph (i.e., appreciable speed shear but no low-level jet) produced chaotically arranged convection.

All of the observations and numerical simulations above suggest that the single most important criterion to examine in order to determine whether MCS convection is linear or not is whether a low-level jet is present. The curvature (or length) of the large-scale hodograph in, say, the lowest 300 mb should exceed a certain value before linear convection is allowed. If linear convection is allowed, the final problem is to determine what its orientation (e.g., north-south, east-west, or whatever) is likely to be. Observations suggest that squall lines are typically aligned nearly normal to a vertical shear vector pointing from the base to core of the low-level jet (e.g., Betts et al. 1976, Barnes and Sieckman 1984, Roux 1988, Keenan and Carbone 1992). Sometimes, however, convective lines are instead observed to be oriented parallel to a midlevel shear vector (e.g. Barnes and Sieckman's "slow" convective lines) as in the Clark numerical simulations discussed above. Alexander and Young (1992) demonstrated, that at least for EMEX convection, whether convective lines are oriented normal to the low-level shear or parallel to the midlevel shear depends on the *magnitude* of the low-level environmental shear. Seven of ten EMEX convective lines were oriented normal to the low-level shear vector—for each of these seven lines the magnitude of this shear exceeded 5 ms^{-1}. For the three exceptions, the magnitude of the shear from the base to the core of the jet was less than 5 ms^{-1}—these lines were oriented parallel to the midlevel shear vector.

In summary, the primary issues that future research should focus on include (1) development of crtieria for deciding when to activate the mesoscale part of the parameterization, (2) development of criteria for determining if and how the environmental momentum is accelerated by the pressure gradient acceleration, and (3) further evaluation of the mesoscale parameterization with an ensemble of independent cases.

REFERENCES

Ackerman, T.P., K.-N. Liou, F.P.J. Valero and L. Pfister, 1988: Heating rates in tropical anvils. *J. Atmos. Sci.*, **45**, 1606-1623.

Alexander, G.D, and G.S. Young, 1992: The relationship between EMEX mesoscale precipitation feature properties and their environmental characteristics. *Mon. Wea. Rev.*, **120**, 554-564.

Arakawa, A., and M-D. Cheng, 1993: The Arakawa-Schubert Cumulus Parameterization. *Meteorological monographs: The representation of cumulus convection in numerical models*, K.A. Emanuel and D.J. Raymond, eds., 123-136.

Asai, T., 1964: Cumulus convection in the atmosphere with vertical wind shear: Numerical experiments. *J. Meteor. Soc. Japan*, **42**, 245-259.

Avissar, R., and F. Chen, 1993: Development and analysis of prognostic equations for mesoscale kinetic energy and mesoscale (subgrid scale) fluxes for large-scale atmospheric models. *J. Atmos. Sci.*, **50**, 3751-3774.

Balaji, V., and T.L. Clark, 1988: Scale selection in locally forced convective fields and the initiation of deep cumulus. *J. Atmos. Sci.*, **45** , 3188-3211.

Barnes, G.M., and K. Sieckman, 1984: The environment of fast- and slow-moving tropical mesoscale convective cloud lines. *Mon. Wea. Rev.*, **112**, 1782-1794.

Barnes, S.L., 1973: Mesoscale objective map analysis using weighted time-series observations. NOAA Tech. Memo. ERL NSSL-62 [NTIS COM-73-10781], March, National Severe Storms Laboratory, Norman, Oklahoma, 60 pp.

Bélair, S., D.-L. Zhang and J. Mailhot, 1994: Numerical prediction of the 10-11 June 1985 squall line with the Canadian Regional Finite Element Model. *Wea. Forecasting*, **9**, 157-172.

Bernstein, B.C. and R.H. Johnson, 1994: A dual-Doppler radar study of an OK PRE-STORM heat burst event. *Mon. Wea. Rev.*, **122** , 259-273.

Betts, A.K., R.W. Grover and M.W. Moncrieff, 1976: Structure and motion of tropical squall lines over Venezuela. *Quart. J. Roy. Meteor. Soc.*, **102**, 395-404.

Bernstein, B.C. and R.H. Johnson, 1994: A dual-Doppler radar study of an OK PRE-STORM heat burst event. *Mon. Wea. Rev.*, **122**, 259-273.

Bograd, S.J., 1989: The mesoscale structure of precipitation in EMEX cloud clusters. M.S. thesis, University of Washington, 143 pp.

Bretherton, C.S., and P.K. Smolarkiewicz, 1989: Gravity waves, compensating subsidence and detrainment around cumulus clouds. *J. Atmos. Sci.*, **46**, 740-759.

Browning, K.A., A. Betts, P.R. Jonas, R. Kershaw, M. Manton, P.J. Mason, M. Miller, M.W. Moncrieff, H. Sundqvist, W.K. Tao, M. Tiedtke, P.V. Hobbs, J. Mitchell, E. Raschke, R.E. Stewart and J. Simpson, 1993: The GEWEX Cloud System Study (GCSS). *Bull. Amer. Meteor. Soc.*, **74**, 387-399.

Chen, S., and W.R. Cotton, 1983: A one-dimensional simulation of the stratocumulus-capped mixed layer. *Bound.-Layer Meteor.*, **25**, 289-321.

Cheng, M.-D., 1989: Effects of downdrafts and mesoscale convective organization on the heat and moisture budgets of tropical cloud clusters. Part I: A diagnostic cumulus ensemble model. *J. Atmos. Sci.*, **46**, 1517-1538.

Cheng, M.-D., and M. Yanai, 1989: Effects of downdrafts and mesoscale convective organization on the heat and moisture budgets of tropical cloud clusters. Part III: Effects of mesoscale convective organization. *J. Atmos. Sci.*, **46**, 1566-1588.

Chong, M., and D. Hauser, 1989: A tropical squall line observed during the COPT81 experiment in West Africa: Part II: Water budget. *Mon. Wea. Rev.*, **117**, 728-744.

Churchill, D.D., and R.A. Houze, Jr., 1984: Development and structure of winter monsoon cloud clusters on 10 December 1978. *J. Atmos. Sci.*, **41**, 933-960.

Cotton, W.R., G.D. Alexander, R. Hertenstein, R.L. Walko, R.L. McAnelly, M. Nicholls, and J. Eastman, 1995: Cloud venting. *Earth Sci. Rev.*, **39**, 169-206.

Cotton, W.R., and R.A. Anthes, 1989: *Storm and Cloud Dynamics. Int. Geophys. Ser.*, Vol. 44. Academic Press, 883 pp.

Cotton, W.R., G.J. Tripoli, R.M. Rauber and E.A. Mulvihill, 1986: Numerical simulation of the effects of varying ice crystal nucleation rates and aggregation processes on orographic snowfall. *J. Climate Appl. Meteor.*, **25**, 1658-1680.

Cotton, W.R., M.-S. Lin, R.L. McAnelly and C.J. Tremback, 1989: A composite model of mesocale convective complexes. *Mon. Wea. Rev.*, **117**, 765-783.

Cram, J.M., R.A. Pielke and W.R. Cotton, 1992: Numerical simulation and analysis of a prefrontal squall line. Part I: Observations and basic simulation results. *J. Atmos. Sci.*, **49**, 189-208.

Cunning, J.B., 1986: The Oklahoma-Kansas Preliminary Regional Experiment for STORM-Central. *Bull. Amer. Meteor. Soc.*, **67**, 1478-1486.

Donner, L.J., 1993: A cumulus parameterization including mass fluxes, vertical momentum dynamics, and mesoscale effects. *J. Atmos. Sci.*, **50**, 889-906.

Flatau, P.J., G.J. Tripoli, J. Verlinde and W.R. Cotton, 1989: The CSU-RAMS cloud microphysics module: General theory and code documentation. Colorado State University Department of Atmospheric Science Research Paper No. 451, 88 pp.

Fortune, M.A., Willam R. Cotton and R.L. McAnelly, 1992: Frontal wave-like evolution in some mesoscale convective complexes. *Mon. Wea. Rev.*, **120**, 1279-1300.

Frank, W.M., 1978: The life cycles of GATE convective systems. *J. Atmos. Sci.*, **35**, 1256-1264.

Fritsch, J.M., and C.F. Chappel, 1980: Numerical prediction of convectively driven mesoscale pressure systems. Part I: Convective parameterization. *J. Atmos. Sci.*, **37**, 1722-1733.

Fritsch, J.M., R.J. Kane and C.R. Chelius, 1986: The contribution of mesoscale convective weather systems to the warm-season precipitation in the United States. *J. Clim. Appl. Meteor.*, **25**, 1333-1345.

Gallus, W.A., Jr., and R.H. Johnson, 1991: Heat and moisture budgets of an intense midlatitude squall line. *J. Atmos. Sci.*, **48**, 122-146.

Gallus, W.A., Jr., and R.H. Johnson, 1992: The momentum budget of an intense midlatitude squall line. *J. Atmos. Sci.*, **49**, 422-450.

Gamache, J.F., and R.A. Houze, Jr., 1982: Mesoscale air motions associated with a tropical squall line. *Mon. Wea. Rev.*, **110**, 118-135.

Gamache, J.F., and R.A. Houze, Jr., 1983: Water budget of a mesoscale convective system in the tropics. *J. Atmos. Sci.*, **40**, 1835-1850.

Gamache, J.F., F. Marks, Jr. and R.W. Burpee, 1987: EMEX data report: The Equatorial Mesoscale Experiment. AOML/HRD Report, National Oceanic and Atmospheric Administration, Atlantic Oceanographic and Meteorological Laboratory, Hurricane Research Division, Miami.

Gunn, B.W., J.L. McBride, G.J. Holland, T.D. Keenan, N.E. Davidson and H.H. Hendon, 1989: The Australian summer monsoon circulation during AMEX Phase II. *Mon. Wea. Rev.*, **117**, 2554-2574.

Hauf, T., and T.L. Clark, 1989: Three-dimensional numerical experiments on convective forced internal gravity waves. *Quart. J. Roy. Meteor. Soc.*, **115**, 309-333.

Hendon, H.H., N.E. Davidson and B. Gunn, 1989: Australian summer monsoon onset during AMEX 1987. *Mon. Wea. Rev.*, **117** , 370-390.

Holton, J.R., 1979: *An Introduction to Dynamic Meteorology.* Academic Press, 391 pp.

Houze, R.A., Jr., 1977: Structure and dynamics of a tropical squall line system. *Mon. Wea. Rev.*, **105**, 1540-1567.

Houze, R.A., Jr., 1982: Cloud clusters and large-scale vertical motions in the tropics. *J. Meteor. Soc. Jap.*, **60**, 396-409.

Houze, R.A., Jr., 1989: Observed structure of mesoscale convective systems and implications for large-scale heating. *Quart. J. Roy. Meteor. Soc.*, **115**, 425-461.

Houze, R.A., Jr., and A.K. Betts, 1981: Convection in GATE. *Rev. Geophys. Space Phys.*, **19**, 541-576.

Houze, R.A., Jr., S.A. Rutledge, M.I. Biggerstaff and B.F. Smull, 1989: Interpretation of Doppler weather-radar displays in midlatitude mesoscale convective systems. *Bull. Amer. Meteor. Soc.*, **70**, 608-619.

Houze, R.A., Jr., B.F. Smull and P. Dodge, 1990: Mesoscale organization of spring-time rainstorms in Oklahoma. *Mon. Wea. Rev.*, **118**, 613-654.

Johnson, R.H., 1976: The role of convective-scale precipitation downdrafts in cumulus and synoptic-scale interactions. *J. Atmos. Sci.*, **33**, 1890-1910.

Johnson, R.H., and D.L. Bartels, 1992: Circulations associated with a mature-to-decaying midlatitude mesoscale convective system. Part II: Upper level features. *Mon. Wea. Rev.*, **120**, 1301-1320.

Johnson, R.H., S. Chen and J.J. Toth, 1989: Circulations associated with a mature-to-decaying midlatitude mesoscale convective system. Part I: Surface features—heat bursts and mesolow development. *Mon. Wea. Rev.*, **117**, 942-959.

Johnson, R.H., and D.C. Kriete, 1982: Thermodynamic and circulation characteristics of winter monsoon tropical mesoscale convection. *Mon. Wea. Rev.*, **110**, 1898-1911.

Johnson, R.H., and G.S. Young, 1983: Heat and moisture budgets of tropical mesoscale anvil clouds. *J. Atmos. Sci*, **40**, 2138-2147.

Keenan, T.D., and R.E. Carbone, 1992: A preliminary morphology of precipitation systems in tropical northern Australia. *Quart. J. Roy. Meteor. Soc.*, **118**, 283-326.

Keenan, T.D., J. McBride, G. Holland, N. Davidson and B. Gunn, 1989: Diurnal variation during the Australian Monsoon Experiment (AMEX) Phase II. *Mon. Wea. Rev.*, **117**, 2535-2552.

Klemp, J.B., and R.B. Wilhelmson, 1978a: The simulation of three-dimensional convective storm dynamics. *J. Atmos. Sci.*, **35**, 1070-1096.

Klemp, J.B., and R.B. Wilhelmson, 1978b: Simulations of right- and left-moving storms produced through storm splitting. *J. Atmos. Sci.*, **35**, 1097-1110.

Lafore, J.-P., and M.W. Moncrieff, 1989: A numerical investigation of the organization and interaction of the convective and stratiform regions of tropical squall lines. *J. Atmos. Sci.*, **46**, 521-544.

Leary, C.A., and R.A. Houze, Jr., 1980: The contribution of mesoscale motions to the mass and heat fluxes of an intense tropical convective system. *J. Atmos. Sci.*, **37**, 784-796.

Lee, T.J., 1992: The impact of vegetation on the atmospheric boundary layer and convective storms. Ph.D. dissertation, Colorado State University, 137 pp.

LeMone, M.A., and M.W. Moncrieff, 1994: Momentum and mass transport by convective bands: Comparisons of highly idealized dynamical models to observations. *J. Atmos. Sci.*, **51**, 281-305.

Lord, S.J., and A. Arakawa, 1980: Interaction of a cumulus ensemble with the large-scale environment. Part II. *J. Atmos. Sci.*, **37** , 2677-2692.

Louis, J.F., 1979: A parametric model of vertical eddy fluxes in the atmosphere. *Bound.-Layer Meteor.*, **17**, 309-322.

Maddox, R.A., 1980: Mesoscale convective complexes. *Bull. Amer. Meteor. Soc.*,

61, 1374-1387.

Maddox, R.A., K.W. Howard, D.L. Bartels and D.M. Rodgers, 1986: Mesoscale convective complexes in the middle latitudes. Pp. 390-413 in *Mesoscale Meteorology and Forecasting.* P.S. Ray, Ed. Amer. Meteor. Soc., Boston.

Mapes, B.E., 1992: The Australian monsoon and its mesoscale convective systems. Ph.D. dissertation, University of Washington.

Mapes, B.E., 1993: Gregarious tropical convection. *J. Atmos. Sci.*, **50**, 2026-2037.

Mapes, B., and R.A. Houze, 1992: An integrated view of the 1987 Australian monsoon and its mesoscale convective systems. I: Horizontal structure. *Quart. J. Roy. Meteor. Soc.*, **118**, 927-963.

Mapes, B., and R.A. Houze, Jr., 1993: An integrated view of the 1987 Australian monsoon and its mesoscale convective systems. II: Vertical structure. *Quart. J. Roy. Meteor. Soc.*, **119**, 733-754.

McBride, J.L., and W.M. Gray, 1980: Mass divergence in tropical weather systems. I. Diurnal variations. *Quart. J. Roy. Meteor. Soc.*, **106**, 501-516.

McCumber, M.C., and R.A. Pielke, 1981: Simulation of the effects of surface fluxes of heat and moisture in a mesoscale numerical model. Part I: Soil layer. *J. Geophys. Res.*, **86**, 9929-9938.

Miller, D., and J.M. Fritsch, 1991: Mesoscale convective complexes in the western Pacific region. *Mon. Wea. Rev.*, **119**, 2978-2992.

Moncrieff, M.W., 1981: A theory of organized steady convection and its transport properties. *Quart. J. Roy. Meteor. Soc.*, **107**, 29-50.

Moncrieff, M.W., 1992: Organized convective systems: Archetypal dynamical models, mass and momentum flux theory, and parametrization. *Quart. J. Roy. Meteor. Soc.*, **118**, 819-850

Nebuda, S.E., 1995: Development of an upper-level cloud parameterization for large scale models. Atmospheric Science Paper No. 582, Colorado State University, Dept. of Atmospheric Science, Fort Collins, CO 80523, 125 pp.

Nicholls, M.E., R.A. Pielke and W.R. Cotton, 1991: Thermally forced gravity waves in an atmosphere at rest. *J. Atmos. Sci.*, **48**, 1869-1884.

Olsson, P.Q., 1995: Evolution of balanced flow in a simulated mesoscale convective complex. Ph.D. dissertation, Colorado State University, 177 pp.

Peters, J.L., 1989: A case study of a quasi-stationary tropical convective line. M.S. thesis, Pennsylvania State University, 84 pp.

Pielke, R.A., W.R. Cotton, R.L. Walko, C.J. Tremback, W.A. Lyons, L.D. Grasso, M.E. Nicholls, M.D. Moran, D.A. Wesley, T.J. Lee and J.H. Copeland, 1992: A comprehensive meteorological modeling system — RAMS. *Meteorol. Atmos. Phys*, **49**, 69-91.

Randall, D.A., and G.J. Huffman, 1980: A stochastic model of cumulus clumping. *J.*

Atmos. Sci., **37**, 2068-2078.

Randall, D.A., and D.-M. Pan, 1993: Implementation of the Arakawa-Schubert Cumulus Parameterization with a prognostic closure. *Meteorological monographs: The representation of cumulus convection in numerical models*, K.A. Emanuel and D.J. Raymond, eds., 137-144.

Rotunno, R.J., J.B. Klemp and M.L. Weisman, 1988: A theory for strong, long-lived squall lines. *J. Atmos. Sci.*, **45**, 463-485.

Roux, F., 1988: The West African squall line observed on 23 June 1981 during COPT 81: Kinematics and thermodynamics of the convective region. *J. Atmos. Sci.*, **45**, 406-426.

Roux, F., and S. Ju, 1990: Single-Doppler observations of a West-African squall line on 27-28 May 1981 during COPT 81: Kinematics, thermodynamics and water budget. *Mon. Wea. Rev.*, **118**, 1826-1854.

Shaw, B.L., 1995: The effect of soil moisture and vegetation heterogeneity on a great plains dryline: A numerical study. Colorado State University Department of Atmospheric Science Research Paper No. 576, 93 pp.

Simpson, J., N.E. Westcott, R.J. Clerman and R.A. Pielke, 1980: On cumulus mergers. *Arch. Meteorol. Geophys. Bioklimatol., Ser. A* **29** , 1-40.

Stensrud, D.J., and R.A. Maddox, 1988: Opposing mesoscale circulations, a case study. *Wea. Forecasting*, **3**, 189-204.

Sui, C.-H., and M. Yanai, 1986: Cumulus ensemble effects on the large-scale vorticity and momentum fields of GATE. Part I: Observational evidence. *J. Atmos. Sci.*, **43**, 1618-1642.

Szeto, K.K., and H.-R. Cho, 1994: A numerical investigation of squall lines. Part I: The control experiment. *J. Atmos. Sci.*, **51**, 414-424.

Tao, W.-K., J. Simpson, C.-H. Sui, B. Ferrier, S. Lang, J. Scala, M.-D. Chou and K. Pickering, 1993: Heating, moisture, and water budgets of tropical and midlatitude squall lines: Comparisons and sensitivity to longwave radiation. *J. Atmos. Sci.*, **50**, 673-690.

Tiedtke, M., 1993: Representation of clouds in large-scale models. *Mon. Wea. Rev.*, **121**, 3040-3061.

Tollerud, E.I., and S.K. Esbensen, 1983: An observational study of the upper-tropospheric vorticity fields in GATE cloud clusters. *Mon. Wea. Rev.*, **111**, 2161-2175.

Tremback, C.J., and R. Kessler, 1985: A surface temperature and moisture parameterization for use in mesoscale numerical models. *Preprints, 7th AMS Conference on Numerical Weather Prediction*, June 17-20, Montreal, Amer. Meteor. Soc., Boston, 433-434.

Tripoli, G.J., and W.R. Cotton, 1982: The Colorado State University three-dimensional cloud/mesoscale model—1982. Part I: General theoretical framework and sensitivity experiments. *J. de Rech. Atmos.*, **16**, 185-220.

Tripoli, G.J., and W.R. Cotton, 1989a: Numerical study of an observed orogenic mesoscale convective system. Part I: Simulated genesis and comparison with observations. *Mon. Wea. Rev.*, **117**, 273-304.

Tripoli, G.J., and W.R. Cotton, 1989b: Numerical study of an observed orogenic mesoscale convective system. Part II: Analysis of governing dynamics. *Mon. Wea. Rev.*, **117**, 305-328.

Webster, P.J., and R.A. Houze, Jr., 1991: The Equatorial Mesoscale Experiment (EMEX): An overview. *Bull. Amer. Meteor. Soc.*, **72**, 1481-1505.

Weisman, M.L., 1992: The role of convectively generated rear-inflow jets in the evolution of long-lived mesoconvective systems. *J. Atmos. Sci.*, **49**, 1826-1847.

Weisman, M.L., and J.B. Klemp, 1982: The dependence of numerically simulated convective storms on vertical wind shear and buoyancy. *Mon. Wea. Rev.*, **110**, 504-520.

Weissbluth, M.J., and W.R. Cotton, 1993: The representation of convection in mesoscale models. Part I: Scheme fabrication and calibration. *J. Atmos. Sci.*, **50**, 3852-3872.

Wetzel, P.J., W.R. Cotton and R.L. McAnelly, 1983: A long-lived mesoscale convective complex. Part II: Evolution and structure of the mature complex. *Mon. Wea. Rev.*, **111**, 1919-1937.

Williams, M., and R.A. Houze, Jr., 1987: Satellite-observed characteristics of winter monsoon cloud clusters. *Mon. Wea. Rev.*, **115**, 505-519.

Wilson, M.F., and A. Henderson-Sellers, 1985: A global archive of land cover and soils data for use in general circulation climate models. *J. Climatol.*, **5**, 119-143.

Wong. T., G.L. Stephens, P.W. Stackhouse, Jr. and F.P.J. Valero, 1993: The radiative budgets of a tropical mesoscale convective system during EMEX-STEP-AMEX Experiment. II: Model results. *J. Geophys. Res.*, **98**, 8695-8711.

Wu, X., 1993: Effects of cumulus ensemble and mesoscale stratiform clouds in midlatitude convective systems. *J. Atmos. Sci.*, **50**, 2496-2518.

Wu, X., and M. Yanai, 1994: Effects of vertical wind shear on the cumulus transport of momentum: Observations and parameterization. *J. Atmos. Sci.*, **51**, 1640-1660.

Xu, K.-M., 1995: Partitioning mass, heat, and moisture budgets of explicitly simulated cumulus ensembles into convective and stratiform components. *J. Atmos. Sci.*, **52**, 551-573.

Yanai, M., S. Esbensen and J.-H. Chu, 1973: Determination of bulk properties of tropical cloud clusters from large-scale heat and moisture budgets. *J. Atmos. Sci.*, **30**, 611-627.

Zhang, D.-L., K. Gao and D.B. Parsons, 1989: Numerical simulation of an intense squall line during 10-11 June 1985 PRE-STORM. Part I: Model verification, *Mon. Wea. Rev.*, **117**, 960-994.

Zipser, E.J., 1982: Use of a conceptual model of the life-cycle of mesoscale convective systems to improve very-short-range forecasts. *Nowcasting*, Academic Press, Inc., 191-204.